Université Libre de Bruxelles
Faculté des Sciences Appliquées
Service de Chimie-Physique E.P.
Pr. J.C. Legros

Année Académique 2003-2004

Evolution and stability of falling liquid films with thermocapillary effects

Février 2004

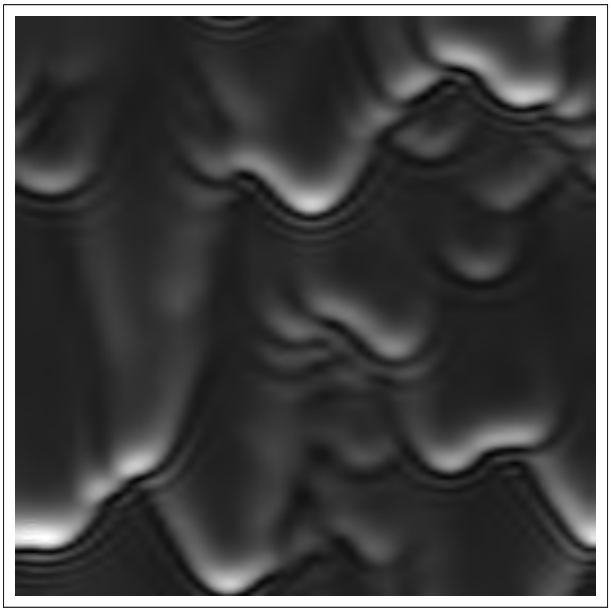

Promoteur : Dr. P. Colinet
Co-promoteur : Pr. O.A. Kabov

Thèse présentée par Benoit Scheid pour obtenir le grade de Docteur en Sciences Appliquées.

Remerciements (Aknowledgements)

Cette thèse est le fruit de diverses collaborations toutes aussi intenses qu'enrichissantes. Nombreuses sont donc les personnes que je tiens ici à remercier personnellement.

Ma profonde gratitude va tout d'abord au professeur Jean Claude Legros, directeur du service de Chimie-Physique, pour la confiance et le soutien qu'il m'a apportés tout au long de ce travail. Sa bienveillance à mon égard et les conditions de travail optimales qu'il m'a offertes ont rendu possible la réalisation de cette thèse.

De la même manière, Pierre Colinet, promoteur de cette thèse m'a aiguillé et supporté tout au long de celle-ci. Sa rigueur scientifique implacable, tant pour la forme que pour le fond, sa clairvoyance et ses commentaires judicieux ont très nettement contribué à l'amélioration de ce manuscrit. Merci d'avoir été, et d'être toujours d'ailleurs, "mi padre spiritual".

Oleg Kabov de l'Institut de Thermophysique de Novosibirsk en Russie a pris une part active dès le début de cette thèse. Il en est le co-promoteur, et à ce titre, m'a enseigné les ficelles du métier d'expérimentateur. L'expérience que nous avons montée ensemble au laboratoire a motivé, pour la plupart, les travaux rapportés dans le présent manuscrit. Qu'il trouve ici toute ma reconnaissance.

Mes remerciements les plus sincères vont également au professeur Alexander Oron. L'étroite collaboration qui s'est opérée durant cinq mois passés au sein de son service de mécanique à Haïfa en Israël fût sans conteste très fructueuse quant à l'apprentissage des méthodes numériques et à la qualité de son support scientifique.

Je voudrais aussi remercier Uwe Thiele et Jan Skotheim pour leur aide précieuse concernant ma "première" analyse de stabilité linéaire, durant leur séjour à l'Institut Pluridisciplinaire de Madrid. Uwe m'a de plus guidé à plusieurs reprises lors des phases sinueuses que sont celles de la préparation d'articles. Je lui en serai toujours très reconnaissant.

Ensuite, quatre mois passés à Madrid m'ont permis de découvrir le personnage étonnant qu'est Manuel Velarde, directeur de l'unité des fluides à l'Institut Pluridisciplinaire de Madrid. Quarante années au service de la science n'ont moins que jamais eu raison de sa passion fulgurante et débordante pour la physique des fluides dont il est devenu un élément incontournable, du moins si l'on en croit les multiples visiteurs scientifiques qu'il draine chaque année au sein de son service. C'est donc une véritable chance pour moi d'avoir pu collaborer avec lui. Je le remercie ici très vivement pour l'enthousiasme qu'il a porté à mon travail, l'ouverture qu'il lui a donnée grâce à ces nombreux commentaires et 'analogies' et son soutien toujours extrêmement motivant.

La dernière collaboration en date que je voudrais mentionner ici est sans aucun doute la plus dynamique et prolifique. Il s'agit de celle avec Christian Ruyer-Quil du laboratoire FAST (Fluides, Automatique et Systèmes Thermiques) de l'université de

Paris-Sud à Orsay. Les six mois passés à Paris ont constitué une période mémorable, emprunte de multiples et intenses surprises, joies et discussions qu'ont procurées nos travaux en commun. Je voudrais le remercier ici très profondément pour ses innombrables coups de mains, ses encouragements de tous les jours, son enthousiasme toujours renouvelé et surtout le temps précieux qu'il m'a consacré généreusement à m'enseigner les ficelles de la dynamique des films minces.

Je voudrais maintenant remercier les nombreuses personnes du laboratoire qui m'ont aidé ou soutenu durant cette thèse. Qu'ils reçoivent ici mes plus chaleureux remerciements: Christophe Minetti pour son aide précieuse en programmation ou plutôt pour ses programmes très précieux; Marcel Hennenberg pour les nombreuses discussions et la mine d'or que constituent ses connaissances bibliographiques; Andrei Vedernikov pour m'avoir fait changer d'air en apesanteur et pour ses encouragements quotidiens; Frank Dubois, Olivier Dupont, Luc Joannes et Jean-Luc Dewandel pour leur aide et conseils concernant la méthode optique de Schlieren; André Muylaert pour les nombreuses oeuvres d'art qu'il a réalisées durant le montage expérimental; Jean-Charles Dupin pour son support logistique à toute épreuve; Patrick Queeckers pour les nombreuses (re)configurations des PC's et sa grande disponibilité; et puis tous ceux qui m'ont donné un coup de pouce par-ci par-là, dont Eric Istasse, Stefan Van Vaerenbergh, Carlo Iorio, Denis Melnikov, Valentina Shevtsova et Rachid Naji.

Il y a également des personnes étrangères au service qui m'ont aidé ou avec qui j'ai eu l'occasion de discuter, voire de collaborer pour des parties bien spécifiques de mon travail: Slavtcho Slavtchev, Svetla Miladinova, Hein Auracher, Alexander Maun, Radyadour Zeytounian, Serafim Kalliadasis, Philip Trevelyan, Michael Bestehorn, Paul Manneville, Dominique Salin et la très efficace Maria-Jesus Martin.

Les objectifs de cette recherche n'auraient pas pu être atteints sans le support financier de la communauté européenne dans le cadre d'abord du réseau I.C.O.P.A.C. qui m'a permis d'effectuer trois séjours prolongés à l'étranger, l'un de cinq mois en Israël en 2001 et deux de quatre et six mois à Madrid en 2002 et 2003; et ensuite grâce à la bourse Marie-Curie qui m'a permis de travailler six mois à Paris en 2002-2003. La coopération CGRI-FNRS-CNRS 2003-2004 a également facilité la collaboration avec le FAST à Paris.

Parmi tous ceux qui m'ont encouragé inlassablement dont ma famille et mes précieux amis, je voudrais surtout remercier ma maman, mon papa et ma sœur. Ils m'ont toujours supporté dans mes choix avec énormément de vigueur, de confiance et d'amour. Je voudrais aussi remercier mon grand-père qui n'est plus parmi nous mais qui m'a donné le goût pour la science et l'impulsion nécessaire pour démarrer une thèse. Merci aussi à Lala et François pour l'atmosphère tellement chaleureuse et productive qu'il m'ont offerte durant les longues périodes de rédaction.

J'aimerais finalement couvrir de mille et une fleurs de merci celle qui depuis plus de quatre magnifiques années ensoline chacune de mes journées.

Contents

Nomenclature

Remark: unless units are specified in parenthesis, the quantities are dimensionless.

Quantities	
$A = (h_{\max} - h_{\min})/h_{\mathrm{N}}$	reduced wave amplitude
A	amplitude of harmonic disturbance (Ch.7)
b_{s}	basic state temperature gradient
$\mathrm{Bi} = \alpha\nu^{2/3}/\left[\lambda(g\sin\beta)^{1/3}\right]$	Biot number (at the film surface)
$\mathrm{B} = h_{\mathrm{N}}\mathrm{Bi}$	film Biot number
c	wave speed
c_p	liquid heat capacity (J/kgK)
$\mathrm{C} = \cos\beta$	normal component of the gravity
$\mathrm{Ct} = \cot\beta$	slope coefficient
$\mathcal{C} = \mathrm{Ct}/\kappa$	reduced slope coefficient
F_{w}	heating function at the wall
g	gravitational acceleration (m/s^2)
h	film thickness
$h_{\mathrm{N}} = \bar{h}_{\mathrm{N}}/l_\nu = (3\mathrm{Re})^{1/3}$	Nusselt film thickness
h_{res}	thickness of the residual layer
$\mathrm{i} = \sqrt{-1}$	imaginary number
k	wave number
$\mathrm{Ka} = \sigma_\infty/\left[\rho\nu^{4/3}\,(g\sin\beta)^{1/3}\right]$	Kapitza number
l	characteristic wavelength (m)
$l_\nu = \nu^{2/3}/(g\sin\beta)^{1/3}$	viscous length (m)
$l_\sigma = (\sigma_\infty/\rho g\sin\beta)^{1/2}$	capillary length (m)
L	heater length
$\mathcal{L} = (\mathrm{Ka}h_{\mathrm{N}})^{1/3}$	characteristic length for capillary ripples
$\mathrm{Ma} = \gamma\Delta T\mathrm{Ka}/\sigma_\infty$	Marangoni number based on l_ν
$\mathrm{M} = \mathrm{Ma}/h_{\mathrm{N}}^2$	film Marangoni number (TC)
$\mathrm{M} = \mathrm{Ma}/h_{\mathrm{N}}$	film Marangoni number (HFC)
$\mathrm{M}^\star = \mathrm{M}b_{\mathrm{s}}h_{\mathrm{N}}$	M based on the base state temperature gradient
$\mathcal{M} = \mathrm{M}/\kappa$	reduced Marangoni number
$\mathbf{n}$	unit normal vector
p	pressure (Ch.1)
$p = \int_0^h w\,dy$	spanwise local flow rate
P	base state pressure

$\mathrm{Pr} = \nu/\chi$	Prandtl number
$\mathrm{Pe} = \mathrm{Pr}\,\mathrm{Re}$	Péclet number
q_w	heat flux at the wall (W/m^2)
$q = \int_0^h u\,dy$	streamwise local flow rate
$Q = q - c\,h$	flow rate in the moving reference frame
$r_1,\ r_2,\ r_3$	corrections to the transverse parabolic profile
$\mathrm{Re} = u_\mathrm{N}\bar{h}_\mathrm{N}/\nu = g\sin\beta\bar{h}_\mathrm{N}^3/3\nu^2$	film Reynolds number
$\mathrm{R} = 3\mathrm{Re} = h_\mathrm{N}^3$	Re based on the linear wave speed $3u_\mathrm{N}$
$\mathrm{R_s} = 3\mathrm{Re}/2$	Re based on the film surface velocity
$\mathcal{R} = \mathrm{Re}/\kappa$	reduced Reynolds number
s	real growth rate
$s_1,\ s_2,\ s_3$	corrections to the streamwise parabolic profile
$\mathrm{S} = \sin\beta$	longitudinal component of the gravity
t	time
$t_\nu = \nu^{1/3}/(g\sin\beta)^{2/3}$	viscous characteristic time (s)
$t_1,\ t_2,\ t_3,\ t_4$	corrections to the temperature profile
T	temperature
ΔT	characteristic temperature difference (K)
$\mathbf{v} = (u, v, w)$	velocity
$U,\ V,\ W$	base state velocity
$\mathrm{We} = \mathrm{Ka}/h_\mathrm{N}^2 = \sigma/\left(\rho g\bar{h}_\mathrm{N}^2\sin\beta\right)$	Weber number
$x,\ y,\ z$	streamwise, cross-stream and spanwise coordinates

Greek letters	
α	heat transfer coefficient (W/m^2K)
β	wall inclination angle (rad)
$\gamma = -\partial\sigma/\partial T$	positive surface tension gradient (N/mK)
γ_1, γ_2	families of travelling wave solutions
$\Gamma = k\,c + \mathrm{i}\,s$	complex pulsation
$\delta = \Delta T/\Delta T_\mathrm{w}$	ratio between uniform and non-uniform heating
ε	film parameter
$\epsilon = \bar{h}_\mathrm{N}/l$	aspect ratio
η	amplitude of the film thickness perturbation (Ch.1)
$\eta = 1/\kappa^2$	viscous dispersion number
θ	surface temperature
Θ	base state temperature
$\kappa = \mathcal{L}/h_\mathrm{N}$	scale factor
λ	heat conductivity (W/mK)
μ	dynamic viscosity (kg/ms)
$\nu = \mu/\rho$	kinematic viscosity (m^2/s)
$\xi = x - c\,t$	coordinate in a moving frame of reference
ρ	density (kg/m^3)
σ	surface tension (N/m)
ς	wavenumber shift
$\boldsymbol{\tau_x},\ \boldsymbol{\tau_z}$	unit tangent vector
τ	amplitude of the temperature perturbation
ϕ	amplitude of the cross-stream velocity perturbation
φ	amplitude of the stream function
$\chi = \lambda/\rho c_p$	heat diffusivity (m^2/s)
ψ	stream function

Symbols & operators	
$\mathrm{d}/\mathrm{d}t \equiv \partial_t + (\mathbf{v}\cdot\boldsymbol{\nabla})$	material derivative
$\mathrm{D} \equiv \mathrm{d}/\mathrm{d}y$	derivative with respect to y
∂_i	partial derivative with respect to i
$\boldsymbol{\nabla} \equiv (\partial_x, \partial_y, \partial_z)^\mathrm{t}$	gradient operator
$\boldsymbol{\nabla}_s$	surface gradient operator
$\boldsymbol{\nabla}_{xz} \equiv (\partial_x, 0, \partial_z)^\mathrm{t}$	parallel gradient operator
$\Re$	real part of a complex number
$\Im$	imaginary part of a complex number
$\langle\cdot\rangle_i$	average along one wavelength (period) of the variable i
$\cdot\big\vert_h$	evaluation at the free surface $y = h$

Subscripts	
c	critical (for instability)
∞	ambient air far from the interface
L	linear problem
m	maximum
ν	based on the length scale l_ν
N	based on the length scale $\bar{h}_{\rm N}$ (N for Nusselt)
$\perp$	vertical wall ($\sin\beta = 1$)
s	surface
w	wall
x, y, z	components in x, y, z directions

Superscripts	
$\star$	base state temperature
$*$	saddle-node bifurcation
(i)	$i^{\rm th}-$order in the gradient expansion

Overscripts	
$-$	dimensional quantity (when necessary)
$\wedge$	average value
$\sim$	perturbed quantity

Acronyms	
BE	Benney equation
BL	boundary layer (model)
CL	closed (flow)
HB	Hopf bifurcation
HFC	heat flux condition
IBL	integral boundary layer (model)
OP	open (flow)
PD	period doubling
TC	temperature condition
WIBL	weighted integral boundary layer (model)

Introduction

Interest for thin falling films and aims of this work

The development of efficient means for interfacial heat and mass transfer in engineering applications has received a great deal of interest for several decades. Thin liquid film flows play a central role in such equipments because of their small thermal resistance and their large contact area at small specific flow rates. Typical examples involving falling liquid films include heat transport from a hot wall to a film, vapor condensation and absorption of dilute gas (see *e.g.* Alekseenko, Nakoryakov & Pokusaev [1]). In coating technology, the hydrodynamic behaviour of the initial liquid film can affect the quality of the final coated surface. Thin films are also used as lubricant layers for the flow of crude oil in pipes and channels. In rocket engines the liquid film is used for thermal protection of the combustion chamber walls. Falling films are also commonly used in cooling of microelectronic equipment (local heat source). Falling film evaporators are widely used for separation of multicomponent mixtures in chemical and food industries. They even represent the state-of-the-art technique in sugar industry. They are also the basic components in salt sea-water distilling plants. Finally, film heat exchangers are used as condensers of cooling agents in cryogenic technology. Some of the above-mentioned industrial applications involving falling liquid films are detailed in appendix A.

The length of film flows may vary from several centimeters in cooling processes of electronic components to about ten meters in industrial thin film evaporators. In thin film flows, the most widely observed phenomena, such as formation of surface waves, breaking of a stream into rivulets, and evaporation with termination of the liquid layer at a contact line, are caused by various interfacial instability mechanisms. Therefore, the understanding of the stability and evolution of falling heated films will help to improve predictions of heat and mass transfer rates. For instance, instabilities of free film surfaces play a crucial role by inducing wavy regimes that are known to enhance heat and/or mass transfer [23]. Frisk & Davis [37] and Goren & Mani [44] have shown that heat and mass transfer across a laminar film can increase by as much as 10-100% as compared to flat films, when large amplitude solitary waves appear at the interface.

From a fundamental point of view, thin viscous film flow driven by gravity is a reference problem in the theory of spatio-temporal chaos. We can observe a well-organized cascade of bifurcations that leads from the flat film state (or laminar) to a state of disorder (or turbulence). The instabilities responsible for these bifurcations

are typically associated with **long-wave modes**, as based on the Cross & Hohenbreg classification [24], depending on the behaviour of the growth rate in the neighborhood of the critical point. In the context of the present work, "long wave" means that the waves are always long as compared to the film thickness.
In this thesis, we will focus on two distinct long-wave instability mechanisms: one occurring when a thin layer is heated from below and induced by the so-called 'Marangoni effect', and the other producing waves when the layer is flowing along an inclined plate (falling liquid film). The main objectives of this work are to study the coupling between those two mechanisms in the linear and nonlinear regimes, to propose the most appropriate models with respect to the flow conditions considered and to compare our theoretical results with available experimental data.

Phenomenology

In this section, we present the phenomenology of the both above-mentioned mechanisms, including their coupling. We also show some experimental results for an inhomogeneously heated falling liquid film.

Marangoni effect

Theoretical and experimental studies of various aspects of Marangoni convection are numerous in literature (see *e.g.* Colinet, Legros & Velarde [23] or Velarde & Zeytounian [142]). The Marangoni effect arises from the fact that surface tension at the interface between two fluids (here a liquid and a gas) is temperature or concentration–dependent; the effect will be referred to as the thermocapillary or solutocapillary effect, respectively. When a temperature (or concentration) gradient is applied along a fluid layer having a free surface, the emergence of temperature (or concentration) non uniformity at the interface leads to tangential stresses equal to the surface tension gradient. Despite the similarity between thermocapillary and solutocapillary effects (that are both referred to as the Marangoni effect), only the latter will be studied in this work.
When a temperature gradient is applied across a horizontal fluid layer, the layer being heated from below, two mechanisms related to the Marangoni (thermocapillary) effect can lead the liquid layer from a quiescent conducting state to convective motions [23]. Both of them originate from the interfacial stress generated at the interface by the surface tension gradient. This gradient can have two origins, a modification of the temperature distribution in the bulk due to the advection by the velocity field, or a modulation of the free surface elevation, both of them generating a temperature gradient at the interface. The two mechanisms were classified by Goussis & Kelly [46] as the P-mode and the S-mode, respectively. The **P-mode** generally yields convection rolls or hexagonal or square cells, the size of which is of the same order of magnitude than the depth of the layer. This instability is referred to as the *Marangoni–Bénard instability* and was theoretically evidenced by Pearson [100]. The **S-mode** produces large-scale deformations, the horizontal size of which is much larger than the depth

of the layer, and may generally lead to dry spots. This instability is referred to as the *long-wave Marangoni instability* and was first theoretically evidenced by Scriven & Sterling [125], who neglected the gravity, which was later corrected by Smith [129]. Since in this thesis, devoted to the problem of long-wave instabilities, we are only interested in very thin films – the thickness of which is much smaller than a millimeter –, the P-mode which is of short-wave type is not relevant here. Therefore, from now and in the remaining of this work, speaking about the Marangoni effect will always refer to the thermocapillary long-wave instability, or S-mode.

Let us then detail the mechanism of this long-wave thermocapillary instability, assuming that, as for most of fluids, the surface tension decreases with the temperature. As said above, this instability is triggered by the modification of the basic temperature at the free surface by the surface deformation (Goussis & Kelly [45]). Consider a cross-section of a horizontal liquid layer heated from below at the temperature T_w as sketched on figure 1; T_∞ being the temperature of the ambient gas far from the interface. If an infinitesimal deformation occurs at the interface, what corresponds to the stage "1" in figure 1, the film temperature in the trough of a depression will be hotter than at the crest of an elevation, given that $T_\mathrm{w} > T_\infty$. Because the surface

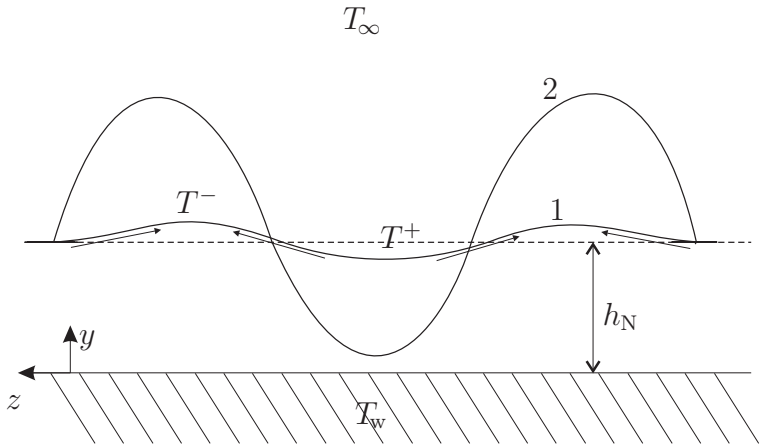

Figure 1: Mechanism of a pure long-wave Marangoni instability.

tension decreases with the temperature, a flow is induced along the interface from a hot spot to a cold spot. This flow acts in a way to amplify the initial perturbation (stage "2" in figure 1) such that the basic flat film is unstable. What mainly opposes the deformation is the gravity which tends to maintain the layer flat. For disturbances of sufficiently short wavelength, surface tension also acts so as to suppress surface deformation. Therefore instability with respect to this mode takes the form of large-wavelength disturbances for which the hydrostatic pressure is the only stabilizing force. Instability occurs then when the balance between the Marangoni stress produced by the temperature gradient across the layer and the hydrostatic pressure turns in favour of the former. This instability can effectively lead to dry spots formation as evidenced experimentally by VanHook *et al.* [141].

Let us now figure out the consequence of tilting the plate: the liquid layer will fall down, driven by gravity, and the long-wave Marangoni instability will lose its isotropy,

which means that the flow will align the deformations into rivulets as drawn on figure 2, and demonstrated theoretically by Joo *et al.* [54].

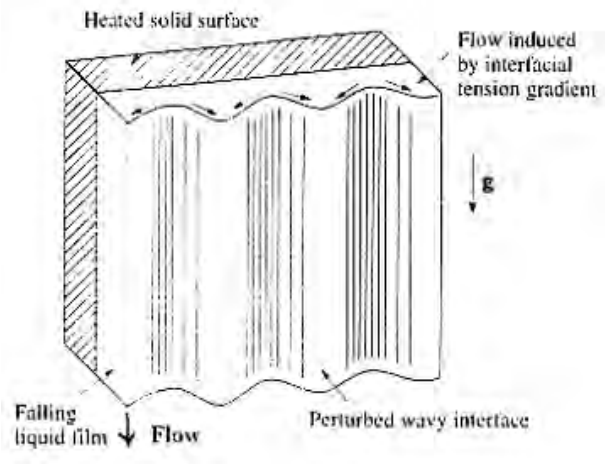

Figure 2: Rivulet pattern at the surface of a falling liquid film.

Yet, non heated (isothermal) falling film can also be unstable with respect to surface wave instability, the mechanism of which is detailed below.

Surface wave instability

Thin liquid film flowing along an inclined plate in isothermal conditions experiences long wavelength deformations at the film surface as sketched on figure 3. These

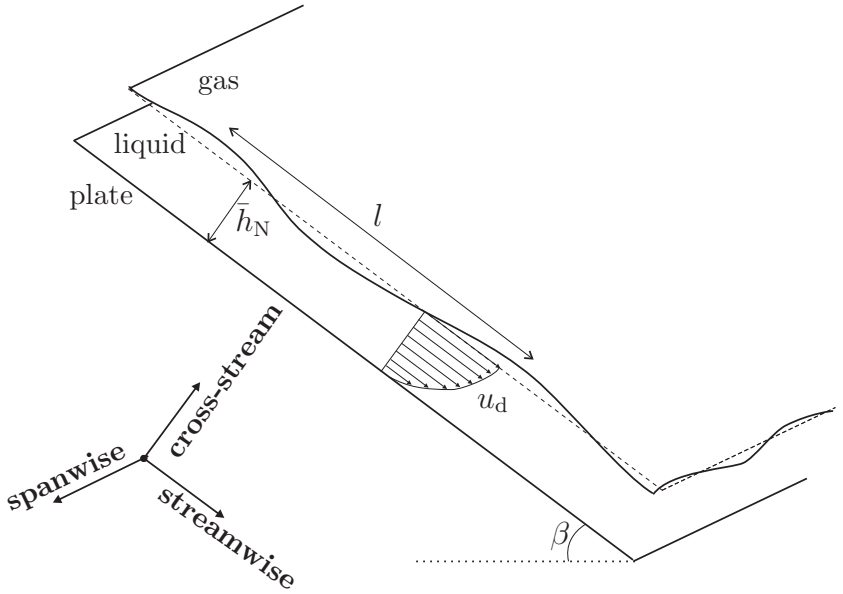

Figure 3: Sketch of a thin liquid film of mean film thickness $\bar{h}_N$ flowing down an inclined wall of inclination angle β; u_d is a parabolic velocity profile corresponding to a fully-developed viscous film flow.

waves result from a long-wave instability classified by Goussis & Kelly [46] as the hydrodynamic or **H-mode**. Smith [130] provides a detailed discussion about the three related mechanisms influencing this *long-wave hydrodynamic instability*: the first one is due to gravity and triggers the wave motion, the second one involves inertia and amplifies the wave motion, the third one is due to the hydrostatic pressure and can prevent the wave motion. Let us describe these three mechanisms in general terms [130] (see chapter 1 for mathematical formulations):

I Consider a disturbance to the liquid film in which the top surface is deflected upward slightly over a lengthscale l that is much longer than the depth $\bar{h}_{\mathrm{N}}$ of the film. Because the height of the top surface varies slowly in the streamwise direction, the velocity profile u at each streamwise location will remain close to a fully-developed viscous film flow characterized by a parabolic velocity profile as depicted by u_{d} in figure 3. It can be shown that the net longitudinal flow rate in the film is positive and that it increases with the depth of the film. Thus, at the crest of the deflection the longitudinal flow rate is a maximum and it decreases at the troughs. The net result of this, as shown on figure 4, is that gravity draws fluid toward the front face of the crest, deflecting it upward, and gravity drains fluid from the rear face, deflecting it downward. This first

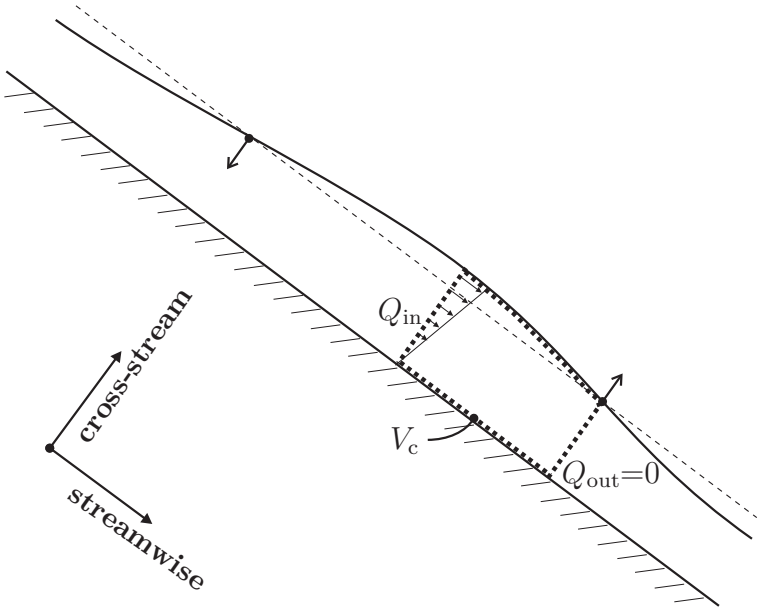

Figure 4: A disturbance to the free surface. The dashed line is the undisturbed free-surface position. It shows a control volume V_{c} (dotted box) enclosing the film on the right-hand side of the disturbance crest. There is a net inflow Q_{in} on the left-hand side of the control volume, but no outflow on the right-hand side. To conserve mass, the interface must move in the positive cross-stream direction. Likewise, for a control volume on the left-hand side of the crest, the interface must move in the negative cross-stream direction. These interface motions (indicated by arrows) result in a translation of the disturbance to the streamwise direction.

mechanism produces a forward motion of the disturbance without growth at a phase speed larger than the velocity of any fluid particle in the undisturbed film (this will be shown in chapter 1). This wave motion will be referred to as **kinematic waves**.

II Now, at a particular instant in time, consider a streamwise location that is at the front face of a disturbance crest. Here, the surface height is increasing because of the forward motion of the disturbance. The flow in the bulk of the film is accelerating at this position because it is attempting to follow the fully-developed viscous velocity profile dictated by the surface height increase. However, inertial effects prevent the flow from accelerating fast enough to completely follow this velocity. The result is that the volume flux in the film is not as large as it should be if this was truly a fully-developed film flow. At the rear face of the crest, the velocity is decreasing, but inertial effects similarly prevent the flow from decelerating rapidly enough. Thus the volume flux in the film is larger than that due to a fully developed film flow. The net effect of these two volumes fluxes can result in an accumulation of fluid underneath the disturbance crest and an increase in the interfacial displacement, as shown on figure 5.

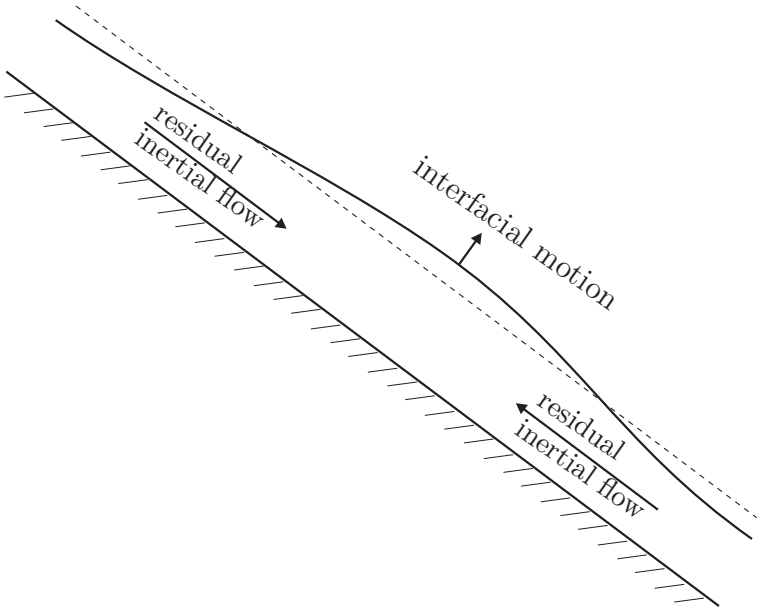

Figure 5: Film flow and induced interfacial motion produced by the effects of inertia. The dashed line is the undisturbed free-surface position.

III The disturbance also produces an increase in the hydrostatic pressure under the crest proportional to the local depth of the film. This pressure tends to push fluid away from the disturbance crest, towards the troughs were the hydrostatic pressure is lower, resulting in a depletion of the fluid under the crest and a decrease in the depth of the film, as shown on figure 6. This stabilizing flow

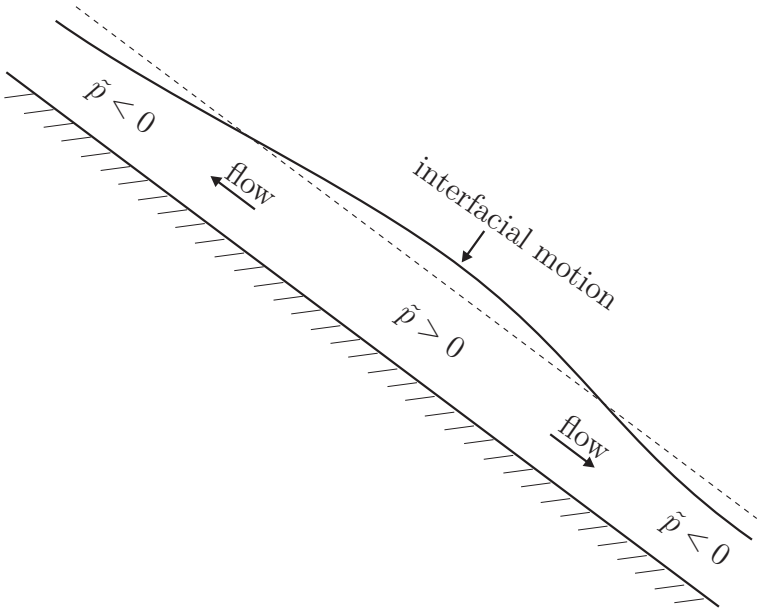

Figure 6: The direction of the disturbance film flow and the induced interfacial motion when an increase of the hydrostatic pressure lies underneath a disturbance crest; $\tilde{p}$ is the change of hydrostatic pressure due to disturbances. The dashed line is the undisturbed free-surface position.

competes with the inertial accumulation of fluid under the crest. If the inertial effect, as measured by the Reynolds number, is large enough, the film is unstable and the disturbance grows. Hence, a film falling along a vertical wall is always unstable with regards to free surface disturbances since the effect of hydrostatic pressure cancels (Yih [147]). Because of the competing forces of inertia and hydrostatic pressure involved in the growing of the initial kinematic waves, one speaks then about **dynamic waves**.

In conclusion, a key point of the hydrodynamic instability mechanism (H-mode) is the fact that the kinematic waves generated at the interface travel much faster than any fluid particles inside the film, such that inertia plays a central role in the growth of the instability by introducing a shift between the vorticity field generated by the kinematic waves and the film surface displacement (Ruyer-Quil [107]). The threshold of this H-mode and its linear stability properties were first scrutinized by Benjamin [6].

Many experimental studies have been devoted to the wavy regime of film flows since the first observations by Kapitza & Kapitza [69]. Thin films generally exhibit a cascade of symmetry-breaking bifurcations leading from two-dimensional waves, *i.e.* is independent of the spanwise coordinate, to three-dimensional solitary waves (see below, figure 7).

Surface wave instability and Marangoni effect

Let us consider now the coupling between the thermocapillary and the surface wave instability. Conditions obtained from linear stability analysis of a heated falling liquid film by Goussis & Kelly [46] has revealed that the thermocapillary S-mode predominates at low flow rates – or equivalently for thin films – where the Marangoni stress in the presence of surface deformation, generated by the temperature gradient across the layer is large and the stabilizing hydrostatic pressure is small. On the other hand, the hydrodynamic H-mode prevails at large flow rates where the destabilizing inertial effects become dominant. Nevertheless, Joo *et al.* [53] have shown that for a large range of parameters, the S and H-modes are both present and actually reinforce each other.
Interestingly, figure 7 shows an experimental picture recently obtained by Kabov *et al.* [60] which evidences the possible coexistence between rivulet structures produced by transverse thermocapillarity (see figure 2) and three-dimensional hydrodynamic waves (that are also modified by thermocapillarity).

Figure 7: Picture showing the coexistence between three-dimensional hydrodynamic waves flowing downstream and rivulets aligned with the flow induced by thermocapillary effect. The wall is heated at constant temperature and Re = 22. Courtesy of O.A. Kabov [60].

Inhomogeneous heating

Many experimental studies performed by Kabov and coworkers have also focused on thin films falling down inhomogeneously heated vertical plates and have revealed the occurrence of novel instabilities [55, 62, 59, 58, 119], specifically in the case of a locally heated film at small Reynolds number, as shown on figure 8. At the upper edge of the heater, the temperature of the plate increases along the flow direction. Consequently, as the temperature of the fluid surface increases, the surface tension decreases. The concomitant surface tension gradient produces a Marangoni flow opposed to the gravitationally driven flow. As first reported by Kabov, Diatlov &

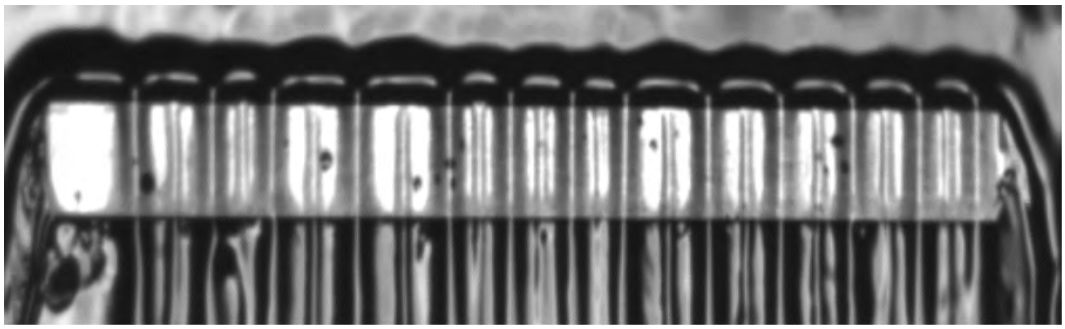

Figure 8: Steady regular structure for a 10% ethyl-alcohol aqueous solution, Re = 1 [63]. The bright rectangular zone corresponds to the heater. The characteristic wavelength of the structure is 10 mm, while the film thickness before the heater is about $100\,\mu m$.

Marchuk [61], the competing flow produces a horizontal bump of increased film thickness at the upper edge of the heater, which may become unstable and develop rivulets periodic in the spanwise direction, as shown on figure 8.
The phenomena shown on both figures 7 and 8 present some of the milestones for this thesis. In both cases, the Marangoni effect plays a crucial role in the pattern formation. In the homogeneous heating case of figure 7, the Reynolds number is moderate (Re = 22) such that hydrodynamic waves have large amplitudes and become rapidly three-dimensional. On the contrary, in the local heating case of figure 8, the Reynolds number is small (Re = 1) such that hydrodynamic waves have small amplitudes (at least not detected by the optical technique) while thermocapillary effect is dominant and induces steady regular patterns. Therefore, depending on the flow regime, as measured by the Reynolds number, different levels of simplification can apply to the model equations (Navier-Stokes/Fourier equations), as discussed in the next section.

Modelling

As already mentioned, the interfacial deformations (as those of figures 7 and 8) are always long as compared to the film thickness. The cross-stream and streamwise/spanwise scales are thus separated, similar to the separation of scales sustaining the boundary layer theory (Schlichting [123]). The approximations that lead to the boundary layer equations also apply for thin film flows where the pressure is here mostly governed by gravity and surface tension (Chang *et al.* [15, 16]). In thin film theory, the separation of scales leads to the so-called **lubrication approximation**. The large ratio between a typical wavelength of the instability and the average film thickness enables us to perform a gradient expansion of the temperature and velocity fields and subsequently to obtain systems of equations of reduced dimensionality which model the real dynamics of the flow. In the region where inertia is not important, namely if the Reynolds number is small, the temperature and velocity fields turn

out to be slaved to the kinematics of the free surface and a single evolution equation for the film thickness h can be derived, as shown in next chapters.
For isothermal films, this was done first by Benney [7] followed by Gjevik [41, 42], Lin [79], Atherton & Homsy [3] and many other authors (see the review by Oron, Davis & Bankoff [97]). Benney's approach is exact in the limit of small Reynolds numbers but it breaks down at an $O(1)$ Reynolds number leading to equations that may exhibit non-physical finite-time blow-up (Pumir, Manneville & Pomeau [103]). This behaviour is a sign of the own dynamics of the slaved modes for larger Reynolds numbers. A solution to this unrealistic behaviour was proposed by Ooshida [93] who modified the Benney expansion by using a Padé approximants regularization procedure for divergent asymptotic series. Though the equation he obtained does not suffer from the drawback of finite-time blow-up, it does fail to describe accurately the dynamics of the film at moderate Reynolds numbers (in the region $\sim 10 - 30$) since its solitary-wave solutions exhibit unrealistically small amplitudes and speeds.
On the other hand, the so-called integral-boundary-layer (**IBL**) approach performs much better in the region of moderate Reynolds numbers. This formulation combines the assumption of a parabolic velocity profile within the film with the Kármán-Polhausen averaging method of boundary-layer theory. The approach was first suggested by Kapitza to describe stationary waves and later on extended by Shkadov and coworkers [69, 126, 28, 29] to non-stationary and three-dimensional films. Nonlinear waves far from criticality obtained from the IBL model are in quantitative agreement with the boundary layer [28] and full Navier-Stokes equations for moderate Reynolds numbers [27, 115, 104].
Despite the success of the IBL model in the nonlinear regime, it does not predict very accurately neutral and critical conditions, except for large inclination angles; indeed for a vertical falling film, the IBL model gives the correct value for the critical Reynolds number, i.e. zero so that the flow is unstable for all Reynolds numbers. For all other inclination angles, the IBL model introduces an error, typically of the order of 20% for the critical Reynolds number. As shown by Ruyer-Quil & Manneville [108], this discrepancy is due to the velocity profile assumed in the Shkadov method. Although this profile seems to be in agreement with the experiments by Alekseenko, Nakoryakov & Pokusaev [1], and hence does capture most of the physics, corrections to the profile, known to exist at first order in the long-wave expansion (see chapter 2), are important for an accurate prediction of the linear instability threshold. Ruyer-Quil & Manneville [109] have then cured this discrepancy by combining a systematic gradient expansion with weighted residual techniques using polynomials as test functions, obtaining models referred to hereafter as weighted-integral-boundary-layer models (**WIBL**). Applying a Galerkin method, they obtained a new first-order model, involving two coupled evolution equations only for the film thickness h and the local flow rate q, as for the Shkadov's equation. The only difference is in the coefficients of the terms originating form inertial effects which allows to obtain a correct instability threshold for all inclination angles. Another advantage of their model is that it enables a correct representation of the velocity profile accounting for its deviations with respect to the parabolic profile. Next, Ruyer-Quil & Manneville derived a second-order model involving four equations, allowing the corrections themselves

to evolve according to their own dynamics. Moreover they also proposed a simplified second-order model involving two fields only, that can be derived by applying a genuine Galerkin method. They pointed out the role played by the second-order viscous dispersion on homoclinic chaos, wave profiles and stationary wave selection, using the tools of dynamical-systems theory to study waves stationary in their moving frame. The spatial evolution of the solutions of their model in the presence of noise or periodic forcing compares favourably to both experiments and time-dependent simulations of the boundary layer equations [109, 110].
For the problem of a film flowing down along a uniformly heated wall, Joo, Davis & Bankoff [53] included in addition to thermocapillary effects, evaporation and intermolecular forces. They used the Benney long-wave (lubrication) approximation to obtain an equation for the evolution of the local film thickness. In the absence of evaporation effects and intermolecular forces, their evolution equation will be referred to hereafter merely as the Benney equation (**BE**), even though it includes the Marangoni effect. These authors compared the influence of the H and S-modes on the shape of the nonlinear waves by performing numerical experiments in time using periodic boundary conditions. They observed, as already mentioned, that both instability modes reinforce each other. They also noted that the H-mode is more sensitive to the local layer thickness – with the humps growing more rapidly than the troughs – than the S-mode for which the growths at the crests or at the troughs are similar.
To our knowledge, the interaction between S and H-modes has only been studied recently for moderate Reynolds numbers (*i.e.* outside the range of validity of BE) by Kalliadasis *et al.* [67]. Their model is based on the Shkadov integral boundary layer approximation. Therefore, as for the isothermal case, it does not suffer any blow-up like the Benney equation and Kalliadasis *et al.* [67] could indeed calculate solitary wave solutions for larger Reynolds numbers than the Benney equation, where inertia effects are dominant as compared to the Marangoni effect. They recovered the Benney equation as derived by Joo *et al.* [53] as a limit of their IBL model for reasonably low Reynolds numbers where the velocity and temperature fields are effectively slaved to the kinematics of the film thickness. Kalliadasis *et al.* [67] also showed that for a vertically falling film the onset of the long-wave instability, of either H or S-type, can be described by the Kuramoto-Sivashinsky equation, or the Kawahara equation if dispersion is taken into account [72]. Nevertheless, the IBL model obtained by Kalliadasis *et al.* [67] for the heated falling film suffers from the same limitations than with the Shkadov IBL model for isothermal films, *i.e.* it does not predict accurately the behavior of the film close to criticality when the plate is inclined. One of our purposes in this work will be to overcome the limitations of the model equations derived by Kalliadasis *et al.* [67].

Structure of this work

We introduced so far the main concepts and issues related to the investigations reported in the present work. Let us now see how the latter is organized.
In **chapter 1** are presented the governing equations and the boundary conditions

to describe deformable film flows along a heated inclined plate. Two heat boundary conditions at the plate are considered in parallel, namely a temperature and a heat flux condition. In both cases, the base state is a flat film with a parabolic velocity profile and a linear temperature profile across the layer. Then, a linear stability analysis is performed with respect to two-dimensional normal mode disturbances from the flat film solution. The two long-wave instabilities, namely the thermocapillary (S) and the hydrodynamic (H) modes are mathematically identified. Finally, we apply the boundary layer approximation for thin heated falling films, and obtain the "boundary layer equations", which form the main model equations for the present study. From these equations, two levels of simplification yield the Benney equation or the weighted integral boundary layer equations, depending on the flow regime as measured by the Reynolds number. Therefore, the remaining of this work is divided into two parts corresponding to the low and the moderate Reynolds number cases, respectively.

Part I: Low Reynolds numbers

In **chapter 2**, we use a the long-wave asymptotic expansion to reduce the governing equations into one single evolution equation for the film thickness, namely the Benney equation. This equation describes the dynamics of a thin falling liquid film at small Reynolds numbers, including the Marangoni effect when the plate is at uniform temperature. Since this equation experiences singularities (finite-time blow-up) when increasing the Reynolds number, we determined its "validity domain" in the parameter space by considering the boundedness of its solutions as well as their accuracy. To this purpose, a weighted integral boundary layer model (developed later in Part II) valid at higher Reynolds number than the Benney equation is used as reference. Stationary solutions for both models are followed through parameter space using continuation techniques. To consider stationary travelling waves the flow rate in the moving frame has to be specified. Open and closed flow conditions are both analysed.

In **chapter 3**, we extend the Benney equation developed in chapter 2 in the case of a vertical plate with a *non-uniform, sinusoidal* temperature distribution. Therefore, in addition to the thermocapillary long-wave instability, a second thermocapillary effect appears due to the non-uniform heating imposed at the plate and leads to steady-state deformations of the liquid-gas interface. The analysis is performed in the situation when both thermocapillary effects are of the same order of magnitude. Actually, the dynamics of such interaction is very rich and is described by means of stationary solutions and direct numerical simulations. The enhancement of the heat transfer due to permanent deformations and travelling waves is also assessed.

In **chapter 4**, we study theoretically and experimentally the rivulet instability occurring when a falling film is locally heated from the wall (see figure 7). Firstly, the base state that now depends on the streamwise coordinate is calculated and compared with profiles measured in experiments. Secondly, a linear stability analysis of this base state is performed. An energy analysis is applied in order to identify the instability mechanisms. Finally, we explore the nonlinear regime using direct three-dimensional

numerical simulations and make a comparative survey with our previously obtained experimental data.

Part II: Moderate Reynolds numbers

In **Chapter 5**, the weighted integral boundary layer (WIBL) model valid for moderate Reynolds numbers is obtained in the case of a constant temperature imposed at the plate. To this purpose, we outline the weighted residual approach and use a gradient expansion combined with a Galerkin projection with polynomial test functions for both velocity and temperature fields. We obtain two model equations for the evolution of the velocity and temperature amplitudes at first and second-order in the expansion parameter. However, these equations are complex and hence not convenient for practical applications. A procedure is then described that enables us to simplify our set of equations and to formulate models fully compatible with the Benney expansion up to second order. This approach results in systems of three coupled nonlinear partial differential equations for the evolution of the local film thickness, flow rate and interfacial temperature.
In **chapter 6** we examine in detail the linear stability properties of the models developed in chapter 5 and in particular we compare their neutral stability curves with those obtained from the Orr-Sommerfeld eigenvalue problem of the full Navier-Stokes/energy equations. This allows us to identify a model of reduced dimensionality that is in very good agreement with Orr-Sommerfeld. The model is then used to obtain nonlinear waves far from criticality. Particular emphasis is given to solitary waves. We scrutinize the influence of the thermocapillary effect on the instability and the properties of the solitary waves and we analyze the effect of Reynolds and Prandtl numbers on the shape of the waves, flow patterns and temperature distributions in the film.
In **chapter 7**, we extend our new model to the three-dimensional case in order to describe solitary waves and rivulet pattern such as those of figure 8. For isothermal conditions, we compare results of our 3D numerical simulations with experimental data available in the literature, by considering two kind of external perturbations, namely a periodic forcing and a white noise. Finally, a constant temperature at the wall is also considered in the 3D simulations.
In **chapter 8**, we discuss two further topics. First, we formulate our new model in the case of a heat flux condition imposed at the wall. We show that the formulation is also applicable in the case of a temperature distribution dependent on the streamwise coordinate. Secondly, we show the modification of our new model when considering the small Biot number limit (*i.e.* small heat transfer coefficient).

Even though some conclusions are given at the end of each chapter, general **conclusions and perspectives** are presented at the end of this text.

Original contributions

The present work has been written with the intention of being as self-contained as possible. For this purpose, it has been necessary to recall several well-established concepts and theories.
Thereby, chapter 1 is devoted to the derivation of the basic equations and boundary conditions, and does not contain any original contribution, except in §1.4 where linear stability analysis is applied for two different heat boundary conditions at the wall, namely the temperature and the heat flux conditions (including heat losses at the substrate). To our knowledge, linear stability results related to this latter condition is not available in the literature; the same as for the small-wavenumber expansion performed in §1.4.2 in the case of a heated substrate (*i.e.* our analysis extending the isothermal case).
In chapter 2, §2.1 recalls some generalities about the Benney equation. In §2.2, we re-established earlier results through the long-wave expansion leading to the Benney equation, including the Marangoni effect. However, this expansion is completed here in the case of the heat flux condition imposed at the plate. Moreover, even in the case of the temperature condition, the Benney equation obtained at second-order is not available in the literature (§2.2.2). The remaining sections, from §2.3 to §2.8, are original contributions reported in [122]. However, the Floquet analysis of §2.7 has been performed by Christian Ruyer-Quil.
Chapter 3 about periodic heated falling films is an entirely original contribution that was initially reported in [120, 118].
Chapter 4 compiles several previous works (performed in the frame of DEC2 and DEA) about the instability of a thin film due to localized heating: the linear stability analysis reported in [118, 128], the experimental data reported in [116, 117] and the 3D numerical simulations reported in [118]. Nevertheless, the chapter includes new elements in the comparison between theory and experiments.
Chapter 5 and 6 present the modelling of a film flowing along an inclined plate of uniform temperature, at moderate Reynolds numbers [111, 121]. The first and second-order models have been obtained for isothermal conditions by Ruyer-Quil & Manneville [108, 109, 110] who developed a suitable mathematical technique based on the weighted residual method. Our original contributions are to have added second-order corrections accounting for inertia, and to have included the Marangoni effect in their model.
Chapter 7 shows the extension of our new models for three-dimensional films when the local flow rate in the spanwise direction is of the same order of magnitude than the one in the streamwise direction. This contribution is original, as well as comparisons with available experimental data in the literature.
Chapter 8 presents the modifications in our new models to account for the heat flux condition at the wall as well as for the small Biot number limit. They are both original contributions.
Unless specified by "courtesy of", or if a reference is given, all the figures of this work are original.

Chapter 1

Definition of the general problem and primary instability

This chapter presents the main hypotheses sustaining the governing basic equations (Navier-Stokes/Fourier) plus the boundary conditions for a falling and heated liquid film with a "free surface" (§1.1). Because of relatively low (dynamic) shear viscosity of the gas, we can expect that the influence of the gas motion in the liquid is negligible, and hence the terminology "free surface", in the case of which a simplified mathematical model may be used. Also we can ignore the temperature field in the gas using some empirical boundary conditions for temperature. In this case, we can consider the processes that take place *only* in the liquid phase. Such "one-fluid" approach may be justified only under some conditions (see, e.g., Golovin *et al.* [43]), and in some cases makes it difficult to permit a comparison with experiments in the framework of such an approach (because of unmeasurable empirical coefficients used). Nevertheless, this approach may be useful for the qualitative description of the physical phenomena (see Nepomnyashchy, Velarde & Colinet [90]), and will be adopted here.

In our formulation, two heat boundary conditions at the substrate are considered in parallel, namely a temperature and a heat flux distribution. For the latter condition to be realistic, heat losses at the plate should be included, which implies one empirical parameter more in the system of equations. The dimensionless equations are obtained in §1.2. The base states are calculated from the system of governing equations and a discussion on the heat transfer at the interfaces is addressed for both heating conditions (§1.3). In both cases, the base state is a flat film referred to as the "Nusselt solution" with a parabolic velocity profile and a linear temperature profile across the layer. In §1.4 is performed a linear stability analysis of the base state identifying mathematically the two instability modes mentioned in the Introduction, *i.e.* the long-wave thermocapillary (S) and hydrodynamic (H) modes; the former existing in both longitudinal and transverse directions while the latter only in the longitudinal (streamwise) direction. In §1.5, we truncate the basic equations to obtain the so-called "boundary layer" equations in which the inertia terms in the cross-stream momentum equation are neglected. The relevant sets of dimensionless parameters are classified in §1.6. Finally, we present in §1.7 in terms of those parameters the two

class of reduced models that will be studied in the remaining of this work.

1.1 Governing equations and boundary conditions

We consider a liquid film flowing down a wall of inclination β to the horizontal. The flow is driven by gravity whose g is the acceleration factor. The mean film thickness is noted $\bar{h}_{\mathrm{N}}$. The wall can be heated either through a fixed temperature distribution $T_{\mathrm{w}}(x)$ or a fixed heat flux distribution $q_{\mathrm{w}}(x)$. Figure 1.1 shows the geometry of the problem and the coordinate system (x, y, z) with the origin at the wall, x directed streamwise, y normal to the wall (cross-stream) increasing into the liquid and z spanwise. The hypotheses are the following:

H1: The density ρ of the liquid is assumed to be constant, *i.e.* the liquid remains incompressible. This assumption holds for very thin films ($h_{\mathrm{N}} << 1\,mm$), as the ones considered in this work, where the buoyancy effect can be neglected (see, *e.g.* , Birikh *et al.* [10] or Colinet *et al.* [23]).

H2: The liquid is Newtonian, implying a linear stress-strain relationship whose proportionality factor is the dynamic viscosity μ. The kinematic viscosity is

$$\nu = \mu/\rho.$$

H3: In the heat equation, we shall neglect the frictional viscous heating which has negligible influence for shallow liquid layers [23].

H4: The wall is rigid and solid.

H5: The evaporation is neglected so that the unknown position of the interface can be described by its variable height

$$y = h(x, z, t),$$

taken as a single-valued function of the horizontal coordinates x and z (see figure 1.1).

H6: Above the liquid layer, we assume the air to be passive. Its temperature T_∞ and pressure p_∞ are supposed to be constant sufficiently far from the interface. A necessary condition for a gas to be passive is that the viscous stress from the air is negligible compared to that from the liquid side because the dynamic (shear) viscosity of air is generally negligible compared with that of the liquid (for instance, $\mu_{\mathrm{air}}/\mu_{\mathrm{water}} \approx 10^{-2}$). This means that both phases are mechanically decoupled, which enables to solve the momentum equation for the liquid without having to solve it for the air. Note that despite the smallness of the dynamic viscosity ratio between air and liquid, the opposite is true for the kinematic viscosity (for instance, $\nu_{\mathrm{air}}/\nu_{\mathrm{water}} \approx 10$) [10].

H7: The surface tension is assumed to decrease linearly with the temperature,

$$\sigma = \sigma_\infty - \gamma(T_\mathrm{s} - T_\infty), \tag{1.1}$$

where σ_∞ is the surface tension at the gas temperature and $\gamma = -\partial\sigma/\partial T$ is positive for common liquids.

H8: When a boundary (either the liquid-solid or liquid-gas boundary) possesses a non-negligible thermal resistance, a difference of temperature may exist across the boundary, and the continuity of the heat flux is often written

$$\pm\lambda\partial_y T = \alpha(T - T_0), \tag{1.2}$$

where λ is the heat conductivity of the liquid, T is the liquid temperature at the boundary, T_0 is the temperature on the other side of the boundary, and α is the heat transfer coefficient. Equation (1.2) is referred to as "Newton's law of cooling" in the absence of radiation. This relation is mathematically convenient since it eliminates the need for solving Fourier's equation at the solid and at the gas phases. However, it is phenomenological in the sense that it defines the heat transfer coefficient α and its validity thus depends on the particular situation considered. Because the problem we have to solve is by nature non stationary, α depends on time and position. Indeed, heat transfer at the liquid-air interface, for instance, will be modified by the presence of thermal and momentum boundary layers and the possible presence of convection. Moreover, evaporation tough neglected in this work plays most often in reality a major role in heat transfer. Therefore, evaluating the heat transfer coefficient is not a straightforward task. Nevertheless, in our specific problem, we expect the wavy regimes to more or less regularize the process of heat transfer (as discussed in §3.4) and for simplicity α in the following will be assumed to be constant.

H9: The system geometry is assumed to be infinite in x and z directions.

For description of the bulk motions of the liquid we shall use the Boussinesq approximation (see, *e.g.* , [90]). In short, this approximation amounts to considering all parameters like viscosity, heat diffusivity, etc., as having values not significantly altered by the action of the (not too strong) thermal gradients. Within this approximation, the values of dynamic viscosity μ, kinematic viscosity ν, heat conductivity λ and heat diffusivity χ are then assumed to be constant. Under these conditions, the governing equations (using H1, H2 and H3) are respectively the momentum balance (Navier-Stokes), the energy balance (Fourier) and the continuity equations,

$$\frac{\mathrm{d}\mathbf{v}}{\mathrm{d}t} = -\rho^{-1}\boldsymbol{\nabla}p + \nu\boldsymbol{\nabla}^2\mathbf{v} + \mathbf{F}, \tag{1.3}$$

$$\frac{\mathrm{d}T}{\mathrm{d}t} = \chi\boldsymbol{\nabla}^2 T, \tag{1.4}$$

$$\boldsymbol{\nabla}\cdot\mathbf{v} = 0, \tag{1.5}$$

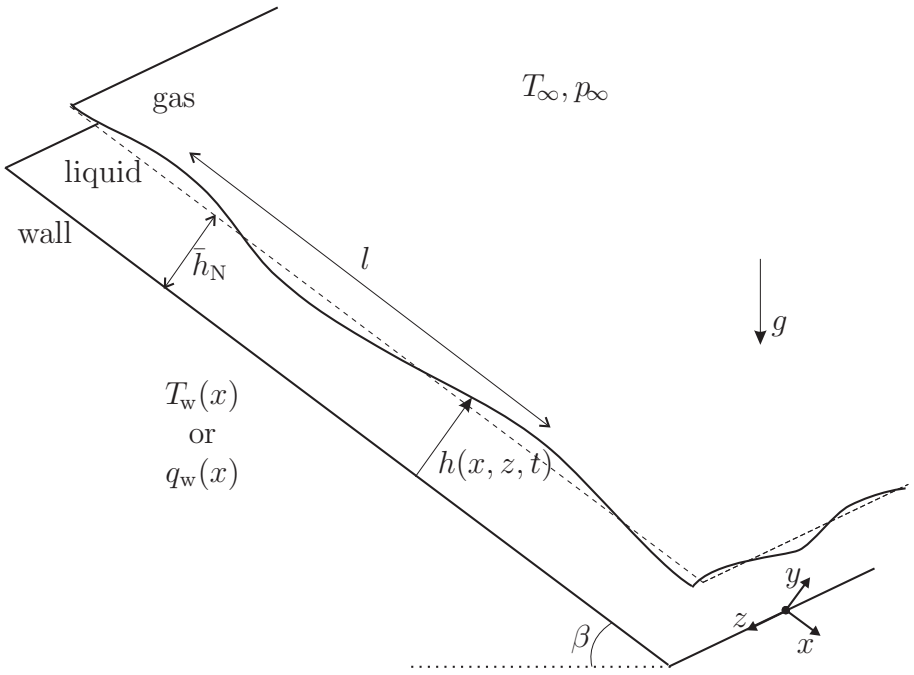

Figure 1.1: Sketch of a viscous liquid film flowing down an inclined wall.

where $\mathrm{d}/\mathrm{d}t \equiv \partial_t + (\mathbf{v}\cdot\boldsymbol{\nabla})$ stands for the material derivative, ∂_t is the partial derivative with respect to time t and $\boldsymbol{\nabla} \equiv (\partial_x, \partial_y, \partial_z)^{\rm t}$ is the gradient operator. The fields $\mathbf{v} = (u, v, w)$, T and p are respectively the fluid velocity, temperature and pressure while $\mathbf{F} = (g\sin\beta, -g\cos\beta, 0)$ is the body force. Finally, $\chi = \lambda/\rho c_p$ is the thermal diffusivity where c_p is the heat capacity of the liquid. Equations (1.3-1.5) should be completed by the following boundary conditions:

At the wall $y = 0$,

- the no-slip velocity condition (H2 + H4),

$$\mathbf{v} = 0, \tag{1.6}$$

- the heating condition that can be either the *temperature condition* (TC)

$$T = T_{\rm w}(x), \tag{1.7}$$

  in which case the wall is assumed to be a perfect conductor of heat of infinite heat capacity; or the *heat flux condition* (HFC), using the Newton's law (H8),

$$\lambda\partial_y T = -q_{\rm w}(x) + \alpha_{\rm w}(T - T_0), \tag{1.8}$$

  where $q_{\rm w}(x)$ is the imposed heat flux and $\alpha_{\rm w}$ is the heat transfer coefficient that quantifies the heat loss through the wall driven by a temperature difference in which T_0 is a constant temperature at the other side of the wall. For the sake of simplicity, T_0 will be set equal to T_∞ in the following. The acronyms TC and

HFC will be used hereafter to refer to the corresponding heating condition at the wall, as one of our goals will be to compare these conditions.

The temperature or heat flux distribution at the wall can be split into two components, namely the average ($\hat{}$) and the non-uniform ($\tilde{}$) quantities:

$$T_{\mathrm{w}}(x) = \hat{T}_{\mathrm{w}} + \tilde{T}_{\mathrm{w}}(x) \quad \text{or} \quad q_{\mathrm{w}}(x) = \hat{q}_{\mathrm{w}} + \tilde{q}_{\mathrm{w}}(x). \tag{1.9}$$

This chapter deals essentially with the uniform heating but chapter 3 and 4 will focus on the non-uniform heating in the case of which relations (1.9) will be useful.

At the free surface $y = h$,

- the liquid-gas interface kinematic condition obtained by differentiating $y = h(x, z, t)$ with respect to t [23] (see H5),

$$\frac{\mathrm{d}}{\mathrm{d}t}(h - y) = 0.$$

Using the definition of the material derivative, it provides a relationship between the film thickness and the normal velocity component $v = \mathrm{d}y/\mathrm{d}t$ at the free surface:

$$v = \partial_t h + \mathbf{v} \cdot \boldsymbol{\nabla} h. \tag{1.10}$$

- the momentum jump condition (see H6 and H7),

$$(p_\infty - p)\ \mathbf{n} + \mathbf{P} \cdot \mathbf{n} = \sigma(\boldsymbol{\nabla} \cdot \mathbf{n})\mathbf{n} - \boldsymbol{\nabla}_{\!s}\sigma, \tag{1.11}$$

where $\mathbf{P} = \mu\left(\boldsymbol{\nabla}\mathbf{v} + (\boldsymbol{\nabla}\mathbf{v})^{\mathrm{t}}\right)$ is the shear (viscous) stress tensor in the liquid phase, $\mathbf{n}$ is the unit normal vector directed outwards the liquid phase and $\boldsymbol{\nabla}_{\!s} = (I - \mathbf{nn}) \cdot \boldsymbol{\nabla}$ is the surface gradient operator* [21]. Figure 1.2 shows the unit normal vector at the point P of the film surface where the slope is positive in x and $z-$directions. Then, proceeding from geometrical projections [2], its expression in the Cartesian coordinates reads

$$\mathbf{n} = \frac{1}{n}(-\partial_x h, 1, -\partial_z h),$$

where $n = \left(1 + (\partial_x h)^2 + (\partial_z h)^2\right)^{1/2}$ is the metric. The projection of (1.11) on the normal $\mathbf{n}$ gives the *normal stress boundary condition*

$$p_\infty - p + (\mathbf{P} \cdot \mathbf{n}) \cdot \mathbf{n} = 2\sigma K(h). \tag{1.12}$$

where the mean film surface curvature is defined by

$$K(h) = -\frac{1}{2}\boldsymbol{\nabla} \cdot \mathbf{n} = \frac{1}{2}\frac{\partial_{xx} h\left(1 + (\partial_z h)^2\right) + \partial_{zz} h\left(1 + (\partial_x h)^2\right) - 2\partial_x h \partial_z h \partial_{xz} h}{\left(1 + (\partial_x h)^2 + (\partial_z h)^2\right)^{3/2}}.$$

*The definition comes from the decomposition of the gradient operator $\boldsymbol{\nabla}$ on the film surface as $\boldsymbol{\nabla} = (I - \mathbf{nn}) \cdot \boldsymbol{\nabla} + \mathbf{nn} \cdot \boldsymbol{\nabla} = \boldsymbol{\nabla}_{\!s} + \mathbf{nn} \cdot \boldsymbol{\nabla}$.

Defining two unit tangent vectors by

$$\boldsymbol{\tau_x} = \frac{1}{n_x}(1, \partial_x h, 0) \quad \text{and} \quad \boldsymbol{\tau_z} = \frac{1}{n_z}(0, \partial_z h, 1),$$

with $n_i = (1 + (\partial_i h)^2)^{1/2}$, the projections of (1.11) on them give the *tangential stress boundary conditions*

$$(\mathbf{P} \cdot \boldsymbol{\tau_i}) \cdot \mathbf{n} \;=\; \boldsymbol{\tau_i} \cdot \boldsymbol{\nabla}_s \sigma \qquad i = x, z. \tag{1.13}$$

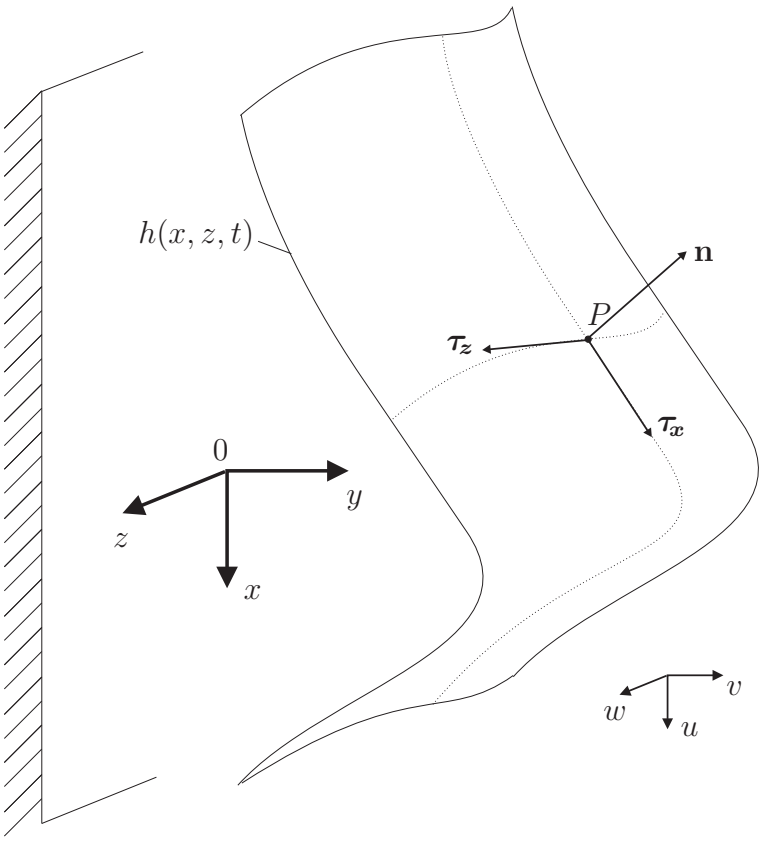

Figure 1.2: Definition of normal and tangent unit vectors at the film surface.

- the Newton's cooling law (see H8),

$$-\lambda \boldsymbol{\nabla} T \cdot \mathbf{n} = \alpha(T - T_\infty), \tag{1.14}$$

where α is the heat transfer coefficient between the liquid film and the ambient air sufficiently far from the interface.

1.2 Dimensionless equations and parameters

When the flow is stationary, of constant film thickness $\bar{h}_{\rm N}$ and in the case of uniform heating ($\tilde{T}_{\rm w} = \tilde{q}_{\rm w} = 0$), the solution of the Navier-Stokes/Fourier equations is a parallel flow where the viscosity balances exactly the gravity (Nusselt flow) and the heat is propagated by pure conduction:

$$U(y) = \frac{g\sin\beta}{2\nu} y(2\bar{h}_{\rm N} - y) \tag{1.15a}$$

$$V(y) = 0 \tag{1.15b}$$

$$W(y) = 0 \tag{1.15c}$$

$$P(y) = p_\infty + \rho g\cos\beta(\bar{h}_{\rm N} - y) \tag{1.15d}$$

$$\Theta(y) = \hat{T}_{\rm w} - \frac{\alpha(\hat{T}_{\rm w} - T_\infty)}{\lambda + \alpha\bar{h}_{\rm N}} y \qquad \text{(TC)} \tag{1.15e}$$

$$\Theta(y) = T_\infty + \frac{\hat{q}_{\rm w}(\lambda + \alpha(\bar{h}_{\rm N} - y))}{\lambda(\alpha + \alpha_{\rm w}) + \alpha\alpha_{\rm w}\bar{h}_{\rm N}}, \qquad \text{(HFC)} \tag{1.15f}$$

Equation (1.15a) has been initially obtained by Nusselt [92]. Following Ruyer-Quil & Manneville [108], the physical characteristics of the film, the viscosity ν and the streamwise gravity component $g\sin\beta$, are used to define the length and the time scales as follows,

$$l_\nu = \left(\frac{\nu^2}{g\sin\beta}\right)^{1/3} \quad \text{and} \quad {\rm t}_\nu = \left(\frac{\nu}{(g\sin\beta)^2}\right)^{1/3}.$$

The velocity and pressure scales are selected as

$$u_\nu = \frac{l_\nu}{t_\nu} = (\nu g\sin\beta)^{1/3} \qquad \text{and} \qquad p_\nu = \rho u_\nu^2 = \rho(\nu g\sin\beta)^{2/3}.$$

For a layer of thickness l_ν, (1.15a) yields that u_ν equals twice the film surface velocity. Therefore, l_ν is twice the distance covered by a fluid particle at the film surface, during the time t_ν, in a gravity-driven Nusselt flow of constant film thickness l_ν. Note that choosing to base our scaling on the streamwise gravity acceleration does not allow to consider the limit of horizontal plane.
The temperature scale is chosen as

$$\Delta T = \hat{T}_{\rm w} - T_\infty \qquad \text{(TC)} \tag{1.16a}$$

or

$$\Delta T = \hat{q}_{\rm w} l_\nu/\lambda \qquad \text{(HFC)}, \tag{1.16b}$$

depending on the heating condition. Note that the temperature difference for the TC is suitable for the problem at hand while the one for the HFC corresponds to the particular case of a perfectly insulating wall ($\alpha_{\rm w} = 0$) and a perfectly conducting gas phase ($\alpha \to \infty$). Certainly, the base state temperature (1.15f) would provide a more realistic approximation of the temperature difference between the wall and the ambient air,

$$\Theta\big|_{y=0} - T_\infty = \frac{\hat{q}_{\rm w}(\lambda + \alpha\bar{h}_{\rm N})}{\lambda(\alpha + \alpha_{\rm w}) + \alpha\alpha_{\rm w}\bar{h}_{\rm N}}. \qquad \text{(HFC)}$$

Nevertheless, the impractical consequence is that it depends *a priori* on the flow characteristics through the Nusselt film thickness $\bar{h}_{\mathrm{N}}$. This could be avoided by choosing as reference, a film of thickness l_ν. However the relation between l_ν and the film thickness h of a deformed film surface is not trivial, which would make the subsequent equations cumbersome. We therefore stick to the definition 1.16b.
Here the temperature T and the pressure p will be reckoned relative to their reference values in the gas phase T_∞ and p_∞. Keeping the same symbols for the dimensionless quantities, the dimensionless governing equations read therefore

$$\begin{aligned}
\partial_t u + u\partial_x u + v\partial_y u + w\partial_z u &= -\partial_x p + \partial_{xx} u + \partial_{yy} u + \partial_{zz} u + 1, && (1.17)\\
\partial_t v + u\partial_x v + v\partial_y v + w\partial_z v &= -\partial_y p + \partial_{xx} v + \partial_{yy} v + \partial_{zz} v - \mathrm{Ct}, && (1.18)\\
\partial_t w + u\partial_x w + v\partial_y w + w\partial_z w &= -\partial_z p + \partial_{xx} w + \partial_{yy} w + \partial_{zz} w, && (1.19)\\
\mathrm{Pr}\,(\partial_t T + u\partial_x T + v\partial_y T + w\partial_z T) &= \partial_{xx} T + \partial_{yy} T + \partial_{zz} T, && (1.20)\\
\partial_x u + \partial_y v + \partial_z w &= 0, && (1.21)
\end{aligned}$$

and the dimensionless boundary conditions read

- at the wall $y = 0$:

$$u = v = w = 0, \qquad (1.22)$$

$$\begin{aligned}
T &= 1 + F_{\mathrm{w}}(x) \qquad \text{(TC)} && (1.23a)\\
&\text{or}\\
\partial_y T &= -1 - F_{\mathrm{w}}(x) + \mathrm{Bi}_{\mathrm{w}} T \qquad \text{(HFC)}, && (1.23b)
\end{aligned}$$

  where $F_{\mathrm{w}}(x)$ is the dimensionless distribution function of the non-uniform heating and has a zero average (see chapter 3). The uniform heating case corresponds therefore to $F_{\mathrm{w}} = 0$ in both cases TC and HFC.

- at the film surface $y = h$:

$$\begin{aligned}
v &= \partial_t h + u\partial_x h + w\partial_z h, && (1.24)\\
p &= \frac{2}{n^2}\left[(\partial_x h)^2\partial_x u + (\partial_z h)^2\partial_z w + \partial_x h\partial_z h(\partial_z u + \partial_x w)\right.\\
&\quad \left. -\partial_x h(\partial_y u + \partial_x v) - \partial_z h(\partial_z v + \partial_y w) + \partial_y v\right]\\
&\quad -\frac{1}{n^3}(\mathrm{Ka} - \mathrm{Ma}\,T)\left[\partial_{xx} h\left(1 + (\partial_z h)^2\right) + \partial_{zz} h\left(1 + (\partial_x h)^2\right)\right.\\
&\quad \left. -2\partial_x h\,\partial_z h\,\partial_{xz} h\right], && (1.25)\\
0 &= \frac{1}{n}\left[2\partial_x h(\partial_y v - \partial_x u) + \left(1 - (\partial_x h)^2\right)(\partial_y u + \partial_x v)\right.\\
&\quad \left. -\partial_z h(\partial_z u + \partial_x w) - \partial_x h\partial_z h(\partial_z v + \partial_y w)\right]\\
&\quad +\mathrm{Ma}(\partial_x T + \partial_x h\partial_y T), && (1.26)\\
0 &= \frac{1}{n}\left[2\partial_z h(\partial_y v - \partial_z w) + \left(1 - (\partial_z h)^2\right)(\partial_y w + \partial_z v)\right.
\end{aligned}$$

$$
\begin{aligned}
& -\partial_x h(\partial_z u + \partial_x w) - \partial_x h \partial_z h(\partial_y u + \partial_x v)] \\
& +\mathrm{Ma}(\partial_z T + \partial_z h \partial_y T), \qquad (1.27)
\end{aligned}
$$

$$
\mathrm{Bi}\, T = \frac{1}{n}(\partial_x h \partial_x T + \partial_z h \partial_z T - \partial_y T). \qquad (1.28)
$$

The set of dimensionless numbers is:

- the *inclination number*

$$
\mathrm{Ct} = \cot\beta, \qquad (1.29)
$$

  which compares the normal (cross-stream) component of the gravitational force to its streamwise component. It quantifies the hydrostatic pressure force that vanishes for a film falling vertically, *i.e.* $\mathrm{Ct} = 0$.

- the *Prandtl number*

$$
\mathrm{Pr} = \frac{\nu}{\chi} \qquad (1.30)
$$

  which represents the ratio of momentum and heat diffusivities.

- the *Kapitza number*

$$
\mathrm{Ka} = \frac{\sigma_\infty}{\rho\,(g\sin\beta)^{1/3}\,\nu^{4/3}}, \qquad (1.31)
$$

  which compares surface tension force $\propto \sigma_\infty l_\nu$ to force of inertia $\propto \rho(u_\nu l_\nu)^2 = \rho\nu^2$.

- the *Marangoni number*[†]

$$
\mathrm{Ma} = \frac{\gamma\,\Delta T}{\rho\,(g\sin\beta)^{1/3}\,\nu^{4/3}} = \mathrm{Ka}\frac{\gamma\,\Delta T}{\sigma_\infty}, \qquad (1.32)
$$

  which compares the force induced by surface tension gradient $\propto \gamma\,\Delta T l_\nu$ to force of inertia $\propto \rho\nu^2$.

- the *Biot number*

$$
\mathrm{Bi} = \frac{\alpha\, l_\nu}{\lambda} = \frac{\alpha\,\nu^{2/3}}{\lambda\,(g\sin\beta)^{1/3}}, \qquad (1.33)
$$

  describing the rate of heat transport from the liquid to the ambient gas.

- the *wall Biot number*

$$
\mathrm{Bi_w} = \frac{\alpha_\mathrm{w}\, l_\nu}{\lambda} = \frac{\alpha_\mathrm{w}\,\nu^{2/3}}{\lambda\,(g\sin\beta)^{1/3}}, \qquad (1.34)
$$

  describing the rate of heat transport from the liquid to the wall. This number appears only if the heat flux condition is used.

[†]The Marangoni number Ma differs by a factor Pr to the usual definition $Ma = \frac{\gamma \Delta T l_\nu}{\mu\chi}$, used to quantify thermocapillary convection in horizontal layers [90].

The original definition of the Kapitza number $\mathrm{Ka}_\perp = \sigma_\infty/\rho g^{1/3}\nu^{4/3}$ [69] implies only the liquid properties and remains thus fixed once the liquid is selected. The reason is that Kapitza made experiments on a vertical wall for which $\sin\beta = 1$ and therefore the streamwise acceleration is simply g. However, the alternative definition $\mathrm{Ka}_\perp = \mathrm{Ka}\big|_{\sin\beta=1}$ – and so forth for the other dimensionless numbers with the subscript $\perp$ – may be useful to study separately the influence of the wall inclination keeping constant all the other parameters (see §2.6.3). In this case, we will introduce for readability the two following numbers

$$\mathrm{S} = \sin\beta \quad \text{and} \quad \mathrm{C} = \cos\beta.$$

In the above unit system, the Reynolds number $u_\nu l_\nu/\nu$ that compares inertia to viscous forces is equal to unity and does not appear explicitely in the equations. The Reynolds number based on the film thickness $\bar{h}_\mathrm{N}$ and on the average velocity $\bar{u}_\mathrm{N}$ is hidden in the inlet boundary condition that defines the Nusselt solution (1.15a), used as reference. In experiments, the control parameter that determines the Nusselt film thickness $\bar{h}_\mathrm{N}$ is the specific volumetric flow rate[‡]

$$\bar{q}_\mathrm{N} = \int_0^{\bar{h}_\mathrm{N}} U(y)dy = \frac{g\sin\beta\bar{h}_\mathrm{N}^3}{3\nu}. \tag{1.35}$$

It provides an other velocity scale $\bar{u}_\mathrm{N} = \bar{q}_\mathrm{N}/\bar{h}_\mathrm{N}$ allowing to construct the film Reynolds number

$$\mathrm{Re} = \frac{\bar{u}_\mathrm{N}\bar{h}_\mathrm{N}}{\nu} = \frac{\bar{q}_\mathrm{N}}{\nu} = \frac{g\sin\beta\bar{h}_\mathrm{N}^3}{3\nu^2}. \tag{1.36}$$

The Reynolds number appears therefore simply as the dimensionless flow rate $q_\mathrm{N} = \bar{q}_\mathrm{N}/\nu$. Consequently, the dimensionless film thickness reads

$$h_\mathrm{N} = \frac{\bar{h}_\mathrm{N}}{l_\nu} = (3\mathrm{Re})^{1/3}. \tag{1.37}$$

The definition of the Reynolds number can vary depending if the chosen characteristic velocity is the mean velocity $\bar{u}_\mathrm{N}$, the velocity at the interface $3\bar{u}_\mathrm{N}/2$ (see 1.15a) or the speed of linear waves $3\bar{u}_\mathrm{N}$ (see later).
Another set of dimensionless numbers could be defined based on the Nusselt solution, with $\bar{h}_\mathrm{N}$ and $\bar{h}_\mathrm{N}/\bar{u}_\mathrm{N}$ as the length and time scales, with

- the *Weber number*

$$\mathrm{We} = \frac{\sigma_\infty}{\rho g\bar{h}_\mathrm{N}^2\sin\beta} = \frac{\mathrm{Ka}}{h_\mathrm{N}^2}, \tag{1.38}$$

  that compares the surface tension pressure $\propto \sigma_\infty/\bar{h}_\mathrm{N}$ to the viscous normal stress generated by gravity at the film surface $\propto \mu\bar{u}_\mathrm{N}/\bar{h}_\mathrm{N} = \rho g\bar{h}_\mathrm{N}\sin\beta$. For large We, the fluid behaviour is mainly determined by surface tension (*e.g.* at

[‡]The bar is used to distinguish dimensional from dimensionless quantities unless the distinction is obvious.

small $\bar{h}_{\rm N}$), while gravity dominates for small We. The transition between these two regimes occurs at a length scale obtained by setting We = 1. We then get the capillary length scale, for a vertical wall ($\sin\beta = 1$),

$$l_\sigma = \left(\frac{\sigma_\infty}{\rho g}\right)^{1/2} \tag{1.39}$$

which is about 2.5 mm for water.

- the *film Marangoni number*

$$\mathrm{M} = \frac{\gamma \Delta T}{\rho g \bar{h}_{\rm N}^2 \sin\beta} = \frac{\mathrm{Ma}}{h_{\rm N}^2} \qquad \text{(TC)} \tag{1.40}$$

that compares stress induced by surface tension gradient $\propto \gamma\Delta T/\bar{h}_{\rm N}$ to the viscous normal stress generated by gravity at the film surface $\propto \mu\bar{u}_{\rm N}/\bar{h}_{\rm N} = \rho g \bar{h}_{\rm N} \sin\beta$. We have specified in (1.40) that the definition of M applies for the TC when ΔT is given by (1.16b). This is important since the definition of M is different for the HFC. Indeed, in this case, the temperature difference (1.16b) is dependent on the lengthscale l_ν and should be rescaled here with $\bar{h}_{\rm N}$ such that

$$\Delta T_{\rm N} = \frac{q_{\rm w}\bar{h}_{\rm N}}{\lambda}$$

$$\text{and} \quad \mathrm{M} = \frac{\gamma \Delta T_{\rm N}}{\rho g \bar{h}_{\rm N}^2 \sin\beta} = \frac{\mathrm{Ma}}{h_{\rm N}} \qquad \text{(HFC)}. \tag{1.41}$$

Both definitions (1.40) and (1.41) will be used hereafter depending on the heating condition.

- the *film Biot numbers*

$$\mathrm{B} = \frac{\alpha \bar{h}_{\rm N}}{k} \quad \text{and} \quad \mathrm{B_w} = \frac{\alpha_{\rm w} \bar{h}_{\rm N}}{k}. \tag{1.42}$$

1.3 Base state and discussion on the Biot number

In dimensionless form, the base state solution (1.15), using the scaling based on the characteristic length l_ν and for a uniform heating ($F_{\rm w} = 0$), reads

$$U(y) = \frac{1}{2} y(2h_{\rm N} - y) \tag{1.43a}$$

$$V(y) = W(y) = 0 \tag{1.43b}$$

$$P(y) = \mathrm{Ct}(h_{\rm N} - y) \tag{1.43c}$$

$$\Theta(y) = \frac{1 + \mathrm{Bi}(h_{\rm N} - y)}{1 + \mathrm{Bi} h_{\rm N}} \qquad \text{(TC)} \tag{1.43d}$$

$$\Theta(y) = \frac{1 + \mathrm{Bi}(h_{\rm N} - y)}{\mathrm{Bi} + \mathrm{Bi_w}(1 + \mathrm{Bi} h_{\rm N})} \qquad \text{(HFC)}. \tag{1.43e}$$

In the following, we discuss separately the TC and HFC cases. For each of them, we will analyse the influence of the Biot number on the base state surface temperature and how it affects the Marangoni effect. Then, we will define a new Marangoni number appropriate to the base state solution.

1.3.1 Temperature condition (TC)

The temperature of the undeformed free surface is obtained from 1.43d as

$$\Theta\big|_{y=h_\mathrm{N}} = \frac{1}{1+\mathrm{Bi}h_\mathrm{N}}\,, \tag{1.44}$$

and consequently, the gradient of temperature between the surface and the wall

$$b_\mathrm{s} \equiv \frac{\Theta\big|_{y=0} - \Theta\big|_{y=h_\mathrm{N}}}{h_\mathrm{N}} = \frac{\mathrm{Bi}}{1+\mathrm{Bi}h_\mathrm{N}}\,. \tag{1.45}$$

Now let us consider the behaviour of (1.44) and (1.45) in the limits of $\mathrm{Bi} = 0$ and $1/\mathrm{Bi} = 0$. The former corresponds to a null heat transfer coefficient, that is an insulated free surface, and the latter to a null thermal conductivity, that is a layer of fluid conducting the heat very poorly.

- If $\mathrm{Bi} = 0$, (1.44) shows that the dimensionless temperature at the free surface is unity, which means simply that the wall and the free surface have the same temperature. Actually, the fluid temperature is uniform.
- In the limit $1/\mathrm{Bi} = 0$, (1.44) shows that the dimensionless temperature at the free surface is equal to zero so that the free surface and the air have the same temperature.

In both cases, the temperature of the free surface is independent of the film thickness so that any perturbation of h does not affect the free surface temperature and the Marangoni instability (the S-mode) does not occur. This can be made obvious by defining a Marangoni number based on the base state solution, namely a flat film of thickness $\bar{h}_\mathrm{N}$ with the temperature difference between the wall and the free surface

$$\Delta T_\mathrm{s} \equiv (T_\mathrm{w} - T_\mathrm{s}) = b_\mathrm{s} h_\mathrm{N} (T_\mathrm{w} - T_\infty),$$

such as

$$\mathrm{M}^\star = \frac{\gamma\,\Delta T_\mathrm{s}}{\rho \bar{h}_\mathrm{N}^2 g \sin\beta} = \frac{\mathrm{MaBi}}{h_\mathrm{N}(1+\mathrm{Bi}h_\mathrm{N})}\,, \tag{1.46}$$

where the product MaBi appears explictly through (1.45) and therefore goes to zero if Bi goes to zero. Nevertheless, it can be noted that, in the case of a small Biot number $\mathrm{Bi} \ll 1$, which is generally the case for liquid films in contact with gases, the base state temperature gradient can be assumed to be independent of the film thickness, $b_\mathrm{s} \approx \mathrm{Bi}$. Within this limit, the base state temperature gradient is uniquely defined by the heat transfer α and the conductivity λ. The small Biot number limit is treated in details in §8.2.

1.3.2 Heat flux condition (HFC)

In this case, the temperature of the undeformed free surface is obtained from 1.43e as

$$\Theta_{\rm s} \equiv \Theta\big|_{y=h_{\rm N}} = \frac{1}{{\rm Bi} + {\rm Bi_w}(1 + {\rm Bi}h_{\rm N})}\,, \tag{1.47}$$

and the gradient of temperature between the surface and the wall reads

$$b_{\rm s} \equiv \frac{\Theta\big|_{y=0} - \Theta\big|_{y=h_{\rm N}}}{h_{\rm N}} = \frac{{\rm Bi}}{{\rm Bi} + {\rm Bi_w}(1 + {\rm Bi}h_{\rm N})}\,. \tag{1.48}$$

Comparing to the TC case, the limit $1/{\rm Bi} = 0$ leads to the same conclusion while the limit ${\rm Bi} = 0$ is different. Actually, in this latter case, (1.47) shows that the dimensionless temperature at the free surface is $1/{\rm Bi_w}$, and depends therefore on the conduction properties of the wall.
Let us emphasize that the surface temperature $\Theta_{\rm s}$ depends on the film thickness only through the parameter ${\rm Bi_w}$. If the latter is equal to zero, $\Theta_{\rm s} = 1/{\rm Bi}$ remains constant. In other words, the thermocapillary instability is ineffective for an insulating wall boundary condition [120]. Actually, in this case, the temperature gradient across the film layer is independent of h ($b_{\rm s} = 1$), which implies that any elevation (depression) of the film thickness will be accompanied by an increase (decrease) of the wall temperature $\Theta|_{y=0} = (1 + {\rm Bi}h_{\rm N})/{\rm Bi}$ such that the film surface temperature remains constant. Therefore, enabling heat losses at the wall through the mixed boundary condition (1.8) is the only mean to enable a Marangoni effect when a heat flux is imposed at the wall.
As for the TC case, let us define a temperature difference between the wall and the free surface

$$\Delta T_{\rm s} = b_{\rm s} h_{\rm N} \frac{q_{\rm w} \bar{h}_{\rm N}}{\lambda}$$

such as

$${\rm M}^\star = \frac{{\rm MaBi}}{{\rm Bi} + {\rm Bi_w}(1 + {\rm Bi}h_{\rm N})}. \tag{1.49}$$

The Marangoni number ${\rm M}^\star$ based on the base state solution will be useful in the linear stability analysis when the perturbations are precisely applied on the base state temperature field.

1.4 Linear stability analysis

Referring to the isothermal case, it is known that the flat film solution appears very rapidly after the inlet[§]. Nevertheless, because the Prandtl number Pr can be large for liquids, we cannot assume the linear temperature profile to be obtained as soon as the

[§]It depends of course on the initial film thickness $h_{\rm i}$ provided by the distributor. One can find in Alekseenko *et al.* [1] that for $h_{\rm i}/\bar{h}_{\rm N} = 3$, the distance x_h necessary for the film to reach the Nusselt flat film solution with an accuracy of 10^{-4}, is $x_h/\bar{h}_{\rm N} \approx 1.2{\rm Re}$. For instance, a water film with $\bar{h}_{\rm N} = 0.15mm$ and ${\rm Re} = 11$ gives $x_h \sim 2mm$.

flat film solution is formed. An approximation of the position of the plane after which the temperature profile is linear can be obtained by considering the development of a thermal boundary layer in a flat film (see [5]). It has been proved [5] that the thermal boundary layer thickness grows proportionally to the Péclet number

$$\mathrm{Pe} = \mathrm{Re}\ \mathrm{Pr}. \tag{1.50}$$

Using integral boundary layer theory, with the approximation of a parabolic temperature distribution $T = 1 - 2(y/\delta_T) + (y/\delta_T)^2$ in the thermal layer of thickness δ_T, one gets for the position $x^\star$ on the plane where the thermal boundary layer thickness is equal to the film thickness, $x^\star/\bar{h}_\mathrm{N} \approx 0.04\mathrm{Pe}$ so that for moderate Prandtl and Reynolds numbers, the linear temperature distribution can be assumed soon after the inlet. We will therefore make the assumption that the film reaches a state governed by Equation (1.15) before it undergoes any instability.
Therefore we study here the stability of the flat film solution with regards to small disturbances. In order to proceed analytically, the boundary conditions should be homogeneous and the heating will still remain constant, *i.e.* $F_\mathrm{w} = 0$ (the case of non-uniform heating will be studied later). Goussis and Kelly performed this analysis in the case of a constant temperature imposed at the wall (TC). However, they used the film surface temperature T_s as reference which makes tricky the comparison with experiments since T_s is unknown. Hence, we will rather use our scaling based on T_∞, and extend the development to the constant heat flux condition (HFC).
Let us introduce the following perturbation quantities of the base state solution (1.43)

$$\mathbf{v} = (U + \tilde{u}, \tilde{v}, \tilde{w}), \quad T = \Theta + \tilde{T}, \quad p = P + \tilde{p}, \quad h = h_\mathrm{N} + \tilde{h},$$

into the Navier-Stokes/Fourier/continuity equations (1.17)-(1.20) and linearize with respect to the perturbations to obtain

$$\begin{aligned}
\partial_t\tilde{u} + U\partial_x\tilde{u} + \mathrm{D}U\tilde{v} + \partial_x\tilde{p} - \boldsymbol{\nabla}^2\tilde{u} &= 0 && (1.51)\\
\partial_t\tilde{v} + U\partial_x\tilde{v} + \partial_y\tilde{p} - \boldsymbol{\nabla}^2\tilde{v} &= 0 && (1.52)\\
\partial_t\tilde{w} + U\partial_x\tilde{w} + \partial_z\tilde{p} - \boldsymbol{\nabla}^2\tilde{w} &= 0 && (1.53)\\
\partial_t\tilde{T} + U\partial_x\tilde{T} + \mathrm{D}\Theta\tilde{v} - \mathrm{Pr}^{-1}\boldsymbol{\nabla}^2\tilde{T} &= 0 && (1.54)\\
\partial_x\tilde{u} + \partial_y\tilde{v} + \partial_z\tilde{w} &= 0, && (1.55)
\end{aligned}$$

with $\mathrm{D} = \mathrm{d}/\mathrm{d}y$. The perturbed and linearized boundary conditions become

- at the wall $y = 0$:

$$\tilde{u} = \tilde{v} = \tilde{w} = 0 \tag{1.56}$$

$$\tilde{T} = 0 \qquad \text{(TC)} \tag{1.57a}$$

or

$$\partial_y\tilde{T} = \mathrm{Bi}_\mathrm{w}\tilde{T} \qquad \text{(HFC)}. \tag{1.57b}$$

The above conditions can be related to the effect of wall conductivity on the instability and lead to two limiting cases of $1/\mathrm{Bi_w} = 0$ and $\mathrm{Bi_w} = 0$ that make the wall a perfect conductor or an insulator, respectively [132]. Actually, when the film becomes unstable, the temperature perturbation is quickly suppressed along the plate if the conductivity of the wall is much higher than that of the liquid film. In the limiting case of a perfect conductor ($1/\mathrm{Bi_w} = 0$), the temperature perturbation along the wall vanishes and HFC (1.57b) reduces to TC (1.57a). In the other case of an extremely poor conductor ($\mathrm{Bi_w} = 0$), the temperature perturbation in the film hardly has enough time to alter the base flow heat flux at the onset of instability because of its extremely poor conductivity. This corresponds to a constant heat flux case $\partial_y \tilde{T} = 0$. However, this second case is very difficult to realize in experiments. It is therefore the goal of having introduced the mixed condition (1.57b) which is more realistic. Under this condition, the wall temperature is altered by the perturbations of the base state.

- at the film surface $y = h_\mathrm{N}$:

$$\begin{aligned}
\tilde{v} &= \partial_t \tilde{h} + U\partial_x \tilde{u} && (1.58)\\
\tilde{p} &= \mathrm{Ct}\ \tilde{h} - (\mathrm{Ka} - \mathrm{Ma}\Theta)\boldsymbol{\nabla}_{xz}^2 \tilde{h} + 2\partial_y \tilde{v} && (1.59)\\
\tilde{h} &= \mathrm{Ma}(\mathrm{D}\Theta\ \partial_x \tilde{h} + \partial_x \tilde{T}) + \partial_y \tilde{u} + \partial_x \tilde{v} && (1.60)\\
0 &= \mathrm{Ma}(\mathrm{D}\Theta\ \partial_z \tilde{h} + \partial_z \tilde{T}) + \partial_z \tilde{v} + \partial_y \tilde{w} && (1.61)\\
\partial_y \tilde{T} &= -\mathrm{Bi}(\mathrm{D}\Theta\ \tilde{h} + \tilde{T}), && (1.62)
\end{aligned}$$

where $\mathrm{D}^2 U = -1$, $\mathrm{D}^2\Theta = 0$, $\mathrm{D}P = -\mathrm{Ct}$, $\mathrm{D}U|_{h_\mathrm{N}} = 0$, $P|_{h_\mathrm{N}} = 0$ and the continuity equation (1.55) have been used. $\boldsymbol{\nabla}_{xz}^2 = \partial_{xx} + \partial_{zz}$ is the laplacian operator at the film surface.

The above system of equations can be rearranged to make appear only the perturbations of the normal velocity $\tilde{v}$, the temperature $\tilde{T}$ and the film thickness $\tilde{h}$. Let us first apply the divergence operator to the Navier-Stokes equation in its vectorial form, *i.e.* $[\partial_x(1.51) + \partial_y(1.52) + \partial_z(1.53)]$. With the use of the continuity equation (1.55), it reduces to

$$\boldsymbol{\nabla}^2 \tilde{p} = -2\mathrm{D}U\partial_x \tilde{v}. \tag{1.63}$$

Applying then the Laplacian operator to the normal component of the Navier-Stokes equation, *i.e.* $[\boldsymbol{\nabla}^2(1.52)]$, and with the use of (1.63) to eliminate the pressure, plus $\mathrm{D}^2 U = -1$, we obtain

$$\boldsymbol{\nabla}^2(\partial_t \tilde{v} - \boldsymbol{\nabla}^2 \tilde{v}) + (1 + U\boldsymbol{\nabla}^2)\partial_x \tilde{v} = 0. \tag{1.64}$$

We do the same for the normal stress boundary condition to which we apply the Laplacian operator. Given that, from (1.63), $\boldsymbol{\nabla}^2 \tilde{p}|_{h_\mathrm{N}} = 0$, and using the continuity equation, $[\boldsymbol{\nabla}^2(1.59)]$ becomes independent on the pressure and yields

$$\mathrm{Ct}\boldsymbol{\nabla}_{xz}^2 \tilde{h} - (\mathrm{Ka} - \mathrm{Ma}\Theta)\boldsymbol{\nabla}_{xz}^2 \boldsymbol{\nabla}_{xz}^2 \tilde{h} + 2\boldsymbol{\nabla}^2 \partial_y \tilde{v} = 0. \tag{1.65}$$

Besides, an other way to eliminate the pressure is to perform the operation $[(1.52) - \partial_y(1.59)]$ that leads to

$$\partial_t \tilde{v} - \boldsymbol{\nabla}_{xz}^2 \tilde{v} + \partial_{yy}\tilde{v} + U\partial_x \tilde{v} = 0. \tag{1.66}$$

Finally, the difference $[(1.65)\text{-}\partial_y(1.66)]$ gives the final form of the normal stress boundary condition

$$\mathrm{Ct}\boldsymbol{\nabla}_{xz}^2\tilde{h} - (\mathrm{Ka} - \mathrm{Ma}\Theta)\boldsymbol{\nabla}_{xz}^2\boldsymbol{\nabla}_{xz}^2\tilde{h} + 3\boldsymbol{\nabla}_{xz}^2\partial_y\tilde{v} + \partial_{yyy}\tilde{v} - \partial_{yt}\tilde{v} - U\partial_{xy}\tilde{v} = 0. \tag{1.67}$$

Applying now the divergence operator to the vectorial tangential stress boundary condition, *i.e.* $[\partial_x(1.60) + \partial_z(1.61)]$, and with the use of the continuity equation, we get

$$\partial_x\tilde{h} - \mathrm{Ma}(\mathrm{D}\Theta\boldsymbol{\nabla}_{xz}^2\tilde{h} + \boldsymbol{\nabla}_{xz}^2\tilde{T}) - (\boldsymbol{\nabla}_{xz}^2 - \partial_{yy})\tilde{v} = 0. \tag{1.68}$$

Proceeding with the linear stability analysis we now substitute the perturbed quantities by their normal mode expression

$$\begin{pmatrix} \tilde{v} \\ \tilde{T} \\ \tilde{h} \end{pmatrix} = \begin{pmatrix} \phi(y) \\ \tau(y) \\ \eta \end{pmatrix} \exp\{\mathrm{i}(k_x x + k_z z - \Gamma t)\}. \tag{1.69}$$

where k_x and k_z are the wavenumbers in the x- and z-directions and Γ is the complex pulsation. We rescale the variables from the base state film thickness h_N through the following transformation: $(x, y, z, \eta, \Gamma) \to h_\mathrm{N}(x, y, z, \eta, \Gamma)$, $(t, k_x, k_z) \to (t, k_x, k_z)/h_\mathrm{N}$, $(\phi, U) \to h_\mathrm{N}^2(\phi, U)$. This has the advantage that the dimensionless space interval $y \in [0, h_\mathrm{N}]$ is now $[0, 1]$. The transformation makes also appear the set of parameters $\{\mathrm{Re}, \mathrm{Ct}, \mathrm{We}, \mathrm{M}, \mathrm{B}\}$ introduced in §1.2, and more appropriate to the linear problem. The base state in this scaling is described by

$$U(y) = \frac{1}{2}y(2-y) \tag{1.70a}$$

$$V(y) = W(y) = 0 \tag{1.70b}$$

$$P(y) = \mathrm{Ct}(1-y) \tag{1.70c}$$

$$\Theta(y) = 1 - \frac{\mathrm{B}y}{1+\mathrm{B}} \qquad (\mathrm{TC}) \tag{1.70d}$$

$$\Theta(y) = \frac{1+\mathrm{B}(1-y)}{\mathrm{B}+\mathrm{B_w}(1+\mathrm{B})} \qquad (\mathrm{HFC}). \tag{1.70e}$$

Introducing (1.69) into the governing equations (1.64,1.54) and the boundary conditions (1.56,1.57,1.58,1.62,1.67,1.68) leads to

$$\left(\mathrm{D}^2 - k^2\right)^2 \phi + \mathrm{i}3\mathrm{Re}\left[(\Gamma - k_x U)(\mathrm{D}^2 - k^2) - k_x\right]\phi = 0 \tag{1.71a}$$

$$\left(\mathrm{D}^2 - k^2\right)\tau - 3\mathrm{RePr}\left[\mathrm{D}\Theta\ \phi - \mathrm{i}\left(\Gamma - k_x U\right)\tau\right] = 0 \tag{1.71b}$$

$$\phi(0) = 0 \tag{1.71c}$$

$$\tau(0) = 0 \qquad (\mathrm{TC}) \tag{1.71d}$$

$$\mathrm{D}\tau(0) = \mathrm{B_w}\tau(0) \qquad \text{(HFC)} \tag{1.71e}$$

$$\phi(1) + \mathrm{i}\frac{1}{2}\eta\,(2\Gamma - k_x) = 0 \tag{1.71f}$$

$$\eta\, k\left[\mathrm{Ct} + (\mathrm{We} - \mathrm{M}\Theta(1))\, k^3\right] = \left[(\mathrm{D}^2 - 3k^2) + \mathrm{i}\,\frac{3}{2}\mathrm{Re}\,(2\Gamma - k_x)\right]\mathrm{D}\phi(1) \tag{1.71g}$$

$$\left(\mathrm{D}^2 + k^2\right)\phi(1) + \mathrm{M}\left[\eta\mathrm{D}\Theta + \tau(1)\right]k + \mathrm{i}k_x\eta = 0 \tag{1.71h}$$

$$\mathrm{D}\tau(1) + \mathrm{B}\left[\eta\mathrm{D}\Theta + \tau(1)\right] = 0, \tag{1.71i}$$

where $k^2 = k_x^2 + k_z^2$, 3Re has been substituted for h_N^3 (1.37), and $U(1) = \frac{1}{2}$ has been used. Let us stress that k_x and k_z play very different roles, even at linear perturbation analysis, as the next two sections show explicitely.

1.4.1 Pure transverse perturbations: $k_x = 0$, $k = k_z$

When the film is horizontal, a mean flow does not exist and the instability is of thermocapillary origin with no preferred direction [45, 23]. As announced in §1.2, our scaling does not allow the $\beta = 0$ limit. Nevertheless, when the plane is slightly tilted ($\beta \ll 1$), Sreenivasan & Lin [132] show that the instability at $k = \mathcal{O}(1)$ assumes the form of longitudinal rolls. In this case ($k_x = 0$), the basic velocity is absent from the governing equations and the pure spanwise instability is stationary, which implies the transformation $\Gamma \to \mathrm{i}s$, where s is the real growth rate. The system (1.71), with $k = k_z$ becomes

$$\left(\mathrm{D}^2 - k^2\right)^2\phi - 3\mathrm{Re}\,s\left(\mathrm{D}^2 - k^2\right)\phi = 0 \tag{1.72a}$$

$$\left(\mathrm{D}^2 - k^2\right)\tau - 3\mathrm{RePr}\left[\mathrm{D}\Theta\ \phi + s\tau\right] = 0 \tag{1.72b}$$

$$\phi(0) = 0 \tag{1.72c}$$

$$\tau(0) = 0 \qquad \text{(TC)} \tag{1.72d}$$

$$\mathrm{D}\tau(0) = \mathrm{B_w}\tau(0) \qquad \text{(HFC)} \tag{1.72e}$$

$$\eta = \frac{\phi(1)}{s} \tag{1.72f}$$

$$\eta\, k\left[\mathrm{Ct} + (\mathrm{We} - \mathrm{M}\Theta(1))\, k^3\right] = \left[(\mathrm{D}^2 - 3k) - 3\mathrm{Re}\,s\right]\mathrm{D}\phi(1) \tag{1.72g}$$

$$\left(\mathrm{D}^2 + k^2\right)\phi(1) + \mathrm{M}\left[\eta\mathrm{D}\Theta + \tau(1)\right]k = 0 \tag{1.72h}$$

$$\mathrm{D}\tau(1) + \mathrm{B}\left[\eta\mathrm{D}\Theta + \tau(1)\right] = 0, \tag{1.72i}$$

$$\text{with} \qquad \mathrm{D}\Theta = \frac{-\mathrm{B}}{1+\mathrm{B}} \qquad \text{(TC)} \qquad \text{or} \qquad \mathrm{D}\Theta = \frac{-\mathrm{B}}{\mathrm{B} + \mathrm{B_w}(1+B)} \qquad \text{(HFC)}.$$

For usual liquids, $\mathrm{M} \ll \mathrm{We}$ and $\Theta(1) = 1/(1+\mathrm{B}) = \mathcal{O}(1)$ such that we can neglect the surface tension variation due to temperature in the normal stress boundary condition (1.72g). Moreover, assuming that the marginal state is stationary [45], *i.e.* $s = 0$, the

system (1.72) yields an analytic solution. The marginal (neutral) state, for the heat flux condition first, is found as

$$\mathrm{M}_\mathrm{c}^\star = \left[\frac{16k\left[(\mathrm{B}+\mathrm{B_w})k\cosh k + (\mathrm{BB_w}+k^2)\sinh k\right](2k-\sinh 2k)}{3\mathrm{PrRe}\left[(3k^2+12k^4(\mathrm{B_w}-1))\cosh k - k\cosh -4\mathrm{B_w}\sinh^3 k \right.} \right. \\ \left. \left. +4k^2(2+k^2)\sinh k\right] - 32k^5(\mathrm{B_w}\cosh k + k\sinh k)(\mathrm{Ct}+k^2\mathrm{We})^{-1} \right] \qquad \text{(HFC)} \tag{1.73}$$

where the relation $\mathrm{M}^\star = \mathrm{M}b_\mathrm{s}h_\mathrm{N} = -\mathrm{MD}\Theta$, based on the base state solution (see 1.46 and 1.49), has been used for sake of generality. Indeed, it allows the limit $\mathrm{B_w} \to \infty$ of (1.73) to yield

$$\mathrm{M}_\mathrm{c}^\star = \frac{4k(k\cosh k + \mathrm{B}\sinh k)(2k-\sinh 2k)}{3\mathrm{PrRe}\left(k^3\cosh k - \sinh^3 k\right) - 8k^5\cosh k\,(\mathrm{Ct}+k^2\mathrm{We})^{-1}}, \qquad \text{(TC)} \tag{1.74}$$

that corresponds to a perfect conducting wall. This latter expression (1.74) is identical to the critical Marangoni number found by Scriven & Sterling [125] and Smith [129] for cellular convection in a horizontal layer heated from below. This may be surprising since as announced in §1.2, our scaling does not allow to consider the limit of horizontal layers. Hence, it merely means that the pure transverse instability modes are decoupled to the gravity driven-flow and match therefore with the ones for a horizontal layer, under the same conditions; the Reynolds number appearing in (1.74) accounting only for the change of the mean film thickness with the flow rate.
In the same vein, note that (1.74) reduces to Pearson's relation [100] in the limit $\mathrm{Ct}, \mathrm{We} \to \infty$, *i.e.* for an horizontal layer with non-deformable interface. Within this limit, Pearson obtained also the critical Marangoni number in the case of a really poorly heat conducting plate, *i.e.* $\mathrm{Bi_w} = 0$, that can also be obtained directly from (1.73).
Now, for finite Ct and We, a significant modification of the neutral stability result occurs in the region of long waves ($k \to 0$). Taking the zero wavenumber case $k = 0$ reduces (1.73) and (1.74) to

$$\mathrm{Ct} = \frac{3\mathrm{B_w}\mathrm{M}^\star}{2(\mathrm{B}+\mathrm{B_w}(1+\mathrm{B}))} \qquad \text{(HFC)} \tag{1.75a}$$

$$\mathrm{Ct} = \frac{3\mathrm{M}^\star}{2(1+\mathrm{B})} \qquad \text{(TC)}, \tag{1.75b}$$

which makes the critical Marangoni number constant. In the case of a perfectly conducting plate (TC), $\mathrm{M}^\star \sim h_\mathrm{N}^{-1}$ such that the long-wave instability is dominant for very thin films unless the film is vertical ($\mathrm{Ct} = 0$), in the case of which the film is always unstable, *i.e.* for all h_N (say Re). Let us consider then the vertical case and the long-wave expansion of $\mathrm{M}_\mathrm{c}^\star$, *i.e.* $k \ll 1$. Under those conditions, (1.73) and (1.74) yield the so-called cut-off wavenumbers that read

$$k_\mathrm{c} = \left(\frac{3\mathrm{B_w}\mathrm{M}^\star}{2\mathrm{We}(\mathrm{B}+\mathrm{B_w}(1+\mathrm{B}))}\right)^{1/2} \qquad \text{(HFC)} \tag{1.76a}$$

$$k_{\rm c} \;=\; \left(\frac{3{\rm M}^\star}{2{\rm We}(1+{\rm B})}\right)^{1/2} \qquad \text{(TC)}, \tag{1.76b}$$

depending whether the wall is a poor or a perfect conductor, respectively. The cut-off wavenumber provides the band of unstable normal modes $0 < k < k_{\rm c}$ for which the linear growth rate of the corresponding disturbances is positive. The resulting instability was classified by Goussis & Kelly [46] as the **S-mode**. Equations (1.76) can also be obtained for an inclined wall by truncating the long-wave expansion at first-order, provided $k^2{\rm We} = \mathcal{O}(1)$. Indeed, the surface tension is the only mechanism that provides a cut-off wavenumber beyond which small wave disturbances are damped.

1.4.2 Pure longitudinal perturbations: $k = k_x$, $k_z = 0$

Yih [146] extended the Squire's theorem to free surface flows [50]. He demonstrated for zero Marangoni number, that the stability of the primary flow with respect to two-dimensional disturbances determines also its stability with respect to three-dimensional ones. Actually, he found that when the film is isothermal, the most unstable disturbance, *i.e.* with the largest growth rate, consists of longitudinal waves ($k_z = 0$). The situation remains the same in the non-isothermal case, at least in the long-wave $k \to 0$ limit [46]. The equations governing the stability of the flow with respect to streamwise disturbances are obtained from (1.71) by use of the transformations

$$\phi = ik_x\varphi, \quad \Gamma = k_x c,$$

where φ is the normal mode amplitude of the stream function and c is the complex wave speed. The use of the stream function – usually noted ψ and defined as $u = \partial_y\psi$ and $v = -\partial_x\psi$ – is justified here for an incompressible and a bidimensional flow. The governing equations with $k = k_x$ become

$$\left({\rm D}^2 - k^2\right)^2\varphi + {\rm i}3{\rm Re}\,k\left[(c-U)({\rm D}^2-k^2) - 1\right]\varphi = 0 \tag{1.77a}$$

$$\left({\rm D}^2 - k^2\right)\tau + {\rm i}3{\rm RePr}k\left[{\rm D}\Theta\;\varphi + (c-U)\,\tau\right] = 0 \tag{1.77b}$$

$$\varphi(0) = {\rm D}\varphi(0) = 0 \tag{1.77c}$$

$$\tau(0) = 0 \qquad \text{(TC)} \tag{1.77d}$$

$${\rm D}\tau(0) = {\rm B_w}\tau(0) \qquad \text{(HFC)} \tag{1.77e}$$

$$\eta = \frac{\varphi(1)}{c - 1/2} \tag{1.77f}$$

$$\left[({\rm D}^2 - 3k^2) + {\rm i}\frac{3}{2}{\rm Re}k(2c-1)\right]{\rm D}\varphi(1) - {\rm i}\eta k\left[{\rm Ct} + ({\rm We} - {\rm M}\Theta(1))\,k^2\right] = 0 \tag{1.77g}$$

$$\left({\rm D}^2 + k^2\right)\varphi(1) + {\rm i}k{\rm M}\left[\eta{\rm D}\Theta + \tau(1)\right] - \eta = 0 \tag{1.77h}$$

$${\rm D}\tau(1) + {\rm B}\left[\eta{\rm D}\Theta + \tau(1)\right] = 0. \tag{1.77i}$$

Equation (1.77a) is referred to as the Orr-Sommerfeld equation. Let us perform now a small-wavenumber analysis of the above system, following the method proposed by

Yih [147] for the isothermal case. It consists in expanding φ, τ and c around their solutions for $k = 0$. When $k = 0$, the system (1.77) reduces to

$$\varphi'''' = 0 \tag{1.78a}$$

$$\tau'' = 0 \tag{1.78b}$$

$$\varphi(0) = \varphi'(0) = 0 \tag{1.78c}$$

$$\tau(0) = 0 \qquad \text{(TC)} \tag{1.78d}$$

$$\tau'(0) = \mathrm{B_w}\tau(0) \qquad \text{(HFC)} \tag{1.78e}$$

$$\varphi'''(1) = 0 \tag{1.78f}$$

$$\varphi''(1) - \frac{\varphi(1)}{c - 1/2} = 0 \tag{1.78g}$$

$$\tau'(1) + \mathrm{B}\left[\frac{\varphi(1)}{c - 1/2}\Theta' + \tau(1)\right] = 0, \tag{1.78h}$$

where the prime is equivalent to the differential operator D. The integration of (1.78a) gives: $\varphi = A_0 y^3 + B_0 y^2 + C_0 y + D_0$. The no-penetration and no-slip conditions at the wall (1.78c) and the normal stress condition at the free surface (1.78f) lead to $A_0 = C_0 = D_0 = 0$. The tangential stress condition (1.78g) at the free surface determine the phase speed $c_0 = 1$. The constant B_0 remains undetermined since the system is linear and homogeneous. For convenience, we will take $B_0 = 1$ and therefore,

$$\varphi_0 = y^2. \tag{1.79}$$

At zero-order, the perturbed streamwise velocity is thus linear, $\varphi_0' = 2y$, whose origin is the viscous shear stress. Since c_0 has no imaginary part, the perturbation is neither amplified nor damped. The axis $k = 0$ is part of the marginal stability curve and corresponds to the transition between one Nusselt solution to another one by change of the flow rate, which is always a neutrally stable perturbation.
The integration of (1.78b) gives:

$$\tau_0 = E_0\ y + F_0. \tag{1.80}$$

The heat transfer conditions at the wall (1.78d) or (1.78e) and at the free surface (1.78h) leads to

$$\begin{aligned} E_0 &= 2\,\mathrm{D}\Theta^2, \qquad F_0 = 0 \qquad && \text{(TC)} \\ E_0 &= 2\,\mathrm{B_w}\,\mathrm{D}\Theta^2, \qquad F_0 = 2\,\mathrm{D}\Theta^2 \qquad && \text{(HFC)}, \end{aligned}$$

where $c_0 = 1$ has been used. Let expand now c, φ and τ around their solutions for $k = 0$, as

$$\begin{aligned} c &= c_0 + \mathrm{i}kc_1 - k^2c_2 - \mathrm{i}k^3c_3 + \mathcal{O}\big(k^4\big) \\ \varphi &= \varphi_0 + \mathrm{i}k\varphi_1 - k^2\varphi_2 - \mathrm{i}k^3\varphi_3 + \mathcal{O}\big(k^4\big) \end{aligned}$$

$$\tau = \tau_0 + \mathrm{i}k\tau_1 - k^2\tau_2 - \mathrm{i}k^3\tau_3 + \mathcal{O}\big(k^4\big)\,,$$

and substituting their expression in (1.77). In the same way as for the zeroth order, the resolution of the system at first-order leads to

$$\varphi_1 = \mathrm{Re}\left(\frac{y^5}{20} - \frac{y^4}{4}\right) + \frac{\mathrm{Ct}}{3}y^3 + B_1 y^2 \tag{1.81}$$

$$\tau_1 = \mathrm{Pe}\left(-\frac{3}{40}E_0 y^5 - \frac{1}{8}(2\mathrm{D}\Theta - 2E_0 + F_0)y^4 - \frac{1}{2}(E_0 - F_0)y^3 - \frac{3}{2}F_0 y^2\right) + E_1 y + F_1 \tag{1.82}$$

$$c_1 = \frac{2}{5}\mathrm{Re} - \frac{1}{3}\mathrm{Ct} - \frac{\mathrm{M}}{4}(2\mathrm{D}\Theta + \mathrm{E}_0 + F_0). \tag{1.83}$$

The constant B_1 is unspecified (it actually replicates the solution at zeroth-order, corresponding to a redefinition of B_0). Since $\mathrm{i}kB_1y^2 \propto \varphi_0$, let us set $B_1 = 0$ such that φ_1 appears as a true correction to φ_0. The other constants become

$$\begin{aligned} E_1 = G, \quad & F_1 = 0 \qquad && \text{(TC)} \\ E_1 = \mathrm{B_w}\, G, \quad & F_1 = G \qquad && \text{(HFC)}, \end{aligned}$$

$$\text{where} \quad G = 2\mathrm{D}\Theta^2(\mathrm{Ct} - \mathrm{Re}) + \frac{2\mathrm{D}\Theta^3\mathrm{M}}{1+\mathrm{B}} - \frac{\mathrm{Pe}\,\mathrm{D}\Theta}{40\mathrm{B}}\left[10(4+\mathrm{B})\mathrm{D}\Theta + (35+13\mathrm{B})E_0 + 5(16+9\mathrm{B})F_0\right].$$

The first-order term of the phase speed $\mathrm{i}kc_1$ being imaginary, k^2c_1 will contribute to the growth rate of the instability. If $c_1 < 0$, the system will be stable and if $c_1 > 0$, the system will be unstable. Therefore, the condition $c_1 = 0$ provides the relations for a neutral disturbance:

$$\mathrm{Ct} = \frac{6}{5}\mathrm{Re} + \frac{3\mathrm{M}^\star}{2(1+\mathrm{B})} \qquad \text{(TC)} \tag{1.84a}$$

$$\mathrm{Ct} = \frac{6}{5}\mathrm{Re} + \frac{3\mathrm{B_w}\mathrm{M}^\star}{2(\mathrm{B} + \mathrm{B_w}(1+\mathrm{B}))} \qquad \text{(HFC)}. \tag{1.84b}$$

The right-hand side terms of (1.84) represent the destabilizing effects of inertia and thermocapillary forces, respectively, while the left-hand side term represents the stabilizing effects of hydrostatic pressure. When $\mathrm{M}^\star = 0$, the above relation reduces to $\mathrm{Ct} = \frac{6}{5}\mathrm{Re}$ which defines the critical conditions for the surface wave or hydrodynamic mode of instability (H-mode). Smith [130] has evidenced the role of inertia in the occurrence of a phase shift between the interface location and the vorticity field that originates this H-mode instability. For longitudinal rolls (say rivulets aligned with the flow) Goussis & Kelly [46] have shown that there is no mechanism to allow energy transfer from the mean flow to the disturbance, so that the term representing the mean shear is absent. Indeed, if the term Re of (1.84) is neglected, one

recovers (1.75), which defines the critical conditions for thermocapillary instability (S-mode) for long-wave disturbances. This result led to the conclusion that in the $k \to 0$ limit, transverse waves are more unstable (*i.e.* with higher growth rate) than longitudinal rolls [46]. In summary, long-wave transverse and longitudinal modes are equally affected by thermocapillarity, but the latter gets an additional destabilizing contribution from inertia; H-mode and S-mode clearly reinforcing each other.
We can proceed further with the wavenumber expansion of the system (1.77) in the same manner as for the first-order. Because of tedious algebra, we only report here the results for the complex phase speed of the TC case:

$$\begin{aligned} c &= 1 + \mathrm{i}k\left[\frac{2}{5}\mathrm{Re} - \frac{\mathrm{Ct}}{3} + \frac{\mathrm{M}^\star}{2(1+\mathrm{B})}\right] \\ &- k^2\left[1 - \frac{10}{21}\mathrm{CtRe} + \frac{4}{7}\mathrm{Re}^2 + \frac{\mathrm{M}^\star}{80(1+\mathrm{B})}\left(57\mathrm{Re} + \frac{15-7\mathrm{B}}{1+\mathrm{B}}\mathrm{Pe}\right)\right] \\ &- \mathrm{i}k^3\left[-\frac{3}{5}\mathrm{Ct} + \frac{471}{224}\mathrm{Re} - \frac{17363}{17325}\mathrm{CtRe}^2 + \frac{75872}{75075}\mathrm{Re}^3 + \frac{2}{15}\mathrm{Ct}^2\mathrm{Re} + \frac{\mathrm{We}}{3} - \frac{\mathrm{M}^\star}{3\mathrm{B}}\right. \\ &+ \frac{\mathrm{M}^\star}{1+\mathrm{B}}\left[\frac{\mathrm{M}^\star}{16(1+\mathrm{B})}\left(5\mathrm{Re} + \frac{3-\mathrm{B}}{1+B}\mathrm{Pe}\right) - \frac{49}{120}\mathrm{CtRe} + \frac{2707}{1792}\mathrm{Re}^2 + \frac{(6+5\mathrm{B})}{6(1+\mathrm{B})}\right. \\ &- \left.\left.\frac{(-5435+\mathrm{B}(2090+749\mathrm{B}))\mathrm{Pe}^2}{44800(1+\mathrm{B})^2} + \frac{(9605-3653\mathrm{B})\mathrm{PeRe}}{22400(1+\mathrm{B})} - \frac{\mathrm{CtPe}(33-7\mathrm{B})}{240(1+\mathrm{B})}\right]\right]. \end{aligned} \tag{1.85}$$

Equation (1.85) will be used in the following to validate the new models. It actually represents an exact asymptotic result that should be compared to simpler asymptotic models. Since the validation will be made on the TC case in the following, we do not report here the similar expression for the HFC case. Remark that the Weber number appears only at the order three in the $k-$expansion. However, the surface tension is the only physical effect that limits the growth rate of short waves ($k \to \infty$) and then prevents waves from breaking. It implies that $k^2\mathrm{We} = \mathcal{O}(1)$ when k corresponds to waves observed experimentally. In this case, the marginal stability curve corresponding to a zero growth rate, *i.e.* $\Im(c) = 0$, can be obtained close to the criticality by truncating the long wavelength expansion (1.85) at lowest order in k:

$$\left(\frac{6}{5}\mathrm{Re} - \mathrm{Ct} + \frac{3\mathrm{M}^\star}{2(1+\mathrm{B})}\right) - k_\mathrm{c}^2\mathrm{We} = 0, \qquad (\mathrm{TC}) \tag{1.86}$$

where k_c is the cut-off wavenumber. Relation (1.86) describes the *neutral curve* in the parameter space, *i.e.* the locus where the growth rate is zero. In the same manner, the wavenumber corresponding to the maximal growth rate, *i.e.* $\partial(k\Im(c))/\partial k = 0$, verifies

$$\left(\frac{6}{5}\mathrm{Re} - \mathrm{Ct} + \frac{3\mathrm{M}^\star}{2(1+\mathrm{B})}\right) - 2k_\mathrm{m}^2\mathrm{We} = 0, \qquad (\mathrm{TC}) \tag{1.87}$$

such that

$$k_\mathrm{m} = \frac{k_\mathrm{c}}{\sqrt{2}}.$$

Finally, the linear growth rate of the most unstable mode reads

$$s_{\rm m} = \Im(k\,c)\big|_{k_{\rm m}} = \frac{(5{\rm Ct}-6{\rm Re})^2}{300{\rm We}} - \frac{{\rm M}^\star(5{\rm Ct}-6{\rm Re})}{20(1+{\rm B}){\rm We}} + \frac{3{\rm M}^{\star 2}}{16(1+{\rm B})^2{\rm We}}. \tag{1.88}$$

Note that similar results are obtained with the HFC case although we will not need them in the following.

1.5 Boundary layer equations

Since the issue of this work is to study the dynamics of thin films, where long-wave instability modes (S and H) are dominant, we may expect an approximation to apply in this context, arising from the smallness of the film thickness modulations as compared to the film thickness itself. The answer is given by the boundary layer approximation leading to the boundary layer equations. Those equations are obtained in this section and will constitute the starting equations for the remaining chapters.
In the boundary layer theory, the strong viscous diffusion in the cross-stream y component of the momentum equation ensures the coherence of the flow across the momentum boundary layer whose thickness is a solution of the problem. Therefore, the flow is laminar in the core of the viscous boundary layer and the inertia effects associated to the motion of the fluid particles along the $y-$coordinate can be neglected. Thin viscous film flows share the same characteristics such that the boundary layer theory applies, but only as an approximation since the film thickness is *a priori* determined by the flow rate.
To express that the slope of the interface is always small with regards to the film thickness itself, we shall introduce a formal parameter $\varepsilon \ll 1$. This parameter, sometimes named the 'film parameter', should ensure slow time and space modulations of the basic flat film solution (1.43). Practically, it consists in applying a gradient expansion through the transformation $(\partial_t, \partial_x, \partial_z) \to \varepsilon(\partial_t, \partial_x, \partial_z)$ in the governing equations. The continuity equation reads therefore

$$\varepsilon\partial_x u + \partial_y v + \varepsilon\partial_z w = 0,$$

which shows that $\partial_y v$, and thus v, are of order ε. This suggests the transformation $v \to \varepsilon v$ such that

$$\partial_x u + \partial_y v + \partial_z w = 0, \tag{1.89}$$

in this scaling (which is used everywhere in what follows). The remaining of the system (1.17-1.20), truncated at $\mathcal{O}(\varepsilon^3)$, then becomes

$$\begin{aligned}
\varepsilon\left(\partial_t u + u\partial_x u + v\partial_y u + w\partial_z u\right) &= -\varepsilon\partial_x p + \varepsilon^2\partial_{xx}u + \partial_{yy}u + \varepsilon^2\partial_{zz}u + 1 && (1.90)\\
\varepsilon^2\left(\partial_t v + u\partial_x v + v\partial_y v + w\partial_z v\right) &= -\partial_y p + \varepsilon\partial_{yy}v - {\rm Ct} + \mathcal{O}\big(\varepsilon^3\big) && (1.91)\\
\varepsilon\left(\partial_t w + u\partial_x w + v\partial_y w + w\partial_z w\right) &= -\varepsilon\partial_z p + \varepsilon^2\partial_{xx}w + \partial_{yy}w + \varepsilon^2\partial_{zz}w && (1.92)\\
\varepsilon{\rm Pr}\left(\partial_t T + u\partial_x T + v\partial_y T + w\partial_z T\right) &= \varepsilon^2\partial_{xx}T + \partial_{yy}T + \varepsilon^2\partial_{zz}T. && (1.93)
\end{aligned}$$

The dimensionless boundary conditions at the wall are still given by (1.22,1.23) – it is necessary to assume slow variation of $F_{\rm w}(x)$ –, while at the free surface, the

kinematic condition is given by (1.24). The other boundary conditions at the free surface (1.25,1.26,1.27,1.28) are expanded in ε up to $\mathcal{O}(\varepsilon^3)$:
at $y = h(x, z, t)$,

$$p = 2\varepsilon(\partial_y v - \partial_x h\partial_y u - \partial_z h\partial_y w) - \varepsilon^2(\mathrm{Ka} - \mathrm{Ma}\,T)(\partial_{xx}h + \partial_{zz}h) + \mathcal{O}\left(\varepsilon^3\right) \tag{1.94}$$

$$\partial_y u = -\varepsilon\mathrm{Ma}\partial_x\theta + \varepsilon^2\left(\partial_z h[\partial_z u + \partial_x w] + 2\partial_x h[2\partial_x u + \partial_z w] - \partial_x v\right) + \mathcal{O}\left(\varepsilon^3\right) \tag{1.95}$$

$$\partial_y w = -\varepsilon\mathrm{Ma}\partial_z\theta - \varepsilon^2\left(\partial_x h[\partial_z u + \partial_x w] + 2\partial_z h[2\partial_z w + \partial_x u] - \partial_z v\right) + \mathcal{O}\left(\varepsilon^3\right) \tag{1.96}$$

$$\partial_y T = -\mathrm{Bi}T - \varepsilon^2\left(\frac{\mathrm{Bi}}{2}T\left[(\partial_x h)^2 + (\partial_z h)^2\right] - \partial_z h\partial_z T - \partial_x h\partial_x T\right) + \mathcal{O}\left(\varepsilon^3\right) \tag{1.97}$$

where the surface temperature $\theta = T\big|_{y=h}$ has been introduced through the relation

$$\left[(\partial_i + \partial_i h\partial_y)T\right]\big|_h \equiv \partial_i\theta \quad \text{with} \quad i = x, z.$$

The notation $\cdot\big|_h$ refers to the evaluation of the corresponding quantity at the free surface $y = h$. The temperature at the film surface will appear as the relevant variable in the following for the derivation of the new models in chapter 5.
At $\mathcal{O}(\varepsilon^2)$, the momentum equations in the streamwise and spanwise directions, as well as the energy equation are still exact. The $\mathcal{O}(\varepsilon^2)$ dissipation terms $\propto \partial_{xx}, \partial_{zz}$ have an effect on wave dispersion, in the linear and in the nonlinear regime, as pointed out by Ruyer-Quil [107] for the isothermal case. Since the pressure is only coupled in (1.90) and (1.92) through its gradient $\propto \varepsilon$, a simple approximation of the pressure valid up to $\mathcal{O}(\varepsilon)$ will be sufficient for its elimination while keeping the model consistent at $\mathcal{O}(\varepsilon^2)$. This elimination of p constitutes the main consequence of the boundary layer approximation as explored initially for the isothermal case by Shkadov [126]. The above procedure would obviously have been impossible with $\mathcal{O}(\varepsilon^3)$ terms because of the second-order inertia terms in (1.91).
Equations (1.95,1.96) show that $\partial_y u, \partial_y w$ are at least of $\mathcal{O}(\varepsilon)$ at the free surface such that (1.94) becomes

$$p\big|_h = 2\varepsilon\partial_y v\big|_h - \varepsilon^2\mathrm{Ka}(\partial_{xx}h + \partial_{zz}h) + \mathcal{O}\left(\varepsilon^2\right), \tag{1.98}$$

where the $\mathcal{O}(\varepsilon^2)$ term corresponding to the surface tension has been conserved. Indeed, as seen in §1.4.2, the surface tension cannot be neglected since it determines the range of unstable wavenumbers $0 < k < k_c$ and ensures the validity of the hypothesis of slow time and space evolution. Setting $\varepsilon^2\mathrm{Ka} \to \mathrm{Ka}$, integrating (1.91) between y and h, and using the boundary conditions (1.98) and (1.22), one obtain

$$p = \mathrm{Ct}(h - y) - \mathrm{Ka}(\partial_{xx}h + \partial_{zz}h) + \varepsilon(\partial_y v + \partial_y v\big|_h) + \mathcal{O}\left(\varepsilon^2\right). \tag{1.99}$$

The first term of the r.h.s. of (1.99) is the hydrostatic pressure that vanishes for vertical walls ($\mathrm{Ct} = 0$) while the third term accounts for higher-order viscous effects. Then, substituting p into (1.90) and (1.92)) leads to

$$\begin{aligned}\varepsilon\left[\partial_t u + \partial_x(u^2) + \partial_y(uv) + \partial_z(uw)\right] - \partial_{yy}u - \varepsilon^2(2\partial_{xx}u + \partial_{zz}u + \partial_{xz}w)\\ = 1 - \varepsilon\mathrm{Ct}\,\partial_x h + \varepsilon^3\mathrm{Ka}(\partial_{xxx} + \partial_{xzz})h - \varepsilon^2\partial_x\left[\partial_y v\big|_h\right]\end{aligned} \tag{1.100a}$$

$$\varepsilon\left[\partial_t w + \partial_x(uw) + \partial_y(vw) + \partial_z(w^2)\right] - \partial_{yy} w - \varepsilon^2(2\partial_{zz} w + \partial_{xx} w + \partial_{xz} u)$$
$$= -\varepsilon \mathrm{Ct}\,\partial_z h + \varepsilon^3 \mathrm{Ka}(\partial_{xxz} + \partial_{zzz})h - \varepsilon^2 \partial_z\left[\partial_y v\big|_h\right], \tag{1.100b}$$

obtained by using the relation $u\partial_x\varphi + v\partial_y\varphi + w\partial_z\varphi = \partial_x(u\varphi) + \partial_y(v\varphi) + \partial_z(w\varphi) - \varphi(\partial_x u + \partial_y v + \partial_z w)$ together with the continuity equation (1.21). We may refer to (1.100) as the second-order boundary layer equations. As for the boundary layer theory, the scale separation between x and y allows to neglect the inertia terms in the cross-stream momentum equation, and therefore to eliminate the pressure from the initial problem. That is the reason for calling (1.100) *boundary layer equations* [78, 26]. The original boundary layer equation in isothermal conditions, that does not contain the $\mathcal{O}(\varepsilon^2)$ terms, was studied in its tri-dimensional version by Chang *et al.* [14]. Yu *et al.* [148] have explored the two-dimensional second-order version of the boundary layer equation but with an heuristic term to approximate the normal pressure gradient, motivated in the case of a wall with curvature (cylindrical geometry). They compared the marginal curve of instability predicted by their model to the one corresponding to the Orr-Sommerfeld analysis as well as to the first-order boundary layer equation. They obtained that for $\mathrm{Re} > 25$ with $\mathrm{Ka} = 3371$, the viscous second-order terms should be taken into account to stay in qualitative agreement with the Orr-Sommerfeld equation (figure 4 in [148]). In the nonlinear regime, the significant role played by viscous dispersion on wave profiles and stationary wave selection has been pointed out by Ruyer-Quil & Manneville [109, 110] already in the range of $1 < \mathrm{Re} < 10$ with $\mathrm{We} = 76.4$ (figure 4 in [109]). For these reasons, the new models that will include also the non-isothermal conditions, will be developed in the following up to second-order.

Because the modification of the surface tension with the temperature is neglected in the normal stress boundary condition, the second-order boundary layer equations (1.100) remain identical in the non-isothermal case. Then they should be completed by the continuity equation (1.89), the energy equation (1.93) and the boundary conditions (1.22, 1.23, 1.24, 1.95, 1.96, 1.97).

1.5.1 Two-dimensional boundary layer equations

The preceding system of equations can be reduced for a 2D flow (or parallel flow), *i.e.* $w = 0$ and $\partial_z = 0$, to

$$\partial_x u + \partial_y v = 0 \tag{1.101a}$$
$$\partial_t u + \partial_x(u^2) + \partial_y(uv) - \partial_{yy} u - 2\partial_{xx} u = 1 - \mathrm{Ct}\partial_x h + \mathrm{Ka}\partial_{xxx} h + \partial_x\left[\partial_x u\big|_h\right] \tag{1.101b}$$
$$\mathrm{Pr}\left(\partial_t T + u\partial_x T + v\partial_y T\right) = \left(\partial_{xx} + \partial_{yy}\right) T \tag{1.101c}$$
$$\partial_t h + u\big|_h \partial_x h = v\big|_h \tag{1.101d}$$
$$\partial_y u\big|_h = 4\partial_x h \partial_x u\big|_h - \partial_x v\big|_h - \mathrm{Ma}\partial_x\left[T\big|_h\right] \tag{1.101e}$$
$$\partial_y T\big|_h = -\mathrm{Bi}\left(1 + \frac{1}{2}(\partial_x)^2\right) T\big|_h + \partial_x h \partial_x T\big|_h, \tag{1.101f}$$

where the formal parameter ε has been omitted. This system is completed by the no-slip (1.22) and the heat boundary (1.23) conditions and will be used in chapter 5 as "starting equations" for the derivation of our new model.

1.5.2 Pure longitudinal linear stability analysis

Let us compare the exact result of the Orr-Sommerfeld equation with the linear stability analysis of (1.101). Introducing the *base state set* of parameters $\{\mathrm{Re}, \mathrm{Ct}, \mathrm{We}, \mathrm{M}, \mathrm{B}\}$, the pure longitudinal linear stability analysis – *i.e.* for a uniform heating $F_\mathrm{w} = 0$ – of the second-order boundary layer model leads to solve

$$\varphi''' - \mathrm{i}k(\mathrm{Ct} + k^2\mathrm{We})\frac{\varphi(1)}{c-1/2} - k^2(2\varphi' + \varphi'(1)) - \mathrm{i}3\mathrm{Re}k((U-c)\varphi' - \varphi U') = 0, \quad (1.102)$$

together with (1.77b) and completed by the boundary conditions (1.77c–1.77f, 1.77h, 1.77i). Following the same steps as in §1.4.2, the expansion of the linear system of equations around $k = 0$ leads also to (1.85) for the TC, except the coefficient $\frac{14513}{6720} \approx 2.16$ instead of $\frac{471}{224} \approx 2.10$ and the correction to the surface tension $\mathrm{i}k^3\mathrm{M}^\star/3\mathrm{B}$ that is missing. The small difference in coefficient is a consequence of the approximation on the pressure gradient in the streamwise Navier-Stokes equation.

1.6 Sets of parameters

In this section, we first introduce a new scaling appropriate for nonlinear regimes and next summarize the different sets of parameters introduced up to now with their respective roles.

Comparisons of the shapes of the different waves can be made easier using a scaling based on the intrinsic length-scales of the structures considered. Therefore let us apply a change of scales due to Shkadov [127]. It will be noticed in next chapter that the characteristic slope of the waves corresponds to fore-running capillary waves that precede the main solitary humps. The breaking of the waves promoted by the streamwise gravity force, which is unity in (1.101b), is stopped by the pressure gradient induced by the surface tension $\mathrm{Ka}\partial_{xxx}h$. Therefore, the streamwise characteristic lengthscale corresponding to this balance reads $\mathcal{L} = (\mathrm{Ka}h_\mathrm{N})^{1/3}$ and the ratio between the two lengthscales is noted $\kappa = \mathcal{L}/h_\mathrm{N}$. The characteristic slope is then given by $1/\kappa = (\rho g h_\mathrm{N}^2 \sin\beta/\sigma_\infty)^{1/3} = \mathrm{We}^{-1/3}$. Applying the transformation

$$\mathcal{T} : x \to \mathcal{L}\,x, \quad (y,h) \to h_\mathrm{N}(y,h), \quad t \to \mathcal{L}\,t/h_\mathrm{N}^2 \quad \text{and} \quad (u,v) \to h_\mathrm{N}^2(u, v/\kappa), \quad (1.103)$$

some equations of the boundary-layer system (1.101) are modified as

$$\begin{aligned}
\mathcal{R}\left(\partial_t u + u\partial_x u + v\partial_y u\right) - (\partial_{yy} + 2\eta\partial_{xx})u - \eta\partial_x[\partial_x u\big|_h] & \\
-1 + \mathcal{C}\partial_x h - \partial_{xxx}h &= 0\,, \qquad (1.104a)\\
\mathrm{Pr}\mathcal{R}\left(\partial_t T + u\partial_x T + v\partial_y T\right) - (\eta\partial_{xx} + \partial_{yy})T &= 0\,, \qquad (1.104b)
\end{aligned}$$

$$\begin{aligned}
\partial_y u\big|_h &= \eta\left(4\partial_x h\partial_x u\big|_h - \partial_x v|_h\right) - \mathcal{M}\partial_x\left[T\big|_h\right]\,, \qquad (1.104c)\\
\partial_y T\big|_h &= -\mathrm{B}\left(1 + \frac{\eta}{2}(\partial_x h)^2\right)T\big|_h + \eta\partial_x h\partial_x T\big|_h\,. \qquad (1.104d)
\end{aligned}$$

A set of 'reduced' parameters appear

$$\mathcal{R} = \frac{h_{\rm N}^3}{\kappa} = \frac{3{\rm Re}}{{\rm We}^{1/3}} = \frac{(3{\rm Re})^{11/9}}{{\rm Ka}^{1/3}} \tag{1.105a}$$

$$\mathcal{C} = \frac{{\rm Ct}}{\kappa} = \frac{{\rm Ct}}{{\rm We}^{1/3}} = \frac{{\rm Ct}(3{\rm Re})^{2/9}}{{\rm Ka}^{1/3}} \tag{1.105b}$$

$$\eta = \frac{1}{\kappa^2} = \frac{1}{{\rm We}^{2/3}} = \frac{(3{\rm Re})^{4/9}}{{\rm Ka}^{2/3}} \tag{1.105c}$$

$$\mathcal{M} = \frac{{\rm Ma}}{\kappa h_{\rm N}^2} = \frac{{\rm M}}{{\rm We}^{1/3}} = \frac{{\rm Ma}}{{\rm Ka}^{1/3}(3{\rm Re})^{4/9}} \tag{1.105d}$$

$${\rm B} = {\rm Bi}\,(3{\rm Re})^{1/3}, \tag{1.105e}$$

along with B already defined in (1.42). $\mathcal{R}$ is the reduced Reynolds number[¶] and $\mathcal{C}$ the reduced slope. The parameter η appears along with every second-order streamwise dissipative terms in the momentum and heat equations. Similarly $\mathcal{M}$ is a reduced Marangoni number. Note that with this scaling, the coefficient appearing in front of the surface tension term $\partial_{xxx}h$ is fixed to unity.
We can summarize now the different sets of parameters and how relevant they are with respect to the problem considered:

I the **natural set** : $\{{\rm Re}, {\rm Ct}, {\rm Ka}, {\rm Ma}, {\rm Bi}, {\rm Pr}\}$ which is independent on the flow characteristics. This set corresponds to the balance between viscosity and gravity. It is useful in the physical interpretation of the numerical results, because each of the physical parameters with which one might control the experiment (*i.e.* the flow rate, the temperature difference or the heat transfer coefficient) appears in only a single non-dimensional number. This is true at least for a vertical wall. If we want to control separately the inclination angle, the set $\{{\rm Re}, {\rm C}, {\rm S}, {\rm Ka}_\perp, {\rm Ma}_\perp, {\rm Bi}_\perp, {\rm Pr}\}$ should be used.

II the **base state set** : $\{{\rm Re}, {\rm Ct}, {\rm We}, {\rm M}^\star, {\rm B}, {\rm Pr}\}$ that is based on the unperturbed Nusselt film thickness $\bar{h}_{\rm N}$ and will therefore be appropriate in the linear stability analysis (see §1.4). For this reason, the Marangoni number $\rm M^\star$ is rather based on the difference of temperature across the undisturbed layer of thickness $h_{\rm N}$ (see 1.46). Note that set II coincides to set I for a liquid film of thickness l_ν, *i.e.* $h_{\rm N} = 1$.

III the **nonlinear set** : $\{\mathcal{R}, \mathcal{C}, \eta, \mathcal{M}, {\rm B}, {\rm Pr}\}$ that will be suitable when studying nonlinear waves. This set is based on the characteristic length of capillary ripples preceding solitary waves. The advantage of this scaling is to make explicit the origin of the different terms in the equations: the inertial terms appearing with $\mathcal{R}$ and the second-order viscous terms appearing with η. An other advantage of this scaling is that the parameters remain close to unity which is interesting on a numerical point of view.

[¶]The reduced Reynolds number defined initially by Shkadov [127] is $\delta = \mathcal{R}/45$. This numerical factor originates from a slightly different change of variables.

In the following, we will refer to the different sets of parameters depending on their usefulness. The two-dimensional boundary layer system of equations is given in appendix B for each set of parameters. This appendix gives also the relations between all the parameters.

1.7 Reduction of the governing equations

The second-order boundary layer equations (1.100) with the energy equation (1.93) do not constitute a real simplification of the initial problem. These equations have actually the same dimensionality than the Navier-Stokes equations. The search of nonlinear solutions of such models requires elaborate numerical techniques to track the film interface. Among others, Ramaswamy *et al.* [105] have developed such a numerical scheme using the finite-element method to simulate in time the film surface location – the latter being updated through the kinematic equation (1.24) – in the case of TC. However, the full-scale computations are complex to implement and numerically time consuming.
The coherence imposed by the strong diffusion in the y–direction in the momentum and heat equations, makes it be possible to eliminate the cross-stream y–coordinate and derive models in terms of evolution equation(s) for one or more meaningful physical quantities that evolve only with position on the plane (x, z) and time t such as the film thickness h, and additionally the flow rate q or, for example, the film surface temperature θ. Many authors since decades (see reviews [28, 1, 15, 107]) have worked in reducing the governing equations to derive such evolution equation(s). We will identify here two main simplifications, depending on the flow regime considered, to which the remaining of this work will be dedicated. It will therefore constitutes the two following parts:

- **Part I : Low Reynolds numbers.** When inertia can be neglected with respect to viscous effects, *i.e.* when $\varepsilon\mathrm{Re} \ll 1$, an asymptotic expansion in ε of the governing equations allows to come up with a single evolution equation for the film thickness h. This method was initially introduced for thin isothermal falling film problems by Benney [7], who was followed by many authors up to nowadays (see the review by Oron *et al.* [97]), having included many physical effects such as heating, chemical reactions, evaporation, topological leveling, etc. The success of this equation is mainly based on its great simplicity even though it may experience singularities already at $\mathrm{Re} = \mathcal{O}(1)$. Therefore, its validity should be carefully established.

- **Part II : Moderate Reynolds numbers.** It is still possible to reduce the dimensionality of the boundary layer equations, while keeping a model valid for $\varepsilon\mathrm{Re} \sim 1$. This is done by integrating the boundary layer equations across the layer following the example of the Kármán-Polhausen method. This method was introduced for falling film problems by Kapitza [69] and Shkadov [126]. In this work, we will use the last improvement of this method developed recently by Ruyer-Quil & Manneville [109, 110] who combined a gradient expansion

to a weighted residual method in the cross-stream direction. The advantage is that the resulting models agree with exact linear (long-wave) asymptotic results while describing properly the nonlinear dynamics of falling films in a wide range of parameters. An other advantage is that this method allows a consistent representation of the velocity and the temperature fields at the given order in ε.

In the case of large Reynolds number (*e.g.* $\mathrm{Re} = \mathcal{O}(100)$), the inertial effects become predominant such that the boundary layer approximation fails in describing the wave dynamics and the full-scale Navier-Stokes equation should be considered instead.
The different levels of simplification of the Navier-Stokes equations are summarized in figure 1.3. Note that two level of simplification are identified depending on the order of approximation in ε: The ε–models are suitable for systems of large Kapitza number ($\mathrm{Ka} \sim 10^3$-10^4) while the ε^2–models are suitable for smaller ($\mathrm{Ka} \sim$ 10-10^2), when the viscous effects are important. This will become apparent in the following.

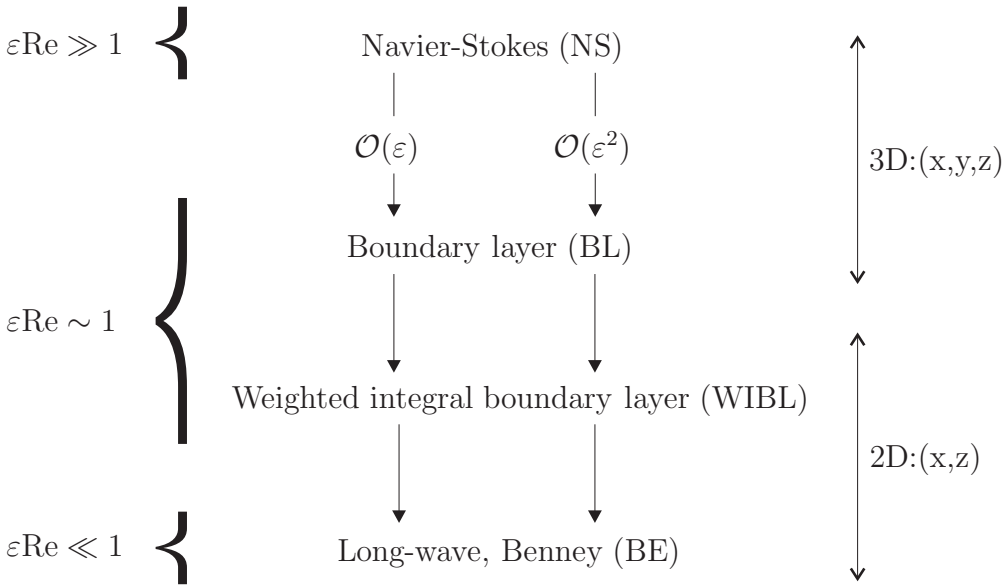

Figure 1.3: Successive reductions of the Navier-Stokes equations.

The different approximations shown in figure 1.3 remain identical when the energy equation is added to the system, *i.e.* for non-isothermal conditions, only if $\mathrm{Pe} = \mathcal{O}(1)$. If $\mathrm{Pe} > 1$, the coupling between the velocity and the temperature fields may be large enough to violate the approximation of small temperature gradients $\partial_x T, \partial_z T \sim \varepsilon$. This situation will be discussed in the last chapter of this work.
Whenever it is possible, we will validate the models developed later with the results obtained in the present chapter, as far as linear stability analysis is concerned.

Part I

Low Reynold number: the Benney equation

Chapter 2

Benney equation including Marangoni effect

In this chapter, the Benney equation including thermocapillary effects is derived and used to study the dynamics of a liquid film flowing down a heated inclined wall. After summarizing the state-of-the-art of the Benney equation (§2.1), we will present the details of the long-wave expansion leading to its formulation (§2.2), as well as the corresponding dynamical system enabling the search of stationary wave solutions in their moving frame of reference (§2.3). The aim of this chapter is also to determine the validity domain of the Benney equation by considering the boundedness of its solutions as well as their accuracy. To this purpose, a weighted integral boundary layer model (presented comprehensively in chapter 5) will be used as for reference model. To consider stationary travelling waves the flow rate in the moving frame has to be specified (§2.4). Open and closed flow conditions will be introduced and it will be shown that only the former resembles experimental conditions and, furthermore, yields bounded solutions for larger Reynolds numbers than the latter one. Stationary wave solutions for both models will be followed through parameter space using continuation techniques (§2.5). In this way, the validity of the Benney equation will be characterized specifying three boundaries, namely the parameter values where (i) amplitudes of solitary waves exceed the ones of the reference model by 10%, (ii) only solitary waves are unbounded yielding finite-time blow-up, and (iii) all the linearly unstable modes lead to blow-up. The influence of surface tension, inclination, and thermocapillarity on the boundaries will be evaluated (§2.6). Especially, the latter two will be shown to strongly reduce the validity range of the Benney equation. Finally, it will be pointed out that the bounded solutions are unstable to disturbances of larger periodicity (§2.7). So, for these solutions, coalescence of solitary waves may be the pathway yielding finite-time blow-up.

2.1 The Benney equation

From a fundamental point of view, thin film flows are a reference topic for the study of long-wave instabilities. Because the waves are always long as compared to the film

thickness, it is a widespread practice to define a small parameter as the ratio of the film thickness and the typical lengthscale of disturbances of the flow. It is called *film parameter* and is denoted here by ε [15]. Though in the linear stage the film parameter can be assimilated with the wavenumber, contrary to usual situations and especially to the boundary-layer theory, the value of ε cannot be assigned a priori but is rather given a posteriori by the (nonlinear) solution itself. Indeed, the separation of scales is enabled by the smallness of the local steepness of the waves. Nevertheless, the latter can vary strongly along the wave due to steepening of the fronts. At low Reynolds number where the flow is dominated by viscosity and surface tension, the maximal steepness of the wave is governed by a balance of the streamwise pressure gradient produced by surface tension and the gravity acceleration along the plane. This leads to a nonlinear estimate $\varepsilon \sim \mathrm{We}^{-1/3}$. In the linear stage, however, this is rather the balance between the pressure drop due to surface tension and the pressure disturbance at the interface that leads to the estimate $k \sim \varepsilon \sim \mathrm{We}^{-1/2}$, hence to the common assumption $\mathrm{We}\,\varepsilon^2 \sim O(1)$ [41].

The incompatibility between these two estimates can be resolved at low Reynolds number where the classical long-wave expansion first proposed by Benney [7] applies. Indeed at low Reynolds number, viscosity ensures the in-depth coherence of the flow which allows to reduce the full set of equations to a single evolution equation for the film thickness. It is usually truncated at the first or second order and still referred to as the Benney equation (see the review by Oron *et al.* [97]). The slaving of the dynamics of the flow to its kinematics is ensured by the smallness of the product $\varepsilon\mathrm{Re}$. In the linear stage, the characteristic wavenumber is the cut-off wavenumber $k_\mathrm{c} \propto \sqrt{\mathrm{Re}/\mathrm{We}}$ for a vertical wall in isothermal conditions (see 1.86) such that $\varepsilon\mathrm{Re} \sim (\mathrm{ReWe}^{-1/3})^{3/2}$. Therefore both nonlinear and linear estimates lead to the definition of a reduced Reynolds number $\propto \mathrm{ReWe}^{-1/3}$ as introduced by Shkadov [127] (see 1.105a).

The Benney equation asymptotically predicts the linear stability threshold for long waves (H-mode) in agreement with the Orr-Sommerfeld equation. It allows for bounded nonlinear *travelling wave* solutions, waves that remain stationary in their moving frame, extending to solitary waves, *i.e.* to infinite wavelength. Pumir *et al.* [103] and Nakaya [89] constructed such solitary waves. However, Pumir *et al.* [103] found that the Benney equation can lead to finite-time blow-up (singularities) when the Reynolds number exceeds a limiting value. Beyond this value no solitary waves can be observed. Obviously, the range of parameters for which the Benney equation provides correct results is much more limited in the highly nonlinear regime corresponding to solitary waves. One simple explanation is that localized objects in real space are delocalized in Fourier space such that solitary waves involve a broad range of wavenumbers.

Yet, the Benney equation is the most simple model of the dynamics of film flows. It faithfully captures all physical mechanisms at low Reynolds number and its widespread use still justify people's interest for it [97].

The Benney equation is a particular case of the following evolution equation for the film thickness $h(x,t)$

$$\partial_t h + \partial_x \left(h^3 + \Phi\, h^m \partial_x h + h^3 \partial_{xxx} h \right) = 0, \tag{2.1}$$

where m is a positive integer and Φ a positive parameter. For $m = 6$, the Benney equation corresponding to a vertical and isothermal film (see §2.6.1) is recovered. Hocherman & Rosenau [48] have conjectured that (2.1) leads to finite-time blow-up when $m > 3$. Bertozzi & Pugh [8] refined this criterion proving that nonlinearities with exponents $m < 5$ can yield yet bounded solutions under certain conditions. Rosenau *et al.* [106] have integrated (2.1) for $m = 6$ in time using a sinusoidal modulation of the film thickness as initial condition. They identified $\Phi^* \approx 0.5$ as limiting value separating uniformly bounded solutions and finite-time blow-up. This value appears to be independent of the initial frequency.

All these previous works agree on identifying the strong nonlinearity $\partial_x(h^6\partial_x h)$ as the cause of the singularities found with the Benney equation. This term comes from the inertial terms of the boundary layer equations. Furthermore, this behaviour seems to be related to the presence or absence of solitary waves for the considered parameters [103]. However, the finite-time blow-up has no physical meaning – experimentally, the film does not break – and reduces strongly the parameter range for which the asymptotic expansion is valid. Unfortunately, the addition of higher order terms reduces the range of validity even more (see Salamon *et al.* [115]), asymptotic series having usually poor convergence properties. Hence the idea appeared to regularize the asymptotic expansion as performed by Ooshida [93] who formulated an evolution equation that does not lead to singularities for any value of the Reynolds number. However, his equation underestimates seriously the phase speed and the amplitude of the waves at moderate Reynolds numbers. A second shortcoming of the Benney equation is the slaving of the film dynamics to its kinematics. Far from threshold the dynamics of the film cannot be described by the evolution of the free surface only. Other variables related to the velocity field should be introduced. This will be the subject of the second part of this work. However, we will already use here the first-order weighted integral boundary layer, that possess one more variable, as reference model in order to define the limit of validity of the Benney equation.

Let us turn now to the thermocapillary effect and first to the pure one, *i.e.* for a horizontal liquid layer. Boos & Thess [11] followed numerically the evolution of a horizontally oriented film profile towards rupture using the full set of equations in combination with a linear temperature field, and identified a cascade of consecutive 'structuring events'. The qualitative agreement between their results and those obtained from the long-wave approximation for horizontal layers [95] indicates that the main features of the physical system are well captured by this approximation, as far as the S-mode is concerned. Weakly nonlinear analysis done by VanHook *et al.* [141] has shown the subcritical character of the pure long-wave Marangoni instability. Thiele & Knobloch [137] studied the transition between a horizontal and a slightly inclined layer in the presence of the Marangoni effect. They showed that their bifurcation analysis in the horizontal case shares similarities with the inclined problem only for very small values of the inclination angle β. For larger inclinations the system behaves much more like a 'falling film' even though their theory does not retain inertial effects and the dominant balance in the direction normal to the wall is still hydrostatic. Furthermore, for very small inclinations, they found the bifurcation from the flat film to be always subcritical as for the case of horizontal films, while for sufficiently large

inclinations it becomes always supercritical.
For inclined and vertical walls, the Marangoni effect has been incorporated into the Benney equation by Joo *et al.* [53]. They examined numerically the interaction of the two instability modes, namely hydrodynamic (H-mode) and thermocapillary instability (S-mode). They found that the thermocapillarity enhances the instability and promotes a 'dramatic behaviour'. They associated this behaviour with the results of weakly nonlinear analysis by Gjevik [41] and Lin [79] where no stationary solutions were found for small wavenumbers. Indeed, weakly nonlinear analysis involves only a small number of harmonics and does not represent the highly nonlinear waves observed by Kapitza [69] and computed by Pumir *et al.* [103] in this range of parameters. In the present chapter, the 'dramatic behaviour' found by Joo *et al.* [53] will be shown to be connected to the finite-time blow-up of the Benney equation (§2.6.4).

2.2 Long-wave asymptotic expansion

As seen in the linear stability analysis (§1.4.2), the critical wavenumber at onset is zero. It implies that the waves are always long as compared to the film thickness such that $k \sim \varepsilon$ and at least not too far from threshold. Therefore, close to the critical Reynolds number $\mathrm{Re_c}$, there is always a Reynolds number for which $\varepsilon\mathrm{Re} \ll 1$ is valid. This hypothesis allows to neglect the inertial effects contained in $\mathrm{d}\mathbf{v}/\mathrm{d}t$ with respect to the viscous effects. Following the steps introduced by Benney [7], one can express the velocity, the pressure and the temperature fields by an asymptotic expansion of the form

$$\begin{aligned} u &= u^{(0)} + \varepsilon u^{(1)} + \varepsilon^2 u^{(2)} + \mathcal{O}\left(\varepsilon^3\right) \\ v &= v^{(0)} + \varepsilon v^{(1)} + \varepsilon^2 v^{(2)} + \mathcal{O}\left(\varepsilon^3\right) \\ w &= w^{(0)} + \varepsilon w^{(1)} + \varepsilon^2 w^{(2)} + \mathcal{O}\left(\varepsilon^3\right) \\ p &= p^{(0)} + \varepsilon p^{(1)} + \varepsilon^2 p^{(2)} + \mathcal{O}\left(\varepsilon^3\right) \\ T &= T^{(0)} + \varepsilon T^{(1)} + \varepsilon^2 T^{(2)} + \mathcal{O}\left(\varepsilon^3\right), \end{aligned} \tag{2.2a}$$

where v is of $\mathcal{O}(\varepsilon)$ by continuity (see 1.89).
This expansion could be also applied to the time-derivative, though not performed in the following, such that $\partial_t = \partial_{t_0} + \varepsilon\partial_{t_1} + \varepsilon^2\partial_{t_2} + \mathcal{O}(\varepsilon^3)$ (one speaks about multiscaling). If so, the long-wave assumption imposes that $\partial_{t_0} = 0$, hence the time will not appear explicitely in the zeroth-order system. This is indicative of the adiabatic elimination of the short time dynamics necessary to establish the gravity/viscosity balance. Indeed, this balance sets up with the short viscous time scale $t_{\mathrm{vis}} = \bar{h}_{\mathrm{N}}^2/\nu$. Therefore, as already mentioned, the basic flow is assumed to be fully developed before it undergoes any instability. The first perturbations due to inertia, introduced at first-order, will set up with the long inertial time scale $t_{\mathrm{ine}} \sim l/u_{\mathrm{N}}$ where $l = 2\pi h_{\mathrm{N}}/k \sim h_{\mathrm{N}}/\varepsilon$ represents the length scale for the film thickness variations (see figure 1.1).
We now proceed with the asymptotic analysis by substituting (2.2a) into the system (1.89–1.97) already expanded in series with respect to ε, and completed by (1.22–1.24). At leading order, for $\varepsilon \to 0$, the system reduces to (still considering $\varepsilon^2\mathrm{Ka} =$

$\mathcal{O}(1)$)

$$\partial_{yy}u^{(0)} = -1 \tag{2.3a}$$
$$\partial_y p^{(0)} = -\mathrm{Ct} \tag{2.3b}$$
$$\partial_{yy}w^{(0)} = 0 \tag{2.3c}$$
$$\partial_{yy}T^{(0)} = 0 \tag{2.3d}$$
$$\partial_y v^{(0)} + \partial_x u^{(0)} + \partial_z w^{(0)} = 0 \tag{2.3e}$$
$$\underline{\text{at } y = 0}$$
$$u^{(0)} = v^{(0)} = w^{(0)} = 0 \tag{2.3f}$$
$$T^{(0)} \overset{(\mathrm{TC})}{=} 1 + F_{\mathrm{w}} \tag{2.3g}$$
$$\partial_y T^{(0)} - \mathrm{Bi}_{\mathrm{w}} T^{(0)} \overset{(\mathrm{HFC})}{=} -1 - F_{\mathrm{w}} \tag{2.3h}$$
$$\underline{\text{at } y = h}$$
$$v^{(0)} - u^{(0)}\partial_x h - w^{(0)}\partial_z h = \partial_t h \tag{2.3i}$$
$$p^{(0)} = -\mathrm{Ka}\left(\partial_{xx}h + \partial_{zz}h\right) \tag{2.3j}$$
$$\partial_y u^{(0)} = 0 \tag{2.3k}$$
$$\partial_y w^{(0)} = 0 \tag{2.3l}$$
$$\partial_y T^{(0)} + \mathrm{Bi} T^{(0)} = 0. \tag{2.3m}$$

This system at leading order corresponds to a steady flow governed by the balance between gravity and viscosity.
The solution of (2.3) reads

$$u^{(0)} = h^2 \bar{y}\left(1 - \frac{\bar{y}}{2}\right) \tag{2.4a}$$
$$v^{(0)} = -h^2 \frac{\bar{y}^2}{2}\partial_x h \tag{2.4b}$$
$$w^{(0)} = 0 \tag{2.4c}$$
$$p^{(0)} = \mathrm{Ct}h(1-\bar{y}) - \mathrm{Ka}\left(\partial_{xx}h + \partial_{zz}h\right) \tag{2.4d}$$
$$T^{(0)} \overset{(\mathrm{TC})}{=} (1 + F_{\mathrm{w}})\frac{1 + \mathrm{Bi}h(1-\bar{y})}{1 + \mathrm{Bi}h} \tag{2.4e}$$
$$T^{(0)} \overset{(\mathrm{HFC})}{=} (1 + F_{\mathrm{w}})\frac{1 + \mathrm{Bi}h(1-\bar{y})}{\mathrm{Bi} + \mathrm{Bi}_{\mathrm{w}}(1 + \mathrm{Bi}h)}, \tag{2.4f}$$

where the reduced coordinate $\bar{y} = y/h$ has been introduced. The zeroth-order approximations for the film surface temperature, which will be used later, are

$$\theta^{(0)} \overset{(\mathrm{TC})}{=} \frac{1 + F_{\mathrm{w}}}{1 + \mathrm{Bi}h} \tag{2.5a}$$
$$\theta^{(0)} \overset{(\mathrm{HFC})}{=} \frac{1 + F_{\mathrm{w}}}{\mathrm{Bi} + \mathrm{Bi}_{\mathrm{w}}(1 + \mathrm{Bi}h)}. \tag{2.5b}$$

Now, the remaining kinematic boundary condition (2.3i) plays the role of solvability condition for the $\varepsilon-$hierarchy of equations. Thereby, introducing the zeroth-order

solutions for the velocity into (2.3i) yields the leading order form of the evolution equation for the film thickness

$$\partial_t h + h^2 \partial_x h = 0, \tag{2.6}$$

which describes the downwards propagation of waves driven by gravity at the film surface where, apparently, h^2 plays the role of wave velocity. As compared to the Burgers equation $\partial_t h + \alpha h \partial_x h = v \partial_{xx} h$ [145], (2.6) contains only the nonlinear propagation effects – with the difference that $\alpha = \alpha(h)$ is not constant here – but not the diffusive effects. However, the latter are needed to prevent wave from breaking and should therefore appear in the next order of the asymptotic expansion. Because the heat transfer and the mechanical equilibrium of the flat film are two decoupled problems in the zeroth-order limit, (2.6) does not involve the Marangoni effect, which appears at first order in the tangential stress conditions (1.95,1.96).
At first-order with respect to ε, we obtain

$$\begin{aligned}
\partial_{yy} u^{(1)} &= \partial_t u^{(0)} + u^{(0)} \partial_x u^{(0)} + v^{(0)} \partial_y u^{(0)} + w^{(0)} \partial_z u^{(0)} + \partial_x p^{(0)} && \text{(2.7a)}\\
\partial_y p^{(1)} &= \partial_{yy} v^{(0)} && \text{(2.7b)}\\
\partial_{yy} w^{(1)} &= \partial_t w^{(0)} + u^{(0)} \partial_x w^{(0)} + v^{(0)} \partial_y w^{(0)} + w^{(0)} \partial_z w^{(0)} + \partial_z p^{(0)} && \text{(2.7c)}\\
\partial_{yy} T^{(1)} &= \mathrm{Pr}^{-1} (\partial_t T^{(0)} + u^{(0)} \partial_x T^{(0)} + v^{(0)} \partial_y T^{(0)} + w^{(0)} \partial_z T^{(0)}) && \text{(2.7d)}\\
\partial_y v^{(1)} + \partial_x u^{(1)} + \partial_z w^{(1)} &= 0 && \text{(2.7e)}\\
\underline{\text{at } \bar{y} = 0} & && \\
u^{(1)} &= v^{(1)} = w^{(1)} = 0 && \text{(2.7f)}\\
T^{(1)} &= 0 \qquad \text{(TC)} && \text{(2.7g)}\\
\partial_y T^{(1)} - \mathrm{Bi_w} T^{(1)} &= 0 \qquad \text{(HFC)} && \text{(2.7h)}\\
\underline{\text{at } \bar{y} = 1} & && \\
v^{(1)} - u^{(1)} \partial_x h - w^{(1)} \partial_z h &= 0 && \text{(2.7i)}\\
p^{(1)} &= 2 \left(\partial_y v^{(0)} - \partial_x h \partial_y u^{(0)} - \partial_z h \partial_y w^{(0)} \right) && \text{(2.7j)}\\
\partial_y u^{(1)} &= -\mathrm{Ma} \left(\partial_x T^{(0)} + \partial_x h \partial_y T^{(0)} \right) && \text{(2.7k)}\\
\partial_y w^{(1)} &= -\mathrm{Ma} \left(\partial_z T^{(0)} + \partial_z h \partial_y T^{(0)} \right) && \text{(2.7l)}\\
\partial_y T^{(1)} + \mathrm{Bi} T^{(1)} &= 0. && \text{(2.7m)}
\end{aligned}$$

We see that the left-hand sides of (2.7) and (2.3) are identical, and thus will be the case at all orders in ε. Instead of the kinematic condition (2.3i) as compatibility condition we could have used the standard *Fredholm's alternative** [142].
The solution of the system at first-order reads

$$u^{(1)} = h^2 \left(\frac{\bar{y}^2}{2} - \bar{y} \right) \left(\mathrm{Ct} \partial_x h - \mathrm{Ka} \left(\partial_{xxx} h + \partial_{xzz} h \right) \right) - \mathrm{Ma} h \bar{y} \partial_x \theta^{(0)}$$

*In short, when a homogeneous system of equation has a trivial solution, the *Fredholm's alternative* states that the non-homogeneous system will have a solution if the linear differential operator (that applies here at the left-hand-side of the system 2.7) will have a non-trivial solution provided the right-hand-side is orthogonal to the solutions of the self-adjoint problem [36].

$$+\frac{1}{3}h^5\partial_x h\left(\frac{\bar{y}^4}{8}-\frac{\bar{y}^3}{2}+\bar{y}\right) \tag{2.8a}$$

$$w^{(1)} = h^2\left(\frac{\bar{y}^2}{2}-\bar{y}\right)\left(\mathrm{Ct}\partial_z h-\mathrm{Ka}\left(\partial_{xxz}h+\partial_{zzz}h\right)\right)-\mathrm{Ma}h\bar{y}\partial_z\theta^{(0)} \tag{2.8b}$$

$$p^{(1)} = -h\partial_x h(\bar{y}+1) \tag{2.8c}$$

$$\begin{aligned} T^{(1)} \overset{(\mathrm{TC})}{=}\ & \frac{\mathrm{PrBi}h^4\partial_x h}{(1+\mathrm{Bi}h)^2}\left[-\frac{\mathrm{Bi}h}{40}\bar{y}^5+\frac{1+3\mathrm{Bi}h}{24}\bar{y}^4-\frac{\mathrm{Bi}h}{6}\bar{y}^3\right. \\ & \left.-\frac{10-\mathrm{Bi}h(5+4\mathrm{Bi}h)}{60(1+\mathrm{Bi}h)}\bar{y}\right] \end{aligned} \tag{2.8d}$$

$$\begin{aligned} T^{(1)} \overset{(\mathrm{HFC})}{=}\ & \frac{\mathrm{PrBiBi_w}h^4\partial_x h}{(\mathrm{Bi}+\mathrm{Bi_w}(1+\mathrm{Bi}h))^2}\left[-\frac{\mathrm{Bi}h}{40}\bar{y}^5+\frac{1+3\mathrm{Bi}h}{24}\bar{y}^4\right. \\ & -\frac{\mathrm{Bi}}{6}\left(h-\frac{1}{\mathrm{Bi_w}}\right)\bar{y}^3-\frac{\mathrm{Bi}}{2\mathrm{Bi_w}}\bar{y}^2+\left(\bar{y}+\frac{1}{\mathrm{Bi_w}h}\right) \\ & \left.\times\frac{30\mathrm{Bi}-10\mathrm{Bi_w}+\mathrm{Bi}h(5(4\mathrm{Bi}+\mathrm{Bi_w})+4\mathrm{BiBi_w}h)}{60(\mathrm{Bi}+\mathrm{Bi_w}(1+\mathrm{Bi}h))}\right], \end{aligned} \tag{2.8e}$$

where the film surface temperature $\theta^{(0)}=T^{(0)}\big|_{\bar{y}=1}$ has been introduced (see 2.5) and $F_\mathrm{w}=0$ for simplicity. The first-order corrections of the surface temperature read

$$\theta^{(1)} \overset{(\mathrm{TC})}{=} \frac{\mathrm{PrBi}h^4\partial_x h(7\mathrm{Bi}h-15)}{120(1+\mathrm{Bi}h)^3} \tag{2.9a}$$

$$\theta^{(1)} \overset{(\mathrm{HFC})}{=} \frac{\mathrm{PrBi}h^3\partial_x h(60\mathrm{Bi}-20\mathrm{Bi_w}+\mathrm{Bi_w}h(35\mathrm{Bi}-15\mathrm{Bi_w}+7\mathrm{BiBi_w}h))}{120(\mathrm{Bi}+\mathrm{Bi_w}(1+\mathrm{Bi}h))^3}, \tag{2.9b}$$

and the first-order contribution to the cross-stream velocity is found by continuity, i.e. $v^{(1)}=-\int(\partial_x u^{(1)}+\partial_z w^{(1)})\,dy$ which is a fifth-order polynomial in $\bar{y}$. To obtain the above solutions, the time-derivatives $\partial_t h$ and $\partial_{xt}h$ have been estimated using the zeroth-order expression (2.6), *i.e.* $\partial_t h=-h^2\partial_x h+\mathcal{O}(\varepsilon)$. This rule also applies for $\partial_t\theta^{(0)}$ since $\theta^{(0)}$ is slaved to the film thickness.

2.2.1 Evolution equation for the film thickness

Substituting now $u^{(1)}$, $v^{(1)}$, $w^{(1)}$ into the kinematic condition (2.7i) yields the first-order correction to the evolution equation of the film thickness. This evolution equation reads in its three-dimensional form

$$\partial_t h+h^2\partial_x h+\varepsilon\frac{2}{15}\partial_x(h^6\partial_x h)+\varepsilon\boldsymbol{\nabla}\cdot\left[-\mathrm{Ct}\frac{h^3}{3}\boldsymbol{\nabla}h-\mathrm{Ma}\frac{h^2}{2}\boldsymbol{\nabla}\theta^{(0)}+\mathrm{Ka}\frac{h^3}{3}\boldsymbol{\nabla}\boldsymbol{\nabla}^2 h\right]=0. \tag{2.10}$$

Equation (2.10) may be written in a conservative form $\partial_t h+\boldsymbol{\nabla}\cdot\mathbf{q}=0$ where $\mathbf{q}=(q,p)$ is the local flow rate in the (x,z)–plane at time t. Let us now consider a parallel flow such that the spanwise component of the flow rate is zero, *i.e.* $p(x,z,t)=0$. The streamwise component of the flow rate written first for the Burgers equation reads $q(x,t)=\frac{1}{2}\alpha h^2-\upsilon\partial_x h$. The comparison to the evolution equation (2.10) yields

$h-$dependent coefficients on the form $\alpha(h) = \frac{2}{3}h$ and $\upsilon(h) = -\frac{2}{15}h^6 + \frac{1}{3}\mathrm{Ct}h^3 - \frac{1}{2}\mathrm{MaBi}h^2/(1+\mathrm{Bi}h)^2$ where $\theta^{(0)}$ from (2.5a) has been used as an example. Since υ accounts for diffusive effects, its terms that are positive will be stabilizing while the ones that are negative will be destabilizing and yield instability. It remains an additional term to the flow rate q, namely $\beta\partial_{xxx}h$ with $\beta = \frac{1}{3}\mathrm{Ka}h^3$, that is a higher-order diffusive term still stabilizing if positive.
Back to (2.10), we can now assess that the third term, that originate from inertia, causes the hydrodynamic instability (H-mode), the fourth one represents the stabilizing effects of the hydrostatic pressure, the fifth one is responsible for the thermocapillary instability (S-mode) and the last one accounts for the stabilizing surface tension. The two-dimensional version $\partial_z = 0$ of (2.10) in isothermal conditions ($\mathrm{Ma} = 0$) is referred to as the *Benney equation*. By extension, this name is often used to designate any long-wave evolution equation obtained to describe the dynamics of thin falling films, specifying which additional physical effect has been included, namely here the Marangoni effect. Equation (2.10) was first obtained by Joo *et al.* [53].

2.2.2 Higher-order terms in the Benney equation

It is useless to proceed at third-order for the following reason: the effects of inertia in the cross-stream component of the Navier-Stokes equation should appear at this order (through the elimination of the pressure). Nevertheless, those effects are neglected by the boundary layer approximation whose depends directly the Benney equation. On the contrary, the second-order is still consistent with the boundary layer approximation and the results will be used in the second part of this work to validate our new models. Because the calculations at this order are cumbersome, we present only the final result here.
Still considering a parallel flow, a uniform heating ($F_\mathrm{w} = 0$), with the temperature condition (TC), the second-order Benney equation reads

$$\partial_t h + \partial_x\left(q^{(0)} + \varepsilon q^{(1)} + \varepsilon^2 q^{(2)} + \varepsilon^3\frac{\mathrm{Ka}}{3}h^3\partial_{xxx}h\right) = 0\,, \tag{2.11}$$

where the flow rate $q(x,t)$ has been expanded relative to the order of its derivative, with

$$q^{(0)} = \frac{1}{3}h^3 \tag{2.12a}$$

$$q^{(1)} = \left(\frac{2}{15}h^6 - \frac{1}{3}\mathrm{Ct}h^3 + \frac{\mathrm{MaBi}h^2}{2(1+\mathrm{Bi}h)^2}\right)\partial_x h \tag{2.12b}$$

$$\begin{aligned} q^{(2)} = {} & \left(\frac{127}{315}h^9 - \frac{8}{15}\mathrm{Ct}h^6 + \frac{7}{3}h^3\right. \\ & \left. +\mathrm{MaBi}h^5\frac{6(5\mathrm{Pr}+11) - 5\mathrm{Bi}(2\mathrm{Pr}-15)h + \mathrm{Bi}^2(-7\mathrm{Pr}+9)h^2}{120(1+\mathrm{Bi}h)^4}\right)(\partial_x h)^2 \\ & + \left(\frac{4}{63}h^{10} - \frac{10}{63}\mathrm{Ct}h^7 + h^4 + \mathrm{MaBi}h^6\frac{15\mathrm{Pr}+57+\mathrm{Bi}(-7\mathrm{Pr}+57)h}{240(1+\mathrm{Bi}h)^3}\right)\partial_{xx}h\,. \end{aligned} \tag{2.12c}$$

Note that $q^{(2)}$ has been obtained without having to solve for the gradient expansion of the surface temperature θ at second order. Indeed, θ is coupled to q through its gradient – already of $\mathcal{O}(\varepsilon)$ – such that only $\theta^{(1)}$, expressed by (2.9a) was necessary.
As already mentioned, in order to keep every relevant physical effects in our formulation, the first contribution of the surface tension – though of $O(\varepsilon^3)$ – has been kept in (2.11). However, due to the poor convergence of the present asymptotic expansion (see §2.5.2), the contributions of the surface tension at higher order have been removed.

2.2.3 Weakly nonlinear models

It is still possible to simplify the long-wave evolution equation if we assume the wave amplitude η of the free surface to be limited. This is always true in the vicinity of the critical point, at $\mathrm{Re_c}$ (*e.g.* $\mathrm{Re_c} = 0$ for a vertical wall). This procedure has the advantage to retain only a small number of nonlinear terms and thus to suppress the strong nonlinearities introduced by the inertial effects that may be responsible for the finite-time blow-up.
Let us then substitute $h = h_\mathrm{N}(1 + \varsigma\eta)$ with $\varsigma \ll 1$ into the second-order BE (2.11) for the isothermal conditions ($\mathrm{Ma} = 0$). Its amplitude expansion gives, rescaling $t \to t/3\mathrm{Re}$ and assuming ς at least of $\mathcal{O}(\varepsilon^2)$ through the transformation $\varsigma \to \varepsilon^2\varsigma$ (to keep only the first nonlinearity $\eta\partial_x\eta$ accounting for wave propagation),

$$\begin{aligned}&\partial_t\eta + \partial_x\eta + 2\varepsilon^2\varsigma\eta\partial_x\eta + \varepsilon\left(\frac{2}{5}\mathrm{Re} - \frac{1}{3}\mathrm{Ct}\right)\partial_{xx}\eta\\ &+\varepsilon^2\left(1 + \frac{4}{7}\mathrm{Re}^2 - \frac{10}{21}\mathrm{CtRe}\right)\partial_{xxx}\eta + \varepsilon^3\frac{1}{3}\mathrm{We}\partial_{xxxx}\eta = \mathcal{O}\big(\varepsilon^3\big)\,,\end{aligned} \tag{2.13}$$

where the *base state set* of parameters has been used – with $\varepsilon^2\mathrm{We} = \mathcal{O}(1)$ – since the problem concerns small amplitude deformations about the flat film solution. Proceeding to the following change of variables:

$$T = \frac{12(\mathrm{Re} - \mathrm{Re_c})^2}{25\mathrm{We}}t, \quad X = \left[\frac{6|\mathrm{Re} - \mathrm{Re_c}|}{5\mathrm{We}}\right]^{1/2}(x - t)$$

$$\text{and} \quad H = \frac{25\mathrm{We}}{24(\mathrm{Re} - \mathrm{Re_c})^2}\left[\frac{6|\mathrm{Re} - \mathrm{Re_c}|}{5\mathrm{We}}\right]^{1/2}\eta,$$

with $\mathrm{Re_c} = \frac{5}{6}\mathrm{Ct}$ and $\mathrm{Re} - \mathrm{Re_c} = \mathcal{O}(\varepsilon)$, we obtain the *Kawahara equation* [72]:

$$\partial_T H + 4H\partial_X H + \epsilon_\mathrm{c}\,\partial_{XX}H + \delta\,\partial_{XXX}H + \partial_{XXXX}H = 0, \tag{2.14}$$

where ϵ_c is the sign of $(\mathrm{Re} - \mathrm{Re_c})$ and

$$\delta = \left[\frac{15}{2\mathrm{We}|\mathrm{Re} - \mathrm{Re_c}|}\right]^{1/2}\left[\frac{4}{7}\mathrm{Re}(\mathrm{Re} - \mathrm{Re_c}) + 1\right].$$

The Kawahara equation accounts for wave dispersive terms occuring at second-order. If the dispersion vanishes ($\delta = 0$), the Kawahara equation reduces to the *Kuramoto-Sivashinsky equation*. Both of these equations have been extensively studied in literature in order to model correctly the solitary wave formation [72, 73, 20, 18]. They provide a paradigmatic model for the application of the dynamical systems approach to turbulence [90].
When the Marangoni effect is considered at the film surface then an additional nonlinearity of the form $\partial_x(\eta\partial_x\eta)$ appears [39]. The influence on the dynamical behaviour of this additional term as a destabilizing factor (according to its sign in the equation) was elucidated in [51]. In the same way as (2.13) was obtained, but now with $\mathrm{M}^\star \neq 0$, we can write, up to $\mathcal{O}(\varepsilon^3)$ in order to get the expected nonlinearities,

$$\begin{aligned}
&\partial_t\eta + \partial_x\eta + 2\varepsilon^2\varsigma\eta\partial_x\eta + \varepsilon\left(\frac{2}{5}\mathrm{Re} - \frac{1}{3}\mathrm{Ct} + \frac{\mathrm{M}^\star}{6(1+\mathrm{B})}\right)\partial_{xx}\eta \\
&+\varepsilon^2\left(1 + \frac{4}{7}\mathrm{Re}^2 - \frac{10}{21}\mathrm{CtRe} + \frac{\mathrm{M}^\star\mathrm{Re}(57 + \mathrm{B}(57 - 7\mathrm{Pr}) + 15\mathrm{Pr}))}{240(1+\mathrm{B})^2}\right)\partial_{xxx}\eta \\
&+\varepsilon^3\varsigma\left(\frac{12}{5}\mathrm{Re} - \mathrm{Ct} + \frac{\mathrm{M}^\star}{3(1+\mathrm{B})^2}\right)\partial_x(\eta\partial_x\eta) + \varepsilon^3\frac{1}{3}\mathrm{We}\partial_{xxxx}\eta = \mathcal{O}\left(\varepsilon^4\right), \qquad (2.15)
\end{aligned}$$

that can be rewritten, using a suitable Galilean transformation in order to eliminate $\partial_x\eta$, in the form

$$\partial_t\eta + \alpha_1\eta\partial_x\eta + \alpha_2\partial_{xx}\eta + \alpha_3\partial_{xxx}\eta + \alpha_4\partial_{xxxx}\eta + \alpha_5\partial_x(\eta\partial_x\eta) = 0. \qquad (2.16)$$

This latter equation is referred to as the *Korteweg-de-Vries-Kuramoto-Sivashinsky-Velarde equation* [22] that reduces to a slightly dissipation-perturbed Korteweg-de-Vries equation when $\alpha_2, \alpha_4, \alpha_5$ are small, while it appears as an extension of the Kuramoto-Sivashinsky equation for small α_3, α_5 [75].
It is worth noting that even though strong nonlinearities do not occur anymore in weakly nonlinear models, they may still yield finite-time blow-up depending on the initial conditions as for instance pointed out by Kliakhander *et al.* [75]. They actually showed that the dissipation-perturbed Korteweg-de-Vries equation may lead a localized and finite-amplitude initial disturbance (like a soliton) to blow-up in a finite-time.

2.2.4 Primary instability

To analyse the linear stability of the uniform flat film in the same way than in §1.4, one imposes a small harmonic disturbance writing

$$h = h_\mathrm{N} + \eta\exp\left\{\mathrm{i}\left(k\,x - c\,t\right) + s\,t\right)\right\}, \qquad (2.17)$$

where η, k, c and s are real and represent, respectively, the amplitude, the wavenumber, the phase speed and the growth rate of the disturbance. Inserting the normal mode representation (2.17) into the two-dimensional form of (2.10) and linearizing in η yield the linear phase speed and growth rate:

$$c_\mathrm{L} \;=\; h_\mathrm{N}^2, \qquad (2.18)$$

$$s = k^2 h_{\rm N}^3 \left(\frac{2}{15} h_{\rm N}^3 - \frac{1}{3}{\rm Ct} + \frac{1}{2}\frac{{\rm Bi\,Ma}}{h_{\rm N}(1+{\rm Bi}h_{\rm N})^2} - \frac{1}{3}{\rm Ka}\,k^2 \right). \qquad (2.19)$$

The surface waves will grow for $s > 0$, *i.e.* for disturbance wavenumbers smaller than the critical (cut-off) wavenumber

$$k_{\rm c} = \frac{1}{{\rm Ka}^{1/2}} \left(\frac{2}{5} h_{\rm N}^3 - {\rm Ct} + \frac{3}{2}\frac{{\rm Bi\,Ma}}{h_{\rm N}(1+{\rm Bi}h_{\rm N})^2} \right)^{1/2}. \qquad (2.20)$$

This surface wave instability is named *primary instability* and corresponds to a *Hopf bifurcation* from the flat film solution. The emerging branch of solutions will be called *supercritical* (*subcritical*) if it bifurcates towards the region where $k < k_{\rm c}$ ($k > k_{\rm c}$). Equation (2.19) may be written generically as $s(k,\mu) = \mu k^2 - k^4 + \mathcal{O}(k^6)$ (suitably rescaling time and μ) where μ denotes a control parameter. In each case, there exist an eigenvalue $s(k,\mu)$ such that $s(0,\mu) = 0$ for all μ while $s(k,\mu)$ remains small at small k. Such a long-wave mode is named *Goldstone mode* [13] in Condensed Matter Physics and is linked with a particular conservation law. Here, for the surface deformational mode, the corresponding Goldstone mode is a shift of the height of the interface (from one Nusselt solution to another one), which is neutrally stable as long as the shift is uniform [23]. This explains that the axis $k = 0$ in the $(\mu, k)-$plane (with $s = 0$) is part of the neutral stability curve. Notice this long-wave mode had been already obtained in §1.4.2 (see 1.86 with the *base state set* of parameters), what confirms that 2.20 is an exact asymptotic result.

2.3 Search for stationary wave solutions

To study the solution behaviour, we employ bifurcation analysis using numerical continuation techniques [30]. Continuation is a very effective method to determine branches of stationary solutions (possibly in a moving frame) and their bifurcations by following them through parameter space using Newton's method [30]. For thin films continuation was applied in studies of travelling and solitary waves of film flows down inclined walls [15, 109, 110, 120], sliding drops on slightly inclined planes [138, 137], and transversal instabilities of sliding liquid ridges [135].
We seek periodic travelling waves of wavelength λ, in the form of stationary 2D solutions in a frame of reference moving downstream at velocity c [103]. Introducing $h(x,t) = h(\xi)$ with $\xi = x - c\,t$, (2.10) can be integrated once to yield

$$-c\,h + \frac{h^3}{3} - Q + \frac{2}{15}h^6 h' + {\rm Ka}\frac{h^3}{3}h''' - {\rm Ct}\,\frac{h^3}{3}h' + \frac{h^2}{2}\frac{{\rm Bi\,Ma}\,h'}{(1+{\rm Bi}\,h)^2} = 0, \qquad (2.21)$$

where the prime denotes the derivative with respect to ξ. Q is the integration constant and represents the flow rate in the moving frame of reference, as shown in the following by (2.27). Its value is negative because the phase speed c of surface waves is generally larger than the mean velocity of the film (three times at criticality). Assuming that no dry spots are possible ($h \neq 0$), (2.21) can be divided by $-{\rm Ka}\,h^3/3$ to get

$$h''' = F[h,h'] = \frac{1}{\rm Ka}\left(\frac{3}{h^3}(Q + c\,h) - 1 - \frac{2}{5}h^3 h' + {\rm Ct}\,h' - \frac{3}{2}\frac{{\rm Bi\,Ma}\,h'}{h(1+{\rm Bi}\,h)^2} \right). \qquad (2.22)$$

The differential equation (2.22) is recast into a dynamical system, *i.e.* a system of first order differential equations,

$$\left\{\begin{array}{lcl} U_1' &=& U_2 \\ U_2' &=& U_3 \\ U_3' &=& F[U_1, U_2] \end{array}\right. \tag{2.23}$$

where $U_1 = h$, $U_2 = h'$ and $U_3 = h''$.
To determine iteratively the periodic solutions of the dynamical system (2.23), we use the continuation and bifurcation tools for ordinary differential equations AUTO97 [30]. During computations the periodicity of the solution is enforced, the phase is fixed by $U_1|_{\xi=0} = h_{\mathrm{N}}$ and the total volume $\int_0^1 U_1\, d\xi = \langle h \rangle_{\xi}$ will be fixed by the flow condition as explained in §2.4. This amounts to one integral and four boundary conditions, hence the continuation requires three free parameters [74]. Fixing the set of parameters $\{\mathrm{Ka}, \mathrm{Ma}, \mathrm{Bi}, \mathrm{Ct}, h_{\mathrm{N}}\}$ the free parameters are $\{k, c, Q\}$. The continuation is started from the neutral mode corresponding to the Hopf bifurcation point with k_{c} and c_{L}. The starting value of Q is fixed by the Nusselt solution $h(\xi) = h_{\mathrm{N}}$ such that at k_c from (2.21), $Q_{\mathrm{L}} = h_{\mathrm{N}}^3/3 - h_{\mathrm{N}}\, c_{\mathrm{L}}$; the initial solution being given on the following forms

$$\left\{\begin{array}{lcl} U_1 &=& h_{\mathrm{N}} + \eta \sin(2\pi n \xi) \\ U_2 &=& 2\pi n \eta \cos(2\pi n \xi) \\ U_3 &=& -4\pi^2 n^2 \eta \sin(2\pi n \xi), \end{array}\right. \tag{2.24}$$

where $\eta = 5 \times 10^{-4}$.
As announced in §2.1, the aspect ratio[†] $\epsilon = h_{\mathrm{N}}/\lambda$ is obtained a posteriori through the wavenumber $k = 2\pi/\lambda$ of the stationary wave solution, and reads

$$\epsilon = \frac{h_{\mathrm{N}} k}{2\pi}. \tag{2.25}$$

Contrary to several previous works [53, 54, 120], the aspect ratio is not defined a priori. However, doing so results solely in a rescaling of λ. Thereby, in Joo *et al.* [53], the wavenumber is defined as $k_{\mathrm{JDB}} = h_{\mathrm{N}} k/0.2$ where the factor 0.2 originated from an a priori assignment of the aspect ratio ϵ.

The reference model

A new model valid in a wider range of Reynolds number than the Benney equation will be developed in chapter 5. This model will be obtained combining a gradient expansion with a weighted residual method, as applied by Ruyer-Quil & Manneville [109] for an isothermal layer. Let us write here the first-order model including the

[†]Note that ϵ must not be confused with the film parameter ε which is a formal parameter and accounts for the local slope of the wave surface. Indeed this latter might be quite different from the aspect ratio ϵ, as it is evidently the case for solitary-like waves.

Marangoni effect (refer to chapter 5 for the complete derivation):

$$\partial_t h = -\partial_x q, \tag{2.26a}$$

$$\partial_t q = \frac{5}{6}h - \frac{5}{2}\frac{q}{h^2} + \frac{9}{7}\frac{q^2}{h^2}\partial_x h - \frac{17}{7}\frac{q}{h}\partial_x q - \frac{5}{6}\mathrm{Ct}h\,\partial_x h + \frac{5}{6}\mathrm{Ka}\,h\,\partial_{xxx}h + \frac{5}{4}\frac{\mathrm{Ma}\,\mathrm{Bi}\,\partial_x h}{(1+\mathrm{Bi}\,h)^2}, \tag{2.26b}$$

where q is the local flow rate. Equation (2.26a) is the conservation equation. The terms on the right-hand side of (2.26b) account, from the left to the right, for gravity, viscous dissipation, inertia (two terms), hydrostatic effect, surface tension and thermocapillary effect. As announced previously, the above model will be referred to as the first-order WIBL model and will be used as our reference model to define the validity of the Benney equation. Indeed, it will be shown later in this chapter and in chapter 6 that the first-order WIBL model does not experience any singularity.
In a moving frame of reference $\xi = x - c\,t$, (2.26a) and (2.26b) can be integrated to yield

$$q = c\,h + Q. \tag{2.27}$$

and assuming as before $h \neq 0$

$$h''' = F_{\mathrm{WIBL}}[h, h'] = \frac{1}{\mathrm{Ka}}\left(\frac{3}{h^3}(Q + c\,h) - 1 - \frac{54}{35}\frac{Q^2 h'}{h^2} + \frac{6}{35}\frac{c\,h'}{h^2}(c\,h - Q) + \mathrm{Ct}h' - \frac{3}{2}\frac{\mathrm{Bi}\,\mathrm{Ma}\,h'}{h(1+\mathrm{Bi}\,h)^2}\right). \tag{2.28}$$

The value of the integration constant Q represents as in 2.3 the (negative) mean flow rate in the moving frame of reference. The periodic stationary solutions of (2.28) are determined using the dynamical system (2.23) by simply replacing F by F_{WIBL}. Remark that only the terms accounting for inertia differ between (2.22) and (2.28). And this change is a key point since it will prevent the finite-time blow-up for any Re as demonstrated in the following.

2.4 Closed and open flow conditions

To compute travelling periodic waves stationary in their frame of reference an additional constraint is required that specifies the 'flow condition' in the moving frame. It is related to the choice of the conserved quantity. The *closed flow* condition corresponds to the conservation of the mass in a given domain and the *open flow* condition, to the conservation of the flow rate. Chang [15] already mentioned this condition speaking about constant-average thickness or constant-flux formulation. Many authors, as for instance [53, 115, 98, 120], implicitly prescribed the closed flow condition. This is inherent to time-dependent numerical simulations using spectral method, as usual for such problems. Indeed, it forces periodic boundary conditions for which the amount of liquid leaving the domain downstream is reinjected upstream. However,

the open flow condition is the only one that is experimentally meaningful for a flow on an inclined plate independently whether a periodic forcing is imposed at the inlet [69, 83, 82] or a noise [65]. Recently, Ruyer-Quil & Manneville [109] found satisfactory agreement with the phase speeds of travelling waves from experiment using the open flow condition, whereas the closed flow condition resulted in deviations of up to 15%. We shall formally represent both conditions using the conservation equation (2.26a). The space average of (2.26a) gives

$$\frac{\mathrm{d}}{\mathrm{d}t}\left\langle h\right\rangle_{x} = 0 \tag{2.29}$$

where $\left\langle\cdot\right\rangle_{x} = \frac{1}{\lambda}\int_0^\lambda \cdot dx$; it means that the amount of liquid in the domain of length λ is identical at any time t. Indeed, from (2.29), we have $\left\langle h\right\rangle_{x} = \left\langle h\right\rangle_{x}|_{t=0} \quad \forall t$. Thereby, it corresponds to the *closed flow* condition for which the travelling waves are periodic in space, *i.e.* $h|_{x=\lambda} = h|_{x=0}$. In a moving frame of reference with the spatial variable ξ, the *closed flow* condition reads

$$\left\langle h\right\rangle_{\xi} = h_{\mathrm{N}}. \tag{2.30}$$

Now, the time average of (2.26a) gives

$$\frac{\mathrm{d}}{\mathrm{d}x}\left\langle q\right\rangle_{t} = 0, \tag{2.31}$$

where $\left\langle\cdot\right\rangle_{t} = \frac{1}{T}\int_0^T \cdot dt$; it means that the flow rate in a period of time T is identical at any location x. Indeed, from (2.31), we have $\left\langle q\right\rangle_{t} = \left\langle q\right\rangle_{t}|_{x=0} \quad \forall x$. Thereby, it corresponds to the *open flow* condition for which the travelling waves are periodic in time, *i.e.* $h|_{t=T} = h|_{t=0}$. In a moving frame of reference, the *open flow* condition reads

$$\left\langle q\right\rangle_{\xi} = q_{\mathrm{N}}. \tag{2.32}$$

The consequence in the choice of the flow condition appears now by averaging (2.27) as

$$\left\langle h\right\rangle_{\xi} = \frac{\left\langle q\right\rangle_{\xi} - Q}{c}. \tag{2.33}$$

In experiments, the control parameter is the flow rate q_{N} at the inlet whose dimensionless value corresponds to the Reynolds number (1.36). Then using the open flow condition (2.32) with (2.33) shows that the average film thickness $\left\langle h\right\rangle_{\xi} = (q_{\mathrm{N}} - Q)/c$ will be influenced by the wave features c and Q. For instance, Alekseenko *et al.* [1] have observed experimentally a decrease of the average film thickness downstream related to an increase of the phase speed of travelling waves. On the contrary, if we impose the closed flow condition, the insertion of (2.30) into (2.33) gives $\left\langle q\right\rangle_{\xi} = ch_{\mathrm{N}} + Q$. This implies that the effective flow rate $\left\langle q\right\rangle_{\xi}$ will deviate from the imposed one $q_{\mathrm{N}} = h_{\mathrm{N}}^3/3$ (say Re) depending on the development of the travelling wave. Generally, an increase of the phase speed leads to an underestimation of the Reynolds number $q_{\mathrm{N}} < \left\langle q\right\rangle_{\xi}$.

We conclude that the open flow condition is the only one that is experimentally meaningful. Nevertheless, we will continue to compare both conditions because of the intensive use of the closed flow condition in the literature [53, 115, 98, 120].
Having described our methodology and terminology, the parameters, and the used equations, next we describe the families of solutions of interest and relate our results for isothermal vertical films to the work performed by Salamon *et al.* [115] and Oron & Gottlieb [98].

2.5 Blow-up for closed flows

Salamon *et al.* [115] computed travelling wave solutions of the Navier-Stokes equations for a film falling on a vertical (Ct = 0) and isothermal (Ma = 0) wall varying Re at fixed We = 1000 and $\epsilon = 0.04/2\pi$. They imposed the closed flow condition (2.30). The solid line in figure 2.1 shows their results for the reduced maximal film thickness $h_{\max}/h_{\mathrm{N}}$ of the solutions[‡]. Using the dynamical system (2.23) with (2.28), we computed the curve corresponding to the WIBL model (dot-dashed line) and observe that it is quite close to the exact result. We conclude that the WIBL model (2.26) is suitable as reference model in this range of Reynolds numbers. At the contrary, the curve computed for the BE with (2.22) (dashed line) shows a fold at $\mathrm{Re}^* \simeq 4.8$.
Oron & Gottlieb [98] computed corresponding travelling wave solutions performing time-dependent simulations of the BE. They only found stable solutions for the small amplitude part of the solid line (circles in figure 2.1). Those solutions are *bounded* and exist only for $\mathrm{Re} < \mathrm{Re}^*$. For $\mathrm{Re} > \mathrm{Re}^*$, the BE exhibits no stationary wave solution and any perturbation of the flat film is *unbounded*, *i.e.* it yields a finite-time *blow-up*: $h(x^*, t) \to \infty$ at some point x^* as $t \to t^* < \infty$.
Now, we will calculate families of stationary solutions of the BE and the WIBL model and characterize the blow-up of the BE in the whole spectrum of unstable wavenumbers by varying the Reynolds number.

2.5.1 Families of stationary solutions

For a vertically falling and isothermal film, Chang *et al.* [19] constructed the travelling waves bifurcating from the neutral stability curve as a function of their wavenumber for the boundary-layer equation at moderate Reynolds number. They distinguished two main families of waves. The first one, referred to as *holed* waves and denoted by γ_1, terminates at small wavenumbers by slow solitary-like waves with a dominant depression, *i.e.* $h_{\max} - h_{\mathrm{N}} < h_{\mathrm{N}} - h_{\min}$. The second family, called *humped* waves and

[‡]Note that the two parameters We and ϵ (the dimensionless wavenumber) depend on h_{N} as shown by the relations (1.38) and (2.25); remember that $h_{\mathrm{N}} = (3\mathrm{Re})^{1/3}$. Therefore when reading figure 2.1 for increasing Re, the wavenumber k of the travelling wave solution decreases proportionally to $\mathrm{Re}^{-1/3}$ and Ka increases proportionally to $\mathrm{Re}^{2/3}$. The physical interpretation of the curves is therefore less intuitive for the *base state set* of parameters than for the *natural* one where Re accounts alone for the dimensionless Nusselt film thickness (1.37).

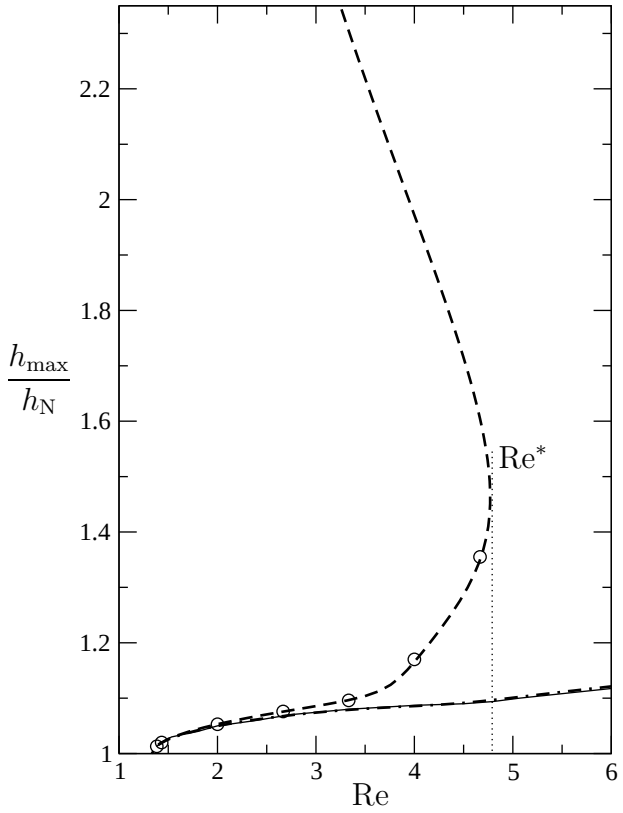

Figure 2.1: maximal thickness of travelling waves $h_{\max}/h_{\mathrm{N}}$ as a function of Re, computed with the BE (dashed curve) and the WIBL model (dot-dashed curve) under the closed flow condition for a film falling on a vertical (Ct = 0) and isothermal (Ma = 0) wall with $\epsilon = 0.04/2\pi$, see (2.25), and We = 1000. For comparison, results of the Navier-Stokes equations (solid curve) obtained by Salamon *et al.* [115] as well as results from time-dependent simulations of the BE (circles) obtained by Oron & Gottlieb [98] are displayed.

denoted by γ_2, corresponds to fast waves with a dominant elevation. Both families can bifurcate either from a Hopf bifurcation and a period doubling bifurcation, or vice versa. Actually, the bifurcations of the families may be reversed if the dispersion of the waves is modified [115]. The *Kawahara equation* (2.14) that contains such dispersion terms has been studied by Chang *et al.* [19]. They showed that the existence of the two families of slow and fast waves bifurcate in an imperfect pitchfork bifurcation [31] from a family of standing waves (that travel at exactly three times the average velocity of the flow). Such a bifurcation is very sensitive to the dispersive effects, as shown below.

The bifurcation diagram in figure 2.2 shows as solid lines two wave families of the BE not much above onset, characterized by the reduced maximal wave thickness $h_{\max}/h_{\mathrm{N}}$ and the phase speed c/c_{L} as a function of the wavenumber k. The parameters are Re = 2.0667, Ka = 3375, Ct = 0 and Ma = 0. They correspond to a vertically falling,

isothermal film of water at $20°C$[§] (see appendix C). The closed flow condition (2.30) is enforced. The first wave family as described by the BE, γ_2 fast waves, starts at the critical wavenumber k_c given by (2.20) corresponding to the Hopf bifurcation point (HB). This bifurcation is *supercritical*, so the wavelength of solutions is larger than the one at threshold $2\pi/k_c$. It leads to stationary one-humped waves that become increasingly nonlinear and have faster phase speed for decreasing k. The wave shape is illustrated in the upper inset of figure 2.2. In the limit $k \to 0$, the solutions correspond to homoclinic orbits in the phase space and will be referred to as *homoclines*. A second family of waves, γ_1 slow waves, appears through a period doubling (PD). They have a slower phase speed and become one-holed on the upper branch of γ_1, *i.e.* after its fold (saddle-node). They are illustrated in the lower inset of figure 2.2.

As the wavenumber decreases, higher harmonics become linearly unstable, at $k_n = k_c/n$ with $n = 2, 3, \ldots$. The resulting families $\gamma_{1,2}(k_n)$ for $n > 1$ correspond therefore to n-humped or n-holed travelling waves. They are not displayed in figure 2.2 because they are *homothetic* in k, *i.e.* given that $\gamma(k_n) = \gamma(k_1)$ it follows that $\gamma(k_n/r) = \gamma(k_1/r)$ for all real $r > 1$. The individual solutions correspond simply to n identical solutions of the $n = 1$ family placed in a domain of size $2n\pi/k$.

The dashed lines in figure 2.2 represent the wave families computed using the WIBL model. Contrary to the BE, the family γ_2 of fast humped waves appears by period doubling while the family γ_1 of slow holed waves emerges by Hopf bifurcation. This disagreement can be understood considering the sensitivity of the imperfect pitchfork bifurcation to slightly different dispersions which originate from the different accounts for the inertial effects (compare 2.22 with 2.28).

The differences between the maximum of humped solutions obtained by the BE and the WIBL model do not exceed 10% and are even much smaller for holed solutions. The comparison of profiles of one-humped travelling waves is displayed in figure 2.3. The corresponding wavenumbers are indicated by arrows at the top of figure 2.2. The solid and dashed lines correspond to wave profiles obtained with the BE and the WIBL model, respectively. We can conclude that for the given parameters, the agreement between BE and WIBL model is satisfactory in the whole spectrum of wavenumbers.

Because the humped solutions have a larger $h_{\max}$ than the holed ones they are more susceptible to blow up at a given k. This is due to the nature of the nonlinear term $\sim \partial_x(h^6\partial_x h)$ responsible for singularities. For the same reason, at a given k the one-humped solutions are also more susceptible to blow up than the multi-humped ones as was checked by Pumir *et al.* [103]. In the following we will therefore concentrate on the family γ_2 of one-humped travelling waves, in order to discuss the validity domain of the BE. The stability of those solutions will be addressed in §2.7.

[§]Some articles we refer to [115, 98] define a Reynolds number $\mathrm{R_s}$ related to the film Reynolds number by $\mathrm{R_s} = 3\mathrm{Re}/2$, *i.e.* $\mathrm{R_s} = 3.1$ for $\mathrm{Re} = 2.0667$. They base their Reynolds number on the surface velocity rather than on the mean velocity. Furthermore, $\mathrm{Ka} = 3375$ corresponds to the value of $\mathrm{We} = 1000$ for the fixed value of $\mathrm{Re} = 2.0667$ ($h_N = 1.8371$) as related by (1.38).

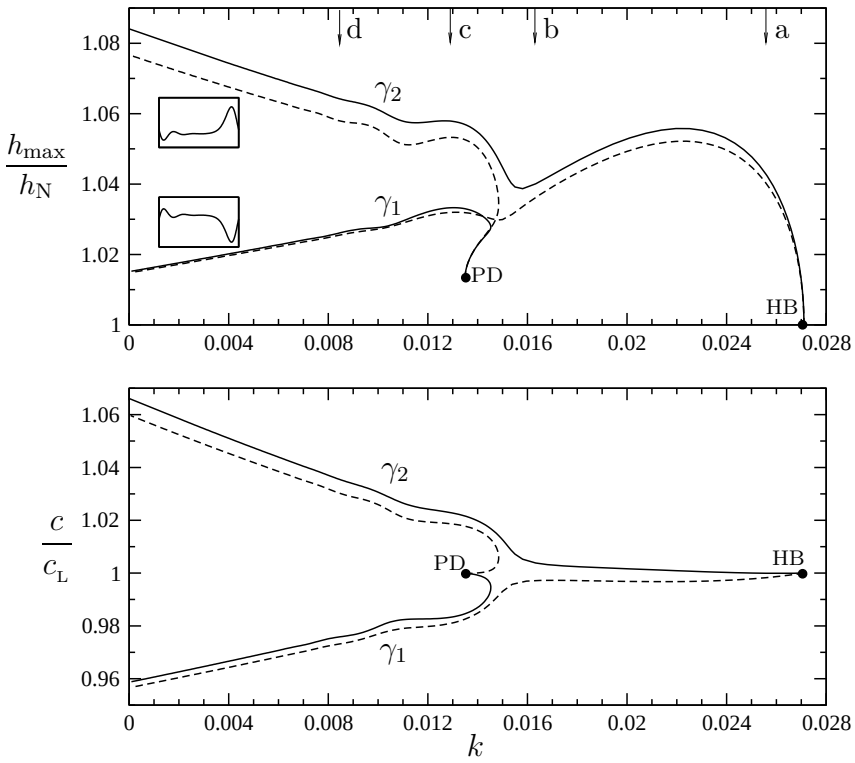

Figure 2.2: Bifurcation diagram showing the phase speed c/c_{L} and maximal amplitude $h_{\max}/h_{\mathrm{N}}$ of travelling waves versus the wavenumber k. The parameters are Ct = 0, Ma = 0 (vertical and isothermal wall), Re = 2.0667 and Ka = 3375. The closed flow condition is imposed. The solid (dashed) lines are families obtained with the BE (WIBL) model. The families γ_2 correspond to fast one-humped waves and γ_1 to slow one-holed waves, as illustrated by the two insets. The arrows and letters refer to solutions plotted in figure 2.3. HB: Hopf Bifurcation - PD: Period Doubling. The HB bifurcates from the Nusselt flat film solution while the PD bifurcates from the families of subharmonic solutions for $n = 2$ (not drawn on the picture).

2.5.2 Blow-up versus wavenumber

In this section, we obtain the blow-up boundary of the Benney equation, by varying the Reynolds number, in the whole spectrum of wavenumbers, *i.e.* from neutrally unstable modes to infinite wavelength solitary waves. This is used to describe the transition from the linear wave regime close to the marginal stability curve to the solitary wave regime at small wavenumber and also to precise how the validity domain of the Benney equation in the parameter space is modified by the type of wave considered.

We will analyse the occurrence of the blow-up in the BE and confirm the link between the absence of the γ_2 wave family and the unbounded behaviour reported by Oron & Gottlieb [98]. The bifurcation diagram in figure 2.4 shows in solid lines families of one-humped travelling waves computed with the BE for several Re. The chosen parameters are Ct = 0, Ma = 0 and Ka = 2950 correspond to a vertically falling,

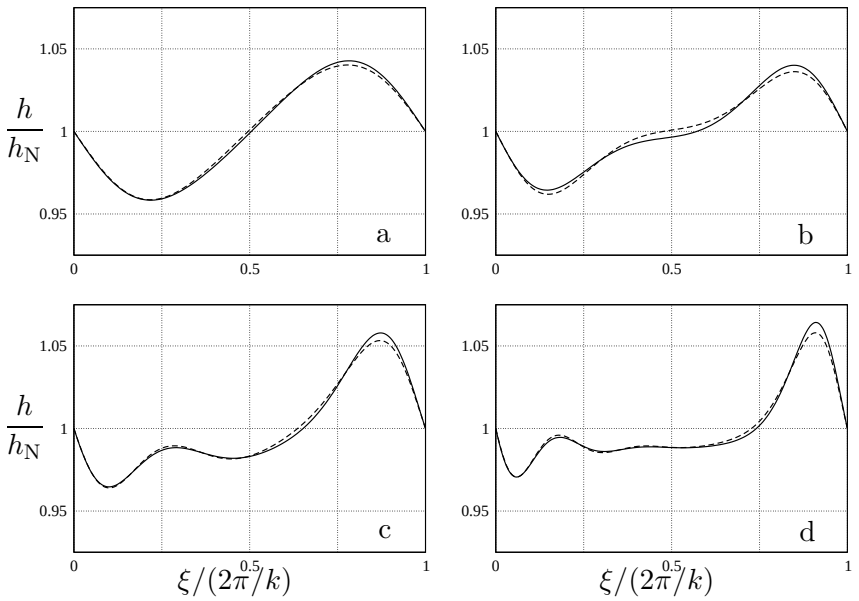

Figure 2.3: Profiles of one-humped travelling waves computed for Ct = 0, Ma = 0, Re = 2.0667 and Ka = 3375 and various values of the wavenumber k: (a) $k = 0.0256$, (b) $k = 0.0169$, (c) $k = 0.0128$, (d) $k = 0.0084$. The closed flow condition (2.30) was imposed. The solid and dashed curves are solutions computed with the BE and the WIBL model, respectively.

isothermal film of water at $15°C$ (see table C.1) as in the experiments by Kapitza & Kapitza [69]. The closed flow condition (2.30) has been used. The dashed curves are the corresponding wave families computed with the WIBL model. For $\mathrm{Re} \gtrsim 3$, the BE wave families feature a *saddle-node*[¶] bifurcation at k^*, indicated by an asterisk in figure 2.4. This implies that for $k < k^*$ the BE has no stationary solution of γ_2 fast wave type. For $k > k^*$, two stationary solution branches coexist but only the one with the smallest amplitude has a physical meaning as found from the WIBL model. The bifurcation at k_c is supercritical for $\mathrm{Re} \leq 5$. However, the interval $[k^*, k_c]$ shrinks at increasing Re until it vanishes. For larger $\mathrm{Re} = 7, 8$ the bifurcation is subcritical. Note that the transition from supercritical to subcritical has an intrinsic structure as can be seen for Re = 5.75 and 6. There the families contain two saddle-nodes, the second one being indicated by a cross. There may be then three solutions of the BE in some small range of k.

In figure 2.5 we plot the locus k^* of the saddle-node bifurcation of the BE family γ_2 as a function of Re (dashed line), together with the critical wavenumber k_c (solid line, see (2.20)). The flat film is linearly stable above k_c, one-humped γ_2 travelling waves can be found between the solid and the dashed line only. The asterisks and crosses indicate the saddle-node bifurcations obtained in figure 2.4 (see also the zoom in the inset of figure 2.5).

Oron & Gottlieb [98] performed time-dependent simulations of travelling waves for

[¶]This bifurcation corresponds qualitatively to the transition from zero to two solutions by changing the control parameter (here k).

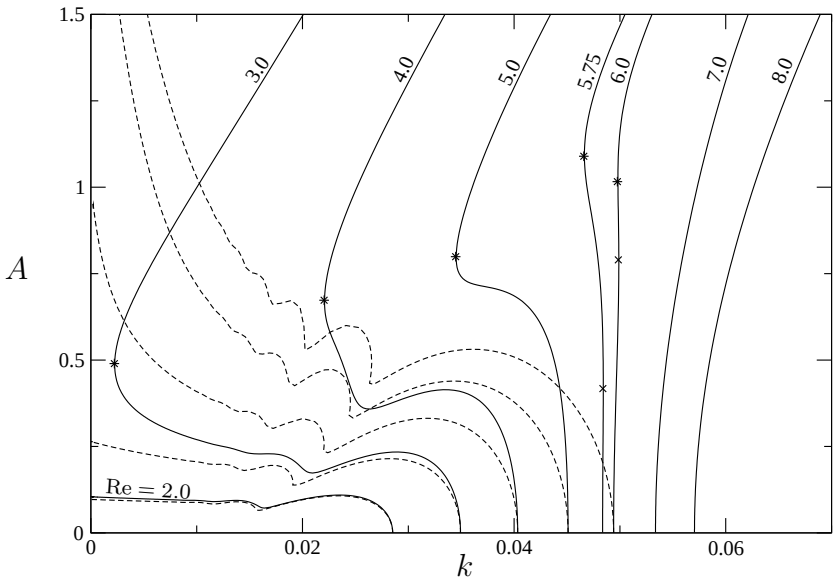

Figure 2.4: Bifurcation diagram showing families of solutions for various Re computed with the BE in solid lines, considering the vertical and isothermal case (Ct = 0, Ma = 0) with Ka = 2950 and the closed flow condition (2.30). $A = (h_{\max} - h_{\min})/h_{\mathrm{N}}$ is the reduced wave amplitude. The dashed lines are the branches computed with the WIBL model for Re $= 2, 3, 4, 5, 6$. Asterisks and crosses indicate saddle-node bifurcations. Their loci are followed through parameter space in figure 2.5.

various k and obtained the corresponding boundaries for blow-up shown by circles in figure 2.5. These points agree with the locus of k^* (dashed line) except the lowest one that most probably corresponds to the blow-up of a two-humped solution ($n = 2$) because it fits perfectly with the corresponding blow-up boundary computed with our method (dotted line in figure 2.5). Nevertheless, the simulations of Oron & Gottlieb [98] confirm that the one-humped solutions are the most "dangerous" ones because they blow up at smaller Reynolds numbers than multi-humped ones. Therefore, our results clearly confirm the connection between the occurrence of blow-up and the absence of γ_2 one-humped fast waves. Indeed, time-dependent simulations of the spatial evolution of the film using the BE equation showed the formation of one-humped solitary-like structures though no stationary wave solutions can be reached, thus leading to blow-up [103]. It seems that whenever any γ_2 humped waves cannot be attained, blow-up occurs.

The inset of figure 2.5 shows that the Benney equation experiences a subcritical behaviour already in a region where it can still yield bounded solutions. This subcritical behaviour is most likely non physical and has not been observed at least with our reference model. This behaviour will be discussed in more details in §2.6.4.

We define two particular values of the Reynolds number as indicated in figure 2.5: $\mathrm{Re}_{\mathrm{h}}^*$ for $k^* \to 0$ and $\mathrm{Re}_{\mathrm{c}}^*$ for $k^* = k_{\mathrm{c}}$. They correspond, respectively, to the Reynolds number where only homoclines blow up and where none of the linearly unstable modes is bounded. $\mathrm{Re}_{\mathrm{h}}^*$ and $\mathrm{Re}_{\mathrm{c}}^*$ (in addition to another characteristics defined later on) will

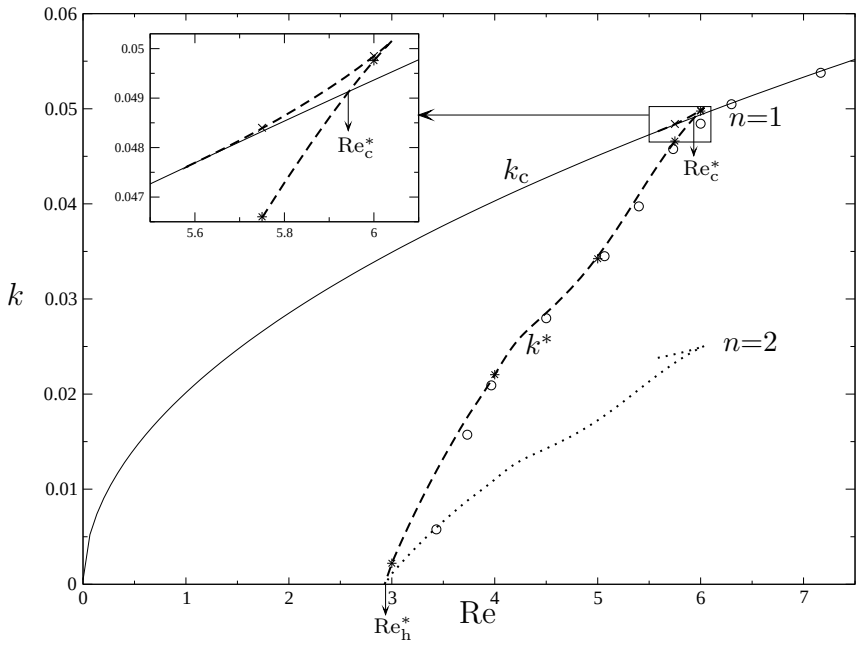

Figure 2.5: Stability diagram computed with the BE for thin water films (same parameters as for figure 2.4). The solid line is the neutral curve, *i.e.* the critical wavenumber k_c. The dashed line is the blow-up boundary separating bounded solutions (on the left) and unbounded ones (on the right). The circles are blow-up boundaries obtained by Oron & Gottlieb [98] using simulations in time. Re_h^* indicates the Reynolds number where only homoclines blow up and Re_c^* the Reynolds number where all the linearly unstable modes blow up. The asterisks and crosses correspond to the saddle-node bifurcations shown in figure 2.4. The inset zooms in on the parameter range where the Hopf bifurcation is subcritical, i.e. where $k^* > k_\mathrm{c}$. The dotted line is the blow-up boundary for two-humped solutions ($n = 2$).

be used to globally characterize the blow-up.

2.6 Parametric study for closed and open flows

In this section, the *nonlinear set* of parameters introduced in §1.6 is used in order to facilitate the parametric study. Then, we track the blow-up boundary through the parameter space investigating successively the influence of the surface tension, the inclination and the thermocapillarity. Below the blow-up boundary the accuracy of the Benney equation is determined checking the wave amplitudes against the reference model. The influence of the Marangoni effect on the subcritical behaviour is also analysed in order to determine whether it has a physical meaning or not.

2.6.1 Reduced systems and parameters

Keeping track of the domain boundaries in parameter space where bounded solutions exist is quite involved. Indeed, five parameters can be varied, namely the inclination

of the plane (Ct), surface tension (Ka), its sensitivity to temperature (Ma), the heat transfer at the interface (Bi) and finally the inlet flow rate (Re). Fortunately at first order, this number can be reduced by one applying a transformation proposed first by Shkadov [127], which introduces the *nonlinear set* of parameters 1.105. The number can even be reduced to three in the reasonable limit of small Biot number (see appendix C).
Using the Shkadov's transformation $\mathcal{T}$ (1.103), the BE (2.10) then becomes for parallel flow ($\partial_z = 0$)

$$\partial_t h + \partial_x \left(\frac{h^3}{3} + \frac{2}{15}\mathcal{R}\, h^6\, \partial_x h - \mathcal{C}\frac{h^3}{3}\partial_x h + \frac{h^3}{3}\partial_{xxx} h + \frac{h^2}{2}\frac{\mathcal{M}\,\mathrm{B}\,\partial_x h}{(1+\mathrm{B}\,h)^2} \right) = 0, \qquad (2.34)$$

where the *nonlinear set* of parameters appears. Since the study here is limited to the first-order, the parameter η that measures the second-order viscous effects does not appear. This is why the number of independent parameters is reduced by one. In this scaling, the Nusselt solution is $h = 1$ and the Hopf bifurcation is characterized by

$$k_{\mathrm{c}} = \left(\frac{2}{5}\mathcal{R} - \mathcal{C} + \frac{3}{2}\frac{\mathcal{M}\,\mathrm{B}}{(1+\mathrm{B})^2} \right)^{1/2}, \quad c_{\mathrm{L}} = 1 \quad \text{and} \quad Q_{\mathrm{L}} = \frac{1}{3} - c_{\mathrm{L}} = -\frac{2}{3}. \qquad (2.35)$$

The wavenumber is rescaled as $k \to k/\mathcal{L}$ where $\mathcal{L} = (\mathrm{Ka}h_{\mathrm{N}})^{1/3}$. Note, that rescaling t by $\frac{1}{3}$ shows the equivalence between (2.34) and (2.1) for $\mathcal{C} = 0$ and $\mathcal{M} = 0$ when $\Phi = 2\mathcal{R}/5$ and $m = 6$.
Using the transformations $\mathcal{T}$ and $q \to h_{\mathrm{N}}^3 q$, the WIBL model (2.26) becomes

$$\partial_t h = -\partial_x q, \qquad (2.36)$$

$$\mathcal{R}\,\partial_t q = \frac{5}{2}h - \frac{5}{2}\frac{q}{h^2} + \mathcal{R}\frac{9}{7}\frac{q^2}{h^2}\partial_x h - \mathcal{R}\frac{17}{7}\frac{q}{h}\partial_x q - \mathcal{C}\frac{5}{6}h\,\partial_x h + \frac{5}{6}h\,\partial_{xxx} h + \frac{5}{4}\frac{\mathcal{M}\,\mathrm{B}\,\partial_x h}{(1+\mathrm{B}\,h)^2}. \qquad (2.37)$$

2.6.2 Vertical and isothermal films

Open and closed flows

Figure 2.6 shows the stability diagram in the (k,$\mathcal{R}$)–plane for a vertically falling, isothermal film, *i.e.* $\mathcal{M} = \mathcal{C} = 0$. The solid line is the neutral curve k_{c} computed with (2.35). The dashed and dot-dashed lines are the blow-up boundaries computed using, respectively, the closed flow condition $\langle h \rangle_{\xi} = 1$ and the open flow condition $\langle h \rangle_{\xi} = (1/3 - Q)/c$, defined with the new scaling. A major difference can be observed between both flow conditions. As displayed in the inset of figure 2.5, for the closed flow condition the Hopf bifurcation can become subcritical. For the open flow condition the Hopf bifurcation is always supercritical, *i.e.* for all $\mathcal{R}$. This implies that close to criticality the BE always gives bounded solutions. However, figure 2.6 also shows that for $\mathcal{R} > \mathcal{R}_{\mathrm{c}}^*|_{\mathrm{OP}}$ the corresponding region of k is very small. The inset of this figure shows the blow-up boundary for open flow in the vicinity of $\mathcal{R}_{\mathrm{c}}^*|_{\mathrm{OP}}$.

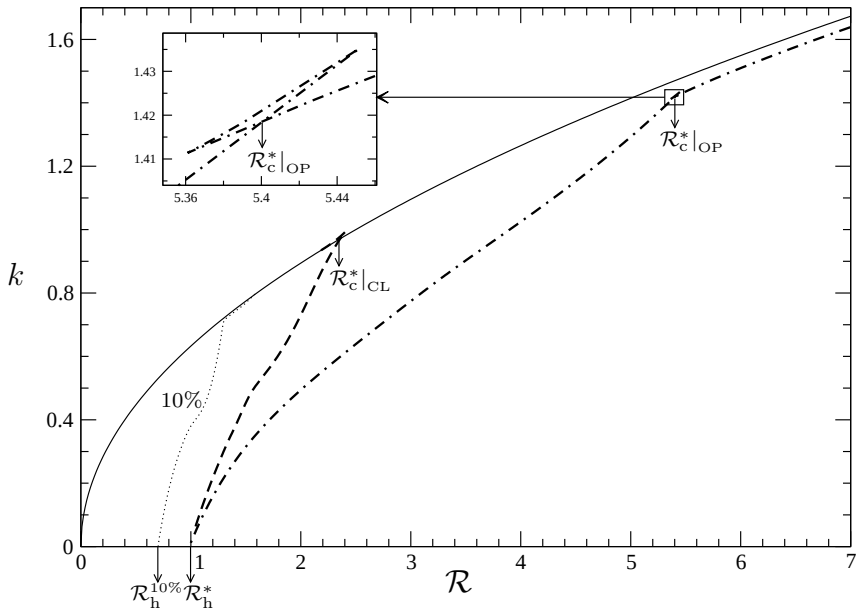

Figure 2.6: Stability diagram in the $(k, \mathcal{R})$–plane for a vertically falling, isothermal film, i.e. $\mathcal{C} = \mathcal{M} = 0$. The solid line is the neutral stability curve. The dashed (dot-dashed) line is the blow-up boundary corresponding to the closed (open) flow condition. The dotted line is the boundary where the amplitude of solutions of the BE exceed by about 10% the one of the WIBL model. The inset zooms in on the behaviour of the blow-up boundary in the vicinity of $\mathcal{R}_c^*|_{OP}$.

The specific reduced Reynolds numbers (as introduced in §2.5.2) that can be extracted from figure 2.6 are

$$\mathcal{R}_h^* = 0.986, \qquad \mathcal{R}_c^*|_{CL} = 2.358 \qquad \text{and} \qquad \mathcal{R}_c^*|_{OP} = 5.401,$$

where the subscripts CL and OP indicate the corresponding flow condition. Note that homoclines being solutions of infinite wavelength, they are by essence independent on the flow condition. Back to the *natural set* of parameters for $\sin\beta = 1$, the one-humped solitary waves – that tend to blow up first, *i.e.* at the smallest Reynolds number – are bounded only if $\mathrm{Re} < 0.330\,\mathrm{Ka}_\perp^{3/11}$ (remember from §1.2 that $\mathrm{Ka}_\perp$ is the Kapitza number for a film falling vertically, *i.e.* $\sin\beta = 1$, and then depending only on the fluid properties). To check, for instance, the validity of the BE in the particular case of a water film at $20°C$ (see table C.1) we use (1.105a) to obtain the specific Reynolds numbers $\mathrm{Re}_h^* = 3.0$, $\mathrm{Re}_c^*|_{CL} = 6.2$ and $\mathrm{Re}_c^*|_{OP} = 12.2$. It is therefore clear that for the open flow condition, the validity domain of the Benney equation is larger than for the closed flow condition. Nevertheless, the stability of the solution should be taken into account for completion (see §2.7).

Accuracy of the bounded solutions: BE versus WIBL

The dotted line in figure 2.6 indicates the loci of bounded solutions of the BE where the amplitude exceeds by about 10% the one computed with the WIBL model. At

the same point the phase speed is overestimated by about 20%. This boundary is approximately identical for both flow conditions. To the right of this boundary, the difference of the amplitudes of BE and WIBL model increases to reach about 100% at the respective blow-up boundaries. Even though the open flow condition gives bounded solutions for larger $\mathcal{R}$ than the closed flow condition, the wave amplitudes become much larger than for the WIBL model. So the 10%-accuracy limit is a good gauge for both flow conditions.
The 10%-accuracy limit approaches asymptotically the neutral stability curve. This can already be seen in figure 2.4 where for $\mathrm{Re} = 4, 5$ and 6 the discrepancy between the BE and the WIBL model becomes already large quite close to the Hopf bifurcation. The accuracy limit in figure 2.6 intersects the $\mathcal{R}$-axis at $\mathcal{R}_{\mathrm{h}}^{10\%}$. This point corresponds to a deviation of 10% of the amplitudes of the respective homoclines, the value of which being

$$\mathcal{R}_{\mathrm{h}}^{10\%} = 0.68.$$

Back to the *natural set* of parameters with $\sin\beta = 1$, the accuracy of the amplitude of solitary wave computed with the BE will be better than 10% for $\mathrm{Re} < 0.243\,\mathrm{Ka}_{\perp}^{3/11}$, which corresponds for water at 20°C to $\mathrm{Re} = 2.23$. Finally, using (1.105a), we conclude that the range of validity of the BE decreases as the Kapitza number decreases, proportional to the surface tension.

2.6.3 Influence of the inclination

Figure 2.7 shows the stability diagram of the BE in the $(\mathcal{C}, \mathcal{R})$–plane using (2.34) for an isothermal film, *i.e.* $\mathcal{M} = 0$. The heavy solid line corresponds to the neutral stability curve $k_{\mathrm{c}} = 0$, *i.e.* $\mathcal{C} = 2\mathcal{R}/5$. Above the flat film is stable, "**s**", and below it is unstable, "**u**". The heavy dashed line indicates the boundary where homoclines blow up ($\mathcal{R}_{\mathrm{h}}^{*}$), whereas at the dashed and the long dashed lines all the linearly unstable modes blow up ($\mathcal{R}_{\mathrm{c}}^{*}$) for closed and nearly all for open flow conditions, respectively. The solutions in the region "$\mathbf{u}_k$" are bounded only in the range of wavenumbers $[k^*, k_{\mathrm{c}}]$ and unbounded in the range $[0, k^*]$. In the region "**b**", waves blow up unconditionally at any wavenumber (except very near threshold for open flow conditions). Finally, the dotted line is the locus of the parameter $\mathcal{R}_{\mathrm{h}}^{10\%}$ defined in §2.6.2.
The dot-dashed lines in figure 2.7 correspond to fixed experimental properties of some common liquids (see table C.1) for two different inclinations of the wall, namely 10 and 30 degrees. These curves are obtained by eliminating Re from $\mathcal{C}$ and $\mathcal{R}$ using (1.105a,1.105b). This leads to the relation

$$\mathcal{C} = \mathrm{C}\left(\frac{\mathcal{R}^2}{\mathrm{S}^{10}\mathrm{Ka}_{\perp}^3}\right)^{1/11}, \tag{2.38}$$

where the *natural set* of parameters with $\sin\beta = 1$ has been used explicitely to isolate the effect of the wall inclination. Increasing $\mathcal{C}$, *i.e.* decreasing S and/or $\mathrm{Ka}_{\perp}$, reduces the range of validity of the BE in the linearly unstable domain.
Joo *et al.* [53] have performed time-dependent simulations of the BE for isothermal falling films under the closed flow condition. Their figures 5-9 present the respective

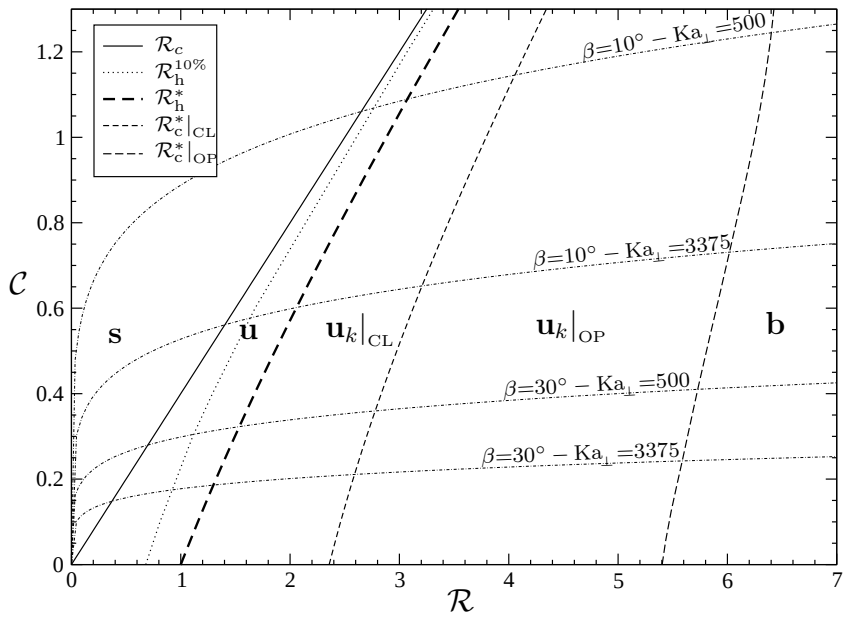

Figure 2.7: Stability diagram in the $(\mathcal{C}, \mathcal{R})$–plane for an isothermal film, i.e. $\mathcal{M} = 0$. The solid line is the neutral stability curve. The different regions from the left to the right are: **s**, the linearly stable region; **u**, the linearly unstable region where the BE gives bounded solutions in the whole range of unstable wavenumbers $k_c > k > 0$; $\mathbf{u}_k|_{CL}$, the linearly unstable region where the BE gives bounded solutions only in the range $k_c > k > k^*$ when the closed flow condition is enforced; $\mathbf{u}_k|_{OP}$, the same when the open flow condition is enforced; **b**, the region where all the linearly unstable modes are unbounded and yield finite-time blow-up. For the meaning of the dot-dashed lines see main text.

wave evolutions for increasing domain size, *i.e.* decreasing wavenumber. The parameters are $\beta = 45°$, Re $= 1.179$, Ka$_\perp = 4.386$ and Ma$_\perp = 0$. This corresponds to $(\mathcal{R}, \mathcal{C}) = (2.751, 0.778)$ in the reduced scaling, *i.e.* to a point in the region "$\mathbf{u}_k|_{CL}$" of figure 2.7 indicating that solutions are only bounded for $k > k^*$. This agrees with the stationary travelling waves found in figures 5, 6 and 7 of Joo *et al.* [53]. On the contrary, figures 8 and 9 of their paper show 'catastrophic behaviour', *i.e.* wave amplitudes growing 'explosively' in finite-time. Our explanation is that $k < k^*$ for these simulations. Using their scaling we computed the value of the blow-up boundary to be $k^*_{JDB} = 1.236$. In conclusion, we are now able to explain and predict the 'catastrophic behaviour' found by Joo *et al.* [53] which results from the blow-up character of the Benney equation and is not associated to a secondary instability as conjectured by these authors. By coincidence, due to the choice of the parameter values in their paper, the transition for the secondary instability at $k_s \approx k_c/2$, found initially by Gjevik [41] using weakly nonlinear analysis, is very close to the blow-up transition for nonlinear solutions found here. Joo *et al.* [53] suggested that waves never equilibrate for $k < k_s$. Yet, the present study shows that waves are bounded in this region, either for $\mathcal{R} < \mathcal{R}^*_h$, or if $k > k^*$. Having also studied the Benney equation with strong Marangoni effect, Joo *et al.* conjectured that the Marangoni effect prevents the trav-

elling waves to be bounded. However, the present work shows a region of bounded solutions for moderate Marangoni number as shown in what follows.

2.6.4 Influence of the Marangoni effect

Limit of small Biot number: $\mathrm{Bi} \ll 1$

The influence of the Marangoni effect is studied in this section in the case of a uniform temperature imposed at the wall (Temperature Condition). Furthermore, for common liquids, the Biot number is usually small (see table C.1). Therefore we use the approximation

$$\frac{\mathcal{M}\,\mathrm{B}}{(1+\mathrm{B}\,h)^2} \approx \mathcal{M}\mathrm{B} \tag{2.39}$$

in (2.34) and (2.37) to study the Marangoni effect with $\mathcal{M}\mathrm{B}$ as a single parameter. In this limit, the Marangoni term approximately behaves as a $m = 2$ term in (2.1). It should therefore not yield to blow-up itself but influence the domain of validity of the BE.

Figure 2.8 represents the stability diagram of the BE in the $(\mathcal{M}\mathrm{B}, \mathcal{R})$–plane for a vertical wall, *i.e.* $\mathcal{C} = 0$. Line styles are as presented for figure 2.7. Note that there exists no linearly stable region. The dot-dashed lines in figure 2.8 correspond again to fixed liquid properties (table C.1). They are calculated using

$$\mathcal{M}\mathrm{B} = \mathrm{Ma}\,\mathrm{Bi}\left(\frac{1}{\mathrm{S}^6\mathrm{Ka}^4\mathcal{R}}\right)^{1/11}, \tag{2.40}$$

obtained by eliminating Re from $\mathcal{M}\mathrm{B}$ and $\mathcal{R}$ with (1.105a,1.105e).

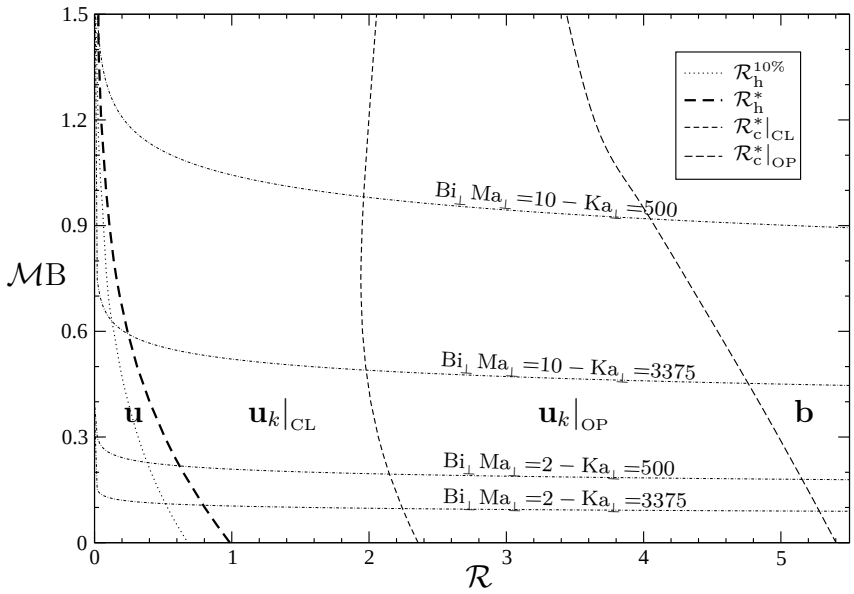

Figure 2.8: Stability diagram in the $(\mathcal{M}\mathrm{B}, \mathcal{R})$–plane for a vertically falling film, i.e. $\mathcal{C} = 0$. Line styles and small letters are as for figure 2.7.

The domain of existence for homoclines obtained with the BE nearly vanishes for large $\mathcal{M}$B. However, as table C.1 indicates, the product $\mathrm{Ma}_\perp \mathrm{Bi}_\perp$ remains small for common liquids [120]. For instance, for a vertically falling water film at 20°C the value $\mathrm{Ma}_\perp \mathrm{Bi}_\perp = 2$ corresponds to $\Delta T = 28K$ when $\alpha = 100W/m^2K$. In this case, the BE can be used with satisfactory accuracy up to $\mathrm{Re} = 1.8$ ($\mathcal{R}_\mathrm{h}^{10\%} = 0.52$).

Joo *et al.* [53] have performed time-dependent simulations of the BE for large Biot number. Considering the case of figure 14 in their paper, for $\beta = 45°$, $\mathrm{Re} = 1.179$, $\mathrm{Ka}_\perp = 4.386$, $\mathrm{Ma}_\perp = 11.696$ and $\mathrm{Bi}_\perp = 5.848$, they observed blow-up of the travelling wave. This result is expected given that even for $\mathrm{Ma}_\perp = 0$ blow-up is observed (see §2.6.3), and that the Marangoni effect further decreases the validity domain of the BE (see figure 2.8). However, at least a small region possessing bounded solutions is present whatever the value of $\mathcal{M}$B.

Subcritical behaviour of the Benney equation

For the isothermal case we have seen in figure 2.4 that the Hopf bifurcation computed with the BE is always subcritical for $\mathrm{Re} > \mathrm{Re}_\mathrm{c}^*$. However, the bifurcation can become subcritical even slightly before that the saddle-node wavenumber k^* reaches k_c at Re_c^* as shown by the inset of figure 2.5. If this is the case, the family has not only one but two saddle-nodes or turning points. We will study now the influence of the strength of the Marangoni effect of the size of the corresponding region.

Figure 2.9 displays the stability diagram for different values of $\mathcal{M}$B for closed (dashed lines) and open (dot-dashed lines) flow conditions. The corresponding neutral stability curves are plotted as dotted lines. The figure shows that for closed flow the region where subcritical bifurcations are found extends towards smaller $\mathcal{R} < \mathcal{R}_\mathrm{c}^*$ for increasing $\mathcal{M}$B. A somehow similar observation is made also for the open flow condition. Although there the bifurcation is always supercritical, the family has an additional turning point slightly above the bifurcation, as illustrated by the inset of figure 2.9. The resulting three turning points allow for a similar shape of the large amplitude part of the bifurcation diagram as for the closed flow condition.

So in both cases, solutions with $k > k_c$ exist already for $\mathcal{R} < \mathcal{R}_\mathrm{c}^*$. In short we will call this behaviour subcritical. On the one hand, the subcritical behaviour seems to agree with results on the Marangoni instability for horizontal films obtained by VanHook *et al.* [141] and Thiele & Knobloch [136] also for the slighlty inclined case. On the other hand, we find that for vertically falling films the WIBL model *does never* yield subcritical behaviour in the considered parameter range. This is illustrated in the inset of figure 2.9. A study by Thiele & Knobloch [136] of the behaviour of a thin film on a slightly inclined heated plane using an equation similar to equation (2.10) *without* the Benney term proved that for sufficiently large (but in our scaling still small) plate inclinations from the horizontal, the bifurcation is always supercritical.

Therefore, we conjecture that the subcritical behaviour of the Benney equation including the Marangoni effect described above is unphysical, in contrast to the subcritical instabilities known for horizontal and slightly inclined planes. Evaluating again figure 2.9 for the closed flow condition, we find that the bifurcation is subcritical for all $\mathcal{R}$

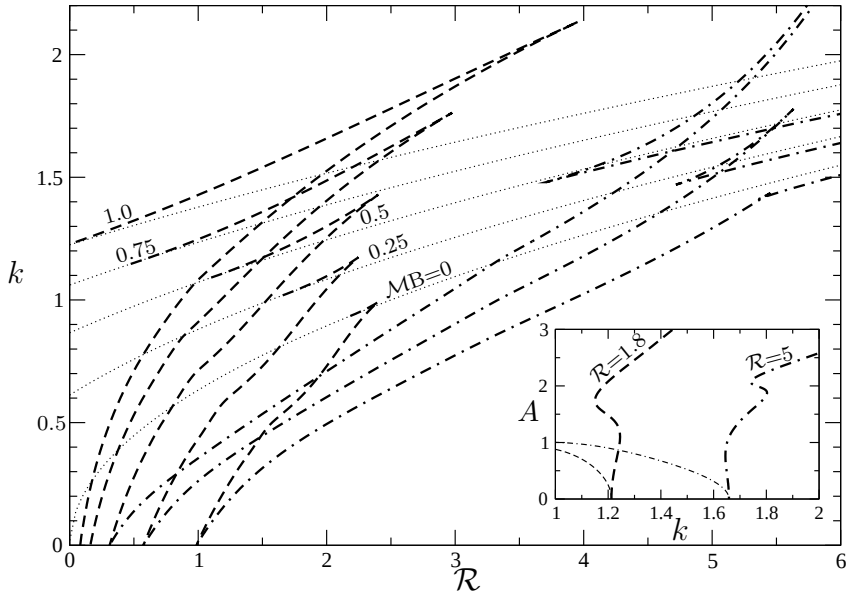

Figure 2.9: Stability diagram in the $(k, \mathcal{R})$–plane for a vertically falling film, i.e. $\mathcal{C} = 0$ and different values of $\mathcal{M}\mathrm{B} = 0, 0.25, 0.5, 0.75$ and 1. The dotted lines are the corresponding neutral curves k_c and the dashed lines are the blow-up boundaries obtained with the closed flow condition. The dot-dashed lines are a selection of the blow-up boundaries obtained with the open flow condition. The inset shows bifurcation diagrams for $\mathcal{MB} = 0.5$ and $\mathcal{R} = 1.8$ ($\mathcal{R} = 5$) with the closed (open) flow condition. The thin lines are computed with the WIBL model.

when

$$\mathcal{M}\mathrm{B} \approx 1.$$

This implies that above this value the Benney equation fails to describe the physics for vertically falling films even quite close to criticality.
We did not investigate the combination of Marangoni effect and wall inclination. However, combining our results with the ones of Thiele & Knobloch [136] indicates that the subcritical behaviour of the Benney equation will only be physically meaningful for very small or vanishing inclination angles. In other words, travelling waves emerge even in the presence of the Marangoni effect always from supercritical bifurcation unless the inclination angle is so small that the film behaves like a 'horizontal layer'. However, then $\mathrm{Re} \ll 1$ and the Benney term $\approx \partial_x(h^6 \partial_x h)$ may be neglected.

2.7 Stability of stationary solutions

This section analyses the two-dimensional stability of the stationary humped solutions discussed up to now. We focus especially on the range $[\mathcal{R}_\mathrm{h}^*, \mathcal{R}_\mathrm{c}^*]$ where only part of the linearly unstable modes results in bounded stationary solutions. We will determine the stability of those solutions to disturbances of larger period that may induce the coalescence of humps. This is done performing a Floquet analysis following, for

instance, Chang *et al.* [19]. Let $h_0(\xi)$ be the stationary solution of wavenumber k in its moving frame of reference. Then the film thickness h is written as the superposition of this solution and a small disturbance

$$h = h_0(\xi) + \eta h_1(\xi) \exp\{\mathrm{i}\varsigma k\xi + \Gamma t\}, \tag{2.41}$$

where $\eta \ll 1$ and h_1 is a real function with the same period as h_0. The real (imaginary) part of Γ corresponds to the growth rate s (relative phase velocity c) of the disturbance. The detuning parameter (often called Floquet coefficient) ς represents the ratio of the wavenumbers of the disturbance and of the stationary wave $h_0(\xi)$. For $\varsigma = 0$ the instability has the same wavelength than the wave, and for $0 < \varsigma \leq \frac{1}{2}$ the instability is *sub-harmonic*. For instance, $\varsigma = \frac{1}{2}$ implies that the disturbance has twice the period of the wave. According to Chang *et al.* [15], when ς is close to zero, the instability is called *side-band*. Substituting (2.41) into (2.10) and linearizing in η, we obtain an eigenvalue problem of the form $\Gamma h_1 = L(h_0, c, Q, \varsigma)h_1$ where L is a linear operator.

Figure 2.10 shows the growth rate $s_{\max}$ of the most amplified disturbance and the corresponding detuning parameter $\varsigma_{\max}$ versus the wavenumber of the unperturbed travelling waves, for $\mathcal{R} = 1.5$ and 3, with $\mathcal{C} = \mathcal{M} = 0$. The heavy and thin lines result from the BE and WIBL model, respectively, whereas solid and dashed lines stand for closed and open flow condition, respectively. The blow-up boundary at k^* is indicated by an asterisk and the neutral mode by a "c". The loci of the stationary solutions analysed here can be found in figure 2.6. For the value of $\mathcal{R}$ considered, the growth rate $s_{\max}$ is positive for all k implying that none of the bounded solutions emerging from the Hopf bifurcation is stable to sub-harmonic disturbances. If the imaginary part of Γ (not shown in figure 2.10) is equal to zero the waves coarse steadily by a relative translation of the humps and by volume transfer between the humps [17]. This is the case for the WIBL model. In contrast, for the BE the imaginary part of s is non-zero. This indicates that the instability leads to oscillating behaviour that may or may not lead to coarsening. Only time-dependent simulations of the BE can clarify this point. An example is presented in figure 2.11. Two periods of a stationary solution calculated with the closed flow condition and corresponding to the point $(\mathcal{R}, k) = (1.5, 0.5)$ in figure 2.6 with additional noise are used as initial condition. The time series for the amplitude at a fixed point in space (figure 2.11) shows that the ongoing process comprises growing sinusoidal oscillations of the relative amplitudes of the two humps that lead to a coalescence mediated finite-time blow-up. We propose to call this type of coalescence *oscillation mediated coalescence*.

The importance of the result of the stability analysis lies in the fact that physically relevant domains are always at least twice larger than the wavelength of the stationary solution. Thereby, sub-harmonics will develop, and for $\mathcal{R} \geq \mathcal{R}_h^*$ (figure 2.6) this leads finally to blow-up as illustrated in figure 2.11. For instance, looking at the blow-up boundary for the closed flow condition on figure 2.6, at any $\mathcal{R}$ larger than $\sim$1.4, a bounded one-humped travelling wave put twice in a domain of doubled size is unstable and yields a finite-time blow-up. The same happens for the open flow condition at any $\mathcal{R}$ larger than $\sim$1.8. It means even though the Benney equation gives bounded

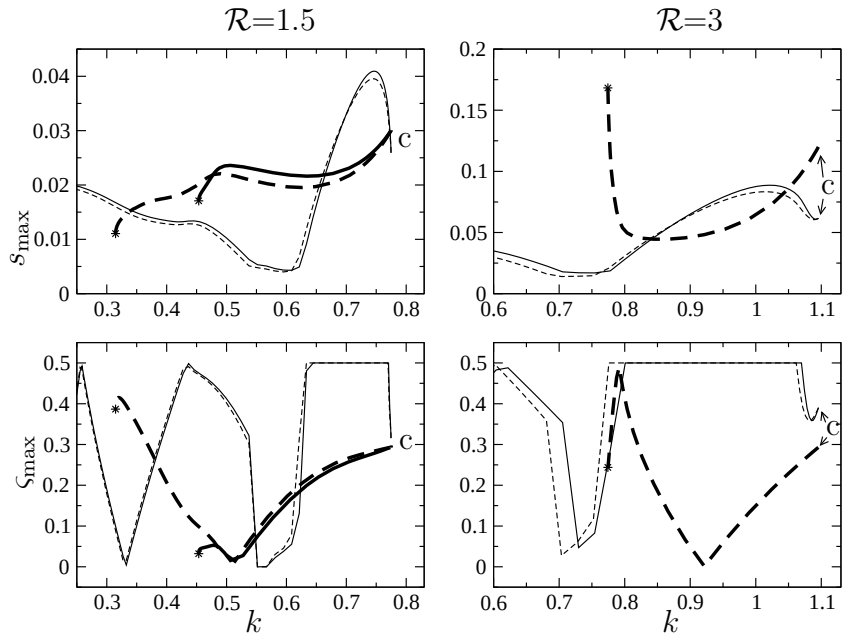

Figure 2.10: maximal real part of the growth rate $s_{\max}$ of disturbances and corresponding wavenumber ratio $\varsigma_{\max}$ versus wavenumber of stationary solutions of the BE (thick lines) and the WIBL model (thin lines). The solid (dashed) lines correspond to closed (open) flow The letter "c" indicates the neutral mode at k_c and the asterisk indicates the solution at the blow-up boundary, for k^*. The calculations are made for a vertically falling, isothermal film, i.e. $\mathcal{C} = \mathcal{M} = 0$.

solutions beyond the blow-up boundary for homoclines, $\mathcal{R}_h^*$, those solutions should be considered with special care independently of the used flow condition.
In conclusion, the stability of stationary solutions that are conditionally bounded, depending on the wavenumber, are all found to be unstable to disturbances of higher periodicity. This gives the possibility to the sub-harmonics to develop and in consequence yields finite-time blow-up promoted by wave coalescence.

2.8 Further discussion about the Benney equation

At this stage, let us present an interesting result obtained from a time-dependent simulation of the Benney equation (2.34), using a finite-difference implicit scheme [107]. Figure 2.12 displays the nonlinear response of a vertically falling and isothermal film submitted to a periodic forcing with small noise at the inlet (left border). The reduced Reynolds number $\mathcal{R} = 0.9$ has been chosen to lie before $\mathcal{R}_h^*$, *i.e.* for bounded homoclines. It is of main interest to observe that at a given position, still a singularity appears in a finite-time, leading to the blow-up of the film thickness. The blow-up is preceeded by a succession of coalescence between adjacent travelling waves. We think the local coalescence of humps in an extended system induces a local increase of the flow rate that locally "pushes" the system beyond the blow-up boundary in the stability diagram of figure 2.6. In conclusion, special care has to be taken since

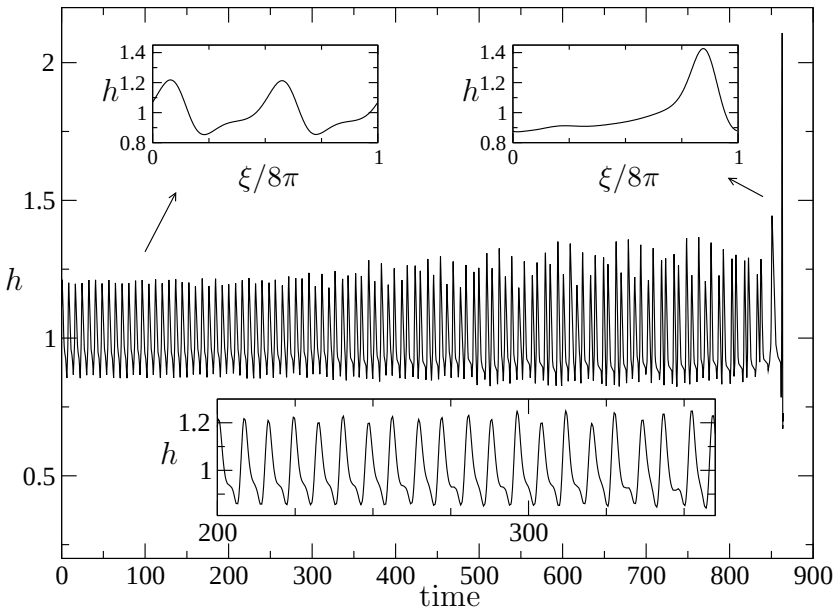

Figure 2.11: Time simulation starting from two periods of a stationary solution of the Benney equation for $\mathcal{R} = 1.5$ and $k = 0.5$, put into a domain of size 8π. A noise of amplitude 10^{-3} is added at $t = 0$. The main plot represents the time series of the film thickness recorded at the point $\xi = 7\pi$. The upper insets show, respectively, the two travelling waves at $t \approx 100$ and the coalesced wave at $t \approx 850$. The lower inset gives a zoom on a part of the time series showing oscillatory mode.

blow-up of travelling waves may occur even slightly before the blow-up boundary.
To conclude, one of the advantages of the Benney equation is to describe with a single evolution equation the different physical effects in a falling film, namely in our case, viscosity, gravity, surface tension and thermocapillarity. We believe this ensures that the Benney equation will remain a helpful model to study thin film flows, especially to identify new phenomena but also in a limited parameter range for quantitative predictions. Actually, many other effects may be added to the Benney equation like evaporation [53], Van der Waals force [134], chemical reaction [139], topographic effects [66], non-uniform heating [87, 64, 120], etc. The validity of the Benney equation should in the future also be addressed including these additional effects.
The weighted integral boundary layer model used in this chapter as the reference model does not suffer any singularity and can be accurate for larger Reynolds number than the Benney equation [109, 110]. Furthermore, the study of stationary solutions with the WIBL model does not require much supplementary effort than the BE. So although for the ranges of validity defined in this chapter, the BE can be used safely, the WIBL represent a promising alternative. This will be the purpose of the second part of this work. However, before that, the two following chapters will be dedicated to the study of non-uniform heating, still using the BE inside its range of validity.

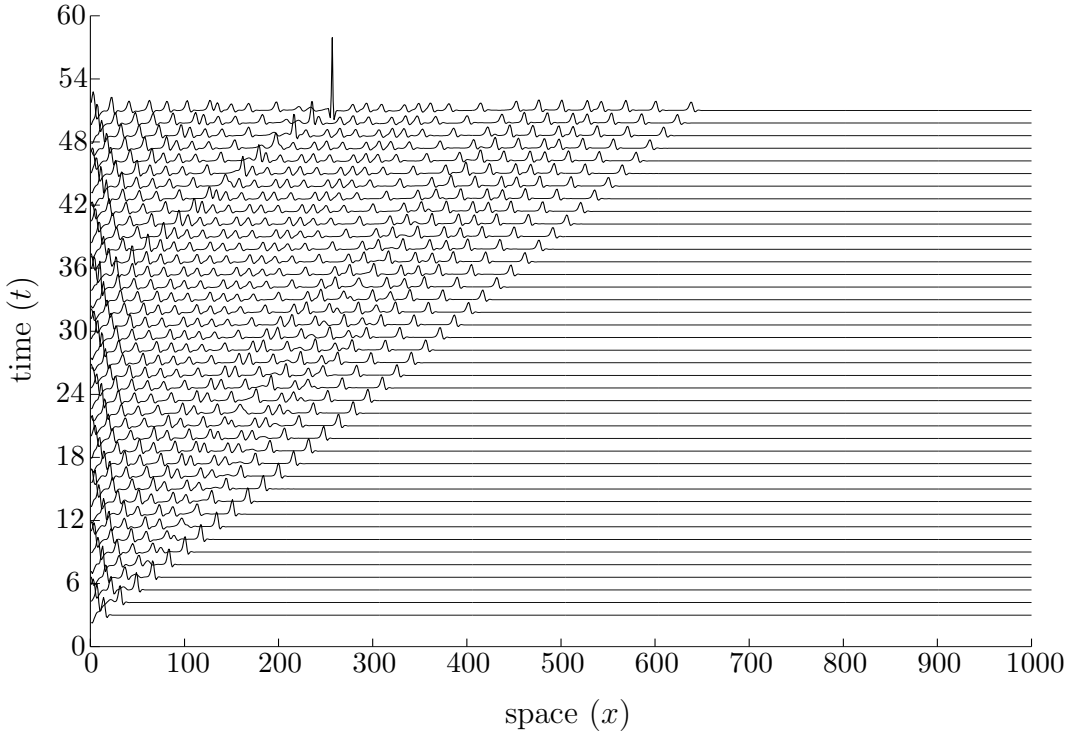

Figure 2.12: Space-time plot showing the evolution of a solution of the Benney equation (2.34) for $\mathcal{R} = 0.9$ in the vertical and isothermal case, *i.e.* $\mathcal{C} = \mathcal{M} = 0$. The film thickness is plotted at regular time intervals. The flow is oriented from left to right. A periodic forcing with noise is imposed at $x = 0$. Courtesy of Ruyer-Quil [107].

Chapter 3

Periodic heating

The present chapter focuses on the evolution of a thin liquid film flowing down an inclined plate along which a periodic array of heaters is embedded. Since it induces perturbations that may remain steady in the laboratory reference frame, we may expect new phenomena triggered by the presence of two frequencies, the one originating from the wave instability and the one corresponding to a periodic array of heaters. The Marangoni effect acts on two levels: on the dispersion and amplification of the travelling waves as for the uniform heating case and on the amplitude of the steady-state deformations induced by the non-uniformities. The coupling between such travelling waves and steady-state deformations causes a variety of nonlinear phenomena, such as oscillatory, quasi-periodic or chaotic regimes depending on the amplitude of the imposed temperature gradient. If this latter is high enough, we may even expect a total suppression of the wave instability, as seen in this chapter.

It can be mentioned here that in industrial applications, one generally uses topography changes to create region of thinning that can enhance the heat transfer. Our aim here, as initially proposed by Kabov [57], is to propose an alternative to topographical obstacles with "thermal obstacles", which can lead to similar heat transfer enhancement.

After a brief presentation of the evolution equation accounting for a non-uniform heating (§3.1), stationary solutions of this equation are calculated either in a moving reference frame in the case of uniform heating or in a fixed reference frame in the case of non-uniform heating (§3.2). The first case allows for travelling wave solutions, as in chapter 2, while the second one gives steady-state deformations. To describe the full dynamics of the film, we solve numerically the two-dimensional evolution equation using the Newton-Kantorovich method (§3.3). The periodic temperature distribution at the plate is chosen to be sinusoidal and the resulting dynamics is compared to the case of a uniform heating with the same average temperature. Finally, we estimate the enhancement of the heat transfer due to the presence of steady-state deformations (§3.4).

3.1 Non-uniform heating

Tan *et al.* [134] examined the steady thermocapillary flow in thin liquid layers on a non-uniformly heated horizontal plate. They showed that a continuous steady profile of the liquid layer can be sustained depending on the sign of the Van der Waals (VdW) forces. Indeed, in their analysis, for very thin film, VdW forces may either lead to spontaneous film rupture, or at the contrary prevent the occurrence of any dry spot at the microscopic scale, depending on the attractive or repulsive character of this force, hence on the nature of liquid and substrate. Small perturbations of uniform heating and their effect on the dynamics of the film were also studied by Van Hook *et al.* [141] for a horizontal layer ($\beta = 0$). They showed that non-uniformity in heating produces a steady-state deformation for any temperature difference across the layer. This steady-state deformation becomes unstable to the long-wavelength instability for smaller Marangoni number than in the absence of non-uniformity. Moreover, the non-uniformity of the plate temperature determines the location of the dry spot and the elevated region to form at the minimum and maximum of the steady-state deformation, respectively. This should not be true anymore when the plate is inclined since the long-wave instability results in travelling waves instead of steady patterns. To our knowledge, few theoretical studies exist about non-uniformly heated falling films (see *e.g.* Marchuk & Kabov [85]), and actually none on periodic heating. Miladinova *et al.* [87, 88] considered the effect of a constant temperature gradient imposed at the plate for an adiabatic liquid-gas interface ($\mathrm{Bi} = 0$) and high Marangoni number. They studied the influence of thermocapillarity on the amplitudes and phase speeds of surface waves resulting from instability and found from linear analysis that a weak increase in heating along the flow direction produces a decrease in the stability threshold, while a decrease of the temperature plays a stabilizing role. In the nonlinear regime, they found finite-amplitude waves, the shape of which depends mostly on the mean flow velocity, while the amplitude itself is influenced by the thermocapillarity.

In the case of an horizontal layer, Or *et al.* [94] found a way to damp out the long-wavelength disturbances by applying a feedback control to the temperature at the substrate. In the same manner, for an inclined layer, we may expect that the non-uniform heating can modify or even kill the wave instability. Analogous works about non-uniform boundary conditions have been reported in literature, *e.g.* in the case of a vertical plate periodically oscillating in its own plane. Oron & Gottlieb [96] found that periodic planar boundary excitation does not alter the fundamental unforced bifurcation structure and the spatial topological structure of the interfacial waves. The film evolution as described by their temporally modulated Benney equation is found to result in mostly quasiperiodic tori complemented by several types of strange attractors. Oron & Gottlieb found that an increase of either the amplitude or the frequency of wall oscillation results in significant decrease of the peak-to-trough size of interfacial waves. Lin & Jiang [80] have further elucidated the physical mechanism of stabilizing an inherently unstable vertical film flow by use of plate oscillations. This was done in the case of very viscous thin films (of thickness of order 100 μm and $\mathrm{Re} = 0.03$) for which the mechanical energy dissipation is increased several times when the plate is oscillated appropriately. Interestingly, in the window of two-

dimensional wave suppression, Lin & Jiang found that the work done by the Reynolds stress tensor enhanced by plate oscillation may cause a falling liquid film, which is stable with respect to two-dimensional waves, to become unstable with respect to three-dimensional disturbances, violating the Squire's theorem.
Let us now turn to a thin liquid film falling down a planar plate maintained at the non-uniform temperature $T_{\mathrm{w}}(x)$ with $\hat{T}_{\mathrm{w}}$ the average plate temperature (see figure 3.1). We focus on the two-dimensional problem considering only the temperature condition

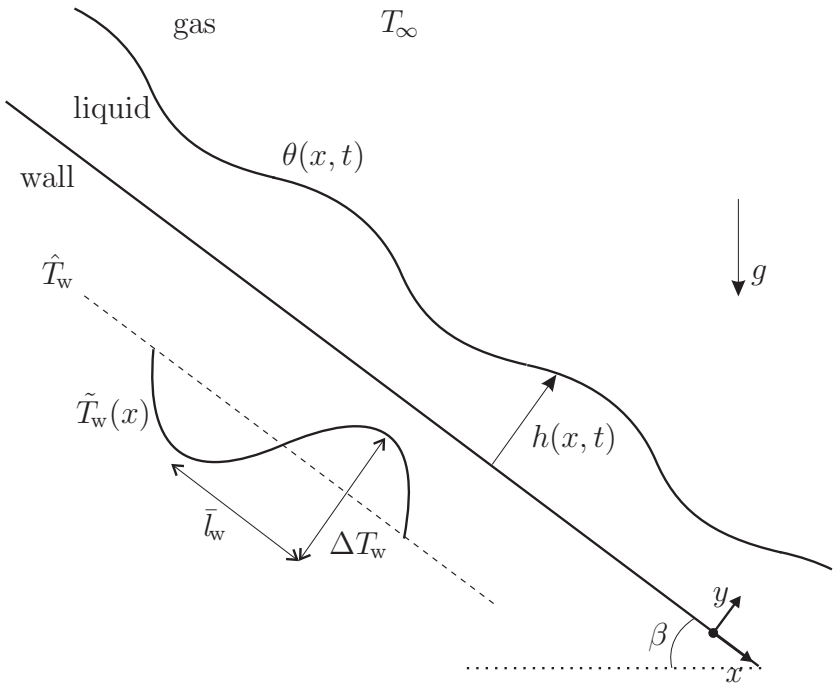

Figure 3.1: Sketch of a falling film in the case of a sinusoidal temperature distribution $T_{\mathrm{w}}(x)$ imposed at the wall with its average component $\hat{T}_{\mathrm{w}}$ and its non-uniform component $\tilde{T}_{\mathrm{w}}(x)$. ΔT_{w} is the characteristic temperature difference applied along the length $\bar{l}_{\mathrm{w}}$. $\theta(x,t)$ is the film surface temperature.

(TC). In this problem, a second characteristic temperature difference applies along the wall on a characteristic distance $\bar{l}_{\mathrm{w}}$, and is defined as

$$\Delta T_{\mathrm{w}} = T_{\mathrm{wmax}} - T_{\mathrm{wmin}}. \tag{3.1}$$

The ratio between the two characteristic temperature differences along the wall and across the layer yields the control parameter for non-uniformities and reads

$$\delta_{\mathrm{w}} = \frac{\Delta T_{\mathrm{w}}}{\Delta T}. \tag{3.2}$$

The dimensionless non-uniform component of the temperature distribution at the wall in (1.23a) then becomes

$$F_{\mathrm{w}}(x) = \frac{\tilde{T}_{\mathrm{w}}(x)}{\Delta T} = \delta_{\mathrm{w}} f(x), \tag{3.3}$$

where $f(x)$ is a continuous function with values in the interval $[-\frac{1}{2}, \frac{1}{2}]$. The zeroth-order solution (2.5a) for the film surface temperature combined with (3.3) becomes

$$\theta^{(0)}(x,t) = \frac{1+\delta_{\rm w} f(x)}{1+{\rm Bi}h(x,t)}. \tag{3.4}$$

Substituting $\theta^{(0)}$ into the Benney equation (2.10) by considering the two-dimensional case ($\partial_z = 0$) yields

$$\partial_t h + h^2\partial_x h + \frac{2}{15}\partial_x(h^6\partial_x h) + \partial_x\left[{\rm Ka}\frac{h^3}{3}\partial_{xxx}h - {\rm Ct}\frac{h^3}{3}\partial_x h \right.$$
$$\left. +{\rm BiMa}\frac{h^2}{2}\frac{(1+\delta_{\rm w} f)\partial_x h}{(1+{\rm Bi}h)^2} - \delta_{\rm w}{\rm Ma}\frac{h^2}{2}\frac{\partial_x f}{1+{\rm Bi}h}\right] = 0, \tag{3.5}$$

The two last terms of (3.5) show that thermocapillarity can act in two different ways. The first one is due to perturbations of the interface temperature induced by variations of h, when heat transfer to the gas phase takes place (${\rm Bi} \neq 0$). The second one is due to the non-uniformity of the heating conditions applied at the plate and, as it will be shown below, can lead the film surface to steady-state deformations. The main purpose of the present chapter is to investigate the effect of coupling between these two mechanisms, both arising from a non-uniformity of the interface temperature.
Note that cancelling $\delta_{\rm w}$ reduces (3.5) to the Benney equation with uniform heating already studied in chapter 2. In the following, the temperature distribution at the wall is chosen sinusoidal as

$$f(x) = \frac{1}{2}\sin\left(\frac{2\pi n_{\rm w} x}{L_x}\right) = \frac{1}{2}\sin\left(\frac{\pi x}{l_{\rm w}}\right) \tag{3.6}$$

where $n_{\rm w}$ is the number of 'temperature wave' in the periodic domain L_x, and

$$l_{\rm w} = \frac{L_x}{2n_{\rm w}} \tag{3.7}$$

is the distance along which the temperature difference $\Delta T_{\rm w}$ is imposed at the wall. With the use of $f(x)$, the last term of (3.5) brings in a new Marangoni number defined as followed,

$${\rm Ma_w} = \frac{\delta_{\rm w}{\rm Ma}}{l_{\rm w}} = \frac{\gamma\left(\Delta T_{\rm w}/\bar{l}_{\rm w}\right) l_\nu^2}{\rho\nu^2}, \tag{3.8}$$

which represents the relevant parameter for non-uniform heating since it involves the characteristic temperature gradient imposed along the wall, *i.e.* $\Delta T_{\rm w}/\bar{l}_{\rm w}$.
Figure 3.2 displays different cases as controlled by the parameter $\delta_{\rm w}$. Small perturbations of a uniform heating, i.e. for $\delta_{\rm w} \ll 2$, were already studied by Van Hook *et al.* [141] in the different context of a horizontal layer. The difference between the horizontal and inclined heated layers is profound (see §2.6.3), since in the latter case the mean flow can prevent the inherent tendency of dry spot formation and allow steady-state deformations of much higher amplitude, arising from the application of a non-uniform heating. When $\delta_{\rm w} > 2$, a section of the whole domain is cooled below the

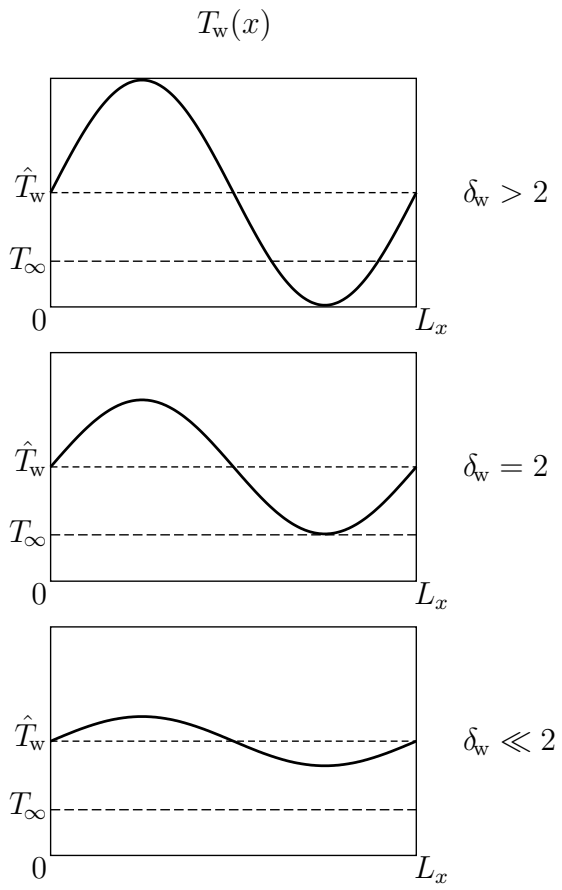

Figure 3.2: Balance between uniform and non-uniform heating as controlled by the parameter δ_w. The temperature distribution at the wall is given by (3.6) with $n_\mathrm{w} = 1$.

ambient temperature T_∞, while the remaining of the domain remains heated. When $\delta_\mathrm{w} = 2$, the minimum of the imposed temperature fits with ambient air temperature T_∞. The remaining of this chapter will focus on this latter case in order to illustrate the coupling between the two thermocapillary mechanisms when the two characteristic temperature differences, ΔT and ΔT_w, are of the same order of magnitude.

3.2 Stationary solutions

Along with the numerical study of the spatio-temporal dynamics of the film, as described by (3.5) and presented in §3.3, we investigate stationary states of the system. In the case of a uniform heating, one can find stationary solutions in the reference frame moving downstream with the phase speed of travelling waves. In the case of a non-uniform heating, the x-dependent temperature distribution imposed at the wall does not allow to seek for travelling waves straightforwardly, because it breaks the translational invariance of the problem. Therefore, we need to split the analysis and to look for stationary solutions either in a moving reference frame with a uniform heating or in the fixed reference frame with a non-uniform heating.

3.2.1 Moving reference frame - Uniform heating

We first seek for stationary solutions of (3.5) with $\delta_w = 0$ in the reference frame moving downstream at a certain velocity c, as already performed in §2.3, that is by introducing $h(x,t) = h(\xi)$ with $\xi = x - ct$. The closed flow condition is enforced (see §2.4). Figure 3.3 presents several stationary wave solutions in the $[h_N k, \mathrm{Ma}]-$plane. The

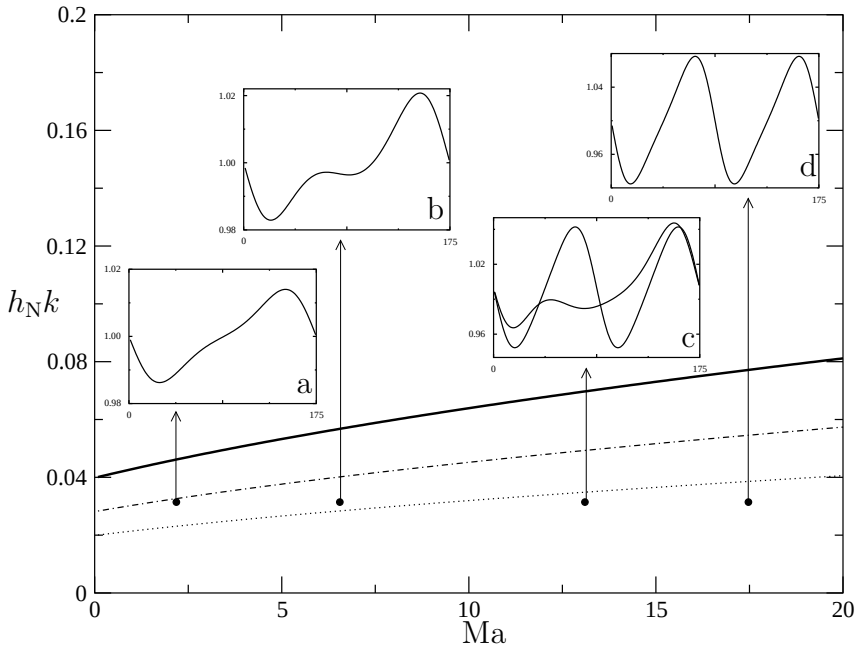

Figure 3.3: Wavenumber of disturbances versus the Marangoni number in the case of uniform heated vertical wall for Re = 0.5, Ka = 497 and Bi = 0.087. The solid line represents the cut-off wavenumber k_c, the dot-dashed line $k = k_c/\sqrt{2}$ represents the most amplified linear mode and the dotted line $k = k_c/2$ is the limit below which the second harmonic mode becomes linearly unstable. The insets display the travelling waves calculated for the fundamental wavenumber $k_1 = 2\pi/175$ and various values of Ma: (a) 2.2, (b) 6.6, (c) 13.1 and (d) 17.5. The phase speeds c/c_L for these solutions are, respectively, 1.0001, 1.0043, [0.9989;1.0217] and 0.9981.

parameters are fixed to Re = 0.5, Ka = 497 and Bi = 0.087 (see tables of parameters in appendix C). The stationary wave solutions are presented for the fundamental wavenumber $k_1 = 2\pi/L_x$ in the domain of fixed size $L_x = 175$. By increasing Ma one observes the change of the solution shape from one hump at Ma = 2.2 (a), to two humps at Ma = 17.5 (d), going through the development of a small amplitude secondary hump at Ma = 6.6 (b) and the coexistence between one and two-humped waves at Ma = 13.1 (c). Indeed, in this latter case, two stationary wave solutions are found to yield an oscillatory regime between the one-humped solution obtained by continuation from a single wave at k_c, and the two-humped solution obtained by continuation from a double wave at $k_c/2$. The phase speed c increases from its critical value for a single humped wave and decreases for a two-humped wave.
Figure 3.4 shows the wave amplitude peak-to-trough $A = (h_{\max} - h_{\min})/h_N$ versus Ma

for the interfacial waves with one and two humps, labeled as "1" and "2", respectively. The slight fold of the curve "1" at Ma ≈ 6.38 indicates the appearance of a secondary

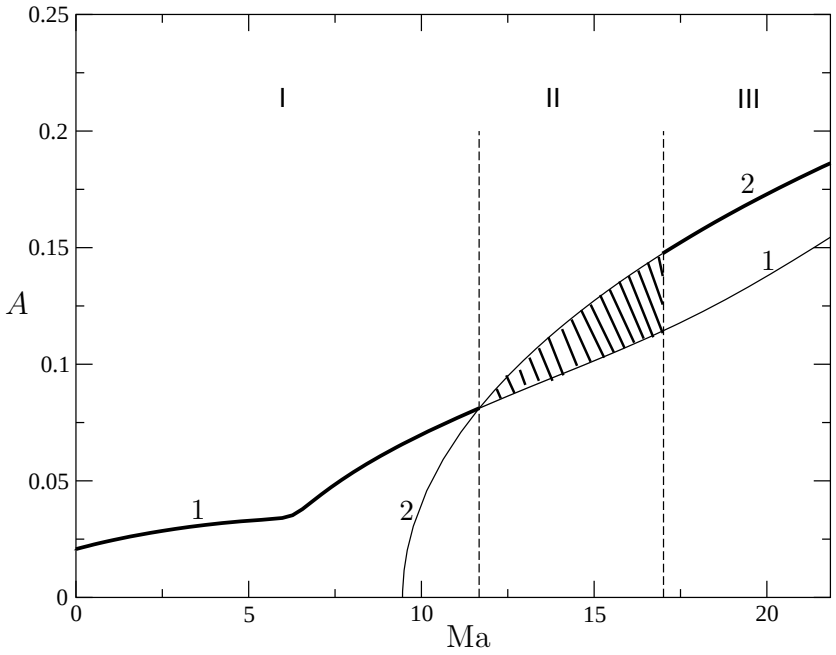

Figure 3.4: Diagram displaying the wave amplitude $A = (h_{\max} - h_{\min})/h_{\mathrm{N}}$ versus the Marangoni number Ma for the same parameters as for figure 3.3. The line labeled "1" corresponds to a one-humped wave solution with the fundamental wavenumber $k_1 = 2\pi/175$, and the one labeled "2" corresponds to a two-humped interfacial wave, i.e. $k_2 = 4\pi/175$. The thick lines indicate that the solution is stable, thin lines that it is unstable, while the dashed area corresponds to oscillatory mode.

small amplitude hump, as seen in figure 3.3b. The curve "2" emerges at Ma $= 9.45$, where the second mode $k_2 = 2k_1$ loses its linear stability. The stability of the solutions corresponding to the curves "1" and "2" was determined by solving the evolution equation (3.5), see §3.3. Three different zones are delineated in figure 3.4: in zone I, the thick solid line represents stable one-humped solutions (see figures 3.3a, 3.3b), in zone II for Ma > 12.1 the two solution branches coexist and compete inside the dashed area (see figure 3.3c), while in zone III for Ma > 16.8 the two-humped solution becomes stable (see figure 3.3d). The transitions I-II and II-III were determined by convergence of numerical time integrations (see §3.3) and with an accuracy of 10^{-1} on the Marangoni number.

3.2.2 Fixed reference frame - Non-uniform heating

The dynamical system in this case is obtained by recasting (3.5) into the set of differential equations

$$\begin{aligned} U_1' &= U_2 \\ U_2' &= U_3 \\ U_3' &= \frac{1}{\mathrm{Ka}}\left(\frac{3}{U_1^3}Q - 1 - \frac{2}{5}U_1^3U_2 + \mathrm{Ct}U_2 - \frac{3}{2}\frac{\mathrm{BiMa}(1+\delta_\mathrm{w}f)U_2}{U_1(1+\mathrm{Bi}U_1)^2} + \frac{3}{2}\frac{\delta_\mathrm{w}\mathrm{Ma}f'}{U_1(1+\mathrm{Bi}U_1)}\right), \end{aligned} \tag{3.9}$$

where the prime denotes here derivative with respect to x. The stationary solutions of the dynamical system (3.9) are calculated using the same method as in §2.3, but now in the fixed reference frame. Therefore, they describe steady-state deformations of the film surface. The size of the domain is chosen to match with an integer n_w of wavelengths corresponding to the function f. We start here the continuation search with a non-perturbed flat film, enforcing the boundary conditions $h = h_\mathrm{N}$, $h' \to 0$, $h''' \to 0$ and $f' \to 0$ and determine the value of the integration constant as $Q = h_\mathrm{N}^3/3$. The solutions obtained with (3.6) in a fixed frame of reference will be presented below in §3.3 and compared to the results of the time-dependent calculations based on (3.5), see for instance figure 3.8.

3.3 2D computations

In this section we study the spatiotemporal dynamics of the falling liquid film, as governed by the evolution equation (3.5) amended with periodic temperature distribution and boundary conditions in the domain $0 \le x \le L_x$. The cases of uniform and non-uniform heating will be separately studied in the framework of (3.5) and the results will be compared with the stationary solutions computed in §3.2.
The initial condition used in this investigation in the case of a uniform heating is

$$h = h_\mathrm{N}\left[1 + 0.05\cos\left(\frac{2\pi}{L_x}x\right)\right], \tag{3.10}$$

while in the case of a non-uniform heating the initial condition is chosen as

$$h = h_\mathrm{N}. \tag{3.11}$$

In the former case stationary travelling waves are always found, while in the latter, either oscillatory modes or pure steady-state deformations of the film interface may be observed.

3.3.1 Numerical method

The numerical method used here to solve the evolution equation (3.5) is based on the Newton-Kantorovich method, as described by Oron [96]. Equation (3.5) can be written in the form

$$\partial_t h + F(h) = 0, \tag{3.12}$$

where

$$F(h) \equiv \partial_x \left[\frac{h^3}{3}(1 - \mathrm{Ct}\partial_x h + \mathrm{Ka}\partial_{xxx} h) + \frac{2}{15}h^6 \partial_x h - \mathrm{Ma}\frac{h^2}{2}\partial_x \theta^{(0)} \right],$$

provided that both $\theta^{(0)}$ and h are periodic in the given domain. Equation (3.12) is discretized in time using the implicit backward Euler method in the form

$$\frac{h^{(n+1)} - h^{(n)}}{\Delta t} = -F(h^{(n+1)}), \tag{3.13}$$

where Δt is the time step and $h^{(n)}$ is the solution of the evolution equation obtained at the time $t_n = n\Delta t$. The right-hand side of (3.13) is linearized by

$$F(h^{(n+1)}) = F(h^{(n)}) + F_h^{(n)}(h^{(n+1)} - h^{(n)}), \tag{3.14}$$

where $F_h^{(n)}$ is the Frechet differential operator evaluated at the time t_n.
Introducing the difference between the solutions calculated for consecutive times $u \equiv h^{(n+1)} - h^{(n)}$, and using the definition of the Frechet derivative

$$F_h^{(n)} u = \lim_{\varepsilon \to 0} \frac{F(h^{(n)} + \varepsilon u) - F(h^{(n)})}{\varepsilon}, \tag{3.15}$$

(3.13) and (3.14) are combined into

$$(I + \Delta t F_h^{(n)})u = -\Delta t F(h^{(n)}), \tag{3.16}$$

where

$$\begin{aligned} F_h u \;=\; & \partial_x(h^2 u) + \left\{ \frac{2}{15}\partial_x(h^6 \partial_x u + 6h^5 \partial_x h u) + \frac{\mathrm{Ka}}{3}\partial_x \left(h^3 \partial_{xxx} u + 3h^2 u \partial_{xxx} h \right) \right. \\ & \left. -\mathrm{Ma}\partial_x \left(h u \partial_x \theta^{(0)} \right) - \mathrm{BiMa}\partial_x \left[\frac{h^2}{2}\partial_x \left(\frac{u\theta^{(0)}}{1 + \mathrm{Bi}h} \right) \right] \right\}, \end{aligned}$$

I is the identity operator and $\theta^{(0)}$ is given by (3.4) in the case of a temperature condition at the wall. Equation (3.16) constitutes a linear differential equation in terms of the variable $u(x,t)$. Discretization of $F(h)$ and F_h are both carried out using a central difference scheme and linear interpolation for half-nodes accurate to $\mathcal{O}(\Delta x^2)$, where Δx is the spatial step. N_x denotes the number of grid-points in the spatial domain. Furthermore, the conservative forms (*i.e.* ∂_x in front of all terms in $F(h)$ and F_h) have been proven to have better convergence properties [47]. Since we impose periodic boundaries, the closed flow condition is naturally enforced (see §2.4). The sets of simultaneous linear algebraic equations resulting from the discretization of (3.16) are solved at each step directly for $u \equiv u_j$ $(j = 1, ...N_x)$ using the *generalized Thomas algorithm* [34] applied to the pentadiagonal* sets with three corner elements

*Because of the third-order derivatives that need five mesh points to be discretized at second-order.

that arise due to spatial periodicity. The computations were typically performed with $N_x = 500$ to 1000 grid points to ensure spatial convergence of the solutions.
As already mentioned, the results are presented for fixed parameter values $\mathrm{Re} = 0.5$, $\mathrm{Ka} = 497$, $\mathrm{Bi} = 0.087$ and $\delta_{\mathrm{w}} = 2$. These values are calculated from the material properties of a 25% ethyl-alcohol aqueous solution in water given in Table C.2. Furthermore, we arbitrarily consider a moderate heat transfer coefficient of $\alpha = 500W/m^2K$ and fix the mean film thickness to $\bar{h}_{\mathrm{N}} = 100\mu m$.
The computations are carried out for a sinusoidal temperature distribution given by (3.6), focusing primarily on the influence of the imposed temperature gradient by varying Ma and n_{w} (the number of periods of the temperature distribution in the domain). Next, the influence of the average temperature on the dynamics is studied by varying the value of the parameter δ_{w}. The results are compared to those obtained in the case of a uniform heating by using (3.5) in the limit of $\delta_{\mathrm{w}} \to 0$ and with (3.10) as the initial condition. We found that no noticeable differences were observed when other initial conditions, such as a random perturbation of the flat film $h \equiv h_{\mathrm{N}}$, were employed.

3.3.2 Influence of the imposed temperature gradient

Figure 3.5 shows the early stage of the evolution of the film thickness in the case of one "temperature wave" ($n_{\mathrm{w}} = 1$) imposed at the wall for $\mathrm{Ma} = 2.2$. The evolution is presented over one period characterized by the time $t_{\mathrm{L}} = L_x/c_{\mathrm{L}}$, where c_{L} is the phase speed of interfacial waves given by (2.18). The flat film is deformed first by the thermocapillary stress that induces a flow from a hotter point to a colder one. This flow creates a trough in the left half of the domain and a crest in the right half of the domain, as shown in figure 3.5a. This deformation is then advected by the flow as shown in figure 3.5b, and grows quickly to reach its maximum at $t \approx t_{\mathrm{L}}/2$, as indicated by the thick long-dashed curve. This quick increase of the amplitude occurs when the phase of the travelling wave matches that of the steady-state deformation. Further, the wave disintegrates into two waves and its amplitude significantly reduces until reaching its minimum at $t \approx t_{\mathrm{L}}$, as shown by the thick dotted curve. Overall, one observes that the travelling wave is modulated by a well-defined envelope. The presence of this envelope is the direct consequence of the periodic temperature profile imposed at the wall. Figure 3.6a shows that an oscillatory regime is reached in the long time limit. Again a sequence of events of total duration t_{L} is displayed and clearly shows the presence of a steady-state envelope.
The fixed stationary solution calculated from the dynamical system (3.9) is also displayed in figure 3.6a. It appears to be in the middle of the above-mentioned envelope (dotted line). Figure 3.6b shows the corresponding evolution in the case of a uniform heating ($\delta_{\mathrm{w}} = 0$) giving rise to a travelling wave. This travelling wave was also calculated as a stationary solution in the moving frame of reference from the dynamical system (2.23) (dotted line). The phase space portraits in both cases of uniform and non-uniform heating, shown in figure 3.6c, demonstrate the similarity between the two waves and suggest that for small non-uniformities of the temperature profile, the

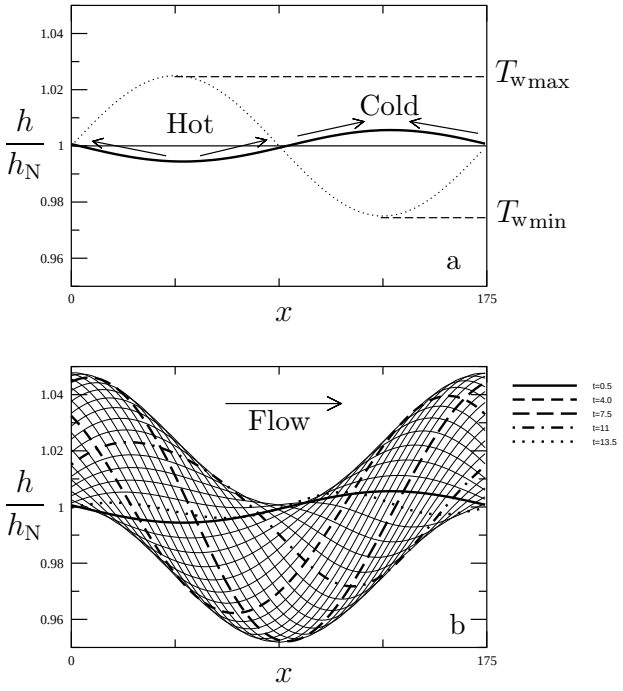

Figure 3.5: Film evolution at the outset as described by (3.5) for Ma = 2.2, $\delta_{\rm w} = 2$, Re = 0.5, Ka = 497, Bi = 0.087 and $L_x = 175$. (a) Deformed film surface from the flat film at time $t = 0.5h_{\rm N}$ (thick line). The location of the temperature distribution is also drawn (dotted line). (b) Evolution of the film surface at the early stage from $t = 0.5h_{\rm N}$ to $t = 13.5h_{\rm N}$ shown with increments of $0.5h_{\rm N}$. The factor $h_{\rm N} = 1.147$ here is used for convenience to handle with rounded-off numbers. The time scale is still the one of the *natural set*, namely l_ν.

oscillatory mode can be expressed as

$$h_{\rm s}(x,t) \approx h_1(x) + h_2(x - ct) - h_{\rm N}, \tag{3.17}$$

representing a superposition of the fixed and travelling stationary waves, h_1 and h_2, respectively. Figure 3.6d demonstrates an excellent agreement between the superposition of the two above-mentioned stationary solutions and the wave computed with time-dependent simulations (solid line).
This superposition is found to be valid for sufficiently small Marangoni number however. Figure 3.7a presents the modulated wave, i.e. the oscillatory regime, obtained for Ma = 6.6, $n_{\rm w} = 1$ and $\delta_{\rm w} = 2$, while figure 3.7b shows the corresponding case of a uniformly heated wall for $\delta_{\rm w} = 0$. The apparently thick line region in both cases is the locus of the fold between two humps already mentioned above (see figure 3.3b). This reflects the fact that in these conditions the wave preserves its characteristics, whatever is the temperature gradient applied at the wall. Nevertheless, the phase space portrait shown in figure 3.7c now exhibits some differences which reveal the non-exactness of the superposition of h_1 and h_2 in (3.17). When $n_{\rm w} = 2$, i.e. the strength of the imposed temperature gradient is doubled, the film surface becomes steady (fixed point in the phase plane) instead of a propagating wave (limit cycle),

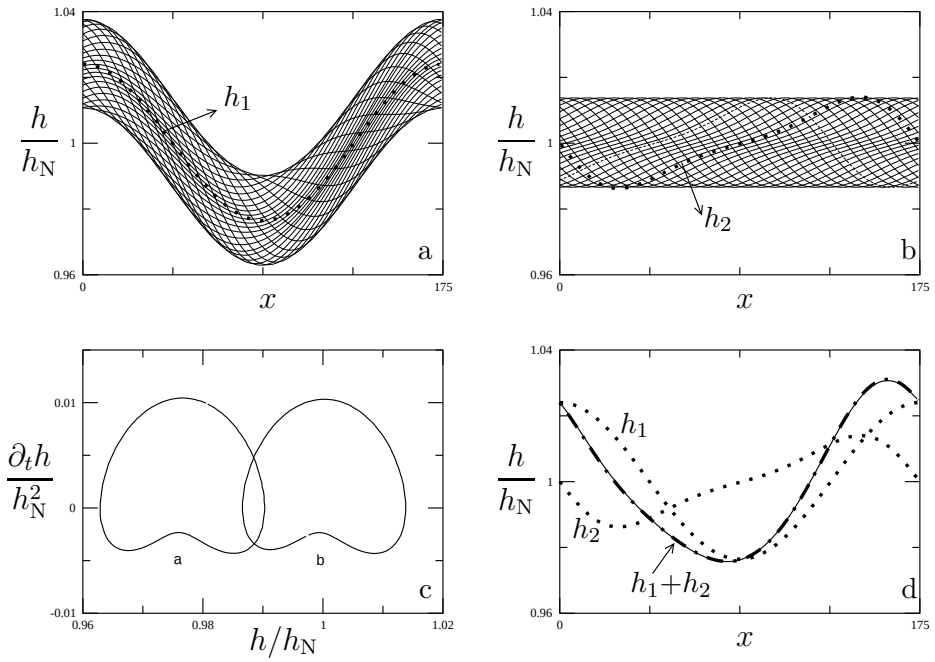

Figure 3.6: Film evolution at steady-state as described by (3.5) for $\mathrm{Ma} = 2.2$, $\delta_\mathrm{w} = 2$, $\mathrm{Re} = 0.5$, $\mathrm{Ka} = 497$, $\mathrm{Bi} = 0.087$ and $L_x = 175$. (a) Oscillatory mode from $t = 3486.5h_\mathrm{N}$ (dashed line) to $t = 3500h_\mathrm{N}$ shown with increments of $0.5h_\mathrm{N}$. (b) Same as (a) but for a uniform heating, $\delta_\mathrm{w} = 0$. (c) The evolution of the cases shown in (a) and (b) at the fixed location $x = L_x/2$ projected onto the phase plane. (d) Superposition of stationary solutions (dot-dashed line) that almost coincides with the computed steady-state solution for $t = 3498h_\mathrm{N}$ (solid line).

as depicted by figure 3.7d. This result suggests that a sufficiently strong temperature gradient along the wall can suppress the wave instability. Figure 3.8 displays a comparison between the cases of a steady film surface obtained from numerical solution of (3.5) (solid line) and the stationary solution calculated in the fixed frame of reference using the dynamical system (3.9) (dashed line). The excellent agreement evident from figure 3.8 provides also a verification of our numerics, since the solutions were calculated by two totally different numerical methods. It is found by comparing graphs in figure 3.8, that the amplitude of the emerging wave is approximately proportional to the value of the imposed temperature gradient along the wall. This can be made explicit by taking the limit of small Biot number ($\mathrm{Bi} \ll 1$) and small deformations of the film surface, which implies also $f' \ll 1$. Indeed, under those conditions, (3.5) has an approximated steady-state solution of the form

$$h \approx h_\mathrm{N} + \frac{1}{2}\delta_\mathrm{w}\mathrm{Ma}f' = h_\mathrm{N} + \frac{\pi}{2}\mathrm{Ma}_\mathrm{w}\cos\left(\frac{\pi x}{l_\mathrm{w}}\right), \tag{3.18}$$

where (3.6) and (3.8) have been used. The value of Ma_w in figure 3.8 varies from 0.1 (a) to 1.2 (e) and is directly proportional to $n_\mathrm{w}\mathrm{Ma}$. The amplitude of the steady-state deformations follows this rule with an excellent agreement. Nevertheless, the departure from the sinusoidal shape is observed in figure 3.8e through the slight

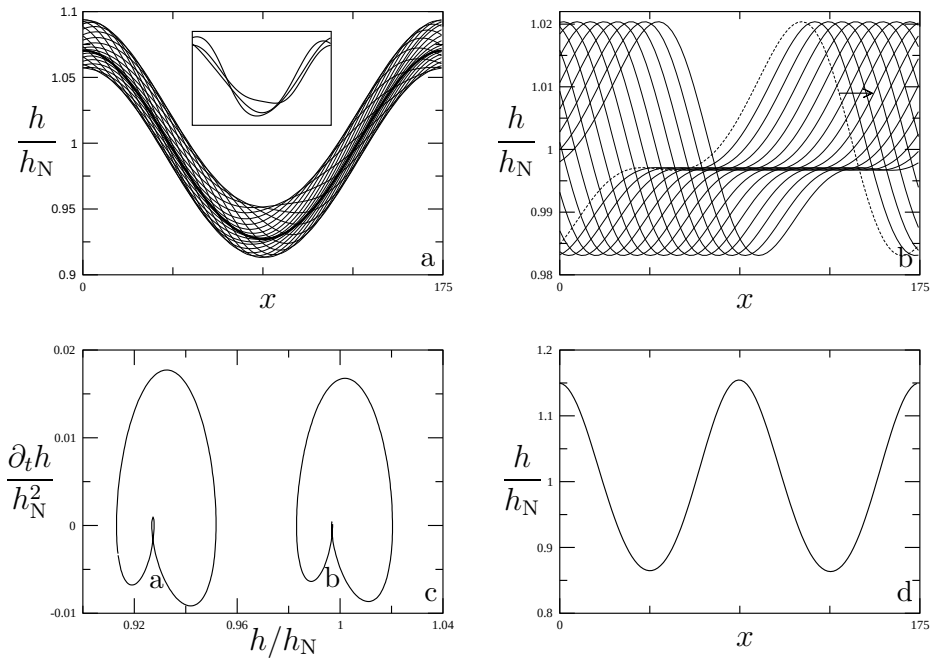

Figure 3.7: The film evolution at steady-state as described by (3.5) for Ma = 6.6, $\delta_w = 2$, Re = 0.5, Ka = 497, Bi = 0.087 and $L_x = 175$. (a) Film evolution from $t = 3486.5h_N$ (dashed line) to $t = 3500h_N$ shown by increments of $0.5h_N$. (b) Same as (a) for the case of a uniform wall temperature with $\delta_w = 0$. The arrow indicates the direction of propagation. (c) Phase plane portraits corresponding to (a) and (b) at the location $x = L_x/2$. (d) Same as (a) for the case of two "temperature waves", $n_w = 2$. In this case the deformation of the interface is steady in time (no oscillations).

asymmetry of the troughs. This is a clear manifestation of nonlinearities neglected in (3.18).

Figure 3.9 presents the film evolution for Ma = 17.5 that corresponds to the case of a uniform heating with $\delta_w = 0$ belonging to the zone III in figure 3.4. Hence the emergence of a two-humped travelling wave is expected, as shown in figure 3.9b. This two-humped wave persists when the wall temperature is non-uniform (figure 3.9a). However, the phase velocity slightly decreases by 1.3% with respect to the case of a uniform heating, as if the presence of the steady-state deformation induced a slowdown of the wave propagation. This effect is even more pronounced for larger temperature gradients, actually, the phase velocity decreases by 5.3% when $n_w = 2$, see figure 3.9c. Finally, the propagation becomes quasi-periodic when $n_w = 4$ (figure 3.9d). These evolutions are summarized in the phase plane portraits presented in figure 3.9e where (a,b,c) corresponds to limit cycle and (d) to a quasi-periodic behaviour (see figure 3.10). The time series of the film thickness recorded in the middle of the periodic domain $x = L_x/2$ are plotted in figures 3.10a and 3.10c and correspond to the cases presented in figure 3.7 for Ma = 6.6 and figure 3.9 for Ma = 17.5, respectively. These cases belong to zones I and III in figure 3.4. The time series are marked by the number of temperature waves n_w and by "0" for the case of a uniform

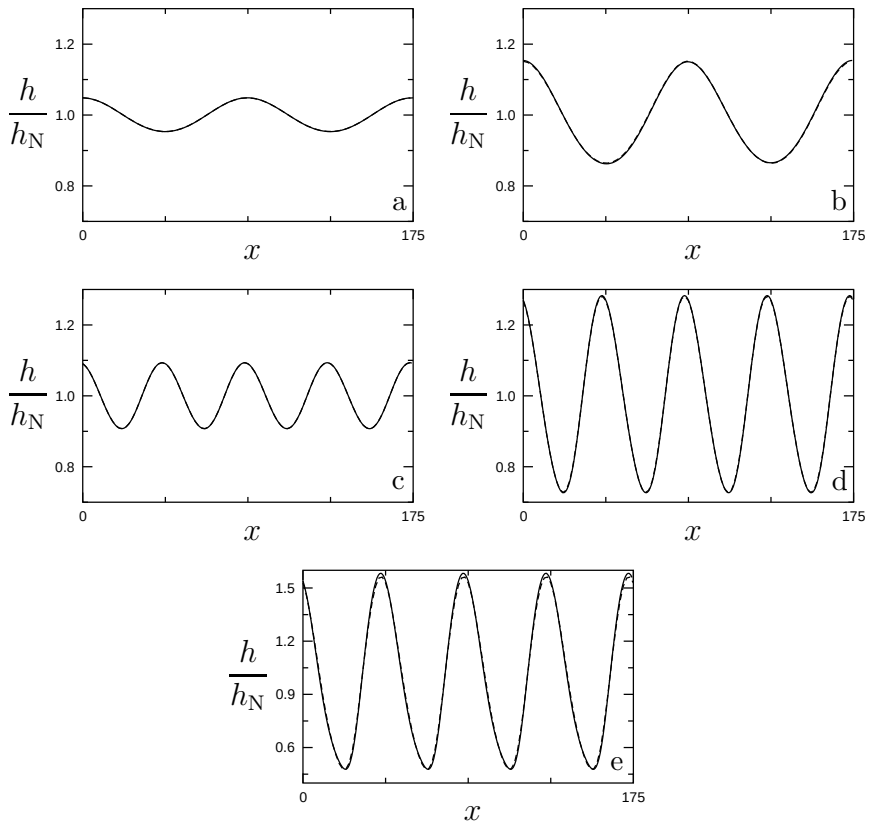

Figure 3.8: Steady solutions obtained by time integration (solid lines) and stationary solutions calculated in the fixed reference frame from the dynamical system (3.9) (dashed lines). The parameter values are $L_x = 175$, $\delta_w = 2$, Re $= 0.5$, Ka $= 497$ and Bi $= 0.087$. (a) Ma $= 2.2$, $n_w = 2$; (b) Ma $= 6.6$, $n_w = 2$; (c) Ma $= 2.2$, $n_w = 4$; (d) Ma $= 6.6$, $n_w = 4$; (e) Ma $= 13.1$, $n_w = 4$.

heating on the right side of each plot. Figure 3.10b shows the modulated time series for Ma $= 13.1$ corresponding to zone II in figure 3.4, where the film surface oscillates between two competing modes. This modulation is sustained for $n_w = 1$, while for $n_w = 2$ the two-humped wave is dominant. In the case of $n_w = 4$ the wavy dynamics of the film surface is even suppressed giving rise to a steady-state deformation.

In summary, the non-uniform heating can affect significantly the wave dynamics (with respect to the uniform heating case) in different ways: (i) by decreasing the phase speed of waves, (ii) by modifying the wave regime, for instance, from oscillatory to stationary waves, or from stationary to quasi-periodic waves, (iii) by suppressing waves. Nevertheless, these conclusions hold in the situation where the temperature differences across the film and along the wall are of the same order of magnitude. The next section will briefly present other situations.

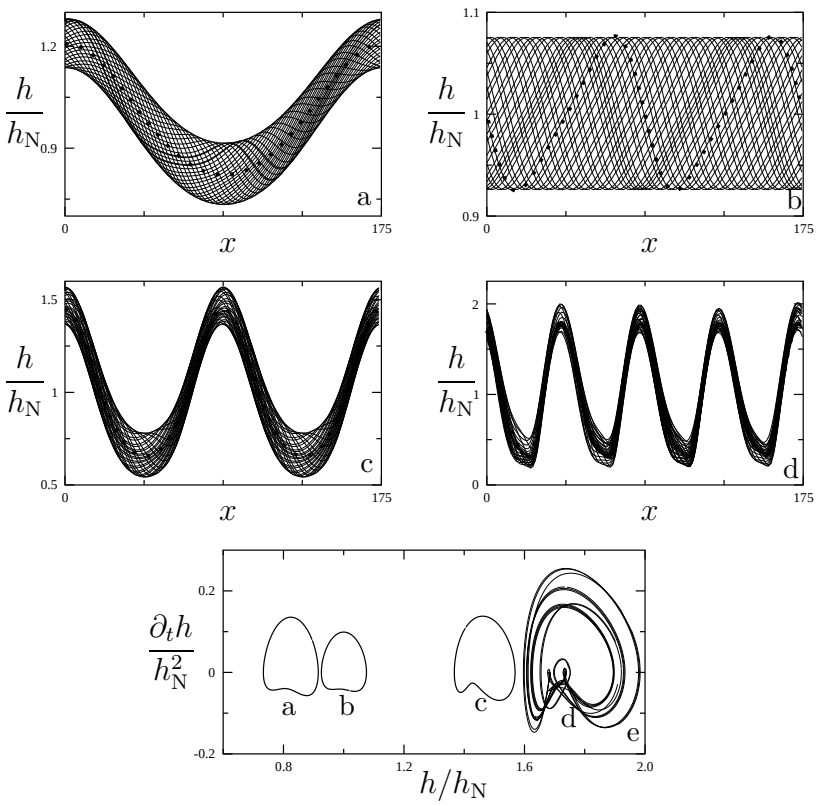

Figure 3.9: The film evolution as described by (3.5) for Ma = 17.5, $\delta_w = 2$, Re = 0.5, Ka = 497 and Bi = 0.087. (a) Film evolution from $t = 3486.5h_N$ (dashed line) to $t = 3500h_N$ shown by increments of $0.5h_N$. The dotted line indicates the corresponding stationary solution calculated in the fixed reference frame. (b) Same as (a) for the case of the uniform wall temperature with $\delta_w = 0$. (c) Same as (a) for the case of two "temperature waves" $n_w = 2$. (d) Same as (a) for the case of four "temperature waves" $n_w = 4$. (e) Phase plane portraits corresponding to (a), (b), (c) and (d) at $x = L_x/2$.

3.3.3 Non-uniform versus uniform heating.

Up to now, the parameter δ_w as given by (3.2) was fixed. Let us explore different cases as classified in figure 3.2. Figure 3.11 displays on the left the envelopes of the surface oscillations and on the right the corresponding time series for Ma = 6.6 and various values of n_w and δ_w (recall that δ_w is the ratio between the temperature drop along the solid wall and the one across the layer). The width of the envelopes decreases when increasing δ_w, showing the damping effect of the non-uniformities on the development of travelling waves. However, changing δ_w does not change the shape of the envelopes that is only determined by n_w (for fixed L_x) and therefore by the steady-state profile calculated in a fixed reference frame (thick dot-dashed line).

Figure 3.11b shows the transition from a one-humped to a two-humped modulated wave with a decrease of δ_w. When the value of n_w is doubled (figure 3.11c-d) a large non-uniformity as compared to the average temperature ($\delta_w = 6.25$) acts in

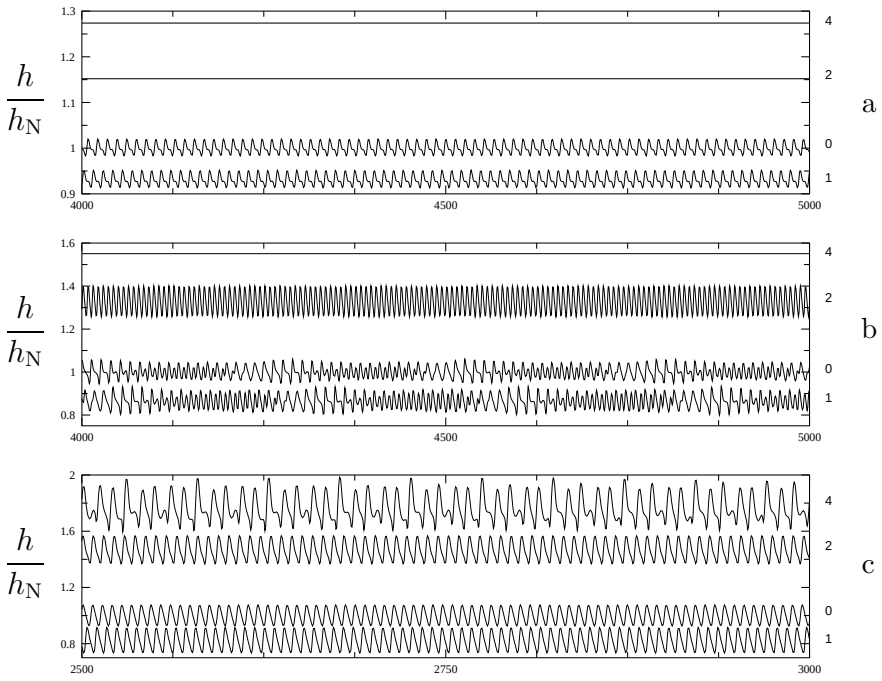

Figure 3.10: Time series of the film thickness at $x = L_x/2$ for $\delta_w = 2$, Re $= 0.5$, Ka $= 497$, Bi $= 0.087$, $L_x = 175$. On the right side of each plot the value of $n_w = 0, 1, 2, 4$ is displayed. Here $n_w = 0$ corresponds to the case of the uniform wall temperature ($\delta_w = 0$). The corresponding Marangoni numbers are (a) Ma $= 6.6$, (b) Ma $= 13.1$ and (c) Ma $= 17.5$.

suppressing interfacial travelling waves. The same is observed in figures 3.11e-f for $n_w = 4$, even for a smaller value of $\delta_w = 1$. In this case, the evolution of the interface for $\delta_w = 0.5$ becomes aperiodic due to strong nonlinearities involved in the dynamics.

3.4 Heat transfer

In the area of heat transfer enhancement a non-uniform heating of falling liquid films is thought to be a promising solution since it induces steady-state deformations of the liquid-gas interface which are beneficial to the heat transfer process [55]. It is then essential to understand the influence of non-uniformities in heating and how they can improve the heat transfer through the film.
For this purpose, we define a reduced heat transfer coefficient, based on the dimensionless temperature difference between the wall and the interface, so that using the zeroth-order solution for the temperature field given by (2.4e), it reads

$$\tilde{\alpha}(x,t) = \frac{-\partial_y T}{T|_{y=0} - T|_{y=h}} = \frac{1}{h(x,t)}. \tag{3.19}$$

This reduced coefficient $\tilde{\alpha}$ gives locally the deviation due to a change of the film thickness, from the heat transfer coefficient of the Nusselt flat film ($\alpha_N = \lambda/h_N$). In

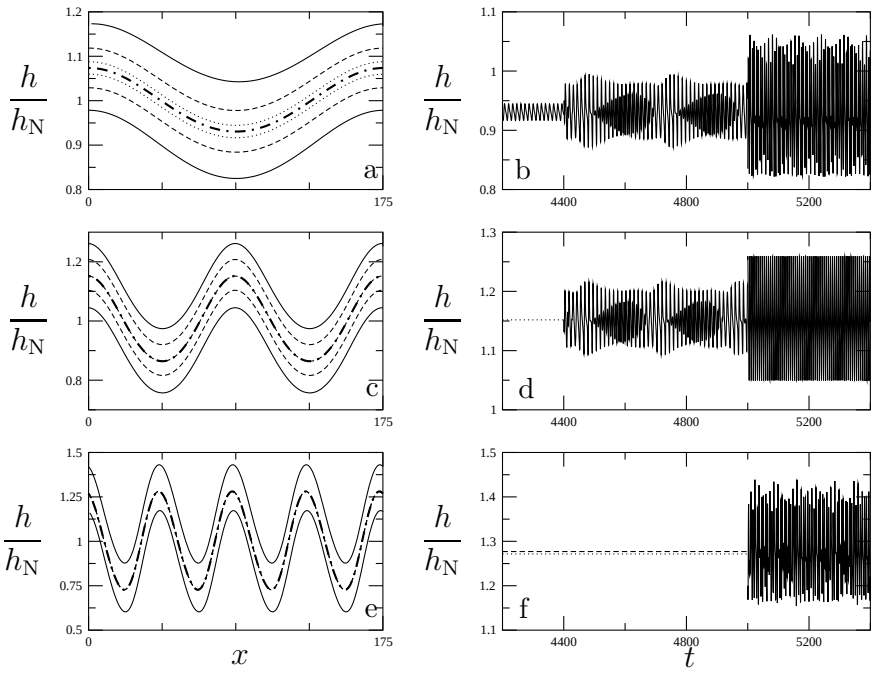

Figure 3.11: The envelopes and time series of the film thickness calculated for Ma = 6.6 and (a,b) $n_{\rm w} = 1$; (c,d) $n_{\rm w} = 2$; (e,f) $n_{\rm w} = 4$. In the left column the dotted, dashed and solid curves correspond to the envelopes for $\delta_{\rm w} = 6.5$, $\delta_{\rm w} = 1$, and $\delta_{\rm w} = 0.5$, respectively. The dot-dashed curves depicts the corresponding steady-state solutions calculated in the fixed frame of reference. In the right column the corresponding time series recorded at $x = L_x/2$ are shifted one with respect to the other for clarity.

order to estimate the heat transfer enhancement induced by surface deformations, $\tilde{\alpha}$ should be averaged over one period L_x of the domain as

$$\hat{\alpha} = \frac{1}{L_x} \int_0^{L_x} \frac{1}{h} dx. \tag{3.20}$$

Therefore, the enhancement of the heat transfer is expected only if $\hat{\alpha} > 1$. For $\hat{\alpha} = 1$, the heat transfer coefficient at the interface is simply the one predetermined for the Nusselt flat film solution $\alpha_{\rm N}$.

The reduced coefficients $\tilde{\alpha}$ and $\hat{\alpha}$ – that can also be obtained for HFC – merely claim that at leading-order, the heat transfer is inversely proportional to the film thickness. Moreover, it also shows that the free-surface deformation is not a sufficient condition for the enhancement of the heat transfer. To achieve such an enhancement the deformation must induce a sufficiently large zone of thinning.

Figure 3.12 presents the average reduced heat transfer coefficient given by (3.20) for the steady-state deformations calculated in the fixed reference frame using the dynamical system (3.9), with the temperature distribution at the wall (3.6) for $n_{\rm w} = 1, 2$ and 4. We also represent the same result for an artificial sinusoidal film surface (dot-dashed line). It appears that the deviation from the sinusoidal shape strongly

diminishes the heat transfer efficiency. Nevertheless, the heat transfer coefficient cannot diverges like in our artificial case since the flow should be maintained anywhere (at least in a 2D flow). As a consequence, the minima cannot be zero and $\hat{\alpha}$ keeps finite values.

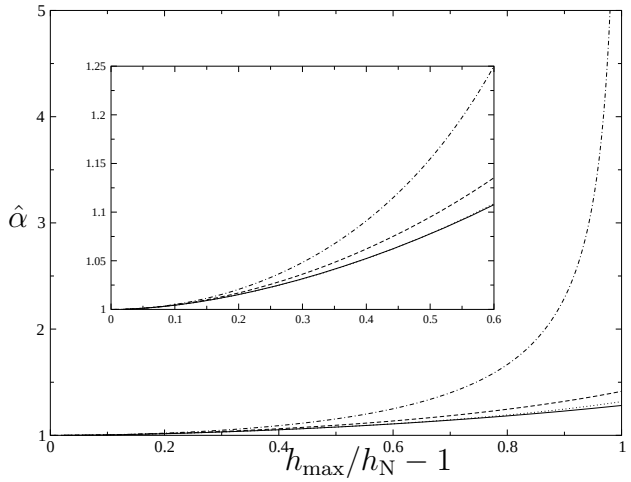

Figure 3.12: Average reduced heat transfer coefficient $\hat{\alpha}$ versus the maximal deviation of the film thickness from the flat state $h = h_{\mathrm{N}}$ for the case of steady deformations. The solid, dotted and dashed lines are calculated for the stationary solutions in the fixed reference frame for the sinusoidal temperature distribution with $n_{\mathrm{w}} = 1, 2$ and 4, respectively. The parameter values are $\delta_{\mathrm{w}} = 2$, Re $= 0.5$, Ka $= 497$, Bi $= 0.087$ and $L_x = 175$. The dot-dashed line corresponds to the artificial case of a sinusoidal shape of the film surface. The inset is a zoom in for small values of $\hat{\alpha}$. Note that the dotted curve almost coincides with the solid one.

Figure 3.13 displays $\hat{\alpha}$ plotted versus Ma_{w} for steady-state deformations calculated with the Benney equation (3.5) in a fixed reference frame. It presents also the results obtained from time-dependent numerical simulations of (3.5). As shown in §3.3, they correspond to oscillatory regimes in the form of travelling waves modulated by the steady-state deformation. It appears that the coefficient $\hat{\alpha}$ of these regimes is only slightly enhanced by the travelling waves and its main contribution comes from the steady-state deformations induced by the non-uniform heating.
The situation can differ however if the average wall temperature is increased, this is for decreasing δ_{w}. Figure 3.14 shows the coefficient $\hat{\alpha}$ as a function of δ_{w}. The white symbols correspond to the cases studied in figure 3.11 when Ma $= 6.6$ and the black ones when Ma $= 13.1$. It appears that the value of δ_{w} does not significantly affect the heat transfer coefficient, except for small value of δ_{w} for which the temperature difference across the film is much higher than the temperature difference along the wall, *i.e.* $\Delta T \gg \Delta T_{\mathrm{w}}$. This effect is further increased with Ma and n_{w}.

We can conclude, therefore, that steady-state deformations induced by a non-uniform heating are the main agent of heat transfer enhancement, while the amplitude of travelling waves depending on the average wall temperature does not play a significant

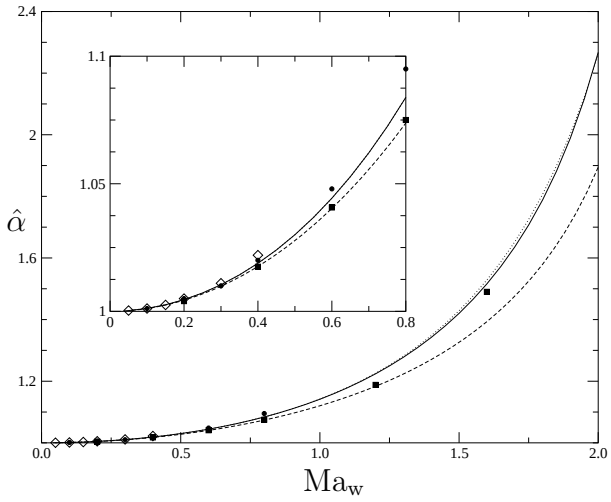

Figure 3.13: Average heat transfer coefficient for stationary solutions versus $\mathrm{Ma_w}$. The parameters are $\delta_\mathrm{w} = 2$, Re $= 0.5$, Ka $= 497$, Bi $= 0.087$ and $L_x = 175$. The curves correspond to steady-state solutions calculated in the fixed reference frame, while the symbols correspond to the related oscillatory regimes obtained by time integration (see Sec.3.3). The results shown are $n_\mathrm{w} = 1$ (solid line and diamond), $n_\mathrm{w} = 2$ (dotted line and black circle) and $n_\mathrm{w} = 4$ (dashed line and black square).

role, except when the average temperature is much larger than the amplitude of the non-uniform temperature distribution.

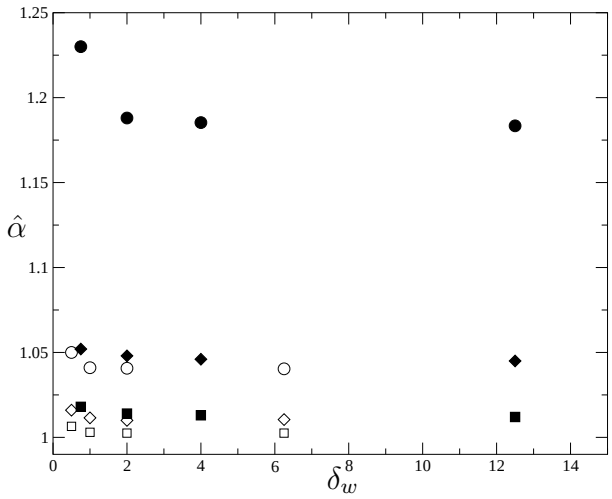

Figure 3.14: Average heat transfer coefficient as a function of the parameter δ_{w} for $\mathrm{Re} = 0.5$, $\mathrm{Ka} = 497$, $\mathrm{Bi} = 0.087$ and $L_x = 175$. The white symbols denote the results for $\mathrm{Ma} = 6.6$, while the black ones correspond to $\mathrm{Ma} = 13.1$. The squares correspond to $n_{\mathrm{w}} = 1$, the diamonds to $n_{\mathrm{w}} = 2$ and the circles to $n_{\mathrm{w}} = 4$.

Chapter 4

Local heating

We have seen in the previous chapter that sinusoidal distribution of the imposed wall temperature induced periodic and steady-state deformations due to Marangoni effect. In the present chapter, we will focus on experiments designed in order to study the effect of non-uniform heating. The simplest configuration is a heater embedded into the wall and inducing therefore a local temperature gradient. The concomitant surface tension gradient produces a thermocapillary flow opposed to the gravitational driven flow (for a fluid that has the surface tension decreasing with temperature). The first related experiment was built-up by Kabov [55]. He reported that the competing flow produces a permanent deformation, *i.e.* that remains steady in the laboratory reference frame. Indeed, the thermocapillary counter flow slows down the film surface velocity and it results in a horizontal bump of increased film thickness as shown on the left picture of figure 4.1. This bump occurs at the upper edge of the heater

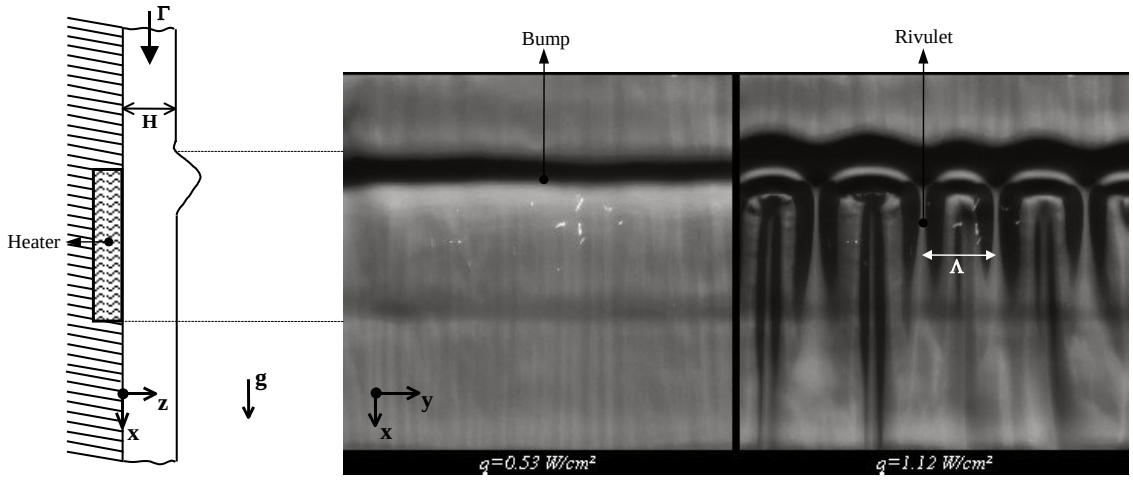

Figure 4.1: Two pictures of the inhomogeneously heated falling film viewed from the $y-$direction (perpendicular to the plate), obtained using the Schlieren technique. Below some threshold, for $\mathrm{Ma} < \mathrm{Ma_c}$, the bump forms at the upper edge of the heater (left), whereas beyond it, for $\mathrm{Ma} > \mathrm{Ma_c}$, the rivulet structure appears (right). The liquid consists of a 25% ethyl-alcohol aqueous solution, $\mathrm{Re} = 0.25$.

where the temperature gradient is maximal. Above some threshold, say $\mathrm{Ma_c}$, this two-dimensional base state becomes unstable with respect to spanwise disturbances. A three-dimensional pattern takes place in the form of rivulets aligned with the flow, which are periodic in the transverse direction as shown on the right picture of figure 4.1. This instability was called *rivulet instability* by Kabov who mentioned this instability for the first time in 1994 [55]. Since then, Kabov and co-workers have worked extensively on this problem, understanding the likely benefit of the new structure on the enhancement of the heat transfer [61, 56, 59, 65]. Indeed, the film thinning occurring between the rivulets may increase drastically the heat transfer, even though it can also be the siege of dry patch formation. Thereby controlling the onset of instability and the development of the resulting nonlinear pattern has became a challenging issue.
In the frame of this work, an experimental set-up has been built up in order to study the bump formation and the rivulet instability. We developed an optical apparatus based on a Schlieren technique for measuring the free surface deformations. The details of this apparatus are reported in [119]. Measurements of bump shapes were reported in [116, 64] and the ones for the temperature field at the film surface using an infrared scanner as well as the velocity field using a high speed camera were reported in [117]. The main experimental results of those works will be compared hereafter with the theoretical approach.
In §4.1 the experimental set-up is presented as well as the main arguments that were used to select the most appropriate design. Then, based on long-wave theory, we calculate the bump profiles (base state) and compare them with experimental data (§4.2). Next, we analyse the linear stability of this base state with regards to spanwise disturbances (§4.3). We perform an energy analysis following the method of Spaid & Homsy [131] to elucidate the instability mechanism. Finally, we performed 3D time-dependent simulations using a pseudo-spectral method in order to describe the dynamics beyond the instability threshold and the formation of the rivulet pattern (§4.5).

4.1 Experimental test section

Figure 4.2 shows the design of the experimental test section to study the case when a local heating is imposed at the wall. The working liquid is a 25%ethyl-alcohol aqueous solution which is injected at constant flow rate $\bar{q}_\mathrm{N}$. The Reynolds number is therefore a control parameter through the relation (1.36). At the inlet the liquid film is generated from the transition between a Poiseuille flow (parabolic velocity profile) and a Nusselt flow (semi-parabolic velocity profile). The heater should therefore be embedded after the distance L_h from the nozzle necessary for the falling film to be fully developed, *i.e.* with a constant film thickness $\bar{h}_\mathrm{N}$.
Three zones corresponding to three different regimes are indicated in figure 4.2:

I A thermal boundary layer takes place in the film from the upper edge of the heater. An analytical expression for the length L_b necessary for the boundary

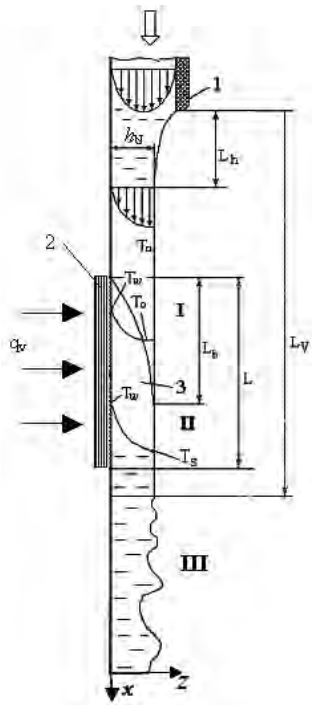

Figure 4.2: Design of the experimental test section. 1: nozzle, 2: heater, 3: thermal boundary layer, T_0: initial temperature, T_w: wall temperature, T_s: film surface temperature, q_v: heat flux density. Courtesy of Kabov [62].

layer to reach the film surface was obtained by Gimbutis [40] and reads

$$L_b = 0.139 l_\nu \mathrm{PrRe}^{3/4}. \tag{4.1}$$

Since the Reynolds numbers considered in the experiments are relatively small, the heater length $L \gg L_b$ in all cases (*e.g.* for Re = 1, $L_b = 0.27\,mm$ while $L \geq 4\,mm$). Moreover, we may expect the Marangoni counter flow to cause a significant decrease of L_b. For Re $\ll 1$, the heated liquid could even rise up along the film surface over the heating element. It means that the real thermal boundary layer can be curved upstream and will be mainly determined by the Marangoni effect, (4.1) becoming irrelevant.

II The thermal boundary layer has reached the film surface. Since the heat flux density q_v is maintained constant, the wall temperature T_w should increase along the $x-$coordinate. However, the heating element being highly conducting, we can expect T_w to be rather homogeneous in this zone.

III As mentioned by several authors (see for example the work by Alekseenko *et al.* [1]), a given distance L_v from the nozzle is necessary for the hydrodynamic waves to develop and reach finite amplitude. This distance L_v is nonlinearly related to Re. It decreases first and then, for Re > 20, increases quickly with Re.

In order to have a test section with a steady layer on both thermal and hydrodynamic point of view, we must therefore place the heating element at a distance from the nozzle larger than L_h and smaller than L_v. In our experiments, the previous requirement was fulfilled by placing the upper edge of the heater at 35 mm from the nozzle. Two different heater lengths of $L = 4$ and 6.7 mm have been used. Hence, L_v was found to be always larger than 41.7 mm, at least for $\mathrm{Re} \leq 2$, which lies in the range used for experiments.
In experiments the heating is controlled by imposing a constant heat flux q_v at the plate. Marchuk & Kabov [86] calculated the heat flux distribution along a local heat source, solving the Fourier equations in the wall, and showed that it cannot be considered as constant along the plate. This non-uniformity is due to the dependence of the heat flux on the characteristics of the flow, which is found to be particularly strong when the Reynolds number is small. They found an intense heat flux in the first quarter of the heater, starting from its upper edge (where the thermal gradients are the highest), and then a slight decrease until the downstream edge. Since the heat flux is far to be constant, and as the heat flux condition requires one more parameter Bi_w (see §1.3.2), we chose in the following to use the temperature condition at the wall. We must then find the most appropriate temperature distribution. For this purpose, we may start from the temperature profile at the film surface measured by infrared scanner as shown in figure 4.3. This can be justified by considering the liquid-gas interface to be a poor conductor, hence rather well insulated from the gas, $\mathrm{Bi} \ll 1$. Therefore, the leading order film surface temperature (3.4) ensures that $f \sim (\theta - 1)/\delta_\mathrm{w}$. The temperature profiles shown in figure 4.3 demonstrate a strong

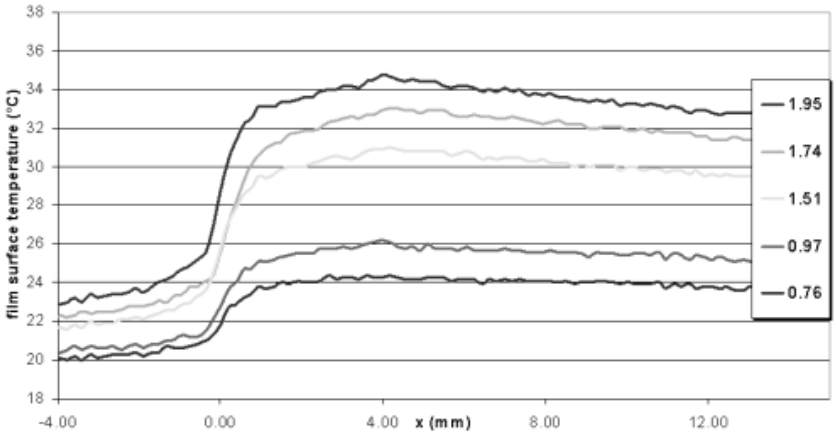

Figure 4.3: Temperature profiles measured at the film surface by infrared scanner for $\mathrm{Re} = 0.3$. The numbers in the legend are the average heat flux density q_v given in W/cm^2. The coordinate $x = 0$ indicates the upper edge of the heater with $L = 4mm$.

temperature jump at the upper edge of the heater and then a small decrease after the heater indicating that the heat transfer at the liquid-gas interface is not very intense. The Biot number should therefore be taken sufficiently small ($\mathrm{Bi} \ll 1$) indeed. The temperature jump in figure 4.3 can be identified to ΔT_w and the heater length L to the length $\bar{l}_\mathrm{w}$ along with ΔT_w applies. This provides us the characteristic temperature

gradient $\Delta T_{\rm w}/\bar{l}_{\rm w}$ necessary to estimate the wall Marangoni number as defined in (3.8), even though an other way to infer the Marangoni number is presented in the next section.

4.2 Base state: comparison with experiments

The Reynolds number being small in the experiments, the long-wave theory applies and the evolution equation (3.5) remains valid. Let us check this statement in the light of §2.6 where the validity of the Benney equation was studied. Given that the wall is vertical in the experiments (Ct = 0), and looking at table C.1, the Kapitza number of the working liquid is $\mathrm{Ka}_\perp = 500$, the maximal $\Delta T \sim 10K$ (see figure 4.3) and $\mathrm{Ma}_\perp \sim 15$. Let us fix the Biot number to $\mathrm{Bi}_\perp = 0.1$. The product $\mathrm{Bi}_\perp \mathrm{Ma}_\perp \sim 2$ such that we read in figure 2.8 that $\mathcal{R} < 0.4$ should be verified, using the Benney equation, to keep a good accuracy. This corresponds to $\mathrm{Re} < 0.8$. The rivulet instability has been observed in experiments for smaller Re than this limit and the Benney equation can therefore be used safely. Nevertheless, the above condition is obtained in the case of a uniform heating and it should be used with care for a non-uniform heating by taking care that the amplitudes of the solutions do not exceed by far the ones of the travelling waves computed in the uniform heating case (to avoid blow-up).
Using the evolution equation (3.5), the temperature distribution should still be given. Based on figure 4.3, let us choose the temperature distribution as follows

$$f(x) = \frac{1}{2}\left(\tanh\left[\frac{\pi}{l_{\rm w}}\left(x - \frac{1}{4}L_x\right)\right] - \tanh\left[\frac{\pi}{0.4L_x}\left(x - \frac{5}{8}L_x\right)\right] - 1\right), \qquad (4.2)$$

which is represented on figure 4.2, as an example, for $L_x = 20$ and $l_{\rm w} = 1$. It actually

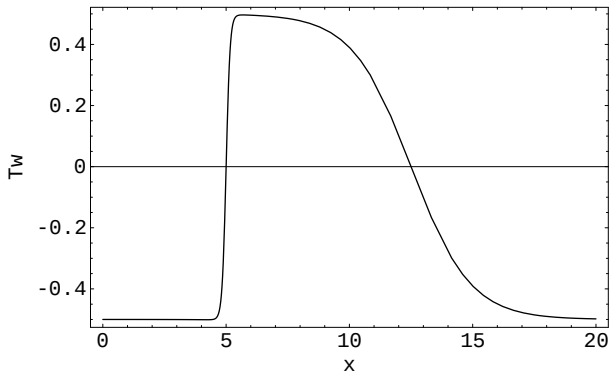

Figure 4.4: Non-uniform component of the temperature distribution, as described by (4.2). The length of the domain is $L_x = 20$ and the length of the positive temperature gradient is $l_{\rm w} = 1$.

models the strong temperature increase at the upper edge of the localized heater, appearing along the length $l_{\rm w} \ll L_x$, and centered at the first quarter of the domain L_x (at $x = 5$ on figure 4.4). Because we want to impose periodic boundary conditions for numerical computations, the condition $f(0) = f(L_x)$ must be satisfied. This is the

reason why (4.2) includes a smooth negative temperature gradient along the length equal to 40% of L_x and centered at $\frac{5}{8}$ of it. Therefore, the negative temperature gradient decreases with increase of the size of the periodic domain L_x. One then expects that for sufficiently large L_x the temperature profile tends to that of the experimental situation.
Figure 4.5 compares the base state calculated with the dynamical system (3.9) (thin lines) with the profiles measured in experiments. Since the temperature gradient im-

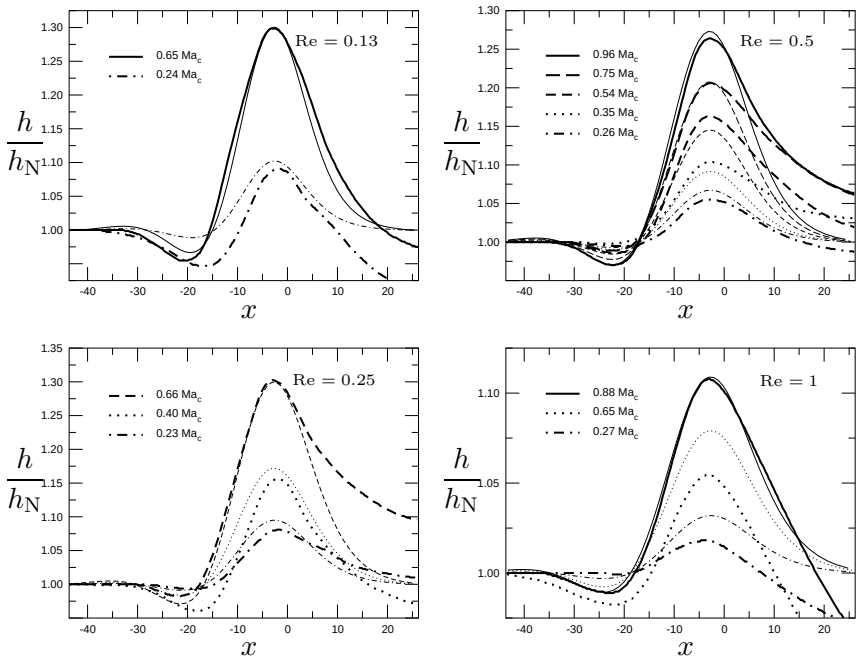

Figure 4.5: Comparison between the profiles of the film thickness measured in the experiments (thick lines), and calculated from (3.9) (thin lines). The parameters are Ka = 500, Bi = 0.087 and $\delta_w = 2$. In the legend, the factor of Ma_c indicates how far the Marangoni number is from the onset of the rivulet instability as observed experimentally.

posed at the wall $\Delta T_w/l_w$ is not known accurately, we must infer the experimental Marangoni number. We used the experimentally measured lengthscale of the bump to determine l_w. Then we calculated theoretically the maximal height as a function of ΔT_w. We take the experimental ΔT_w to be where this height matches the experimentally measured maximal height. This fitting procedure was only performed once (for each Reynolds number) for the bump with the highest amplitude. Then, we decreased the Marangoni number using the ratios given in the legend of figure 4.5 to calculate the bumps of smaller amplitude. The theoretical and experimental profiles are in good agreement, as far as their ascending side and the small depression upstream due to the surface tension effect are concerned. The discrepancy observed at the downstream tail of the bump can be attributed to the accumulating error associated with the integration method used for processing experimental data.
However, to explain this discrepancy, Kabov *et al.* [85, 64] have rather proposed a

model taking into account the temperature dependence of the viscosity. Indeed, this effect could explain at least the decrease of the film thickness below its initial mean value h_{N} due to an increase of the fluid mobility – the flow rate being conserved – induced by the temperature decrease of the liquid viscosity. Kabov *et al.* [85, 64] obtained a better quantitative agreement with some of the experimental curves, especially in the downstream tail of the bump. Remember also that the temperature distribution (4.2) is merely an approximation and the heat transfer coefficient at the wall and at the free surface are not known and could also influence the free surface shape.

Figure 4.6 shows the maximal height of the bump $h_{\max}/h_{\mathrm{N}}$ calculated by continuation using the Marangoni number Ma as the continuation parameter. The amplitude of the

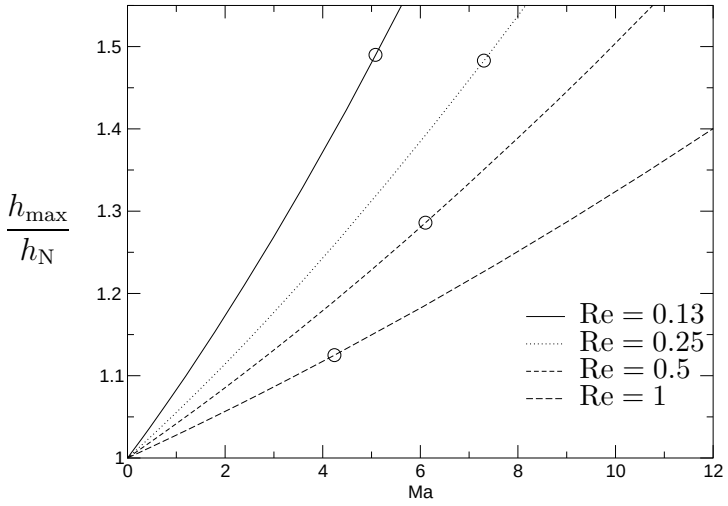

Figure 4.6: Maximal departure of the film surface from its mean dimensionless value h_{N} as a function of the Marangoni number Ma for various values of the Reynolds number Re, for $\delta_{\mathrm{w}} = 2$, $\mathrm{Ka} = 500$ and $\mathrm{Bi} = 0.087$. Circles correspond to the maximal height of the bump at which the instability onset has been experimentally observed.

deformation decreases with an increase of Re when Ma is fixed. This is due to the main flow that counteracts the thermocapillary flow. The circles on figure 4.6 correspond to the maximal height of the bump at which the instability onset has been observed for each Reynolds number. The critical Marangoni number for the experimental rivulet instability denoted by $\mathrm{Ma_c}$ is therefore deduced from figure 4.6. In other words, we identify from this figure which is the Marangoni number that produces theoretically a bump whose the size fits with the one measured experimentally at the instability onset.

The instability threshold $\mathrm{Ma_c}$ is found first to increase and then to decrease with Re, the transition being at $\mathrm{Re} \approx 0.25$ (see figure 4.6). Since such a decrease of $\mathrm{Ma_c}$ with Re has not been observed experimentally, we conjecture here that our model fails in describing the dynamics of the flow for $\mathrm{Re} > 0.25$. The reason mainly is that the convection of heat becomes large enough to modify significatively the film surface temperature and therefore modify the instability behaviour; actually, the Prandtl

number Pr = 21.8 is quite large for ethyl-alcohol aqueous solution (see table C.2) while our model is written for PrRe = $\mathcal{O}(1)$. Therefore, we will restrict the remaining of the study to the case of Re = 0.13 for which our model still can be valid.

4.3 Linear stability analysis

We now study the linear stability of the base state, *i.e.* the bump profile, with respect to spanwise disturbances. For this purpose, the three-dimensional version of the Benney equation (2.10) should be considered together with (3.4) and (4.2). To analyze the spanwise stability of this base state, denoted by h_0, we consider small perturbations h_2 of the free surface shape such as

$$h(x,z,t) = h_0(x) + h_2(x,z,t) \tag{4.3}$$

and use the normal mode form

$$h_2(x,z,t) = \eta h_1(x)\exp\{\mathrm{i}k_z z + \sigma t\} \tag{4.4}$$

where σ $(= s + \mathrm{i}\sigma_i)$ is the complex growth rate of the disturbance, k_z is the spanwise wavenumber and $\eta \ll 1$. Substituting (4.3) and (4.4) into the expression of the film surface temperature (3.4) and expanding at first-order with respect to η yields

$$T_{\mathrm{s}}(x,z,t) = T_{\mathrm{s}_0}(x)\left(1 - \eta\frac{\mathrm{Bi}h_1(x)\exp\{\mathrm{i}k_z z + \sigma t\}}{1+\mathrm{Bi}h_0(x)}\right) \tag{4.5}$$

where

$$T_{\mathrm{s}_0}(x) = \frac{1+\delta_{\mathrm{w}}f(x)}{1+\mathrm{Bi}h_0(x)} \tag{4.6}$$

is the base state film surface temperature. Substituting (4.3), (4.4) and (4.5) into (2.10) and linearizing with respect to η leads to the following fourth-order eigenvalue problem for the eigenfunction $h_1(x)$,

$$\sigma h_1 = -\boldsymbol{L}[h_1] \tag{4.7}$$

where the right-hand side of (4.7) can be explicitely written as a sum of thirteen terms

$$-\boldsymbol{L}[h_1] = -\sum_{m=1}^{13}\boldsymbol{L}_m[h_1] = -\sum_{m=1}^{13}T_m \tag{4.8}$$

and each term may be associated with a perturbation of the base flow in either the streamwise x or spanwise $z-$direction. They depend nonlinearly on the base state solution $h_0(x)$, and are listed with their physical meaning in table 4.3.
Spaid & Homsy [131] studied the stability of a capillary ridge (that corresponds to the base state solution) at a moving contact line by using the long-wave evolution equation and performing a similar decomposition of the r.h.s. of the eigenvalue problem (4.7). Since they did not consider heating, they only had the six terms $T_{2,3,4,5,6,7}$ similar than

T_m	Terms	Physical meaning
T_1	$\left(-\delta_{\mathrm{w}}\mathrm{Ma}h_0h_1T'_{\mathrm{s}_0}\right)'$	Thermocapillary flow in $x-$direction due to the base state temperature gradient ($\mathrm{Bi}=0$)
T_2	$\left(\frac{1}{3}\mathrm{Ka}h_0^3h_1'''\right)'$	Capillary flow in $x-$direction induced by perturbation curvature in x
T_3	$\left(-\frac{1}{3}k_z^2\mathrm{Ka}h_0^3h_1'\right)'$	Capillary flow in $x-$direction induced by perturbation curvature in z
T_4	$\left(h_0^2h_1\right)'$	Flow in $x-$direction due to gravity
T_5	$\left(\mathrm{Ka}h_0^2h_0'''h_1\right)'$	Capillary flow in $x-$direction due to perturbation of the base state pressure gradient
T_6	$-\frac{1}{3}k_z^2\mathrm{Ka}h_0^3h_1''$	Capillary flow in $z-$direction induced by perturbation of curvature along x
T_7	$\frac{1}{3}k_z^4\mathrm{Ka}h_0^3h_1$	Capillary flow in $z-$direction induced by perturbation of curvature along z
T_8	$\left(\frac{\mathrm{Bi}\delta_{\mathrm{w}}\mathrm{Ma}h_0^2h_1T'_{\mathrm{s}_0}}{2(1+\mathrm{Bi}h_0)}\right)'$	Thermocapillary flow in $x-$direction due to the base state temperature gradient ($\mathrm{Bi}\neq 0$)
T_9	$\left(\frac{1}{2}\mathrm{Bi}\delta_{\mathrm{w}}\mathrm{Ma}h_0^2T_{\mathrm{s}_0}\left(\frac{h_1}{1+\mathrm{Bi}h_0}\right)'\right)'$	Thermocapillary flow in $x-$direction due to perturbation of the film thickness
T_{10}	$-\frac{\mathrm{Bi}\delta_{\mathrm{w}}\mathrm{Ma}k_z^2h_0^2h_1T_{\mathrm{s}_0}}{2(1+\mathrm{Bi}h_0)}$	Thermocapillary flow in $z-$direction due to perturbation of the film thickness
T_{11}	$\left(\frac{2}{15}h_0^6h_1\right)''$	Flow in $x-$direction due to inertia
T_{12}	$\left(-\frac{1}{3}\mathrm{Ct}h_0^6h_1\right)''$	Flow in $x-$direction due to hydrostatic pressure
T_{13}	$\frac{1}{3}\mathrm{Ct}k_z^2h_0^3h_1$	Flow in $x-$direction due to hydrostatic pressure

Table 4.1: Terms of the eigenvalue problem of (4.7) and their physical interpretation (the primes indicate the derivative with respect to x)

above (see Table 4.3) and one more term introduced by the precursor film model they used. Their interpretation is that terms T_m of the linear operator that yield positive (negative) contributions to the growth rate are destabilizing (stabilizing). The total energy of the base state perturbation h_2 is defined by

$$E = \frac{1}{2}\int_{L_x} |h_2|^2 \, dx = \frac{1}{2} < h_2, h_2 > \tag{4.9}$$

Following Spaid & Homsy [131], the expression for the rate of energy change may be obtained by forming the inner product of the eigenvalue problem given by (4.7) with the eigenfunction h_1, such as

$$\frac{dE}{dt} = \sigma < h_1, h_1 > = < -\boldsymbol{L}[h_1], h_1 > . \tag{4.10}$$

For convenience, the time derivative of the energy is normalized such that the total 'removal' rate E^* is equal to the eigenvalue σ associated with the eigenmode,

$$E^* = \frac{< h_1, -\boldsymbol{L}[h_1] >}{< h_1, h_1 >} = \sigma. \tag{4.11}$$

Finally the energy analysis consists in the analysis of the energy contribution E_m^* of the disturbances corresponding to each term T_m expressed as

$$E_m^* = \frac{< h_1, -\boldsymbol{L}_m[h_1] >}{< h_1, h_1 >}. \tag{4.12}$$

The eigenfunction h_1 as well as the eigenvalue σ are determined from (4.7). Once thus is done, (4.11) and (4.12) can be evaluated. The results can be cross-checked easily with the relation $\sum_m E_m^* = \sigma$.

Figure 4.7 depicts the energy contribution of the disturbances provided by each term T_m for the case of a vertical wall, i.e. $T_{12} = T_{13} = 0$. Various E_m^* are non-zero for $k_z = 0$; however they always balance to yield a neutrally stable state ($\sigma = 0$), as a characteristics of the long-wave instability. Consequently, interpreting the terms $E_m^* > 0$ to be destabilizing and terms $E_m^* < 0$ to be stabilizing, might not reveal the instability mechanism. The stabilization/destabilization of the marginally stable state arises rather as a result of deviations of the values of E_m^* from their values at $k_z = 0$. This is like each effect listed in table 4.3 was a candidate for a long-wave instability. Hence, the most important instability mechanisms are those in which the associated E_m^* deviate most from their values at $k_z = 0$ as plotted in figure 4.8. This new interpretation was introduced by Skotheim *et al.* [128] to resolve some of the discrepancies between the various physical systems studied by Spaid & Homsy [131] and Kataoka & Troian [70, 71] to elucidate the physical nature of the fingering instability of liquid rims that accompany moving contact lines. We see that term 5, which was previously interpreted as the most destabilizing is now a stabilizing factor while the contrary for term 2.

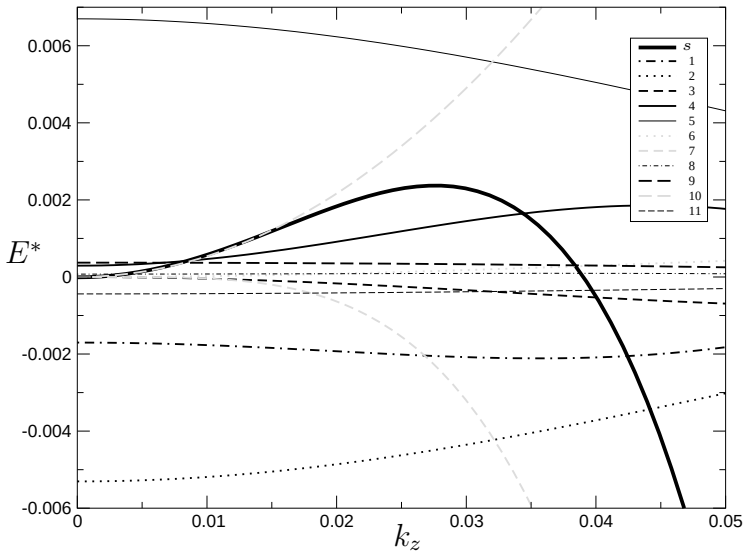

Figure 4.7: Energy contribution E^* of the disturbances corresponding to each term as referenced in Table 4.3 (corresponding to the numbering in the legend) versus the wavenumber k_z. The parameters are Re = 0.13, Ka = 500, Bi = 0.1, $L_x = 850$, $l_w = 94$, $\delta_w = 2$ and Ma = 5.8. The perturbating flows in $x-$direction are represented by the black curves and in $z-$direction by the grey curves. The thicker black curve is the total growth rate σ.

The most destabilizing factor appears to be the pure thermocapillary effect in the $z-$directions (T_{10}). It corresponds to the S-mode describes in §1.4.1 and identified by Joo *et al.* [54] to generate rivulets aligned with the flow and leading in time to spontaneous rupture. As for fingering instability in contact lines on an inclined plate, gravity contributes also in destabilizing the bump. The destabilizing mechanism akin to T_4, proposed by Spaid & Homsy [131], is twofold: since the thicker disturbed regions are more massive, they will be pushed forward more rapidly by the body force, thus causing the fingering instability. Along the same lines, the thick regions will be less affected by the viscous drag of the solid plate, resulting in a higher mobility in thicker regions of the perturbed base state. Accordingly, the fluid will tend to follow the path of least resistance, contributing to the formation of rivulets.

Term 7 is of course always stabilizing (see figure 4.8) and represents the main response of the system to spanwise long-wave instabilities, acting to damp the shorter wavelength perturbations. This term corresponds to the second type of Rayleigh-like term in fluid jets [131]. Terms 3 and 5 are also stabilizing since capillary terms are here diminishing the change in the curvature of the bump in both the spanwise and streamwise directions, thereby flattening the film.

The Marangoni number Ma = 5.8 in figure 4.8 has been chosen to produce a bump height slightly larger than the critical one observed in experiments and corresponding to $\mathrm{Ma_c} \approx 5$ (see figures 4.5a and 4.6). The maximal growth rate, that corresponds to the most amplified mode, was found to have a small but non-zero imaginary part.

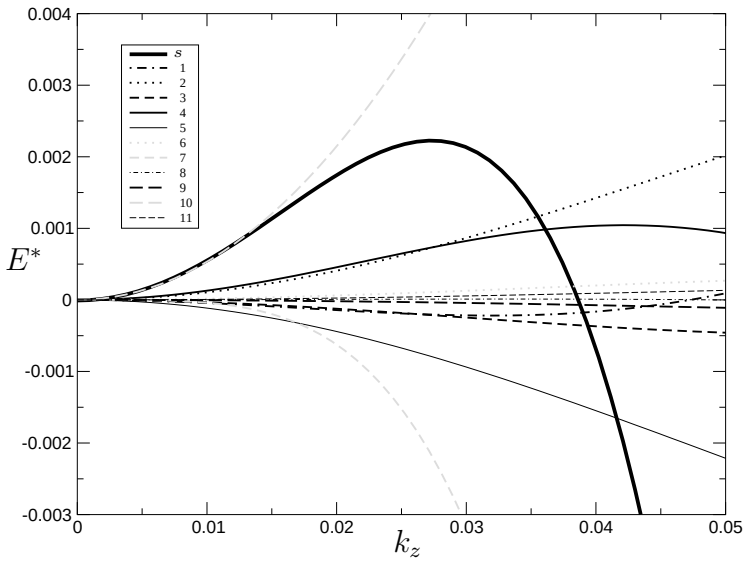

Figure 4.8: Contributions to the largest eigenvalue of the various terms of the operator L relative to their contributions to the marginally stable state at $k_z = 0$ plotted as a function of the wavenumber. The parameters are the same as for figure 4.7.

It means that the base state should be unstable to oscillatory perturbations as well. However oscillations were scarcely observed in experiments [116]. Skotheim *et al.* [128] found that this oscillatory behaviour vanishes for zero Biot number. Yet, we know from experiments that the Biot number is much smaller than unity [64]. An other explanation can be that the oscillatory mode is damped in the nonlinear regime, immediately after the onset. Moreover, we found that increasing the Marangoni number cancels also the imaginary part of the maximal growth rate. In order to understand this change of behaviour when increasing the Marangoni number, we analyse the shape of the eigenfunctions of the most unstable modes as plotted in figure 4.9. The mid-domain corresponds to the location of the upper edge of the heater. For small Marangoni numbers, the eigenfunctions extend over the entire period and the eigenvalue is complex. We will refer to as the **non-localized regime**. On the contrary, when increasing Ma, the eigenfunction is more localized in the region of the steady-state bump and the eigenvalue is real. We will refer to as the **localized regime**. The localized regime only exist for a sufficiently large domain, *i.e.* $L_x \gg l_{\mathrm{w}}$. Since we are most interested in the limiting case of a local heater, we will focus on the localized real mode.

Figure 4.10a shows the dependence of the most unstable mode on Ma as well as the corresponding real eigenvalue (thick lines). It appears that the wavenumber $k_{z\max}$ first increases and then decreases with raising Ma, as found initially by Skotheim *et al.* [128]. The transition is rather well distinguishable at $\mathrm{Ma}_{\mathrm{tr}} \approx 16.3$ (see dashed lines) and corresponds to a drastic increase of the growth rate. On figure 4.10a are also plotted the curves corresponding to the pure spanwise thermocapillary instability and computed for a flat film with $h_0 = h_{\mathrm{N}}$ (thin solid lines). It corresponds therefore to the

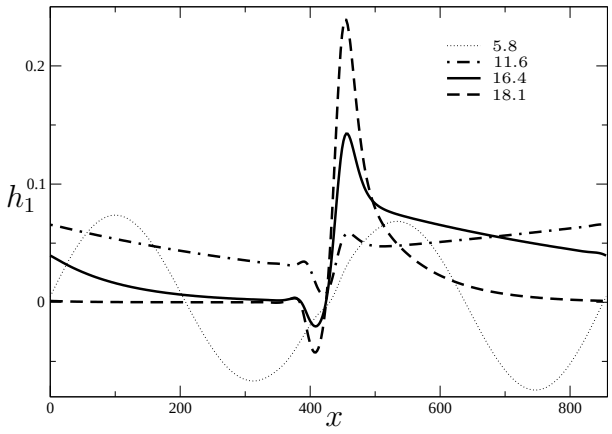

Figure 4.9: Eigenfunctions of the most unstable modes for Re = 0.13, Ka = 500, Bi = 0.1, $L_x = 850$, $l_w = 94$, $\delta_w = 2$ and increasing Ma as indicated in the legend.

S-mode. Interestingly, the presence of the steady-state bump affects significatively the features of the S-mode only when $\mathrm{Ma} > \mathrm{Ma}_{tr}$. We could therefore associate this transition to the bump instability leading to rivulet pattern, as proposed by Skotheim *et al.* [128]. However, the picture is not as simple as it appears since the computations indicate (see figure 4.8) that the growth rate is always positive for a vertical wall. Consequently, the rivulet instability should develop for $\mathrm{Ma} < \mathrm{Ma}_{tr}$ even though with a much smaller growth rate.

In an attempt to clarify the interpretation, we will analyze the destabilizing factors when the Marangoni number lies just above the transition at Ma_{tr}. But before doing so, let us remark the dotted lines on figure 4.10a that behave in a singular way, for $\mathrm{Ma} > 20$, due to term 11 corresponding to the streamwise inertia effect. Figure 4.10b shows that the maximal height of the bump is larger than 2 for $\mathrm{Ma} > 20$. We know from chapter 2 that the risk for this term (originating from the Benney term) to bring singularity is highest when the film thickness is large. Therefore, for large Ma, the validity of the Benney equation should be violated. Since we are interested in the spanwise instability, we cancel T_{11} in the following (as for thick lines in figure 4.10) to avoid singularities. Interestingly enough, doing so results in suppressing the sinusoidal shape of the eigenfunction for Ma = 5.8 in figure 4.8. Note that neglecting T_{11} is similar to the assumption $\mathrm{Re} \ll 1$ which holds in the case analysed here since Re = 0.13. This assumption had been also adopted by Skotheim *et al.* [128].

Figure 4.11 shows now the contribution to the growth rate of the different terms T_i for Ma = 16.4, *i.e.* just above the transition Ma_{tr}. The non-localized and localized regime (referring to the eigenfunction on figure 4.9) are clearly distinguished by the roles of terms 2 and 5: term 2 changes from destabilizing to stabilizing, and term 5 changes from stabilizing to destabilizing as the Marangoni number is increased (compare figure 4.8 and 4.11). At the onset of the instability gravity (term 4) acts with capillary flow in the $x-$direction induced by perturbation thickness variations (term 5) to destabilize the flow. The maxima of $E_4^*(k_z)$ and $E_5^*(k_z)$ shift with increasing

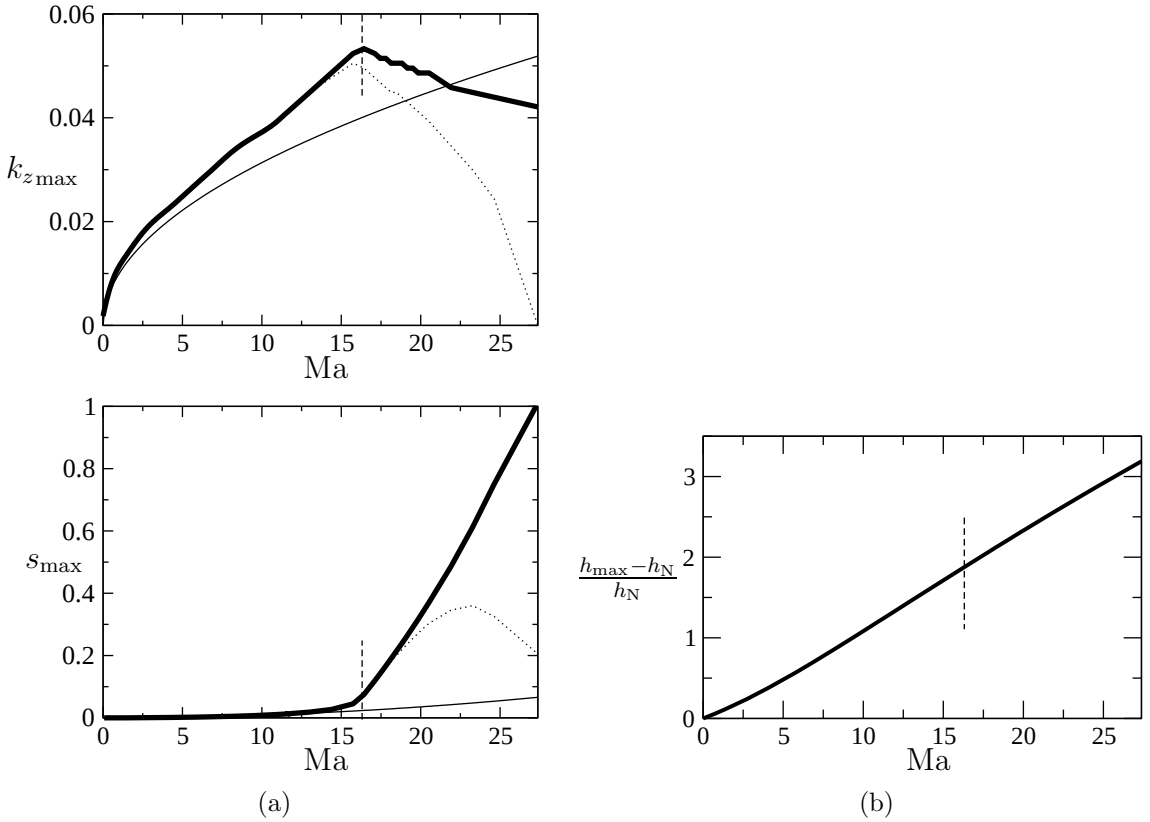

Figure 4.10: (a) The wavenumber $k_{z\max}$ and the growth rate $s_{\max}$ of the most unstable mode, for Re = 0.13, Ka = 500, Bi = 0.1, $L_x = 850$, $l_w = 94$ and $\delta_w = 2$. The thick solid lines correspond to $T_{11} = 0$, the dotted lines to $T_{11} \neq 0$ and the thin solid lines to $h_0 = h_N$. (b) Maximal departure of the steady-state bump solution $h_0(x)$ from the average film thickness h_N.

Ma towards larger and smaller wavenumbers respectively. The change in the relative destabilizing influence of the two terms causes the wavenumber of the fastest growing mode to increase with Ma in the non-localized regime and decrease with Ma in the localized regime (as already shown in figure 4.10). Here, thermocapillarity (term 10) remains a destabilizing mechanism even though less pronounced than in the non-localized regime (figure 4.8). This is in the case of Bi $\neq 0$; indeed, when Bi = 0, term 10 vanishes, as well as term 8 and 9 that are also destabilizing. However, in both the Bi = 0 and Bi $\neq 0$ cases, the main stabilizing influence is the thermocapillary flow in the $x-$direction due to the base state temperature gradient. This can possibly explain what was found in the previous chapter, namely that the travelling waves are suppressed for sufficiently large imposed temperature gradient at the wall in the $x-$direction.

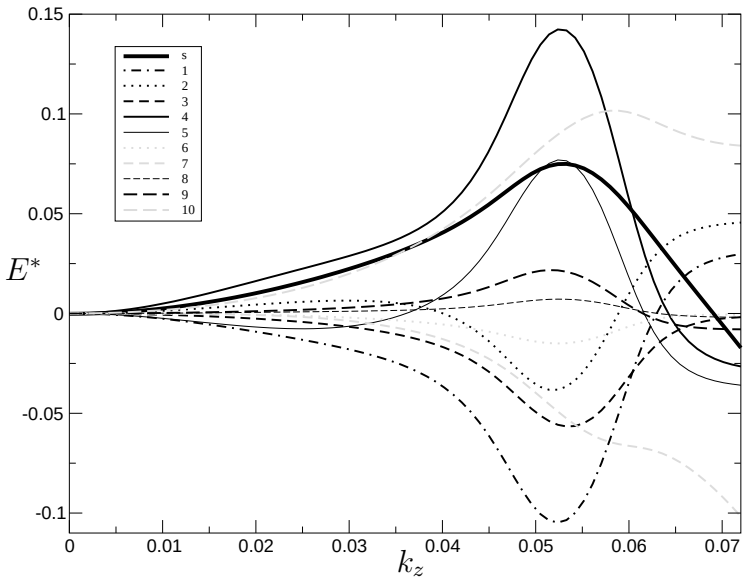

Figure 4.11: Same as for figure 4.8 with Ma = 16.4 and $T_{11} = 0$.

4.4 Linear stability: comparison with experiments

The rivulet instability of a falling film due to localized heating has been initially reported by Kabov [55]. Figure 4.12a shows a sequence of pictures obtained by an optical Schlieren technique [119] and putting in evidence the bump formation ($q_{\rm v} = 1.87 W/cm^2$), the instability onset ($q_{\rm vc} = 2.38 W/cm^2$) and the development of the rivulet structure for increasing heat flux density $q_{\rm v}$ (say Ma). The streamwise heater length was $L = 6.7\,mm$. As mentioned in the previous section, the transition $\mathrm{Ma_{tr}}$ at which the instability growth rate increases drastically can be associated to the onset of the rivulet instability observed in experiments at $\mathrm{Ma_c}$. Nevertheless, the Schlieren imaging does not yield any trace of instability before the transition contrarily to the theory that predicts a small positive growth rate for $\mathrm{Ma} < \mathrm{Ma_{tr}}$ (see figure 4.10). The reason of discrepancy can be attributed to the sensibility of the Schlieren picture that does not capture small amplitude deformations. Actually, infrared imaging shown on figure 4.12b has detected a regular structure for heat fluxes smaller than the threshold for rivulet instability identified at $q_{\rm vc} = 4.8 W/cm^2$ for a streamwise heater length of $L = 4\,mm$. Furthermore, the regular structure of small amplitude has a wavelength (inversely proportional to k_z) that first decreases by raising the heat flux, and then increases after the threshold yielding to large amplitude rivulets. These features are qualitatively in excellent agreement with the linear stability analysis.

Nevertheless, quantitative discrepancies exist: firstly, the minimum wavelength that is about $10\,mm$ in theory ($= 2\pi \mathrm{l}_\nu / k_{z\,\max}$) and $7\,mm$ in experiments [116]. Secondly, for Re = 0.13 and $\delta_{\rm w} = 2$, figure 4.6 shows that $\mathrm{Ma_c} \approx 5$ and the maximal height of the bump at instability onset is about $1.5 h_{\rm N}$. For the same parameters, the stability analysis provides a transition at $\mathrm{Ma_{tr}} \approx 16.3$ where the maximal height of the bump

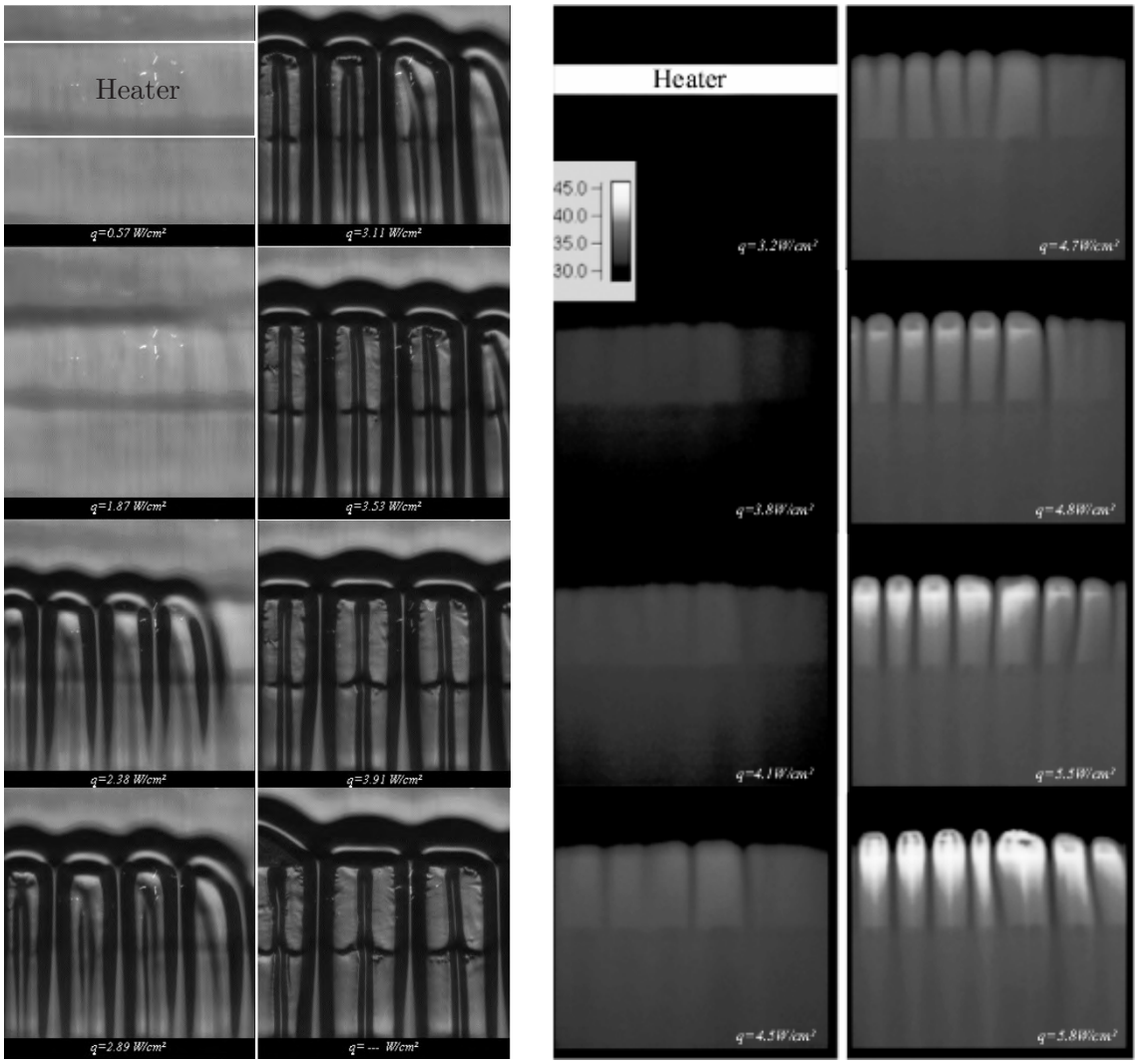

(a) (b)

Figure 4.12: Falling liquid film locally heated for a 25% ethyl-alcohol aqueous solution, Re = 1. (a) Schlieren images of size $20 \times 30\,mm$, in the case of $L = 6.7\,mm$. The threshold for rivulet instability is at $q_{\rm vc} = 2.38 W/cm^2$. (b) Infrared images of size $45 \times 50\,mm$, in the case of $L = 4\,mm$. The threshold for rivulet instability is at $q_{\rm vc} = 4.8 W/cm^2$. The typical distance between two rivulets is 10mm.

is about $2h_{\mathrm{N}}$ (see figure 4.10). Interestingly, the instability threshold in experiments is changed by the streamwise length L of the heater. Actually, figure 4.12 shows that the critical heat flux (say $\mathrm{Ma_c}$) is increased by a factor two when L decreases from 6.7 to 4 mm between figures 4.12 a and b. However, remember that we already fit the length L in our model with the shape of the steady-state bump. It cannot be therefore the reason for the discrepancy between Ma_c and $\mathrm{Ma_{tr}}$. It must be rather something that trigger the rivulet instability in experiments before the theoretical transition. We will invoke here two different causes of this discrepancy.

First, our stability analysis indicates that the steady-state bump is always unstable with respect to spanwise disturbances, even for $\mathrm{Ma} < \mathrm{Ma_{tr}}$. Actually the S-mode is always present, *i.e.* for all Ma, and destabilizes the film in the transverse (spanwise) direction (see figure 4.12b). Therefore, the rivulet instability observed in experiments does not emerge from infinitesimal perturbations of the two-dimensional steady-state bump (as performed in our linear stability analysis) but rather from perturbations of a three-dimensional regular structure of small but finite amplitude. This structure represents a good triggering pattern for the rivulet instability to develop.

Secondly, in the experiments the heater has a finite size in the spanwise direction and as a result, the rivulet instability starts from the sides of the heater as shown in figure 4.13a. Indeed, a temperature gradient exists at the sides of the heater and the concomitant thermocapillary effect always induces a lateral standing "wave". The amplitude of this deformation is always larger than the one of the bump (see figure 4.13b) since the thermocapillary flow is here perpendicular to the gravity driven flow and does not counteract it. Therefore, this lateral standing "wave" can trigger the instability, producing a so-called 'perturbed' or 'imperfect' bifurcation, in contrast with 'perfect' laterally infinite case studied in the theory. Due to this forcing, the spanwise modes can start from the sides earlier than the threshold and then fill the domain in the transverse direction. Such finite size effects due to lateral boundary conditions at or near criticality are discussed by Fauve [32].

Finally note that the convection of heat has been neglected in the long-wave equation, compared to heat diffusion. However, the Prandtl number for a 25% ethyl alcohol aqueous solution at $20°C$ is rather large $\mathrm{Pr} = 21.8$ such that, for $\mathrm{Re} = 0.13$, the Péclet number is $\mathrm{Pe} = 2.8$ $(= \mathrm{PrRe})$. Evidently, the convective terms in the energy equation $\partial_t T + \mathbf{v}\boldsymbol{\nabla} T$ is a non-negligible effect and should therefore be considered. Kalliadasis *et al.* [67] have studied a model for $\mathrm{Re} \ll 1$ and $\mathrm{Pe} = \mathcal{O}(1)$. They got two coupled equations: (i) one for the film thickness which is equivalent to the long-wave equation (2.10) where $\mathrm{Ct} = 0$ (vertical film) and the Benney term $\frac{2}{15}\partial_x(h^6\partial_x h)$ has been neglected; (ii) one for the film surface temperature θ using the integral boundary layer approximation (similar to the one performed in chapter 5). Kalliadasis *et al.* [67] observed that small Péclet numbers decrease the critical Marangoni number for the rivulet instability and hence destabilizes the bump more easily. This statement indicates therefore that taking into account for the convection of heat should decrease the temperature gradient at the film surface and therefore increase the instability threshold. Thus it would not help in explaining the discrepancy between $\mathrm{Ma_{tr}}$ and $\mathrm{Ma_c}$.

We have seen in this section that quantitative comparisons between the stability

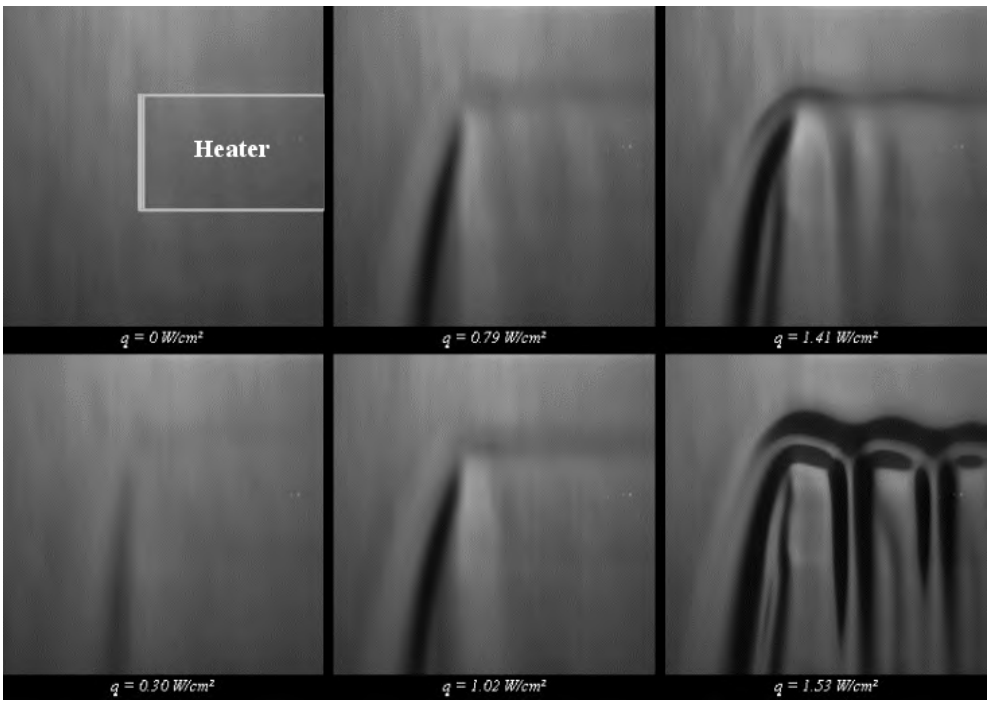

(a)

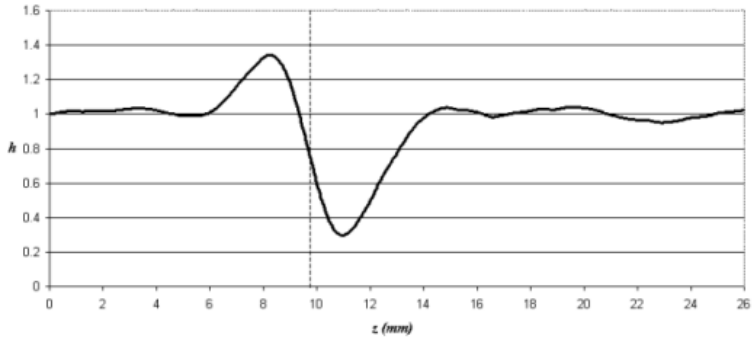

(b)

Figure 4.13: (a) Lateral standing "wave" at the side of the heater for a 10% ethyl-alcohol aqueous solution, Re $= 1$ and $L = 6.7\,mm$. (b) Cross-section showing a typical measured profile in the transverse (spanwise) direction.

analysis and the experimental data are quite difficult since we don't know accurately neither the temperature distribution at the wall, nor the heat transfer coefficient at the film surface. Furthermore, our analysis considers an infinite domain, with heaters distributed periodically in the streamwise direction, which is rather far from the experimental conditions of a local heater with edge effects. Despite of that, the main features of the rivulet instability could be captured here and suggest that we can proceed further with three-dimensional simulations.

4.5 3D simulations

The goal of this section is to find qualitative similarities between numerical simulations and experimental data in the nonlinear regime, *i.e.* beyond the instability threshold. For this purpose, we integrate the evolution equation (2.10) using the backward Euler scheme for the time derivative and a spectral method based on Fast Fourier Transform (FFT) for the space derivatives*. We define N_x and N_z as the number of space steps Δx and Δz used to discretize the domain. They should be taken as an integer power of 2 in order to take advantage of the FFT algorithm [102]. The smaller wavenumbers resolved in the grid are thus

$$k_x = \frac{2\pi}{L_x} \quad \text{and} \quad k_z = \frac{2\pi}{L_z}, \tag{4.13}$$

with $L_x = N_x \Delta x$ and $L_z = N_z \Delta z$ the length and width of the computational domain. The film thickness h can be expressed in terms of Fourier series as

$$h_{i,j}(t) \equiv h(x_i, z_j, t) = \sum_{p=-N_x}^{N_x} \sum_{q=-N_z}^{N_z} a_{p,q}(t) \exp\{\mathrm{i}\,(p k_x x_i + q k_z z_j)\} \tag{4.14}$$

where $x_i = i\Delta x$ and $z_j = j\Delta z$ are the coordinates of the regularly spaced grid points; $a_{p,q}(t)$ is a complex amplitude of the corresponding harmonic. Because h must be real, and the Fourier modes are linearly independent, we have

$$a_{p,q}(t) = a^*_{-p,-q}(t), \quad \forall p, q,$$

where the star denotes the complex conjugate.
The method consists in evaluating the nonlinear terms of (2.10) in the real space after calculating h and its space-derivatives separately in the Fourier space. As just mentioned, the time increment is performed in the Fourier space using the backward Euler scheme:

$$\frac{a_{p,q}^{(n+1)} - a_{p,q}^{(n)}}{\Delta t} = -f(a_{p,q}^{(n)}), \tag{4.15}$$

where Δt is the time step and $a_{p,q}^{(n)}$ is the complex Fourier coefficient obtained at time $t_n = n\Delta t$. The function $f(a_{p,q}^{(n)})$ contains all the terms involving the space derivatives

*The FFT algorithm decreases sensitively the number of operations from N^2 to $N \log N$, where N is the number of spatial discretization points (or Fourier modes) of the periodic domain.

resulting from the substitution of (4.14) into (2.10). In order to improve the stability of the numerical scheme (4.15), the linear part of $f(a_{p,q}^{(n)})$ can be evaluated implicitly. Actually, this linear part can be expressed in the Fourier space as an operator $F_{p,q}^{linear}$ acting on $a_{p,q}^{(n)}$. In this case, (4.15) is rewritten as

$$(1 + \Delta t F_{p,q}^{linear}) a_{p,q}^{(n+1)} = a_{p,q}^{(n)} - \Delta t \left(f(a_{p,q}^{(n)}) - F_{p,q}^{linear} a_{p,q}^{(n)} \right). \tag{4.16}$$

Practically, the experience showed that the surface tension term is the stiffest in terms of numerical convergence. Its linearized form is

$$F_{p,q}^{linear} = -\frac{\mathrm{Ka}}{3} k_{p,q}^4 \tag{4.17}$$

where $k_{p,q} = \sqrt{\left(k_x^{(p)}\right)^2 + \left(k_z^{(q)}\right)^2}$ is the modulus of the two-dimensional wavevector. Finally, we evaluate $a_{p,q}^{(n+1)}$ from (4.16) and determine the film thickness $h_{i,j}^{(n)}$ by inverse Fourier transform.

Some results of simulations using the evolution equation (2.10), are presented below for a film flowing along a vertical plate ($\mathrm{Ct} = 0$) where a periodic array of heaters is embedded. The temperature distribution in one period is given by (4.2). Because this $f(x)$ produces permanent deformations, but is z-invariant, we first ran the code in two dimensions with $N_z = 1$. Moreover, it allowed us to check the validity of the 2D simulated profiles with those obtained by continuation using AUTO97 [30] and presented in figure 4.5. The 2D-profile once steady, is extended in the $z-$direction, and the 3D simulation is then started with additional random perturbations of 10^{-2} amplitude at each grid point. A good convergence was found in the simulation presented below with $N_x = N_z = 128$ and $\Delta t = 10^{-2}$.

As already said, the experimental Biot number should be much smaller than unity by two or three orders of magnitude [64]. However, changing its value does not change significantly neither the bump shape, nor the instability threshold. On the contrary, small values of Bi lead to considerable slowing down of the manifestation of the thermocapillary instability. Indeed, the linear growth rate of the most unstable disturbance, among pure spanwise thermocapillary modes in a vertical film flow, is proportional to Bi^2 (see s_m given by (1.88) with $\mathrm{Ct} = \mathrm{Re} = 0$, together with (1.46)). Therefore, we increased the Bi in simulations in order to save computational time.

In figure 4.14, the evolution of a vertical film with non-uniform heating is shown for $\mathrm{Re} = 0.5$, $\mathrm{Ma} = 10$, $\delta_\mathrm{w} = 2$, $\mathrm{Ka} = 500$, $\mathrm{Bi} = 0.4$, $L_x = 200$, $L_z = 400$ and $L_w = 10$. The random perturbations are damped during the initial period and the film profile looks invariant spanwise at $t = 50$. As the liquid drains downward, the surface-wave instability (H-mode) dominates as shown at time $t = 100$ and $t = 200$. Here, the local phase speed of the interfacial wave is proportional to its thickness as predicted by linear theory (see 2.18). As time progresses, the thinning of the liquid layer becomes more pronounced in some places and thermocapillarity begins to determine the growth of deformations by displacing the fluid from hotter troughs to colder crests ($t = 300$). The Marangoni number has been chosen for the system to lie in the non-localized regime, *i.e.* $\mathrm{Ma} < \mathrm{Ma}_\mathrm{tr}$. It is therefore non surprising if the instability starts

downstream the bump since there the eigenfunction of the linear problem is non-zero. In the non-localized regime, the bump itself keeps its initial shape at this stage and doesn't seem to play a role at the instability onset. Furthermore, at $t = 400$ the resulting three-dimensional pattern develops nearly isotropically as for an horizontal layer (see Oron [95]). This occurs even in the second half of the domain where the imposed temperature decreases streamwise. Next, in the absence of the main flow in the spanwise direction, the liquid is displaced laterally due to thermocapillarity ($t = 500$). Consequently, the previous pattern evolves in rivulets aligned with the flow ($t = 600$). Those rivulets connect quickly with the bump ($t = 700, 800$) and continue to get amplified in the spanwise direction ($t = 900$), up to spontaneous rupture, as described by Joo *et al.* [54] for uniform heating (see also §7.3.3).
The simulation are stopped for $h < 10^{-3}$ where the molecular forces should be taken into account near very thin parts of the film. We consider in this case that the film ruptures and forms dry spots. The last snapshot before this rupture is presented in figure 4.15a. A secondary structure can be observed here in the form of small rivulets in the valley between main ones. A cross section in the spanwise direction at mid-domain shows clearly this secondary structure in figure 4.15b. Note that this structure is also visible in experiments (see figure 4.12a). This process is similar to the evolution of a horizontal thin film heated from below [76]. Boos & Thess [11] identified the mechanism of this secondary stage as a cascade of similar thermocapillary instability but at a different scale. The mechanism proposed by Boos & Thess is as follows: due to the presence of the bottom plate the viscous force under the depressed parts of the surface is larger than in higher regions. By contrast, the thermocapillary force on the lateral surfaces of the valley is larger than on its bottom surface. At some distance from the bottom this difference in acting forces causes the film surface near the trough to flatten. This flat zone increases and can be unstable exactly as the initial flat film was at the onset of the primary instability (at least in the spanwise direction and if $\mathrm{Bi} \neq 0$). However, there are some differences. In contrast to the initial deformation the new structure is located between two elevated regions which have an influence on its behaviour (say an 'imperfect boundary bifurcation').
Figure 4.15c presents cross-sections in the streamwise direction at different positions of the left-side rivulet of figure 4.15a. The similarity between profiles is noticeable. Nevertheless, we see that the amplitude $h_{max} - h_{min}$ is minimum at the crest of the rivulet (dotted line) and maximum at the trough (solid line). Moreover, the latter profile indicates the imminent formation of a dry spot where the downstream side of the bump is approaching the wall.
Figure 4.16a shows the value of the slope at the film surface for the same case as for figure 4.15a. The 'absolute' slope is calculated from the relation $\partial_n h = \sqrt{(\partial_x h)^2 + (\partial_z h)^2}$. The grey scale indicates the amplitude of the slope. The white zones are flat. A direct comparison can be made with experimental 2D Schlieren picture [117] as shown in figure 4.16b. To each grey level corresponds an absolute slope as for figure 4.16a. The shape and size of rivulets, the secondary structure and the location of initial film breakdown are qualitatively similar between the experimental picture and the simulation. Nevertheless, the absence of periodicity in experiments, done for one localized heater, brings a significant difference at the level

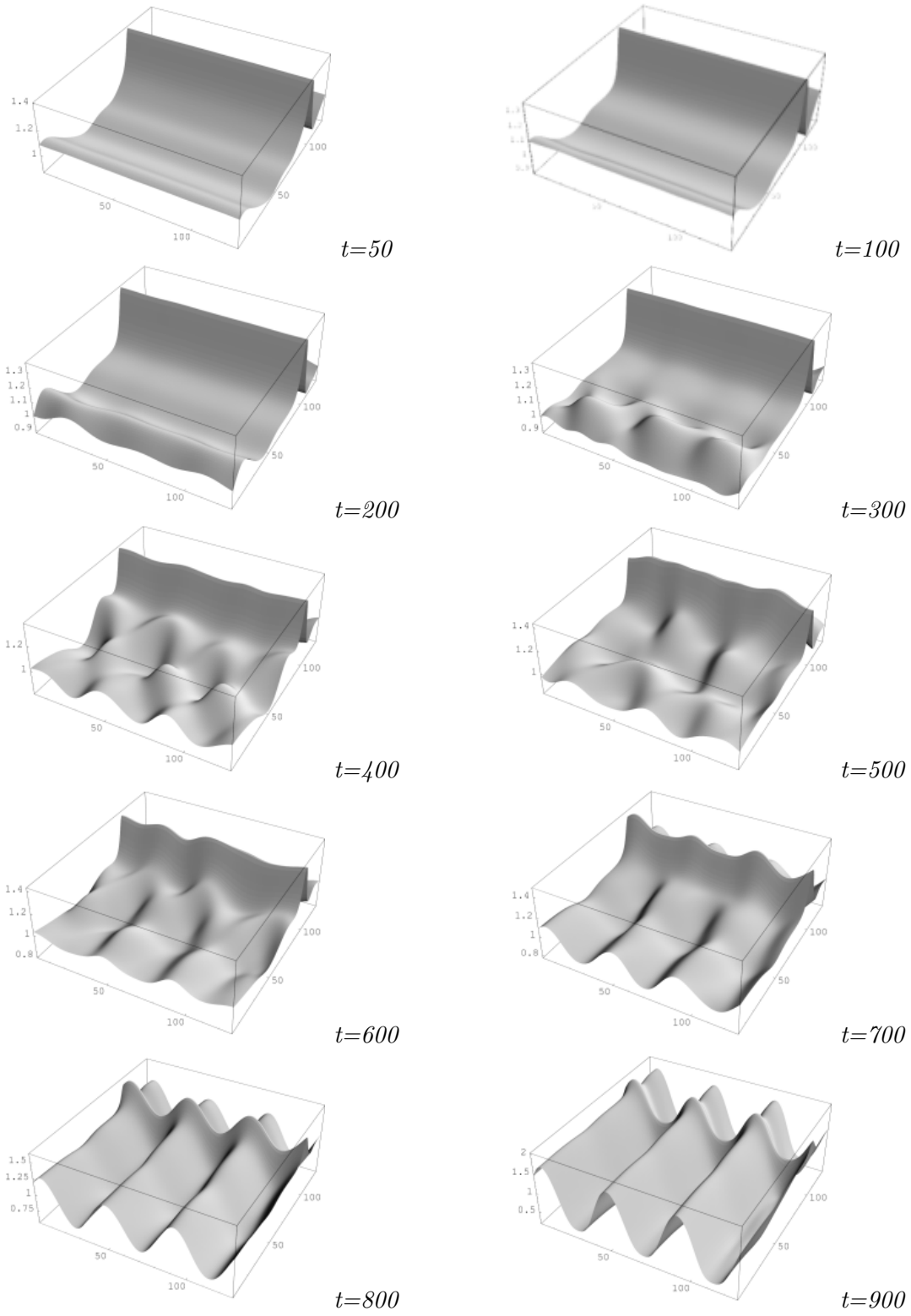

Figure 4.14: Time-dependent simulations for Re = 0.5, Ma = 10, $\delta_w = 2$, Ka = 500, Bi = 0.4, $L_x = 200$, $L_z = 400$ and $L_w = 10$. The spatial grid is 128×128 points. The film flows from the right top border to the left bottom border of each pictures.

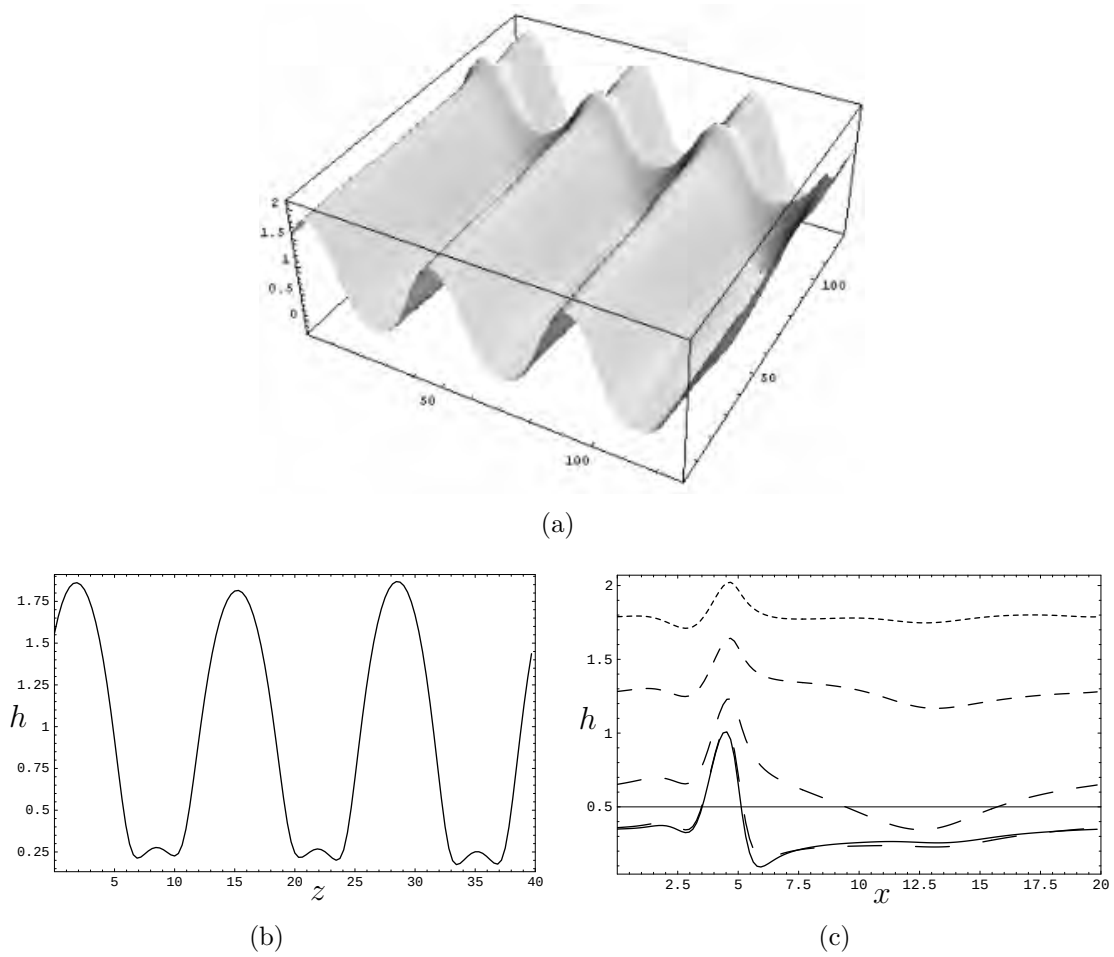

Figure 4.15: (a) Snapshot corresponding to the case of figure 4.14 at $t = 920$. It corresponds to the moment just before the film ruptures. (b) Cross-section of (a) in the spanwise direction at the mid-domain in x. (c) Cross-section in the streamwise direction corresponding to different positions around the left-side rivulet of (a).

of the horizontal bump.

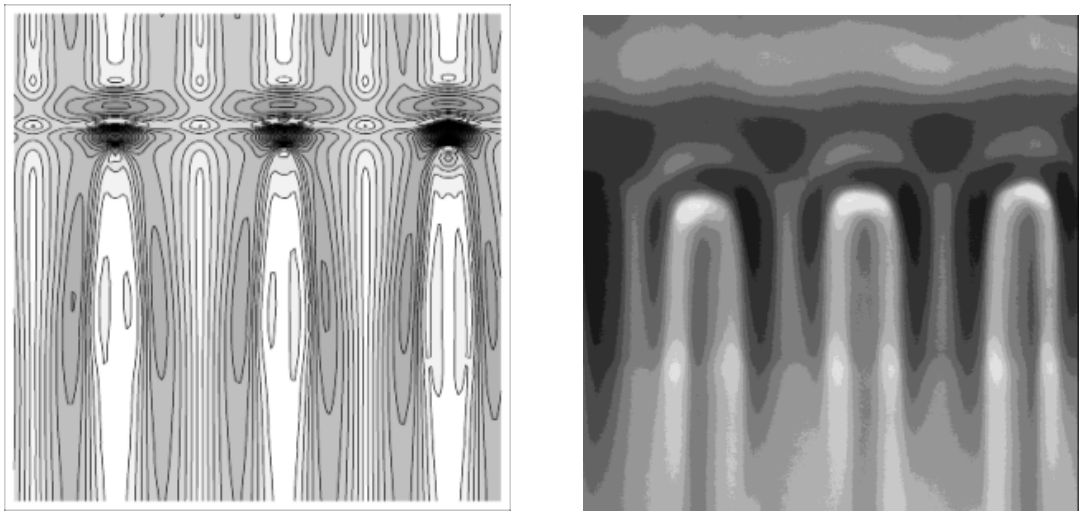

(a) (b)

Figure 4.16: (a) Absolute slope $|\partial_n h|$ of the interfacial deformations corresponding to the case of figure 4.15a. The grey level quantifies the amplitude of the slope, black means minimum and white maximum. (b) 2D Schlieren image providing the experimental measurements of the slope at the film surface for the regime with rivulet structure. The brighter zones corresponds to small deflections while the darker zones to larger ones.

Finally, still in relation with the film thickness calculated in figure 4.15a, we recover the temperature distribution and the velocity field at the film surface. Actually, within the long-wave approximation, those quantities are slaved to the film thickness and given by (2.2) together with (2.4) and (2.8) up to first-order. They read, at the film surface $y = h$ and for a vertical wall $\mathrm{Ct} = 0$,

$$u\big|_h = \frac{h^2}{2}\left(1 + \mathrm{Ka}(\partial_{xxx}h + \partial_{xzz}h)\right) - \mathrm{Ma}h\partial_x\theta^{(0)} + \frac{5}{4}h^5\partial_x h \qquad (4.18)$$

$$w\big|_h = \frac{h^2}{2}\mathrm{Ka}(\partial_{xxz}h + \partial_{zzz}h)) - \mathrm{Ma}h\partial_z\theta^{(0)} \qquad (4.19)$$

$$\theta = \theta^{(0)} + \frac{1}{120}\mathrm{PrBi}h^4\left(\theta^{(0)}\right)^3\partial_x h\left(-15 + 7\mathrm{Bi}h\right) \qquad (4.20)$$

$$\text{with} \quad \theta^{(0)} = \frac{1 + \delta_{\mathrm{w}} f}{1 + \mathrm{Bi}h}$$

Figure 4.17 shows the temperature field. The maximal temperatures are located where the film thinning is maximum, *i.e.* between two rivulets immediately downstream the bump. Also, the liquid is colder in a rivulet than in a trough, what keeps up the thermocapillary forces.
The surface velocity vectors represented in figure 4.18 evidence the lateral thermocapillary flow. Furthermore, a reverse flow takes place between rivulets and is maximum

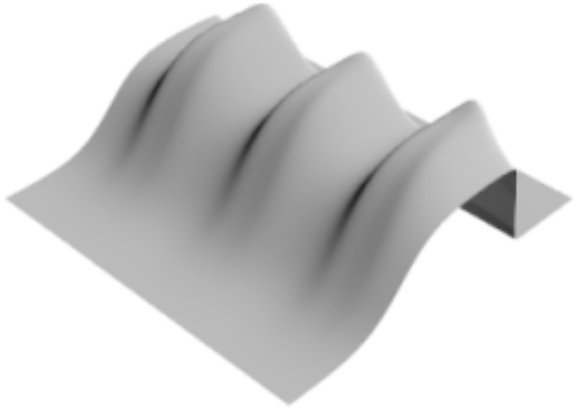

Figure 4.17: Temperature profile at the film surface given by (4.20) and corresponding to the case of figure 4.15a

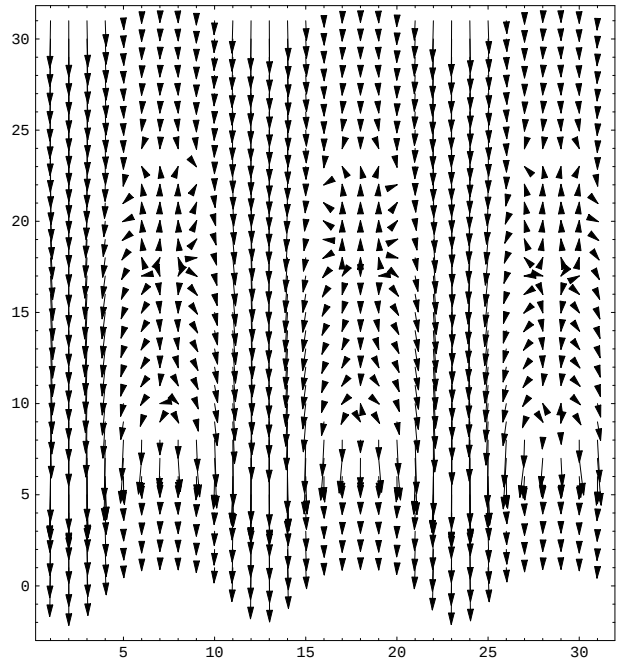

Figure 4.18: Vector plot of the velocity field at the film surface given by (u, w) (4.18,4.19) corresponding to the case of figure 4.15a. It shows a reverse flow between rivulets, as well as stagnation points also observed experimentally [117, 64].

along the crest of the secondary structure. It drains the liquid upstream, driven by the thermocapillary flow existing on the downstream face of the bump. Consequently, a stagnation point should exist at the crest of the bump where the gravity driven flow counteracts this reverse thermocapillary flow (actually, this is possible by the negative sign of the Marangoni term in (4.18)). The presence of a reverse flow has also been evidenced experimentally [64]. Figure 4.19 shows the results of particle tracking at the film surface [117]. Particles of aluminum powder are blown intermittently on the

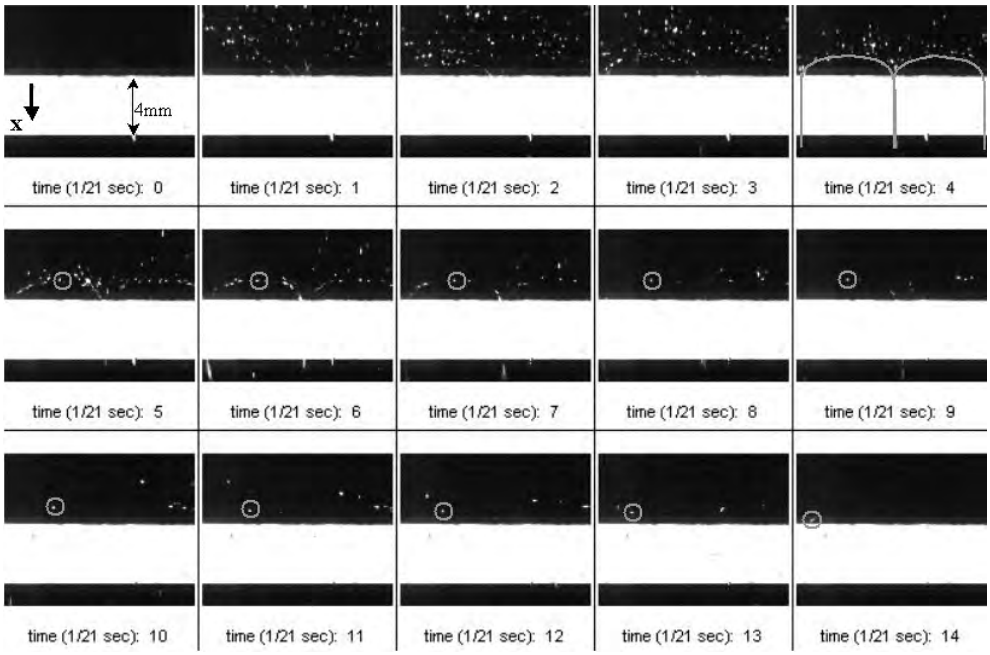

Figure 4.19: Sequence of particle tracking evidencing the stagnation point at the top of the horseshoe structure, the pattern of which is drawn on the top-right snapshot. The white zone is the heater, $\mathrm{Re} = 1$ and $\mathrm{Ma} > \mathrm{Ma_c}$.

film surface and follow the streamlines surrounding the horseshoe structures formed by the bump and the rivulets (see the top-right snapshot). While all the particles flow down, one of them, encircled, sits exactly at the top of the horseshoe structure, showing the presence of the stagnation point. With time, and because the particle is of finite size, it flows slowly, here towards the left rivulet. The distance between the upstream edge of the heater and the stagnation point is about 1 *mm* in experiments but near zero in simulations. Recently, Frank [35] has performed direct 3D numerical simulations, *i.e.* from the Navier-Stokes/Fourier equations. He used a numerical "method of particles" [35] and studied the development of rivulet instability due to localized heating. Among other, he obtained quantitatively the correct shift of 1 mm between the heater and the stagnation point. This shift is attributed to the presence of heat convection that is neglected in our model.
On a general point of view, the rivulet structures obtained in our simulations always lead to film rupture. Nevertheless, structures obtained in experiments are steady (except at larger heat fluxes where dry spots formation occurs), as for figure 4.16a.

Frank [35] also obtained steady rivulet structures without dry spots in its direct simulations, enforcing an open flow condition. The explanation can be found in the difference between closed and open flows (see §2.4). Indeed, because we imposed periodic boundary conditions (mainly to take benefit of the good convergence of the spectral method) we have inherently imposed a closed flow condition. At the same time, we have imposed a non-homogeneous temperature boundary condition at the wall. Our system therefore corresponds to an infinite array of heaters placed in the streamwise direction rather than to a localized heater. The liquid is thus heated periodically, the destabilizing thermocapillary effect is maintained and the amplitude of the rivulets increases until the film reaches its rupture. It happens roughly in the same way than for the spontaneous rupture of a thin horizontal layer homogeneously heated from below [76, 141, 95]. In experiments, the situation is rather different since the flow is open and the fluid flows only over one localized heater. The heating stops after the heater and the only reason why the rivulets keep their shape far downstream the heater in the experiments is due to the poor heat transfers at the insulating wall and at the liquid-gas interface; hence the temperature difference between the crests and the troughs of rivulet vanishes slowly, still yielding a thermocapillary force on the sides of the valley.

Since the results by Frank [35] using the Navier-Stokes/Fourier equations are in excellent agreement with the experimental data (about the bump shapes, the instability threshold, the wavelength increase with Ma, the steady rivulet structure, the secondary structure, and the reverse flow), we believe that using a numerical scheme allowing for an open flow, *i.e.* non-periodic boundary conditions, could provide a satisfactory agreement still using the Benney equation as performed in this chapter. This will be the subject of a future work.

Let us finally remark that the ethyl-alcohol aqueous solution is a mixture rather than a pure liquid. Therefore, the evaporation and solutocapillary effects, caused by gradients of surface concentration, can contribute to the formation or not of the rivulet pattern and of dry spots. The mixture in our experiments is 'negative'. That means that the more volatile fluid (alcohol) has the smallest surface tension (compared to water). Therefore, since the evaporation is more intense in the troughs of depressions than in the crests of elevations, the alcohol concentration is larger at the crests than at the troughs. The concomitant solutocapillary effect would then act in the opposite way than the thermocapillary effect. This argument ensures that evaporation is not playing a significant role, at least at the onset of instability. On the contrary, it might well be of crucial importance in the region of secondary structures where the film thinning is maximum.

Part II

Moderate Reynolds number: the weighted integral boundary layer models

Chapter 5

The weighted residual method

Within the context of integral boundary layer (IBL) model, thermocapillary effects have been taken into account by Zeytounian [149] who derived a three-equations model in terms of the local film thickness, the flow rate and the mean temperature across the layer. However, since the coupling between the temperature and velocity fields arises through the tangential stress balance at the interface, it is more appropriate to choose a weighted residuals approach (see §5.1) for the energy equation that would give more importance on the interfacial temperature so that points near the interface have a 'larger weight' than points near the solid boundary. Such a formulation was proposed by Kalliadasis *et al.* [67] who also recovered the BE as a limit of their IBL model for reasonably low Reynolds and Péclet numbers where the temperature and velocity field are effectively slaved to the kinematics of the flow through the film thickness. Kalliadasis *et al.* showed that the onset of the long-wave instability, of either H- or S-type, can be described by the Kuramoto-Sivashinsky equation or the Kawahara equation (2.14) if dispersion is taken into account [72]. These authors also demonstrated that the BE and IBL models give similar solitary wave solutions up to an $\mathcal{O}(1)$ Reynolds number above which the BE is unrealistic with limit points and branch multiplicity. IBL on the other hand has no limit points and predicts the existence of solitary waves for all Reynolds numbers. Nevertheless, the IBL model obtained by Kalliadasis *et al.* [67] for the heated falling film suffers from the same limitations as the Shkadov IBL model for isothermal films, i.e. it does not predict accurately the behaviour of the film close to criticality (and is qualitative in this sense).

Our purpose here is to overcome the limitations of the model equations derived by Kalliadasis *et al.* [67]. In addition, we wish to introduce the second-order dissipative effects that are known to determine the amplitude of the front-running capillary waves in the case of isothermal flows [109, 110]. These second-order viscous terms were neglected in the formulation by Kalliadasis *et al.* [67] though they indeed play an important role in the dispersion of waves for larger Reynolds numbers. The procedure followed here is effectively an extension of the methodology applied in the case of isothermal flows by Ruyer-Quil & Manneville [109, 110] and is based on a high-order weighted residual approach with polynomial expansions for both velocity and temperature fields (§5.1). This leads to two model equations at first (§5.2) and second-

order (§5.3) in the film parameter. However, these equations are complex and hence not convenient for practical applications. A procedure is then described in §5.4 that enables us to simplify our set of equations and to formulate models fully compatible with the Benney expansion up to second order. This approach results in systems of three coupled nonlinear partial differential equations for the evolution of the local film thickness, the flow rate and the interfacial temperature. A discussion concludes the chapter (§5.5).

5.1 Weighted residuals approach

We now apply the polynomial expansion approach developed by Ruyer-Quil & Manneville [109] for isothermal films. The basic idea is to separate the variables and to expand the velocity and temperature fields on a set of test functions depending on the reduced coordinate $\bar{y} = y/h$ which is a natural reduced variable as it converts the boundary-value problem in the interval $[0, h]$ to a problem in $[0, 1]$. To satisfy the boundary conditions

$$u\big|_0 = v\big|_0 = 0 \quad \text{and} \quad T\big|_0 = 1 \tag{5.1}$$

defining the velocity and temperature distributions at the wall, we write

$$u(x,y,t) = \sum_{i=0}^{i_{\max}} a_i(x,t) f_i\left(\frac{y}{h(x,t)}\right) \tag{5.2a}$$

$$T(x,y,t) = 1 + \sum_{i=0}^{i_{\max}} b_i(x,t) g_i\left(\frac{y}{h(x,t)}\right) \tag{5.2b}$$

where $f_i(0) = g_i(0) = 0$.
It is appropriate to choose polynomial test functions for at least two reasons:

(i) our analysis is based on the assumption of slow modulations of the basic state solution which corresponds to a parabolic velocity profile and a linear temperature distribution. Therefore, it is necessary to introduce the flat film solution (1.43a,d) into the expansion. Note that polynomials as solutions are also suggested by the zeroth and first-order solutions obtained from the long-wave expansion (see 2.4 and 2.8);

(ii) polynomials form a closed set with respect to differentiations and products appearing in the boundary layer model (1.101).

Let us therefore choose

$$f_0 = \bar{y} - \frac{1}{2}\bar{y}^2 \tag{5.3a}$$

$$g_0 = \bar{y}\,, \tag{5.3b}$$

corresponding to the basic state (1.43a,d) and complete the set of test functions with

$$f_1(\bar{y}) = \bar{y}, \qquad f_i(\bar{y}) = \bar{y}^{i+1},\ i \geq 2 \tag{5.3c}$$

$$g_i(\bar{y}) \;=\; \bar{y}^{i+1},\; i \geq 1\,, \tag{5.3d}$$

to obtain the polynomial bases for the projection. Note that the Dirichlet conditions (5.1) are then automatically satisfied.
Since $2i_{\max}+3$ unknowns have been introduced, namely h, a_i and b_i, $2i_{\max}+3$ equations should be written to determine them. The first one is the kinematic condition at the interface (1.101d) which can be replaced by integrating the continuity equation (1.101a) along the normal coordinate to give

$$\partial_t h + \partial_x q = 0\,, \tag{5.4}$$

where $q = \int_0^h u\,dy$ is the flow rate in the streamwise direction. Two additional equations are the boundary conditions (1.101e,f). Defining the weight functions $w_j(\bar{y})$, $1 \leq j \leq 2i_{\max}$, the final equations are obtained by the vanishing residuals

$$\begin{aligned}\mathcal{R}_q(w_j) \;\equiv\; & \int_0^h w_j(\bar{y})\,[\partial_t u + u\partial_x u + v\partial_y u - (\partial_{yy}+2\partial_{xx})u \\ & -1 + \mathrm{Ct}\partial_x h - \partial_x[\partial_x u\big|_h] - \mathrm{Ka}\partial_{xxx}h]\,dy = 0\,, \end{aligned}\tag{5.5a}$$

$$\mathcal{R}_T(w_{i_{\max}+j}) \;\equiv\; \int_0^h w_{i_{\max}+j}\,[\mathrm{Pr}(\partial_t T + u\partial_x T + v\partial_y T) - (\partial_{xx}+\partial_{yy})T]\,dy = 0\,, \tag{5.5b}$$

where $v = -\int_0^y \partial_x u\,dy$ and the velocity and temperature expansions (5.2) will be substituted.
At this point, the method we are using is simply one of the numerous weighting residual strategies which differ from each other only by the specific choice of the weights w_j. As pointed out in previous studies dealing with the isothermal case (see Ruyer-Quil & Manneville [109, 110]), it is not necessary to specify the weighted residuals method we are applying on condition that the number ($i_{\max}$) of test functions and residuals is large enough. Indeed, requiring the momentum and the energy equations (1.101b) and (1.101c) to be satisfied everywhere – and not simply on average –, and inserting the expansions (5.2,5.3) leads to the cancellation of two polynomials in the reduced normal coordinate $\bar{y}$. Then it can be proven by examining the order of magnitude with respect to ε of each term in (1.101b) and (1.101c) that the number of independent conditions on the unknowns a_i and b_i provided by the cancellation of these two polynomials would be equal to the number of the residuals (5.5) if $i_{\max}$ is precisely chosen large enough [110]. If so, any choice of the weighting functions would lead to equivalent systems of equations and then to the same reduced model for the dynamics of the flow, as was the case for an isothermal film [109].
Nevertheless, it is important to keep in mind that we are not simply applying a numerical method to the problem at hand. Our approach is rather to combine some well known numerical strategy (here, in essence, a Galerkin method as seen below) with a perturbation technique to the flat film basic state (1.43a,d) corresponding to

$$a_0 = h^2\,, \qquad b_0 = -\mathrm{Bi}h/(1+\mathrm{Bi}h)\,, \qquad a_i = b_i = 0\,, \qquad i \geq 1.$$

It will thus be helpful to get some information about the different unknowns as compared to the film parameter ε, knowing that any terms of order higher than ε^2 may be dropped during the process.

5.2 Formulation at first order

To illustrate our procedure, let us temporarily restrict our problem to the first order, that is to the formulation consistent at $\mathcal{O}(\varepsilon)$, with all terms of higher order neglected. This is a helpful step for the choice of the simplest methodology to use for the projection of the velocity and temperature fields to the amplitudes of the polynomial expansion appearing at first order. Thus the system of equation (1.101) at $\mathcal{O}(\varepsilon)$ is simplified into

$$\partial_x u + \partial_y v = 0 \tag{5.6a}$$

$$\partial_t u + u\partial_x u + v\partial_y u = \partial_{yy} u + 1 - \mathrm{Ct}\partial_x h + \mathrm{Ka}\partial_{xxx} h \tag{5.6b}$$

$$\mathrm{Pr}\left(\partial_t T + u\partial_x T + v\partial_y T\right) = \partial_{yy} T \tag{5.6c}$$

$$\partial_t h + u\partial_x h = v\big|_h \tag{5.6d}$$

$$\partial_y u\big|_h = -\mathrm{Ma}\partial_x \left[T\big|_h\right] \tag{5.6e}$$

$$\partial_y T\big|_h = -\mathrm{Bi} T\big|_h, \tag{5.6f}$$

together with the Dirichlet conditions (5.1). Thus, the residuals to evaluate are simplified to

$$\begin{aligned} \int_0^h w_j(\bar{y}) \left[\partial_t u + u\partial_x u + v\partial_y u - \partial_{yy} u\right] dy & \\ + h\left[-1 + \mathrm{Ct}\partial_x h - \mathrm{Ka}\partial_{xxx} h\right] \int_0^1 w_j(\bar{y}) d\bar{y} &= 0\,, \end{aligned} \tag{5.7a}$$

$$\int_0^h w_{i_{\max}+j}(\bar{y}) \left[\mathrm{Pr}(\partial_t T + u\partial_x T + v\partial_y T) - \partial_{yy} T\right] dy = 0\,, \tag{5.7b}$$

where contributions from surface tension effects have been conserved. The amplitudes a_i and b_i, $i \geq 1$ result from the slow space and time modulations of the free surface so that they are at least first-order quantities in ε. Therefore, the space and time derivatives of a_i and b_i, $i \geq 1$ are negligible. One then is led to a linear system for a_i and b_i whose coefficients depend at most on a_0, b_0, h and with a right-hand-side that depends on h, a_0, b_0 and their derivatives

$$\sum_{j'=1}^{2i_{\max}} \alpha_{jj'} A_{j'} = \beta_j(h, a_0, b_0, \partial_{x,t} h, \partial_{x,t} a_0, \partial_{x,t} b_0), \qquad 1 \leq j \leq 2i_{\max}, \tag{5.8}$$

where $A_j \equiv a_j$ and $A_{i_{\max}+j} \equiv b_j$, $1 \leq j \leq i_{\max}$. Solving for the A_j leads to explicit formulations of the amplitudes a_j, b_j as functions of a_0, b_0, h and their derivatives, making clear their slaving to the dynamics of the film thickness, and of amplitudes of the parabolic velocity profile and of the linear temperature distribution. Thus, substituting these expressions for a_j and b_j (that will be explicitely formulated below) would lead to a set of three evolution equations for h, a_0 and b_0 modelling the entire dynamics of the film flow.

As was pointed out above, inserting the expansion (5.2, 5.3) in (5.6) leads to the cancellation of two polynomials in the reduced normal coordinate $\bar{y}$, say $\mathcal{P}(\bar{y})$ and $\mathcal{Q}(\bar{y})$, corresponding to the momentum and heat equation, respectively. Because the advection terms $\partial_t u + u\partial_x u + v\partial_y u$ and $\partial_t T + u\partial_x T + v\partial_y T$ are first order quantities, their truncation at $\mathcal{O}(\varepsilon)$ involves only the parabolic and linear profiles corresponding to a_0 and b_0. Consequently, it can be checked that the advection terms are polynomials in $\bar{y}$ of degree four and three only. Therefore, the monomials of highest degree appearing in $\mathcal{P}(\bar{y})$ and $\mathcal{Q}(\bar{y})$ originate from the terms $\partial_{yy} u$ and $\partial_{yy} T$ so that $\mathcal{P}(\bar{y})$ and $\mathcal{Q}(\bar{y})$ are of degree $i_{\max} - 1$. Cancelling those two polynomials give $2i_{\max}$ independent relationships, i.e. the same as the number of residuals (5.7) so that they are equivalent systems of equations leading to the same evolution equations for h, a_0 and b_0 through its $x-$derivative (provided $i_{\max}$ is large enough). Because each different weighting residual technique only differs by its specific definitions for the weighting functions w_j, it is relevant to look for the best choice of w_j that would simplify the algebraic manipulations.

First, let us consider more specifically the residuals (5.7a). Because $\partial_t u + u\partial_x u + v\partial_y u$ are first order terms, the unknowns a_i, $i \geq 1$ may enter into their evaluation only through the integral $\int_0^h w_j \partial_{yy} u$. Two integrations by parts give

$$\int_0^h w_j \left(\frac{y}{h}\right) \partial_{yy} u \, dy = \left[w_j \left(\frac{y}{h}\right) \partial_y u \right]_0^h - \frac{1}{h} \left[{w_j}' \left(\frac{y}{h}\right) u \right]_0^h + \frac{1}{h^2} \int_0^h {w_j}'' \left(\frac{y}{h}\right) u \, dy \,. \quad (5.9)$$

Because $\partial_y u\big|_h$ given by equation (5.6e) is proportional to $\partial_x [T\big|_h]$, at first order it may only involve h, a_0 and b_0. Making also use of the no-slip condition on the plate, $u\Big|_0 = 0$, only three terms are left to consider, namely $w_j(0)\partial_y u\Big|_0$, ${w_j}'(1) u\Big|_h$ and $\int_0^h {w_j}'' \, (y/h) \, u \, dy$. With the introduction of the flow rate $q \equiv \int_0^h u \, dy$, this suggests to choose w_0 to verify $w_0(0) = 0$, ${w_0}'(1) = 0$ and ${w_0}''$ a constant. Interestingly enough, f_0 (5.3a) shares exactly the same characteristics such that we can set merely* $w_0 \propto f_0$. Now it seems appropriate to relate the amplitude of the parabolic profile a_0 to the flow rate q, which is a physical quantity appearing explicitly in the integral form of

*Remember that the parabolic profile f_0 corresponds to the zeroth-order formulation of the problem for the velocity:

$$\partial_{yy} u = -1 \,, \qquad u\Big|_0 = 0 \,, \qquad \partial_y u\Big|_h = 0 \,. \quad (5.10)$$

Therefore, considering the two integrations by parts performed in (5.9), such a similitude – between the weight function w_0 and the test function f_0 – is obviously related to the fact that the linear operator $L \equiv \partial_{yy}$ is self adjoint in the space of functions satisfying the boundary conditions (5.10).

the kinematic condition (5.4). To introduce q explicitly into our expansion let us integrate (5.2) between 0 and h to obtain the expression

$$a_0 = 3\frac{q}{h} - \frac{3}{2}a_1 - \sum_{i=2}^{i_{\max}} \frac{3}{i+2} a_i \,. \tag{5.11}$$

Therefore, evaluating the residual (5.7a) corresponding to $j = 0$ with $w_0 \propto f_0$ leads to

$$\begin{aligned} &\frac{2}{5}\partial_t q - \frac{23}{40}\frac{q}{h}\partial_t h - \frac{18}{35}\frac{q^2}{h^2}\partial_x h + \frac{111}{280}\frac{q}{h}\partial_x q + \frac{q}{h^2} \\ &+\frac{1}{2}\mathrm{Ma}\partial_x\left[T\Big|_h\right] + \frac{1}{3}h\left[-1 + \mathrm{Ct}\partial_x h - \mathrm{Ka}\partial_{xxx} h\right] \;=\; 0\,, \end{aligned} \tag{5.12}$$

where the unknowns a_i do not appear (as a consequence of our weighting strategy). Choosing the weight functions to be the test functions themselves is the essence of the Galerkin method which is equivalent to a variational method, whenever a variational formulation is available (Finlayson [33]).
Turning to the weighted residuals for the heat equation (5.7b) and with the same arguments, the unknowns b_i, $i \geq 1$ may only play a role through the integral $\int_0^h w_j \partial_{yy} T$. Two integrations by parts give

$$\int_0^h w_j\left(\frac{y}{h}\right)\partial_{yy}T\,dy = \left[w_j\left(\frac{y}{h}\right)\partial_y T\right]_0^h - \frac{1}{h}\left[{w_j}'\left(\frac{y}{h}\right)T\right]_0^h + \frac{1}{h^2}\int_0^h {w_j}''\left(\frac{y}{h}\right)T\,dy\,. \tag{5.13}$$

Making use of the boundary condition at the surface (5.6f) and the constant temperature distribution at the wall $T\Big|_0 = 1$ we get

$$\begin{aligned} \int_0^h w_j\left(\frac{y}{h}\right)\partial_{yy}T\,dy \;&=\; -\mathrm{Bi}w_j(1)T\Big|_h - w_j(0)\partial_y T\Big|_0 \\ &\quad +\frac{1}{h}\left[{w_j}'(0) - {w_j}'(1)T\Big|_h\right] + \frac{1}{h^2}\int_0^h {w_j}''\left(\frac{y}{h}\right)T\,dy\,. \end{aligned} \tag{5.14}$$

Following exactly the same approach as before would lead to the choice for the first weight function $w_{i_{\max}}(0) = 0$, ${w_{i_{\max}}}'(1) = 0$ and setting ${w_{i_{\max}}}''$ to a constant would introduce the average temperature across the flow, $(1/h)\int_0^h T\,dy$. This choice would obviously be problematic since the term involving $T\Big|_h$ would remain in (5.14) and in (5.12) through the Marangoni term. On the other hand, it is rather the exchanged heat flux at the surface $\partial_y T\Big|_h$ or the temperature at the surface $T\Big|_h$ which have a physical significance. Thus, because it appears in (5.12), we will prefer to put the emphasis on $\theta \equiv T\Big|_h$ by choosing $w_{i_{\max}}(0) = 0$, ${w_{i_{\max}}}'' = 0$ so that $w_{i_{\max}} \propto \bar{y} = g_0$. This choice has the obvious advantage to dissociate the coupling term $\frac{1}{2}\mathrm{Ma}\partial_x\left[T\Big|_h\right]$ in

(5.12) from the definition of any other amplitudes needed to describe the temperature distribution. Again, we find that the Galerkin method is the most effective one, requiring less algebra. It is therefore appropriate to replace the physically meaningless unknown b_0 by θ through the substitution

$$b_0 = \theta - 1 - \sum_{i=1}^{i_{\max}} b_i \,. \tag{5.15}$$

From the residual (5.7b) corresponding to $w_{i_{\max}} = g_0 = \bar{y}$, we then get

$$\mathrm{Pr}\left[\frac{1-\theta}{3}\partial_t h + \frac{1}{3}h\partial_t\theta + \frac{11}{40}(1-\theta)\partial_x q + \frac{9}{20}q\partial_x\theta\right] + \frac{\theta-1}{h} + \mathrm{Bi}\theta = 0\,. \tag{5.16}$$

Now using the equivalence $\partial_t h = -\partial_x q$ given by the integral formulation of the kinematic condition at the surface (5.4), a model consistent at $\mathcal{O}(\varepsilon)$ can be formulated in terms of three coupled evolution equations for h, q and θ

$$\partial_t h = -\partial_x q\,, \tag{5.17a}$$

$$\partial_t q = \frac{5}{6}h - \frac{5}{2}\frac{q}{h^2} - \frac{17}{7}\frac{q}{h}\partial_x q + \left(\frac{9}{7}\frac{q^2}{h^2} - \frac{5}{6}\mathrm{Ct}h\right)\partial_x h - \frac{5}{4}\mathrm{Ma}\partial_x\theta + \frac{5}{6}\mathrm{Ka}h\partial_{xxx}h\,, \tag{5.17b}$$

$$\mathrm{Pr}\partial_t\theta = 3\frac{[1-(1+\mathrm{Bi}h)\theta]}{h^2} + \mathrm{Pr}\left[\frac{7}{40}\frac{(1-\theta)}{h}\partial_x q - \frac{27}{20}\frac{q}{h}\partial_x\theta\right]. \tag{5.17c}$$

This set of equations (5.17) is quite similar to the model derived by Kalliadasis *et al.* [68, 67]. In fact, the first-order averaged heat equation (5.17c) is nearly identical to the corresponding equation derived in these studies. Noticeable differences originate only from a different choice of the scaling of the temperature. The two approaches differ by the treatment of the momentum equation. Equation (5.17b) contains the same terms as in the corresponding equation in Kalliadasis *et al.* [68, 67] but with different coefficients. These modifications originate from a more complete description of the perturbed velocity field which is not limited in the present approach to remain parabolic as in Kalliadasis [68, 67]. In addition, the present approach is based on a Galerkin projection with weight functions as the test functions themselves unlike the Shkadov IBL treatment of the momentum equation in Kalliadasis [68, 67] which is effectively a weighted residual approach using a single test function (the parabolic profile) and a weight function equal to 1.

We now demonstrate that the more systematic procedure employed here enables to recover the correct prediction of the instability threshold obtained by Goussis & Kelly [46]. Recall that resolving the instability threshold inaccurately is the principal drawback of the model analyzed in Kalliadasis *et al.* [67]. The starting point of the linear stability analysis is to introduce in (5.17) perturbations of the Nusselt solution in the form of normal modes with wavenumber k (taken to be real) and complex pulsation Γ,

$$\begin{pmatrix} h \\ q \\ \theta \end{pmatrix} = \begin{pmatrix} h_{\mathrm{N}} \\ h_{\mathrm{N}}^3/3 \\ 1/(1+\mathrm{Bi}\,h_{\mathrm{N}}) \end{pmatrix} + \eta \begin{pmatrix} 1 \\ A_q \\ A_\theta \end{pmatrix} \exp\{\mathrm{i}(kx - \Gamma t)\}, \tag{5.18}$$

and to linearize for $\eta \ll 1$. For the resulting system of linear algebraic equations to have non trivial solutions it is a necessary and sufficient condition that its principal determinant be equal to zero. This gives the dispersion relation that we can write formally as $D(k, \Gamma)$.

In order to compare our linear stability analysis with the one performed by Kalliadasis *et al.* [67] we must introduce the scalings adopted by these authors. In their study, lengthscales were non-dimensionalized with the Nusselt flat film solution $h_{\rm N}$ instead of the lengthscale for viscous gravitational drainage l_ν adopted here. Let us switch then from the *natural* to the *base state set* of parameters as introduced in §1.6. Notice that it implies the transformation $k \to k/h_{\rm N}$ and $\Gamma \to h_{\rm N}\Gamma$ that converts the phase speed $c = \Gamma/k$ as $c \to h_{\rm N}^2 c$. With this scaling, the averaged velocity of the flat film solution is then 1/3. The *base state set* of parameters is effectively the parameters adopted by Kalliadasis *et al.* [67] except that they expressed the Weber number as the ratio of surface tension over inertia forces instead of surface tension over gravitational forces in (1.38).

Performing now a small wavenumber expansion up to first-order of the dispersion relation $D(k, \Gamma;\, {\rm Re}, {\rm Ct},\, {\rm We},\, {\rm Pr},\, {\rm M}^\star,\, {\rm B})$ similar to the one performed by Kalliadasis *et al.* [67] leads to the following expression for the complex phase speed

$$c = 1 + {\rm i}k\left(\frac{2}{5}{\rm Re} - \frac{\rm Ct}{3} + \frac{{\rm M}^\star}{2(1+{\rm B})}\right) - {\rm i}k^3\frac{\rm We}{3} + \mathcal{O}\big(k^2\big) \tag{5.19}$$

where We is considered to be large such that ${\rm We}\,k^2 = \mathcal{O}(1)$ (in thin film studies this order of magnitude assignment is commonly referred to as 'the strong surface tension case'). Note that the above expansion only yields the root of the dispersion relation that can become unstable. As was pointed out by Kalliadasis *et al.* [67] the other two roots are always stable. The neutral stability condition is now easily found to be

$$c = 1, \quad k = \sqrt{\frac{1}{\rm We}\left(\frac{6}{5}{\rm Re} - {\rm Ct} + \frac{3{\rm M}^\star}{2(1+{\rm B})}\right)} = 0\,, \tag{5.20}$$

which is indeed identical to (1.85) at $\mathcal{O}(k)$, obtained from small wavenumber expansion of the Orr-Sommerfeld eigenvalue problem of the basic Navier-Stokes/Fourier equations. Therefore, the linear waves propagate with a velocity at three times the averaged velocity or twice the interfacial velocity of the flat film. From (5.20) we also notice that increasing the Reynolds number or Marangoni number enlarges the range of unstable wavenumbers while decreasing β or increasing the Weber number has a stabilizing effect.

The critical condition at instability onset (1.84a) has the same functional form as the one derived by Kalliadasis *et al.* [67] for two-dimensional waves at criticality, but some of the coefficients are different: $\frac{6}{5}$ instead of 1 in front of the Reynolds number, i.e. a 20% error and $\frac{3}{2}$ in front of the Marangoni number instead of $\frac{1}{2}$ due to a factor of 3 introduced in the definition of the Marangoni number by Kalliadasis *et al.* [67]. Notice that here we try as much as possible to avoid numerical factors in the definitions of the dimensionless groups – an exception to this rule being the

definition of the Reynolds number – so that numerical factors in the equations do not change with different scalings. Now the discrepancy for the coefficient in front of the Reynolds number corresponds exactly to the one observed using the Shkadov model [126] in the case of an isothermal flow ($M^\star = 0$). This inaccuracy has been cured here by using a more complete description of the velocity field [109], which fully corrects the critical Reynolds number. Notice also that as was pointed out by Kalliadasis *et al.* [67], the Benney long-wave lubrication model for the heated falling film yields the correct critical condition (see 2.19). This is not surprising since the long-wave expansion is exact close to criticality (see our discussion in §2.1).

Let us now consider a falling film whose inclination angle, temperatures at the wall and in the air and all physical quantities are fixed such that the sole control parameter is the liquid flux at the inlet or equivalently the Reynolds number $\mathrm{Re} \propto h_\mathrm{N}^3$. From the *base state set* of parameters, one has $M^\star \propto 1/h_\mathrm{N} \propto \mathrm{Re}^{-1/3}$, $\mathrm{We} \propto 1/h_\mathrm{N}^2 \propto \mathrm{Re}^{-2/3}$ and $\mathrm{B} \propto \mathrm{Re}^{1/3}$. Therefore, in the limit of a vanishing Reynolds number, inertia effects are negligible and the Marangoni effect is very strong. This corresponds to the S-mode described by Scriven & Sterling [125]. In this region of small film thicknesses the destabilizing forces are interfacial forces due to the Marangoni effect (capillary forces are always stabilizing). Since now $M^\star/\mathrm{We} \propto \mathrm{Re}^{1/3}$, the critical wavenumber tends to zero as the Reynolds number tends to zero. This is in agreement with the findings by Kalliadasis *et al.* [67] but seems to contradict the results obtained by Goussis & Kelly [46] which predict the wavenumber to approach infinity in this limiting case. This inconsistency is due to the fact that Goussis and Kelly based the definition of their Marangoni number on the temperature difference across the flat film instead of the temperature difference between the wall and the ambient gas phase. As a concequence their Marangoni number should also depend on B (which in turn depends on Re) but this dependence was not taken into account in their study. Conversely, if the flow rate is large, inertia effects are large and the interfacial forces due to the Marangoni effects are not important compared to the dominant inertia forces so that the H-mode dominates in this region.

5.3 Formulation at second order

As we have already emphasized, for isothermal films, it is well known that the second-order viscous dissipation plays an important role in the dispersion of the waves and we expect this to be the case for non-isothermal films as well. The aim here is to take into account the second order viscous and thermal diffusion terms of the Navier-Stokes/energy equations and to obtain a model for the dynamics of the flow consistent at this order. For this purpose, we will need the solution of equation (5.8) (this is at first-order) for the amplitudes of the projections, which can be found as

$$a_1 = -\frac{6}{5} h \partial_x \left[\frac{q^2}{h}\right] - h\partial_t q - \mathrm{Ma} h \partial_x \theta \tag{5.21a}$$

$$a_2 = q\partial_x q + \frac{1}{2} h \partial_t q \tag{5.21b}$$

$$
\begin{aligned}
a_3 &= -\frac{3}{4}\frac{q^2}{h}\partial_x h - \frac{1}{8}h\partial_t q && \text{(5.21c)}\\
a_4 &= -\frac{3}{40}h^6\partial_x\left[\frac{q^2}{h^6}\right] && \text{(5.21d)}\\
a_5 &= \frac{1}{80}h^6\partial_x\left[\frac{q^2}{h^6}\right] && \text{(5.21e)}\\
b_2 &= \frac{1}{6}\mathrm{Pr}h\left((\theta-1)\partial_x q + h\partial_t\theta\right) && \text{(5.21f)}\\
b_3 &= \frac{1}{8}\mathrm{Pr}h\left(-(\theta-1)\partial_x q + 2q\partial_x\theta\right) && \text{(5.21g)}\\
b_4 &= \frac{1}{40}\mathrm{Pr}h\left((\theta-1)\partial_x q - 3q\partial_x\theta\right) && \text{(5.21h)}\\
b_1 &= 0\,, \quad a_i = b_j = 0\,, \quad i \geq 6\,,\, j \geq 5\,.
\end{aligned}
$$

Note that the amplitudes a_i of the monomials of degree greater or equal to seven are identically equal to zero at first order. This could have been easily foreseen by examining the degree of the polynomial in $\bar{y}$ corresponding to the left-hand-side of (5.6b), *i.e.* the inertial terms $\partial_t u + u\partial_x u + v\partial_y u$. Because f_0 is of degree two, this polynomial is of degree four, so that the right-hand-side of (5.6b) is also a polynomial of degree four. Hence, the amplitude a_n corresponding to $f_n = \bar{y}^{n+1}$ is equal to zero if $n \geq 6$, the operator ∂_{yy} decreasing its degree by two. The same argument can be applied to (5.6c) where the inertial terms $\partial_t T + u\partial_x T + v\partial_y T$ at the left-hand-side are a polynomial in $\bar{y}$ of degree three only.
Consequently, the derivatives of the fields a_i, $i \geq 6$, b_j, $j \geq 5$ are of order higher than ε^2 and can be dropped at this stage of the approximation. Their dynamics are thus slaved to the dynamics of the other unknowns.
Now, from expressions (5.21), it is easy to verify that $a_4 = -6a_5$, $a_2 = -4a_3 + 40a_5$ and $a_1 = 8a_3 - 96a_5 - \mathrm{Ma}h\partial_x\theta$ so that, eliminating these amplitudes in (5.11), we get $a_0 = (3q)/h - \frac{48}{5}a_3 + \frac{816}{7}a_5 + \frac{3}{2}\mathrm{Ma}h\partial_x\theta$. The velocity field at first order can then be written as

$$
u = 3\frac{q}{h}f_0(\bar{y}) + \mathrm{Ma}h\partial_x\theta\tilde{f}_1(\bar{y}) + a_3\tilde{f}_3(\bar{y}) + a_5\tilde{f}_5(\bar{y})\,, \qquad (5.22)
$$

where $\tilde{f}_1 = -\frac{3}{4}\bar{y}^2 + \frac{1}{2}\bar{y}$, $\tilde{f}_3 = \bar{y}^4 - 4\bar{y}^3 + \frac{24}{5}\bar{y}^2 - \frac{8}{5}\bar{y}$ and $\tilde{f}_5 = \bar{y}^6 - 6\bar{y}^5 + 40\bar{y}^3 - \frac{408}{7}\bar{y}^2 + \frac{144}{7}\bar{y}$. Therefore, u is a combination of four independent fields q/h, a_3, a_5 and $h\partial_x\theta$ rather than six as could be expected at first. Similarly, T can be written at first order as a combination of four independent fields, namely θ, b_2, b_3 and b_4. As a consequence, a consistent formulation of a model for the dynamics of the flow at second order would require nine unknowns corresponding to the introduction of eight independent fields to correctly represent the temperature and velocity distributions, plus of course the film thickness h.
The degree of the polynomials f_i, $0 \leq i \leq 5$ and the second-order dissipative term $\partial_{yy}u$ and quadratic nonlinearities of the Navier-Stokes equation, imply that the description of the velocity field at $\mathcal{O}(\varepsilon^2)$ involves polynomials of degree up to fourteen. Therefore, the set of orthogonal test functions for the velocity field needs to be completed by ten other functions in order to obtain a basis for the set of polynomials of degree up to

fourteen satisfying the no-slip condition. Turning now to the modelling of the heat equation at second order, a basis for the set of polynomials of degree up to thirteen verifying the temperature condition at the wall is required at second-order to fully describe the temperature field at that order. This means that ten corresponding amplitudes for the velocity profile and nine for the temperature profile need to be eliminated (through the slaving principle) to obtain a set of eight evolution equations for the eight unknowns required to correctly describe the dynamics of the flow at second-order. It is needless to say that such a task would require a cumbersome calculation such that a short cut would be welcome.

Following the same approach as in the isothermal case, let us construct a new set of polynomial test functions F_i satisfying the orthogonality condition $\int_0^1 F_i F_j d\bar{y} \propto \delta_{ij}$ with the help of a Gram-Schmidt orthogonalization procedure such that $F_0 \equiv f_0$, F_1, F_2 and F_3 are linear combinations of f_0, $\tilde{f}_1$, $\tilde{f}_3$ and $\tilde{f}_5$. The result is

$$F_0 = \bar{y} - \frac{1}{2}\bar{y}^2 , \tag{5.23a}$$

$$F_1 = \bar{y} - \frac{17}{6}\bar{y}^2 + \frac{7}{3}\bar{y}^3 - \frac{7}{12}\bar{y}^4 , \tag{5.23b}$$

$$F_2 = \bar{y} - \frac{13}{2}\bar{y}^2 + \frac{57}{4}\bar{y}^3 - \frac{111}{8}\bar{y}^4 + \frac{99}{16}\bar{y}^5 - \frac{33}{32}\bar{y}^6 , \tag{5.23c}$$

$$F_3 = \bar{y} - \frac{531}{62}\bar{y}^2 + \frac{2871}{124}\bar{y}^3 - \frac{6369}{248}\bar{y}^4 + \frac{29601}{2480}\bar{y}^5 - \frac{9867}{4960}\bar{y}^6 . \tag{5.23d}$$

The functions F_1 and F_2 have been chosen so that they correspond exactly to the polynomials introduced in the isothermal case. The introduction of the polynomial F_3 is made necessary by the Marangoni effect which modifies the stress condition at the interface (5.6e).

Similarly, a set of orthogonal test functions for the temperature field is constructed from linear combinations of g_0, g_2, g_3 and g_4 such that $G_0 \equiv g_0$:

$$G_0 = \bar{y} , \tag{5.24a}$$

$$G_1 = \bar{y} - \frac{5}{3}\bar{y}^3 , \tag{5.24b}$$

$$G_2 = \bar{y} - 7\bar{y}^3 + \frac{32}{5}\bar{y}^4 , \tag{5.24c}$$

$$G_3 = \bar{y} - \frac{56}{3}\bar{y}^3 + \frac{192}{5}\bar{y}^4 - 21\bar{y}^5 . \tag{5.24d}$$

Therefore, the velocity field and the temperature field can be accurately described at $\mathcal{O}(\varepsilon)$ from

$$u = \frac{3}{h}\left(q - s_1 - s_2 - s_3\right) F_0(\bar{y}) + 45\frac{s_1}{h}F_1(\bar{y}) + 210\frac{s_2}{h}F_2(\bar{y}) + 434\frac{s_3}{h}F_3(\bar{y}) \tag{5.25a}$$

$$T = 1 + (\theta - 1 - t_1 - t_2 - t_3)G_0(\bar{y}) - \frac{3}{2}t_1 G_1(\bar{y}) + \frac{5}{2}t_2 G_2(\bar{y}) - \frac{15}{4}t_3 G_3(\bar{y}) . \tag{5.25b}$$

In line with our previous derivation of a second-order consistent model for the isothermal case [109], the first-order fields s_i, $1 \leq i \leq 3$ have been introduced such that u

preserves the definition of the flow rate q, $q = \int_0^h u\,dy$, as it should. These fields correspond to corrections to the amplitude of the parabolic velocity profile and at the same time their role in the velocity profile is similar to that of q so that the final evolution equations for q and s_i will be of similar functional forms. In the same spirit, the introduction of the fields t_i, $1 \leq i \leq 3$ preserves the definition of the temperature at the surface $\theta = T\big|_{y=h}$. Note that G_0 and $-\frac{3}{2}G_1$ are Legendre polynomials. This is quite fortuitous, the Legendre polynomials forming an orthogonal basis for the scalar product $\int_{-1}^1 \cdot d\bar{y}$ instead of $\int_0^1 \cdot d\bar{y}$. Completing our set of test functions in order to obtain a basis for the set of polynomials of degree up to ten satisfying the no-slip condition, we write

$$\begin{aligned} u &= \frac{3}{h}\left(q - s_1 - s_2 - s_3\right) F_0(\bar{y}) + 45\frac{s_1}{h}F_1(\bar{y}) + 210\frac{s_2}{h}F_2(\bar{y}) \\ &\quad + \frac{434}{h}\left(s_3 - \sum_{i=4}^{9} s_i\right) F_3(\bar{y}) + \sum_{i=4}^{9} \frac{1}{\int_0^1 F_i(\bar{y})d\bar{y}}\frac{s_i}{h}F_i(\bar{y}) \end{aligned} \tag{5.26}$$

Nevertheless, as it will be shown below, the explicit formulations of the polynomials F_i, $4 \leq i \leq 9$, will not be required so that in practice the Gram-Schmidt orthogonalization procedure is limited to the determination of F_1, F_2 and F_3.

We now apply the Galerkin method. Let us consider closely the first four residuals for the momentum equation. Being of $\mathcal{O}(\varepsilon^2)$ or higher, the corrective fields s_i, $4 \leq i \leq 9$ may enter into the calculus only through the evaluation of the zeroth order viscous term $\int_0^h F_i(y/h)\partial_{yy}u\,dy$ which after integrating twice by parts becomes $\int_0^h F_i''(y/h)u\,dy$. Notice that $F_0'' = -1$, $F_1'' = 14F_0 - \frac{17}{3}$, $F_2'' = \frac{1485}{28}F_1 + \frac{909}{28}F_0 - 13$ and $F_3'' = \frac{88803}{868}F_1 + \frac{31779}{868}F_0 - \frac{531}{31}$ and are therefore linear combinations of 1, F_0 and F_1. Consequently and making use of the orthogonality of the polynomials F_i, the fields s_i, $i \geq 4$ will not appear in the first four residuals of the momentum equation $\mathcal{R}_q(F_i)$, $0 \leq i \leq 3$. After some algebraic manipulation, they lead to a set of evolution equations for q, s_1, s_2, s_3 which has the formal expression

$$\partial_t \mathbf{U_q} = \mathbf{M_q}\,\mathbf{V_q} \tag{5.27}$$

where $\mathbf{U_q} = (q,\ s_1,\ s_2,\ s_3)^t$, $\mathbf{V_q} = (h - 3q/h^2 - \mathrm{Ct}h\partial_x h + \mathrm{Ka}h\partial_{xxx}h,\ s_1,\ s_2,\ s_3,\ q\partial_x q/h,\ q^2\partial_x h/h^2,\ s_1\partial_x q/h,\ s_2\partial_x q/h,\ s_3\partial_x q/h,\ q\partial_x s_1/h,\ q\partial_x s_2/h,\ q\partial_x s_3/h,\ qs_1\partial_x h/h^2,\ qs_2\partial_x h/h^2,\ qs_3\partial_x h/h^2,\ q(\partial_x h)^2/h^2,\ \partial_x q\partial_x h/h,\ q\partial_{xx}h/h,\ \partial_{xx}q,\ \mathrm{Ma}\partial_x\theta)^t$ and $\mathbf{M_q}$ is a 4×20 matrix.

The same argument applies to the temperature fields so that the set of test functions G_i must be completed at second order with nine polynomials of degree up up to thirteen. Nevertheless, since G_i'', $0 \leq i \leq 3$ are not linear combinations of G_i, $0 \leq i \leq 3$, the four first residuals do not form a closed set of equations for θ, t_1, t_2 and t_3. Yet, a basis for the set of polynomials of degree up to five satisfying the temperature condition at the wall can be obtained by introducing only one polynomial orthogonal to the first four G_i. This polynomial G_4 is given explicitly by

$$G_4(\bar{y}) = \bar{y} - \frac{128}{15}\bar{y}^2 + 24\bar{y}^3 - \frac{192}{7}\bar{y}^4 + 11\bar{y}^5\,. \tag{5.28}$$

The temperature field can now be written at second-order as

$$\begin{aligned} T &= 1+(\theta-1-t_1-t_2-t_3-t_4)\,G_0(\bar{y})-\frac{3}{2}t_1G_1(\bar{y})+\frac{5}{2}t_2G_2(\bar{y}) \\ &\quad -\frac{15}{4}\left(t_3-\sum_{i=5}^{8}t_i\right)G_3(\bar{y})+\frac{105}{4}t_4G_4(\bar{y})+\sum_{i=5}^{8}t_i\frac{G_i(\bar{y})}{G_i(1)}\,. \end{aligned} \tag{5.29}$$

The choice of this formulation ensures that the evaluation of $\int_0^h G_j''(\bar{y})T\,dy$, $0\le j\le 4$ does not require the definitions of G_i, $j\ge 5$. By applying next the Galerkin method to the heat equation, the five first residuals $\mathcal{R}_T(G_i)$, $0\le i\le 4$ constitute a closed set. Since the amplitude t_4 is of $\mathcal{O}(\varepsilon^2)$, its space and time derivatives can be neglected at this order, so that an explicit formulation as function of h, θ, t_1, t_2 and t_3 can be obtained, thus expressing the slaving of the former to the latter. Therefore, after some tedious algebraic manipulation, one gets a set of evolution equations for θ, t_1, t_2, t_3 which can be written formally as

$$\mathrm{Pr}\partial_t\mathbf{U_T}=\mathbf{M_T}\,\mathbf{V_T} \tag{5.30}$$

where $\mathbf{U_T}=(\theta,\,t_1,\,t_2,\,t_3)^t$, $\mathbf{V_T}=([1-(1+\mathrm{Bi}\,h)\theta]/h^2,\,t_1/h^2,\,t_2/h^2,\,t_3/h^2,\,\mathrm{Pr}\,(1-\theta)\partial_x q/h,\;\mathrm{Pr}\,t_1\partial_x q/h,\;\mathrm{Pr}\,t_2\partial_x q/h,\;\mathrm{Pr}\,t_3\partial_x q/h,\;\mathrm{Pr}\,q\partial_x\theta/h,\;\mathrm{Pr}\,q\partial_x t_1/h,\;\mathrm{Pr}\,q\partial_x t_2/h,\,\mathrm{Pr}\,q\partial_x t_3/h,\,\mathrm{Pr}\,(1-\theta)\partial_x s_1/h,\,\mathrm{Pr}\,(1-\theta)\partial_x s_2/h,\,\mathrm{Pr}\,(1-\theta)\partial_x s_3/h,\,\mathrm{Pr}\,s_1\partial_x\theta/h,\,\mathrm{Pr}\,s_2\partial_x\theta/h,\,\mathrm{Pr}\,s_3\partial_x\theta/h,\,(1-\theta)(\partial_x h)^2/h^2+\partial_x h\partial_x\theta/h,\,\mathrm{Bi}\,\theta(\partial_x h)^2/h,\,(1-\theta)\partial_{xx}h/h,\,\partial_{xx}\theta)^t$, and $\mathbf{M_T}$ is a 4×21 matrix.

Finally, we obtain a set of nine coupled evolution equations, namely (5.4, 5.27, 5.30) for nine unknowns, given in appendix D.1.

5.4 Reduced models

Clearly, our full second-order model is of little use because of its complexity. It is hence necessary to obtain reduced models which also retain the dynamic characteristics of the full-size model.

A significant reduction can be achieved expanding our unknowns in series of ε and performing an appropriate gradient expansion of the full model (5.4, 5.27, 5.30), thus writing formally

$$\begin{aligned} q &= q^{(0)}+\varepsilon q^{(1)}+\varepsilon^2 q^{(2)}+\mathcal{O}\big(\varepsilon^3\big) \\ \theta &= \theta^{(0)}+\varepsilon\theta^{(1)}+\varepsilon^2\theta^{(2)}+\mathcal{O}\big(\varepsilon^3\big) \\ s_i &= \varepsilon s_i^{(1)}+\varepsilon^2 s_i^{(2)}+\mathcal{O}\big(\varepsilon^3\big) \\ t_i &= \varepsilon t_i^{(1)}+\varepsilon^2 t_i^{(2)}+\mathcal{O}\big(\varepsilon^3\big)\,. \end{aligned}$$

One then obtains a single evolution equation that is exactly the one resulting from the long-wave expansion presented in §2.2, namely the Benney-type equation at second-order (2.11). This is because the derivation of the system of equations (5.27, 5.30)

is coherent up to second-order, i.e. no terms of order $\mathcal{O}(\varepsilon^2)$ or smaller have been omitted.

However, as we have already pointed out in chapter 2, it is well known [103, 53] that the Benney-type evolution equations exhibit non-physical finite-time blow-up behaviour for sufficiently large Reynolds numbers. Therefore, the aim here is to obtain a prototype set of equations of reduced dimensionality without the drawbacks of Benney's single evolution equation for the film thickness in (2.11) and hence, of higher degree of complexity than Benney's expansion. At the same time, it should be of lower degree of complexity than the full-size system with nine unknowns in (5.4, 5.27, 5.30). This reduced model should fully resolve conditions near criticality (not only correct all critical quantities but also give the full long-wave lubrication equation with an appropriate expansion). Finally, we also expect that it should accurately (*i.e.* better than the first-order model (5.17)) describe the dynamics of the film up to moderate Reynolds and Péclet numbers, since it would capture the second-order dissipative effects.

For this purpose, we consider the expansions for the velocity and temperature fields given by (5.26) and (5.29). It is clear that the corrective fields s_i and t_i correspond to polynomials of increasing degrees and hence, they exhibit increasingly abrupt variations. Therefore, viscosity and thermal diffusivity will tend to damp them relatively strongly. This can be observed for example by linearizing the model equations around the flat film solution assuming no spatial dependency of the perturbations, *i.e.* set the wavenumber equal to zero. With this hypothesis, $dh/dt = 0$ and the film thickness is constant. Furthermore, both systems (5.27) and (5.30) are decoupled and writing $q = h_{\rm N}^3(1/3 + \eta\tilde{q})$, $s_i = \eta h_{\rm N}^3 \tilde{s}_i$, $\theta = (1 + \eta\tilde{\theta})/(1 + {\rm Bi}h_{\rm N})$, $t_i = \eta\tilde{t}_i$ with $\eta \ll 1$, one obtains two linear systems in the form

$$
{\rm Re}\frac{dV}{dt} = \mathbf{A}\,V\,, \quad {\rm PrRe}\frac{dW}{dt} = \mathbf{B}\,W\,, \tag{5.31}
$$

where $V = (\tilde{q}, \tilde{s}_1, \tilde{s}_2, \tilde{s}_3)^t$, $W = (\tilde{\theta}, \tilde{t}_1, \tilde{t}_2, \tilde{t}_3)^t$ and $\mathbf{A}$ and $\mathbf{B}$ are two square matrices of dimensions 4×4. The eigenvalues of $\mathbf{A}$ and $\mathbf{B}$ are -63.6, -26.6, -7.42, -0.82 and -89.1, -21.0, -7.40, -0.82, respectively. Therefore, there is a large gap between the least stable (largest) eigenvalues and the other eigenvalues. The spectra are hence well separated and the perturbations associated with the eigenvalues far from zero are quickly damped. The dynamics of the flow in the limit of long waves is therefore dominated by the eigenvectors corresponding to the eigenvalues closest to zero. These are $(\tilde{q}, \tilde{s}_1, \tilde{s}_2, \tilde{s}_3)^t = (-1.00,\ 1.33\,10^{-2},\ -1.38\,10^{-4},\ 2.22\,10^{-7})$ and $(\tilde{\theta}, \tilde{t}_1, \tilde{t}_2, \tilde{t}_3)^t = (0.976,\ -0.219,\ 8.08\,10^{-3},\ 7.52\,10^{-4})$. In both eigenvectors, the coefficients corresponding to the corrections $\tilde{s}_i$ and $\tilde{t}_i$ are negligible except for $\tilde{t}_1$ which is still four times smaller than the coefficient corresponding to $\tilde{\theta}$. It can then be conjectured that even if nine amplitudes h, q, θ, s_i and t_i, $1 \leq i \leq 3$ are needed to describe the dynamics of the flow at second order, only q, h and θ will play a significant role and the other ones will virtually be slaved to their dynamics, at least for some range of Reynolds numbers. Therefore, it seems possible to develop a reduced model in terms of h, q and θ only reproducing reliably the dynamics of the film up to moderate Reynolds and Péclet numbers.

The first idea that comes to mind is thus to simply consider the velocity distribution to remain parabolic and the temperature field to be linear

$$u = \frac{3q}{h} F_0(\bar{y}) \,, \quad T = 1 + (\theta - 1) G_0(\bar{y}) \tag{5.32}$$

so that the basic assumption here is that the flat film velocity/temperature distributions persist even when the interface is no longer flat. We then apply the Galerkin method by averaging the second-order boundary-layer equation (1.101b) and the energy equation (1.101c) with the weights F_0 and G_0, a procedure exactly similar to the derivation of the first model in §5.2, and which leads to

$$\partial_t h = -\partial_x q \,, \tag{5.33a}$$

$$\begin{aligned} \partial_t q = {} & \frac{5}{6} h - \frac{5}{2}\frac{q}{h^2} - \frac{17}{7}\frac{q}{h}\partial_x q + \left(\frac{9}{7}\frac{q^2}{h^2} - \frac{5}{6}\mathrm{Ct} h \right) \partial_x h \\ & + 4\frac{q}{h^2} \left(\partial_x h\right)^2 - \frac{9}{2h}\partial_x q \partial_x h - 6\frac{q}{h}\partial_{x^2} h + \frac{9}{2}\partial_{x^2} q \\ & - \frac{5}{4}\mathrm{Ma}\partial_x \theta + \frac{5}{6}\mathrm{Ka} h \partial_{xxx} h \,, \end{aligned} \tag{5.33b}$$

$$\begin{aligned} \mathrm{Pr}\partial_t \theta = {} & 3\frac{(1 - \theta - \mathrm{Bi} h\theta)}{h^2} + \mathrm{Pr}\left[\frac{7}{40}\frac{(1-\theta)}{h}\partial_x q - \frac{27}{20}\frac{q}{h}\partial_x \theta \right] \\ & + \left(1 - \theta - \frac{3}{2}\mathrm{Bi} h\theta \right) \left(\frac{\partial_x h}{h} \right)^2 + \frac{\partial_x h \partial_x \theta}{h} + (1-\theta)\frac{\partial_{x^2} h}{h} + \partial_{x^2}\theta \end{aligned} \tag{5.33c}$$

In comparison with (5.17), the additional second-order terms are

$$\mathrm{Dis}_q = 4\frac{q}{h^2} \left(\partial_x h\right)^2 - \frac{9}{2h}\partial_x q \partial_x h - 6\frac{q}{h}\partial_{x^2} h + \frac{9}{2}\partial_{x^2} q \tag{5.34a}$$

$$\mathrm{Dis}_\theta = \left(1 - \theta - \frac{3}{2}\mathrm{Bi} h\theta \right) \left(\frac{\partial_x h}{h} \right)^2 + \frac{\partial_x h \partial_x \theta}{h} + (1-\theta)\frac{\partial_{x^2} h}{h} + \partial_{xx}\theta \,. \tag{5.34b}$$

The origin of Dis_q can be traced back to the viscous streamwise dissipative effects. Similarly, Dis_θ originates from the streamwise diffusion of heat through thermal conduction. As for isothermal film flows, (5.33) can also be obtained making the assumption that the unknowns s_i, t_i are of higher order than ε. Their space and time derivatives can thus be neglected in (5.27, 5.30) and after inversion of the equations, expressions of s_i and t_i as functions of h, q, θ and their derivatives can be obtained, with the equations (5.33a, 5.33b) appearing as *compatibility* relations [109].
Nevertheless, it is clear that the model in (5.33) cannot agree with the second-order gradient expansion (2.12c) since it does not take into account the second-order corrections to the velocity and temperature distributions. For this reason, equations (5.33) will be referred to as the *"approximated" second-order model*. The goal here is therefore to find a cure to this disagreement and formulate a model of reduced dimensionality – i.e. for the three unknowns h, q and θ only – that is in agreement with the long-wave expansion. Such a set of equations will be called *"reduced" second-order model* in contrast with the approximated model (5.33).

Let us consider the two residuals corresponding to the parabolic velocity profile, $\mathcal{R}_q(F_0)$, and to the linear temperature distribution, $\mathcal{R}_T(G_0)$. These two residuals do not involve the fields s_i and t_i directly but only their space and time derivatives, except in products with derivatives of h or q. Therefore, the fields s_i and t_i can be eliminated at second-order provided that explicit expressions of them as functions of h, q and θ and their derivatives, are available at first order. Such relations can easily be obtained by truncating at first order the eight evolution equations (5.27) and (5.30) (or explicitely D.1). Indeed, since the fields s_i and t_i are of $\mathcal{O}(\varepsilon)$, their time and space-derivatives are of $\mathcal{O}(\varepsilon^2)$ and thus disappear in the truncation. Consequently the six unknowns s_i and t_i can be solved algebraically and the two left equations of the system (for q and θ) represent the compatibility conditions. These conditions being of first-order, they should be equivalent to the first-order model (5.17) even though their form are different due to the elimination of the fields s_i and t_i. It comes out that the expressions for the fields s_i and t_i as functions of h, q and θ are *not* unique and can be modified with the help of the two compatibility conditions. Here, we will choose to express the fields s_i and t_i such that we can obtain reduced models whose first-order terms have the same form than the first-order model (5.17). Thus we get

$$
\begin{aligned}
s_1 &= \frac{1}{210}h^2\partial_t q - \frac{19}{1925}q^2\partial_x h + \frac{74}{5775}hq\partial_x q + \frac{1}{40}\mathrm{Ma}\,h^2\partial_x\theta\,, && \text{(5.35a)}\\
s_2 &= \frac{2}{5775}q^2\partial_x h - \frac{2}{17325}hq\partial_x q - \frac{299}{53760}\mathrm{Ma}\,h^2\partial_x\theta\,, && \text{(5.35b)}\\
s_3 &= \frac{5}{3584}\mathrm{Ma}\,h^2\partial_x\theta\,, && \text{(5.35c)}\\
t_1 &= \mathrm{Pr}\left(\frac{1}{15}h^2\partial_t\theta + \frac{133}{5760}h(\theta-1)\partial_x q + \frac{73}{960}hq\partial_x\theta\right)\,, && \text{(5.35d)}\\
t_2 &= \mathrm{Pr}\left(-\frac{111}{22400}h(\theta-1)\partial_x q + \frac{79}{11200}hq\partial_x\theta\right)\,, && \text{(5.35e)}\\
t_3 &= \mathrm{Pr}\left(-\frac{1}{3150}h(\theta-1)\partial_x q + \frac{1}{1050}hq\partial_x\theta\right)\,, && \text{(5.35f)}
\end{aligned}
$$

Substituting the equations above into the residuals of the momentum and heat equations corresponding respectively to a parabolic and a linear weight, $\mathcal{R}_q(F_0)$ and $\mathcal{R}_T(G_0)$, and making use of the kinematic relation $\partial_t h = -\partial_x q$ yields

$$
\begin{aligned}
\partial_t q &= \frac{5}{6}h - \frac{5}{2}\frac{q}{h^2} - \frac{17}{7}\frac{q}{h}\partial_x q + \left(\frac{9}{7}\frac{q^2}{h^2} - \frac{5}{6}\mathrm{Ct}h\right)\partial_x h\\
&\quad +4\frac{q}{h^2}\left(\partial_x h\right)^2 - \frac{9}{2h}\partial_x q\partial_x h - 6\frac{q}{h}\partial_{x^2}h + \frac{9}{2}\partial_{x^2}q\\
&\quad -\frac{5}{4}\mathrm{Ma}\partial_x\theta + \frac{5}{6}\mathrm{Ka}h\partial_{xxx}h + \mathrm{Ine}_q[h,\,q,\,\theta] + \mathrm{MaMar}_q[h,\,q,\,\theta]\,, \quad \text{(5.36a)}
\end{aligned}
$$

$$\begin{aligned}\mathrm{Pr}\partial_t\theta &= 3\frac{(1-\theta-\mathrm{Bi}h\theta)}{h^2}+\mathrm{Pr}\left[\frac{7}{40}\frac{(1-\theta)}{h}\partial_x q-\frac{27}{20}\frac{q}{h}\partial_x\theta\right]\\ &\quad+\left(1-\theta-\frac{3}{2}\mathrm{Bi}h\theta\right)\left(\frac{\partial_x h}{h}\right)^2+\frac{\partial_x h\partial_x\theta}{h}+(1-\theta)\frac{\partial_{x^2}h}{h}+\partial_{x^2}\theta\\ &\quad+\mathrm{Pr}\,\mathrm{Ine}_{q\theta}[h,\,q,\,\theta]+\mathrm{Pr}^2\,\mathrm{Ine}_{\theta}[h,\,q,\,\theta]+\mathrm{MaPr}\,\mathrm{Mar}_{\theta}[h,\,q,\,\theta]\,, \quad (5.36b)\end{aligned}$$

where, hidden in Ine_q, Mar_q, $\mathrm{Ine}_{q\theta}$, Ine_θ and Mar_θ, occur second-order inertial terms induced by the corrections to the flat-film solution (5.35). Ine_q contains terms produced in the momentum equation by the advection of the first-order corrections of the velocity profile (5.35a–5.35c). Mar_q denotes the terms induced in the momentum equation by the Marangoni flow produced by the gradient of temperature at the free surface. Similarly, Ine_θ contains inertial terms originating from the averaged heat equation through the advection of the first-order corrections of the temperature profile (5.35d–5.35f). The terms contained in $\mathrm{Ine}_{q\theta}$ and Mar_θ originate from the advection of the linear flat-film temperature distribution by the first-order corrections of the velocity profile induced by the deformation of the free surface and the Marangoni flow, respectively. They read explicitly

$$\begin{aligned}\mathrm{Ine}_q &= \frac{1}{210}h^2\partial_{tt}q+\frac{17}{630}hq\partial_{xt}q-\frac{1}{105}q\partial_x h\partial_t q\\ &\quad+\frac{1}{42}h\partial_x q\partial_t q-\frac{26}{231}\frac{q^2\partial_x h\partial_x q}{h}+\frac{653}{8085}q(\partial_x q)^2\\ &\quad+\frac{386}{8085}q^2\partial_{xx}q+\frac{104}{2695}\frac{q^3(\partial_x h)^2}{h^2}-\frac{78}{2695}\frac{q^3\partial_{xx}h}{h}\,, \quad (5.37a)\\ \mathrm{Mar}_q &= \frac{5}{112}q\partial_x h\partial_x\theta+\frac{19}{336}h\partial_x q\partial_x\theta+\frac{1}{48}h^2\partial_{xt}\theta+\frac{15}{224}hq\partial_{xx}\theta\,, \quad (5.37b)\\ \mathrm{Ine}_{q\theta} &= -\frac{19}{1400}\left[(1-\theta)\partial_x h-h\partial_x\theta\right]\partial_t q-\frac{19}{2800}(1-\theta)\partial_{xt}q\\ &\quad+\frac{47}{4800}(1-\theta)\frac{\partial_x h\partial_x q}{h}-\frac{613}{33600}(1-\theta)\left[(\partial_x q)^2+q\partial_{xx}q\right]\\ &\quad-\frac{157}{1600}\frac{q^2\partial_x h\partial_x\theta}{h}+\frac{613}{16800}q\partial_x q\partial_x\theta+\frac{157}{11200}\frac{(1-\theta)q^2\partial_{xx}h}{h}\,, \quad (5.37c)\\ \mathrm{Ine}_\theta &= \frac{1}{15}h^2\partial_{tt}\theta+\frac{23}{140}\left(qh\partial_{xt}\theta+q\partial_x h\partial_t\theta\right)\\ &\quad+\frac{23}{280}h\partial_t q\partial_x\theta-\frac{33}{280}h\partial_x q\partial_t\theta-\frac{31}{1680}(1-\theta)h\partial_{xt}q\\ &\quad-\frac{491}{22400}(1-\theta)\left[\frac{\partial_x h\partial_x q}{h}+q\partial_{xx}q\right]+\frac{1391}{67200}(1-\theta)(\partial_x q)^2\\ &\quad+\frac{573}{5600}\left[\frac{q^2\partial_x h\partial_x\theta}{h}+q^2\partial_{xx}\theta\right]+\frac{113}{2800}q\partial_x q\partial_x\theta\,, \quad (5.37d)\\ \mathrm{Mar}_\theta &= \frac{3}{40}h(\partial_x\theta)^2-\frac{3}{40}(1-\theta)\partial_x h\partial_x\theta-\frac{3}{80}(1-\theta)h\partial_{xx}\theta\,. \quad (5.37e)\end{aligned}$$

5.5 Discussion

Although the explicit formulations of Ine_q, $\mathrm{Ine}_{q\theta}$, Ine_θ, Mar_q and Mar_θ are complicated and involve time derivatives, they can be drastically simplified using the relations provided by the zeroth-order flat film solution $q^{(0)}$ and $\theta^{(0)}$ such that

$$q = \frac{h^3}{3} + \mathcal{O}(\varepsilon) \quad \text{and} \quad \theta = \frac{1}{1+\mathrm{Bi}\,h} + \mathcal{O}(\varepsilon)\ . \tag{5.38}$$

Therefore, the second-order terms (5.37) appearing in (5.36) do not have a unique formulation since a large number of asymptotically equivalent expressions is possible by using the equalities (5.38). Moreover, as already pointed out, the first-order expressions of the fields s_i, t_i as provided in (5.35) are not unique and can be changed by using the two compatibility conditions given by the first-order model (5.17). Hence, we end up not only with a single model fully compatible with the Benney long-wave lubrication expansion up to second order (2.11–2.12) but with a whole family of them. These models as already mentioned will be called hereafter *'reduced' second-order models* since they are of reduced dimensionality as compared to the full second-order model. Nevertheless, if all of them are asymptotically equivalent, they might not necessarily behave in the same way at moderate Reynolds and Péclet numbers. Indeed, the methodology presented here is principally based on the assumption that inertia plays effectively a 'secondary' role, with all inertial terms being at least first-order in the film parameter. Yet, in industrial applications, both Reynolds and Péclet numbers are generally large and a formulation that gives a hint on the way both H- and S-modes interact in the high-Reynolds/Péclet numbers flow regimes remains an open question.

In the context of isothermal film flows, the derivation of the Benney equation [7] also requires the assumption of a 'perturbative' role of inertia. Indeed, as we pointed out several times, at sufficiently large Reynolds numbers, a non-physical catastrophic behaviour of the non-stationary solutions leading to blow-up in finite time is observed. The occurrence of finite-time blow-up has been shown to be closely related to the unboundedness of the single-hump solitary wave solutions [103] (see §2.5.2). Ooshida's regularization procedure of the Benney expansion on the other hand, leads to a single evolution equation for the free surface h that does not exhibit this severe drawback [93]. Another single evolution equation including the second-order dissipation effects was recently introduced by Panga & Balakotaiah [99]. The inertial terms appearing in the model equations offered by both Ooshida [93] and Panga & Balakotaiah [99] can be shown to be equivalent to each other by using the lowest order expression $\partial_t h = -h^2\partial_x h + \mathcal{O}(\varepsilon)$ provided by the flat film Nusselt solution (5.38) and the mass conservation equation (see 2.6). Thus, Panga & Balakotaiah's formulation can be modified such that its inertial terms correspond to Ooshida's equation. This simple procedure was shown to cure the non-physical loss of the solitary-wave solutions and thus to avoid the occurrence of finite-time blow-up [114]. Ooshida was then brought to identify two regimes in the solitary-wave solution branch:

- The first one, so called **drag-gravity** regime corresponds to the balance of the gravitational acceleration with the viscous drag and with inertia playing only a

'perturbative' role. This regime is observable at threshold or for low amplitude waves.

- The second one, so called **drag-inertia** regime appears at larger Reynolds numbers and corresponds to a noticeable jump of the speed and amplitude of the observed solitary waves. In such a regime, inertia plays a dominant role, hence the basic assumption of 'perturbative' role of inertia is clearly violated there.

In conclusion, even though the construction of the solitary-wave solutions of Ooshida's equation is still possible in the drag-inertia regime, this equation fails to describe accurately the dynamics of the film since its solitary-wave solutions exhibit unrealistically small amplitudes and speeds. In fact, quantitative agreement cannot be achieved in such a regime using a single evolution equation. On the other hand, comparisons of the wave characteristics obtained using the boundary-layer approximation or the Shkadov model – *i.e.* the original integral-boundary-layer model – consisting of two evolution equations for the film thickness h and the flow rate q, are in good agreement even for large-amplitude waves [19]. However, we have already pointed out the inability of the Shkadov's model to predict accurately the instability threshold. Furthermore, the Shkadov's model being a first-order model, it does not take into account the streamwise dissipative effects that were shown to play a predominant role on the shape and the dispersion of solitary waves [107].
Therefore, it seems possible to select at least one formulation of the reduced second-order model having the form (5.4, 5.36) that will enables us to describe with a better qualitatively – and possibly quantitatively – agreement the wave dynamics in the drag-inertia regime, as compared to Ooshida's or Shkadov's equations. This selection is the subject of chapter 6.

Chapter 6

Linear stability and nonlinear waves

We have seen in the previous chapter that a whole family of asymptotically equivalent models can be obtained, making use of the zeroth-order equalities (5.38). These models, whose generic form is given by (5.36), are called *"reduced second-order models"* because they are of reduced dimensionality as compared to the full second-order model. By contrast, a model is called *"approximated"* if its gradient expansion does not lead to the exact asymptotic answer*.
Though a large number of asymptotically equivalent formulations exist to us, their solutions might not behave equivalently if the assumptions leading to their derivations are no longer verified. Indeed, the procedure described in chapter 5 is principally based on the assumption that the in-depth coherence of the flow is ensured by viscosity, inertia playing a 'perturbative' role. Therefore, our models must give results in reasonable agreement with experiments only for a limited range of Reynolds Re and Péclet numbers $\mathrm{Pe} = \mathrm{PrRe}$. Based on previous studies of isothermal flows [109, 110], our hope is that this range of parameters covers the two-dimensional wave regime that could be observed experimentally before the three-dimensional instabilities start to show up. To this aim, a selection procedure will be followed in two steps:

§6.1 Comparisons of the linear stability analysis of the models to the results of the Orr-Sommerfeld analysis of the linearized basic equations as computed from the system (1.77);

§6.2 Construction of the single-hump solitary wave family – also called 'the principal homoclinic orbits' by Balmforth *et al.* [4] – in order to check the boundedness of solitary waves for the largest possible range of parameters and thus to prevent the occurrence of the non-physical blow-up.

The different possible models investigated in this study are summarized in table 6.1. Our strategy here is inspired from recent work by Ooshida [93] who formulated a

*Remark that the *"approximated"* model given by (5.33) can be recovered from the *"reduced"* model (5.36) by using (5.34) for the dissipative second-order terms and cancelling all the other inertial second-order terms.

Model	Dis_q	Dis_θ	Ine_q	Mar_q	$\mathrm{Ine}_{q\theta}$	Ine_θ	Mar_θ
first-order :	null	null	null	null	null	null	null
second-order :							
"approximated"	**(5.34a)**	**(5.34b)**	null	null	null	null	null
"reduced" (case 0)	|	|	(5.37a)	(5.37b)	(5.37c)	(5.37d)	(5.37e)
"reduced" (case 0')	|	|	(5.37a)	(5.37b)	**null**	**null**	**null**
"reduced" (case 1)	|	|	**(6.2)**	**(6.4)**	|	|	|
"reduced" (case 2)	|	|	|	(6.8)	|	|	|
"reduced" (case 3)	|	|	|	(6.9)	|	|	|

Table 6.1: Summary of the different formulations investigated. The selected model is in bold and reproduced in (6.10).

reduced evolution equation of film flows using Padé approximant technique. His work showed that asymptotically equivalent equations coexist for film flows whose convergence properties to physically acceptable solutions are not equivalent. In particular, equivalent evolution equations might or might not present unrealistic behaviors of their non stationary solutions provided highest nonlinearities – inertial terms – are differently written.
In §6.3, the effect of the Reynolds and Prandtl numbers on the shape, speed, temperature distribution and flow pattern in the waves is investigated. The purpose is to understand how the thermocapillary S-mode and hydrodynamic H-mode influence each other.

6.1 Linear stability results

Let us consider the linear stability of the basic Nusselt flow and compare the results obtained using the different models to the exact answer given by the linearization of the basic equations leading to the classical Orr-Sommerfeld equation (see §1.4.2 for details). As performed previously, we again focus on the temporal stability analysis such that the pulsation Γ is complex and the wavenumber k is real. The dispersion relations corresponding to (5.36) with the different formulations tried here are obtained introducing the normal mode disturbances expressed by (2.41) where $\eta \ll 1$, and then cancelling the corresponding determinant. Similarly, the substitutions of (2.41), plus $s_i = \eta A_{s_i} \exp\{\mathrm{i}(kx - \Gamma t)\}$ and $t_i = \eta A_{t_i} \exp\{\mathrm{i}(kx - \Gamma t)\}$ in the full-size model (see appendix D.1 for an explicit formulation of this model) gives its dispersion relation. This is formulated in terms of the *base state set* of parameters based on the Nusselt flat film solution. We choose to present our results setting the inclination angle β and the physical parameters to constant values – or equivalently – Ct, Ka, Ma, Bi and Pr as in experiments where the inlet flow rate is the control parameter. Therefore only the Nusselt film thickness h_N, or equivalently, the Reynolds number Re is varied. Figure 6.1 shows the neutral stability curves in the plane wavenumber versus Reynolds number for $\mathrm{Pr} = 7$, $\mathrm{Ka} = 250$, $\mathrm{Ct} = 0$, $\mathrm{Ma} = 50$ and $\mathrm{Bi} = 1$ computed from different models. The parameters are chosen in a way to emphasize the differences

existing between the models. Hence the choice of an unrealistically large Biot number since setting Bi to order unity ensures that the Marangoni effect would be effective. In the same spirit, we choose to plot the critical wavenumber k_ν defined through the length-scale l_ν instead of h_N. Indeed as Re goes to zero, the critical wavenumber k given by (5.20) goes to zero as $\sqrt{\mathrm{M}^\star/\mathrm{We}} \propto h_\mathrm{N}^{1/6}$. Thus $k_\nu = k/h_\mathrm{N} \propto h_\mathrm{N}^{-5/6}$ goes to infinity in that limit and the different curves are more easily separated. The first-order

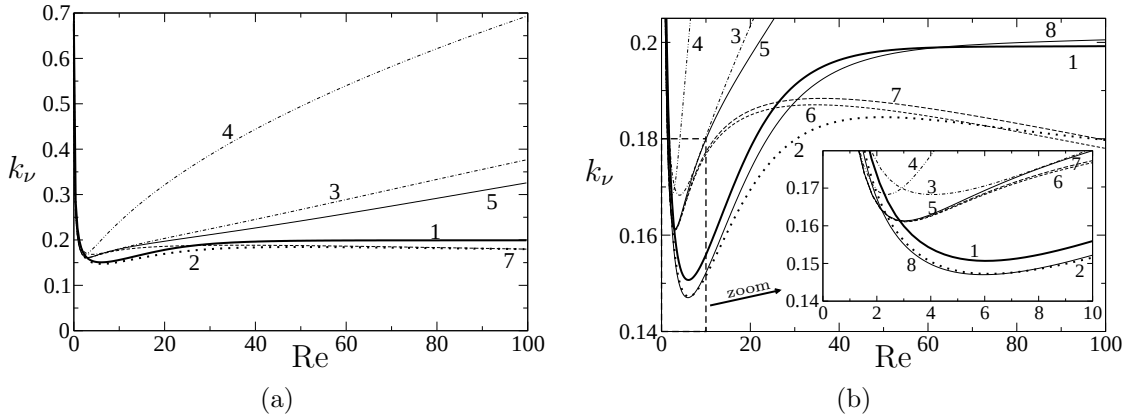

Figure 6.1: Neutral stability curves for Ka = 250, Ct = 0, Pr = 7, Ma = 50 and Bi = 1 from different models. Curve 1: Orr-Sommerfeld; curve 2: full-size second-order model; curve 3: reduced second-order model (case 0); curve 4: first order model; curve 5: reduced second-order model (case 0'); curve 6: "approximated" second-order model; curve 7: reduced second-order model (case 1); curve 8: boundary layer equations. For the sake of clarity, curves 6 and 8 are not plotted on (a) since they are not distinguishable from curves 7 and 1, respectively, because of the scaling for k_ν.

model (curve 4) deviates already at small Reynolds number, because of the smallness of the Kapitza number indicating that the second-order viscous effects are of primary importance in this regime. The full-size second-order model (curve 2) compares very well with the Orr-Sommerfeld results (curve 1) even though it decreases slightly at high Reynolds numbers. However, the light discrepancy cannot be attributed to the boundary layer approximation (curve 8) since the trend is inverted in this latter case. We rather invoke the limited convergence radius of any approximated method to explain the small divergence at high Reynolds numbers. Nevertheless, note the excellent agreement between the full-size model (curve 2) and the boundary layer equations (curve 8) for Re < 10. Notice the saturation of the curves (1,2,8) for high Re.
The critical wavelength $2\pi/k_\nu$ remains roughly constant at high Re and is independent of the film thickness. This feature – that should be recovered experimentally – will constitute the **criterion 1** that should govern our choice of any formulation of a reduced model. Actually, the reduced second-order model (curve 3) with (5.37) does not agree with the criterion 1 while the "approximated" second-order model (curve 6) does, being close to the full-size model (curve 2) at high Re.
At low Reynolds numbers where the dynamics of the flow is slaved to its kinematics and the Benney expansion applies, every model does fit with the solution of the

Orr-Sommerfeld analysis. The corresponding neutral stability curve (curve 1) admits a minimum at $R \approx 5.6$ which corresponds to the transition between the two main long-wave instability modes identified by Goussis & Kelly [46]: The thermocapillary mode (S-mode) which predominates at low Reynolds number and the classical hydrodynamic mode (H-mode) which rather prevails at larger Reynolds number. An accurate recovery of the exact neutral stability curve in the transitional zone between these two instability modes constitutes our **criterion 2**.
Again, the reduced model (curve 3) does not satisfy the criterion 2 as it deviates even earlier than the first-order model. Quite surprisingly, the "approximated" model does better fulfill criteria 1 and 2. Thus adding the second-order corrections (5.37) corresponding to the modification of the velocity profile induced by inertia and the Marangoni effect to the "approximated" model (curve 6) seems not to improve the model at moderate Reynolds number even at linear stage. This statement does not invalidate the whole methodology since the full second-order model fulfills very well both criteria (curve 2). Nevertheless, it makes clear the main difficulty of any asymptotically correct elimination of the corrections to the basic velocity and temperature profiles which is related to the limited radius of convergence of asymptotic expansions. This problem is not particular to the Marangoni driven instability of film flows and is encountered already for the isothermal flow.
In order to have some procedure to formulate properly the second-order terms, let us first make a parenthesis in the linear stability analysis by considering the terms Ine_q. Actually, Ine_q has the particularity to have a vanishing linear part such that it does not contribute to the linear dispersion equation, *i.e.* cancelling this term does not modify the results at linear stage. Indeed, using the zeroth-order equivalence between q and $h^3/3$ and with the relation between the time and space derivatives through the mass-conservation (5.4), Ine_q may reduce to

$$\mathrm{Ine}_q^{(0)} = -\frac{1}{630} h^7 (\partial_x h)^2, \tag{6.1}$$

which is only nonlinear. However, (6.1) is strongly nonlinear similarly to the term $\partial_x(h^6 \partial_x h)$ in the Benney equation (2.10) responsible to the finite-time blow-up. Then, being too 'dangerous', one should look for an intermediate form of Ine_q between (5.37a) and (6.1). Let us get inspired from the study of Ruyer & Manneville [109, 110] who obtained very accurate comparisons with experiments in the drag-inertia regime with their "approximated" model in isothermal conditions using the Galerkin method with the assumption of a parabolic velocity profile. Therefore, we suggest that the form of the second-order inertial corrections should not be far from the first-order inertial terms present in the "approximated" model. Let us then look for an asymptotically equivalent formulation of Ine_q which contains explicitly the first-order inertial terms such as

$$\mathrm{Ine}_q^{(1)} = \mathrm{Fac}(h,q) \left(\partial_t q - \frac{9}{7} \frac{q^2}{h^2} \partial_x h + \frac{17}{7} \frac{q}{h} \partial_x q \right). \tag{6.2}$$

First-order inertial terms $\partial_t q - \frac{9}{7}\frac{q^2}{h^2}\partial_x h + \frac{17}{7}\frac{q}{h}\partial_x q$ are asymptotically equivalent to $-\frac{1}{3}h^4 \partial_x h$. Therefore, to achieve asymptotic equivalence with (6.1), the possible form

of Fac are $\frac{1}{210}h^3\partial_x h$, or $\frac{1}{70}q\partial_x h$, or $\frac{1}{210}h\partial_x q$ or finally $\frac{1}{70}q\partial_x q/h^2$. Each such possibility has been checked by looking after the corresponding one-hump solitary wave family and selecting the form of Fac that enables to recover a behaviour in the drag-inertia regime that is in agreement with the boundary-layer equation and the "approximated" model. This leads to the choice

$$\mathrm{Fac} = \frac{1}{70}q\partial_x h. \tag{6.3}$$

The corresponding model with (6.2) will be shown in chapter 7 to give very good results and to enable an accurate description of the three-dimensional secondary instabilities reported experimentally by Liu *et al.* [84]. Because the adopted formulation should recover the already obtained model in the case of isothermal film (Ma = 0), in the following, the expression (6.2) will be systematically substituted for Ine_q.
Back to the formulation for non-isothermal case, a lot of effort were devoted in vain to the search of correct expressions for the second-order inertial and thermocapillary terms appearing in the heat balance Ine_θ, $\mathrm{Ine}_{q\theta}$ and Mar_θ. But it seems not possible to take into account the second-order corrections appearing in the heat equation and induced by the deviations of the temperature and velocity profiles from the flat-film Nusselt solution if the temperature field is assumed to be slaved to the free surface temperature θ only. This failure suggests to describe the temperature field enabling at least the first correction t_1 to θ to have its own dynamics. Such a study however will not be presented here but is a separate and later work even though some indications will be given in chapter 8. Therefore, $\mathrm{Ine}_{q\theta}$, Ine_θ and Mar_θ will be put to zero in the last part of this study. This crude assumption is still coherent with the gradient expansion at second order since the surface temperature is only coupled to the local flow rate through its gradient (already of $\varepsilon-$order). Yet, Ine_q and Mar_q do contribute to $q^{(2)}$ and should be kept.
Now setting $\mathrm{Ine}_{q\theta} = \mathrm{Ine}_\theta = \mathrm{Mar}_\theta = 0$ in (5.36) and keeping only Ine_q and Mar_q as given by (6.2) and (5.37b) (curve 5) does not lead to an acceptable formulation in view of both criteria 1 and 2. Consequently, we make use of both equivalences (5.38) to obtain asymptotically equivalent expressions of Mar_q. We also use the same procedure as for Ine_q and formulate Mar_q as a correction of the first-order inertial terms such as for example:

$$\mathrm{Mar}_q^{(1)} = \frac{5}{56}\frac{1}{h}\partial_x\theta\left(\partial_t q - \frac{9}{7}\frac{q^2}{h^2}\partial_x h + \frac{17}{7}\frac{q}{h}\partial_x q\right) + \frac{1}{224}qh\partial_{xx}\theta. \tag{6.4}$$

Note that we introduce the superscript (1) since several formulations of Ine_q and Mar_q are possible; it refers also to the 'case 1' in table 6.1. Only the last term of Mar_q brings a linear contribution such that equivalent form of the factor $\frac{5}{56}\partial_x\theta/h$ would lead to the similar results at linear stage. The reduced model (5.36) where $\mathrm{Ine}_{q\theta} = \mathrm{Ine}_\theta = \mathrm{Mar}_\theta = 0$ and Ine_q and Mar_q are given by (6.2) and (6.4) does fulfill our criteria as shown by figure 6.1 (curve 7). The reader should keep in mind that fulfilling the two formulated linear criteria is not sufficient to select an acceptable formulation. Indeed, one has to verify that the obtained nonlinear solutions do behave correctly, *i.e.* do no exhibit catastrophic behaviour such as blow-up in finite time. This will be

done in the next section. Nevertheless, in order to discuss here the linear stability of our modelling as compared to the analysis of the linearized Navier-Stokes and heat equations when the parameters are varied, let us assume that Ine_q and Mar_q given by(6.2) and (6.4) are the formulations of the second-order inertial terms as selected by the whole procedure. This will be verified later on.
To illustrate how the marginal stability curves behave in the plane wavenumber versus Reynolds number again for a vertical plane if the wavenumber is scaled using the film thickness, the curves obtained using the Orr-Sommerfeld analysis, the full-size second-order model and the reduced model have been plot on figure 6.2 along with the curve corresponding to the Benney expansion (2.11). As expected, the curves all tend to the origin as Re is decreased. Note the plateau reached by each curve for $\mathrm{Re} \sim 1$.

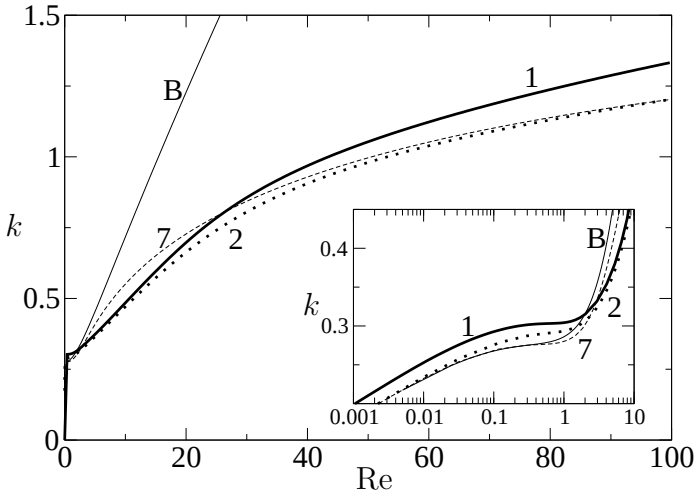

Figure 6.2: Neutral stability curves in the plane wavenumber k versus Reynolds number. k is defined using h_{N}. Parameters and numbering correspond to figure 6.1, see corresponding caption. Curve B corresponds to the Benney long-wave expansion.

On figure 6.3 the growth rate $\Im(\Gamma)$ is plotted against the real wavenumber for the long-wave mode. At a quite low Reynolds number $\mathrm{Re} = 1$, growth rates predicted by the reduced model with $\mathrm{Ine}_q = \mathrm{Ine}_q^{(1)}$ and $\mathrm{Mar}_q = \mathrm{Mar}_q^{(1)}$, the full-size model or the Benney expansion (2.11) are close to the answer provided by the Orr-Sommerfeld stability analysis. For larger Reynolds numbers, the Benney expansion ceases to provide results in reasonable agreement with the Orr-Sommerfeld analysis. Indeed, the Benney expansion assumes the dynamics of the flow to be slaved to its kinematics which is no more true at large Reynolds numbers. At $\mathrm{Re} = 50$, where the H-mode is predominant, note the good agreement of the full-size model and the reduced model with the Orr-Sommerfeld analysis. However at $\mathrm{Re} = 10$, if the full-size model is in remarkable agreement with the correct answer provided by the Orr-Sommerfeld analysis, the growth rate predicted by the reduced model is significantly larger. Again, taking into account the second-order terms appearing in the heat equation is probably

necessary to correctly describe the instability at moderate Reynolds numbers for which the S-mode is significant. This argues again for the derivation of a model involving t_1 along with h, q and θ, which is still to be done (see the discussion based on equation 5.31).

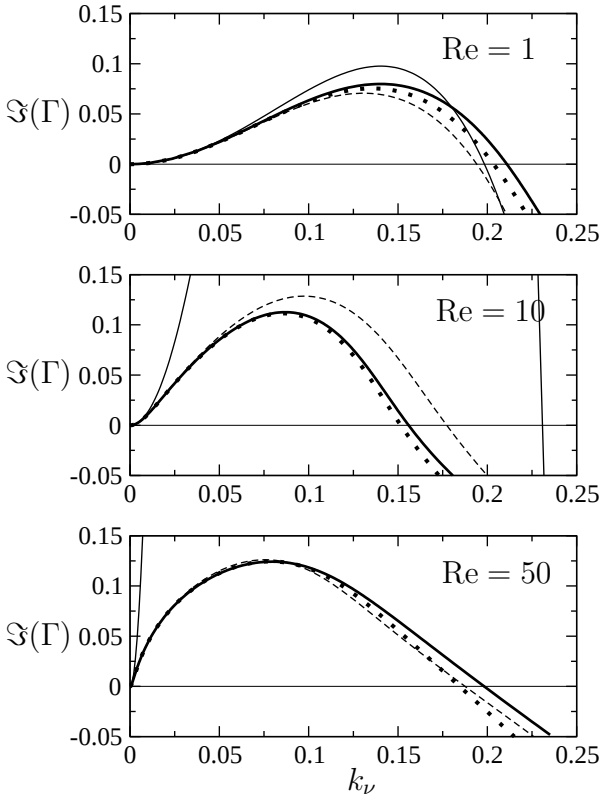

Figure 6.3: Growth rate $\Im(\Gamma)$ versus wavenumber k_ν for different Reynolds numbers. Parameters are given in the caption of figure 6.1. Solid lines stand for the Orr-Sommerfeld analysis, dotted lines for the full-size model and dashed ones for the reduced second-order model (case 1). The thin solid lines correspond to the Benney expansion.

Still for a vertical plane, the marginal stability curves corresponding to the reduced model with $\mathrm{Ine}_q = \mathrm{Ine}_q^{(1)}$ and $\mathrm{Mar}_q = \mathrm{Mar}_q^{(1)}$ for several Biot numbers are shown on figure 6.4. The Marangoni effect is maximum at low and moderate Reynolds numbers if $\mathrm{Bi} \sim 1$. Indeed, if Bi goes to zero or infinity, the free surface temperature of the undisturbed solution (5.38) is independent of the thickness h_N and the Marangoni effect cannot occur (see details in §1.3).
The effect of the Marangoni and Prandtl numbers has been investigated and comparisons of the marginal stability curves are provided on figure 6.5. Note the choice of a smaller Biot number $\mathrm{Bi} = 0.1$ since available experiments correspond to small Biot numbers [56, 62, 65]. As expected if $\mathrm{Ma} = 0$ one recovers the classical hydrodynamic

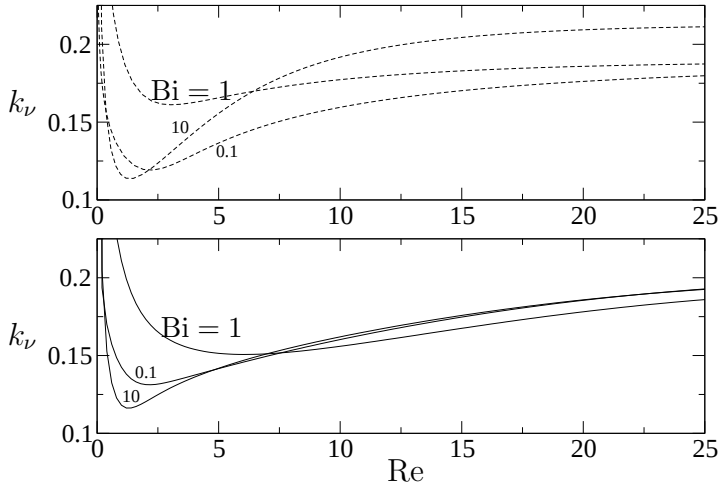

Figure 6.4: Influence of the Biot number on the marginal stability curve. Parameters are Ka = 250, Ct = 0, Pr = 7 and Ma = 50. Solid lines (dashed lines) correspond to Orr-Sommerfeld (reduced model)

H-mode, the corresponding curve emerging from the origin of the plane (k_ν, Re). For Pr = 7, raising the Marangoni number increases the range of unstable wavenumber especially at low Reynolds numbers where the Marangoni effects are predominant (S-mode). Again the results obtained using the reduced model do compare very well with the curves corresponding to the Orr-Sommerfeld analysis. Note however that at large Reynolds numbers, the marginal stability curve obtained with the reduced model do not merge on a single curve whereas Orr-Sommerfeld curves do. Clearly, if Re is large enough, the hydrodynamic H-mode predominates and the thermocapillary effects measured by Ma do not modify significantly the critical wavenumber. The small disparity of the curves corresponding to the reduced model is therefore a consequence of the increased inaccuracy of this model at large Reynolds number. The effect of the Prandtl number on the marginal stability curve is less intuitive. Indeed since the instability is primarily an inertia driven instability, at least if the H-mode predominates, a larger value of Pr should imply a larger range of unstable wavenumbers since the Péclet number Pe = PrRe measuring the inertia effects in the heat equation is also larger. Nevertheless, it can be observed that the Prandtl number has little influence at large Re (H-mode) whereas the curves are strongly affected by it at small Re (S-mode). If the S-mode predominates, the origin of the instability is the gradient of temperature at the surface. This gradient may be weakened by the transport of heat from the troughs to the crests due to the motion of the fluid, a process which is increased with large Prandtl numbers. Note that comparisons between the Orr-Sommerfeld analysis and the reduced model are better at Pr = 1 than for larger values of Pr for which the temperature profile is certainly not properly described by only a single field, namely θ.

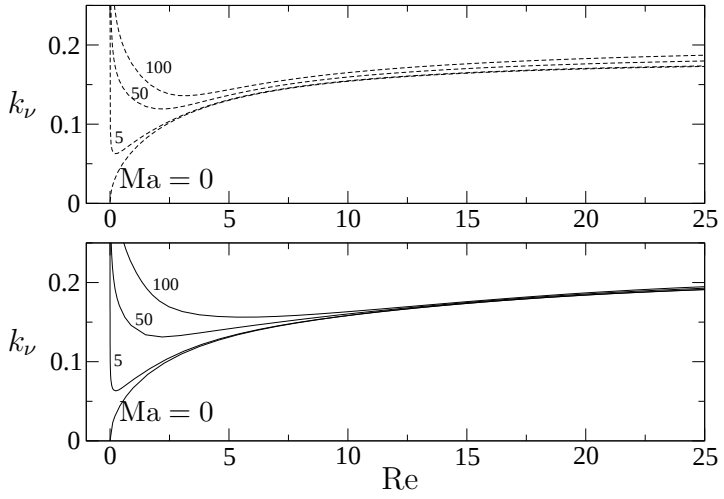

(a)

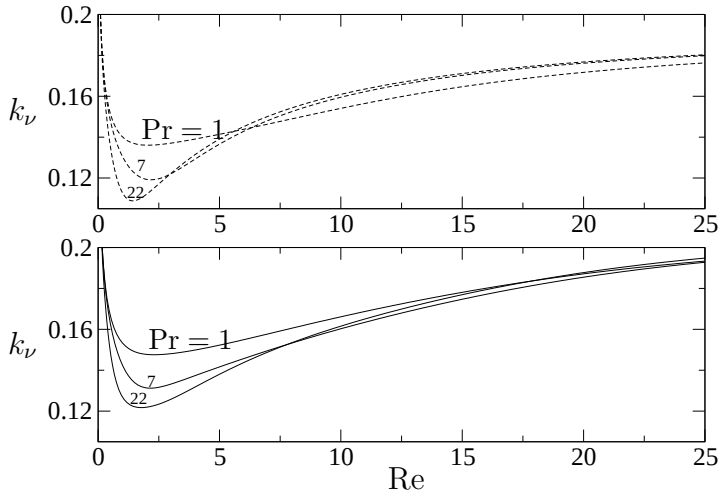

(b)

Figure 6.5: Influence of the Marangoni number (a) and the Prandtl number (b) for a vertical plane, Ka = 250 and Bi = 0.1; (a) Pr = 7, (b) Ma = 50. Solid lines (dashed lines) correspond to Orr-Sommerfeld (reduced model).

For a non-vertical inclined plane and Marangoni numbers Ma of order unity, the critical condition (5.20) can lead to two different values for the onset of the instability corresponding respectively to the H and S modes. This has been checked on figure 6.6 for a plane inclined at an angle $\beta = 15°$ from the horizontal. For moderate values of Ma, two distinct unstable regions are observable each corresponding to a different instability mode as observed initially by Goussis & Kelly [46]. Note the excellent agreement of the curves corresponding to the reduced model with $\mathrm{Ine}_q = \mathrm{Ine}_q^{(1)}$ and $\mathrm{Mar}_q = \mathrm{Mar}_q^{(1)}$ with the Orr-Sommerfeld results in the vicinity of the two thresholds. This agreement results from the account of the second-order dissipative terms in our modelling and from a correct account of the instability threshold. Noticeable discrepancies between the two sets of curves can be observed if the Marangoni number is increased or at larger Reynolds numbers.

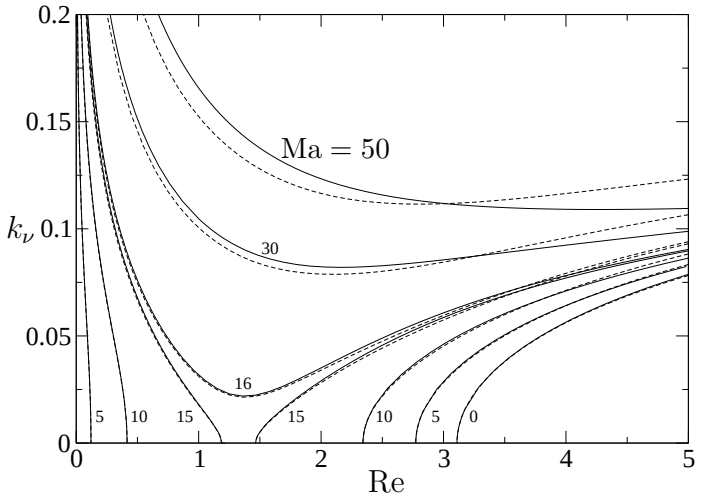

Figure 6.6: Influence of the Marangoni number for an inclined plane of an angle $\beta = 15°$. Parameters are Ka = 250, Pr = 7 and Bi = 1. Solid lines (dashed lines) correspond to Orr-Sommerfeld (reduced model, case 1).

Finally, let us notice again that the choice of the parameters in the above linear study was guided by the concern for emphasizing the differences between the results provided by the different set of equations. In particular, the Kapitza number was chosen quite low (Ka = 250). For example, flows of water on vertical planes correspond to much higher values of Ka (see table C.1). Therefore one expects a much better agreement of our models to the linear Orr-Sommerfeld stability analysis in that case. This can been checked on figure 6.7 where the neutral marginal curves obtained using the reduced model with $\mathrm{Ine}_q = \mathrm{Ine}_q^{(1)}$ and $\mathrm{Mar}_q = \mathrm{Mar}_q^{(1)}$ have been compared to the results of the Orr-Sommerfeld analysis for different Ka. Note the excellent agreement for large values of Ka and especially for Ka = 3175 corresponding to water at $18°C$.

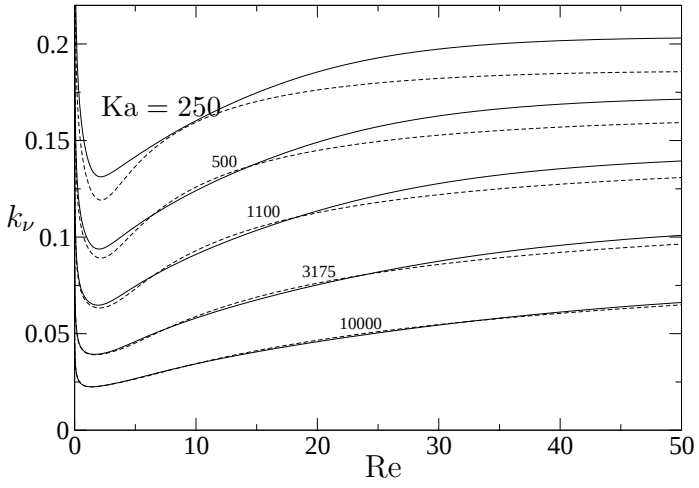

Figure 6.7: Influence of the Kapitza number for a vertical plane (Ka = 3175 corresponds to water at 18°C). Solid lines (dashed lines) correspond to Orr-Sommerfeld (reduced model, case 1).

6.2 Solitary waves

As observed above, comparisons between the Orr-Sommerfeld results and the linear analyses of the different models are not sufficient to completely determine an acceptable reduced model since the influence of the nonlinearities introduced by the second-order inertial terms appearing in (5.36) needs to be investigated. Our attention will be focused on the very nonlinear regime corresponding to solitary waves. Indeed, considering the time evolution of the Benney equation, Pumir *et al.* [103] observed non-physical catastrophic blows up in finite time that seemed to be related to the disappearance of one-hump solitary wave solutions for the parameters considered. This was also the issue of §2.5 where the homoclinic solutions were indeed found to be the most dangerous ones with regards to finite-time blow-up.

Because our approach as well as the classical Benney expansion rely on the assumption of strong viscous effects and small 'perturbative' inertial effects – that is on the *drag-gravity* regime as defined by Ooshida [93] (see §5.5) – special care should be taken to formulate the inertia terms in order to extend them to the *drag-inertia* regime.

Therefore we consider one-hump solitary wave solutions of the reduced model with $\mathrm{Ine}_{q\theta} = \mathrm{Ine}_\theta = \mathrm{Mar}_\theta = 0$, in a frame of reference moving downstream at the speed of the wave. Considering waves that do not change their shape in their moving frame enables to recast the set of equations in a system of ordinary differential equations whose solutions can be computed using the continuation software AUTO97 with the HOMCONT package [30]. Comparisons of the shapes of the different waves is made easier using the scaling based on the intrinsic length-scales of the structures considered. Therefore let us apply the transformation $\mathcal{T}$ (1.103) due to Shkadov [127] and

use the *nonlinear set* of parameters $\{\mathcal{R}, \mathcal{C}, \eta, \mathcal{M}, \mathrm{B}, \mathrm{Pr}\}$ as introduced in §1.6.
Interestingly enough, every parameter goes to zero with the Reynolds number except the reduced Marangoni number which goes to infinity. Therefore for small flow rate, $\mathcal{R} \ll 1$, $\mathcal{C} \ll 1$ and $\eta \ll 1$ can be neglected. Integrating twice the boundary layer equations (1.104) thus leads to

$$q = \frac{h^3}{3}\left(1 + \partial_{xxx} h\right) - \frac{\mathcal{M}}{2} h^2 \partial_x \theta\,, \quad \theta = \frac{1}{1 + \mathrm{B}h} = 1 - \mathrm{B}h + O(\mathrm{B}^2)\,, \tag{6.5}$$

and the mass conservation equation $\partial_t h + \partial_x q = 0$ writes

$$\partial_t h + \partial_x \left[\frac{h^3}{3}\left(1 + \partial_{xxx} h\right) + \frac{\mathcal{M}\mathrm{B}}{2} h^2 \partial_x h\right] \tag{6.6}$$

where the leading order term involving B has been retained. Apart from numerical factors and a different scaling that makes appear the single parameter $\mathcal{M}\mathrm{B}$ in a different way, equation (6.6) is identical to the one obtained by Kalliadasis *et al.* [67]. The reduced parameter they proposed appears $\propto 1/\mathrm{B}\mathcal{M}$. They observed that homoclinic solutions to (6.6) goes to infinity as their parameter goes to zero, that is when $\mathcal{M}\mathrm{B}$ goes to infinity. Because we have $\mathcal{M}\mathrm{B} \propto (3\mathrm{Re})^{-1/9}$, this limit corresponds to the zero Reynolds number limit for which the film is therefore expected to give way to isolated drops separated by very thin layers of fluids for which intermolecular van der Waals forces become increasingly important and could arrest this singularity formation (in the repulsive case). A similar process was found in the time-dependent computations by Joo *et al.* [53] in which the troughs of the waves grow rapidly and lead to very thin regions of the film where van der Waals forces are no longer negligible. Joo *et al.* [53], however, did not construct any solitary wave solutions. In fact the work by Kalliadasis *et al.* [67] is the only study that has traced the solitary wave solution branch for the heated falling film problem (for both free surface and interfacial temperature).
Inversely, if Re goes to infinity, both $\mathcal{M}$ and $\mathcal{M}\mathrm{B}$ go to zero and the velocity and temperature fields are decoupled. Therefore, at large Reynolds numbers, the shape of the wave should be unaffected by the Marangoni effect. Having considered these two limits will enable us to understand more clearly the influence of the Reynolds number on the shape of the wave for chosen slope and physical properties. Indeed, if the properties of the wave – phase speed c, maximal height and profiles – will be compared using the *nonlinear set* of parameters, numerical computations will be performed as in experiments changing only one parameter with the use of the *natural set* $\{\mathrm{Re}, \mathrm{Ct}, \mathrm{Ka}, \mathrm{Ma}, \mathrm{Bi}, \mathrm{Pr}\}$.
Practically, considering stationary solutions in the moving frame $\xi = x - ct$, the set of equations to be resolved can be formally written

$$\frac{d\mathbf{U}}{d\xi} = \mathbf{F}(\mathbf{U};\, \mathcal{R},\, \mathcal{C},\, \eta,\, \mathrm{B},\, \mathcal{M},\, Q)\,, \tag{6.7}$$

where $\mathbf{U}$ corresponds to $(h,\, h',\, h'',\, \theta,\, \theta')^t$ for systems of equations of the form (5.36). The constant Q is the mass flux under the wave in its frame of reference given after

integration of the mass conservation equation $-c\,h' + q' = 0$ by $Q = q - c\,h$. Considering here solitary waves, the Nusselt flat film solution $h = 1$ should be recovered far from the waves and therefore $Q = 1/3 - c$. The speed of the wave being generally larger than the maximal velocity in the liquid, Q is generally negative. Note however that in experiments, the time-averaged film thickness is smaller downstream than at the inlet, the presence of the waves accelerating the fluid motion. As a consequence, the local Reynolds number varying with the third power of the thickness can be significantly smaller than the Reynolds number computed based on the flow rate or the inlet Nusselt film thickness.

Two more possible formulations of Mar_q will be explored here. Yet the reader should keep in mind that a large number of asymptotically equivalent formulations are possible making use of the equalities at zeroth-order (5.38). In the first formulation, we make appear the thermal dissipative terms Dis_θ as given in (5.34b) in an attempt to obtain a system of equations as close as possible to the "approximated" model :

$$\mathrm{Mar}_q^{(2)} = \frac{37-34\theta}{448h(1-\theta)}\partial_x\theta\left(\partial_t q - \frac{9}{7}\frac{q^2}{h^2}\partial_x h + \frac{17}{7}\frac{q}{h}\partial_x q\right) - \frac{hq\theta}{224(1-\theta)} \times \mathrm{Dis}_\theta. \quad (6.8)$$

Another simpler possibility is to modify $\mathrm{Mar}_q^{(1)}$ by changing the term in factor of the first-order inertial terms. Playing with the equivalence $\theta = 1/(1+\mathrm{Bi}h) + O(\varepsilon)$ one gets

$$\mathrm{Mar}_q^{(3)} = -\frac{5}{56}\mathrm{Bi}\frac{\theta^2}{h}\partial_x h\left(\partial_t q - \frac{9}{7}\frac{q^2}{h^2}\partial_x h + \frac{17}{7}\frac{q}{h}\partial_x q\right) + \frac{1}{224}qh\partial_{xx}\theta. \quad (6.9)$$

The superscripts (2) and (3) refers to the corresponding cases in table 6.1.

Figure 6.8 shows the evolution of the speed c and the maximal height $h_{\max}$ as function of the Reynolds number for the families of single-hump homoclinic solutions computed with the different formulations of Mar_q. The parameters are $\mathrm{Ka} = 250$, $\mathrm{Ct} = 0$, $\mathrm{Ma} = 50$ and $\mathrm{Bi} = 0.1$. The formulation $\mathrm{Mar}_q^{(2)}$ (curve 4) leads to a turning point and therefore branch multiplicity. Above $\mathrm{Re} \approx 6.7$ no one-hump solitary wave can be obtained in that case. Solitary-wave families computed by Kalliadasis *et al.* [67] do not present any turning point so that any branch multiplicity is likely to be related to the catastrophic behaviour observed by Pumir *et al.* [103] and Oron & Gottlieb [98] with the Benney equation (see §2.5.2). The expression $\mathrm{Mar}_q^{(2)}$ should therefore be prohibited. The solitary wave branches obtained using $\mathrm{Mar}_q^{(1)}$ and $\mathrm{Mar}_q^{(3)}$, respectively curves 2 and 3 in figure 6.8, do not exhibit such branch multiplicity. It is not easy to say which of these two formulations is preferable since the one-hump solitary wave branch corresponding to the full set of the Navier-Stokes and heat equation is not available. Indeed, constructing such solutions is a formidable task owing to the difficulty of tracking the boundaries of the computational domain and the large range of scales involved . In an attempt to get a point of comparison, the solitary wave branch corresponding to the full-size second-order model was constructed (see curve 5 in figure 6.8). Unfortunately, it seems not possible using AUTO97 to continue this branch of solutions above a quite low value of Re. This is certainly due to the very large dimension of the corresponding dynamical system. Therefore, owing to the good behaviour of the "approximated" model observed at least in the case of

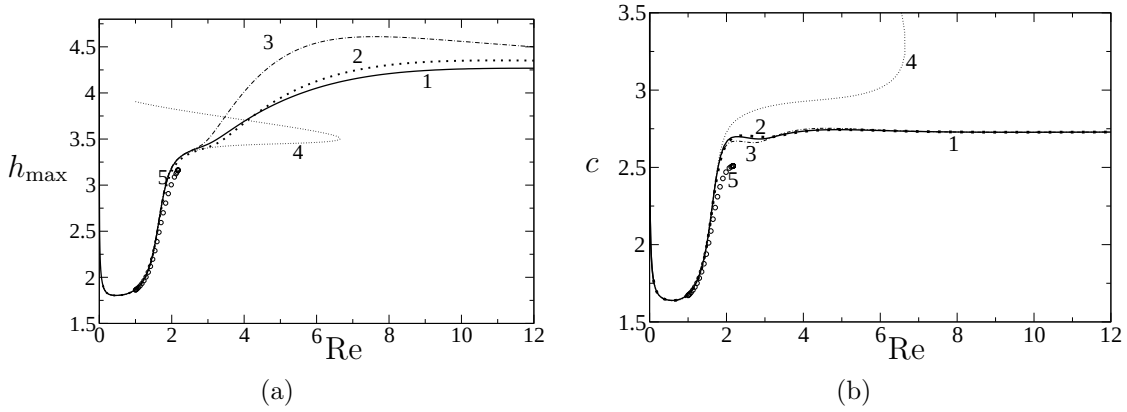

Figure 6.8: Speed and maximal height of solitary wave solutions computed with the reduced model; curve 1: $\mathrm{Mar}_q = 0$; curve 2: $\mathrm{Mar}_q^{(1)}$; curve 3: $\mathrm{Mar}_q^{(3)}$; curve 4: $\mathrm{Mar}_q^{(2)}$; curve 5: full-size for the momentum equation and approximated for the heat equation.

isothermal flow [110], we will keep here a very conservative approach and select the formulation that gives the closest answer to the one provided using the approximated model which is obviously $\mathrm{Mar}_q^{(1)}$. Consequently, the selected model ('case 1' in table 6.1) corresponding to (5.36) with $\mathrm{Ine}_{q\theta} = \mathrm{Ine}_\theta = \mathrm{Mar}_\theta = 0$ and Ine_q and Mar_q given by (6.2) and (6.4) reads explicitly

$$\partial_t h = -\partial_x q\,, \tag{6.10a}$$

$$\begin{aligned}\partial_t q = {} & \frac{9}{7}\frac{q^2}{h^2}\partial_x h - \frac{17}{7}\frac{q}{h}\partial_x q \\ & + \left\{\frac{5}{6}h - \frac{5}{2}\frac{q}{h^2} + 4\frac{q}{h^2}(\partial_x h)^2 - \frac{9}{2h}\partial_x q\partial_x h - 6\frac{q}{h}\partial_{xx}h + \frac{9}{2}\partial_{xx}q\right. \\ & \left. -\frac{5}{6}\mathrm{Ct}h\partial_x h + \frac{5}{6}\mathrm{Ka}h\partial_{xxx}h - \mathrm{Ma}\left(\frac{5}{4}\partial_x\theta - \frac{1}{224}hq\partial_{xx}\theta\right)\right\} \\ & \times\left(1 - \frac{1}{70}q\partial_x h + \mathrm{Ma}\frac{5}{56h}\partial_x\theta\right)^{-1}\,,\end{aligned} \tag{6.10b}$$

$$\begin{aligned}\mathrm{Pr}\partial_t\theta = {} & 3\frac{(1-\theta-\mathrm{Bi}h\theta)}{h^2} + \mathrm{Pr}\left[\frac{7}{40}\frac{(1-\theta)}{h}\partial_x q - \frac{27}{20}\frac{q}{h}\partial_x\theta\right] \\ & + \left(1-\theta-\frac{3}{2}\mathrm{Bi}h\theta\right)\left(\frac{\partial_x h}{h}\right)^2 + \frac{\partial_x h\partial_x\theta}{h} + (1-\theta)\frac{\partial_{x^2}h}{h} + \partial_{xx}\theta\,.\end{aligned} \tag{6.10c}$$

Remark finally on figure 6.8 the jump of the phase speed and the maximal amplitude of the homoclinic branch of solutions. It separates actually the two regimes as already discussed in §5.5, namely the *drag-gravity* regime at the left of the jump and the *drag-inertia* regime at its right. As foreseen previously, all the models agree in the drag-gravity regime while the key-point of our study stands in the formulation that

correctly describes the drag-inertia regime; condition that seems to be fulfilled by (6.10).

6.3 Interactions between H and S-modes

A model of reduced dimensionality having been selected, let us discuss the influence of the different physical effects. However, we will restrict ourself to the case of vertical walls and to solitary waves since vertical apparatuses are the most common in use and solitary waves tend to dominate the wave dynamics at a sufficient distance from the inlet [1] (see chapter 7). We may also only study the influence of the Re, Pr and Ma numbers. Indeed, our interest is mainly to consider how the hydrodynamic and thermocapillary H and S-modes couple each other, putting the emphasis on the case of large amplitude waves, that is on the drag-inertia regime (for which inertia plays a dominant role). We have then fixed throughout this discussion the values of the Biot and Kapitza numbers to Bi = 0.1 and Ka = 250. On the one hand, the Biot is chosen much smaller than unity as for realistic experimental situations (see the discussion in §8.2.1). On the other hand, the Kapitza number as been expressly chosen small with respect to its value for common liquids (see table C.1). The reason is that at such small value, the second-order dissipative and inertia effects become predominant and we precisely want to test our selected model in a situation when its second-order terms are effective.

On figure 6.9, the amplitude and speed of the one-hump solitary-wave family have been plotted against Re for different values of the Prandtl and Marangoni numbers. On the same figure the wave family corresponding to isothermal flows (Ma = 0) is represented for comparisons. As expected, increasing the Marangoni number implies larger amplitude and speed since the two instability modes reinforce each other. This effect is more visible at low Reynolds numbers since the reduced Marangoni number $\mathcal{M}$ defined in (1.105d) is proportional to $\mathrm{Re}^{-4/9}$. Inversely, for the largest values of Re, the curves merge on the isothermal one. The effect of the Prandtl number is more subtle. At low Reynolds numbers (< 0.5), larger values of Pr seem to favor the instability (though the effect is weak), whereas at larger Re, it is the opposite.

In order to understand the effect of the Prandtl number, the streamlines and the isotherms have been computed in the frame of reference of the wave after computing the velocity and temperature fields from the polynomial expansion, the definitions of the polynomial test functions and the first-order approximation of the corrections s_i and t_i (see 5.35). Note that the second-order corrections of both fields could have been computed after writing the residuals corresponding to the corresponding test-functions, and inverting the obtained linear system. Nevertheless, due to the complexity of this procedure, we may avoid it and consider the velocity and temperature fields to be sufficiently described by their representation at first-order, at least for a qualitative discussion. The Marangoni number is Ma = 50 and will not be modified until the end of this section. The isotherms and streamlines computed for a small value of Re = 0.01 are shown on figure 6.10. The reduced parameters are $\mathcal{R} = 0.0022$, $\eta = 0.0053$, $\mathcal{M} = 37.6$ and B = 0.031. The product Pr$\mathcal{R}$, η and B being

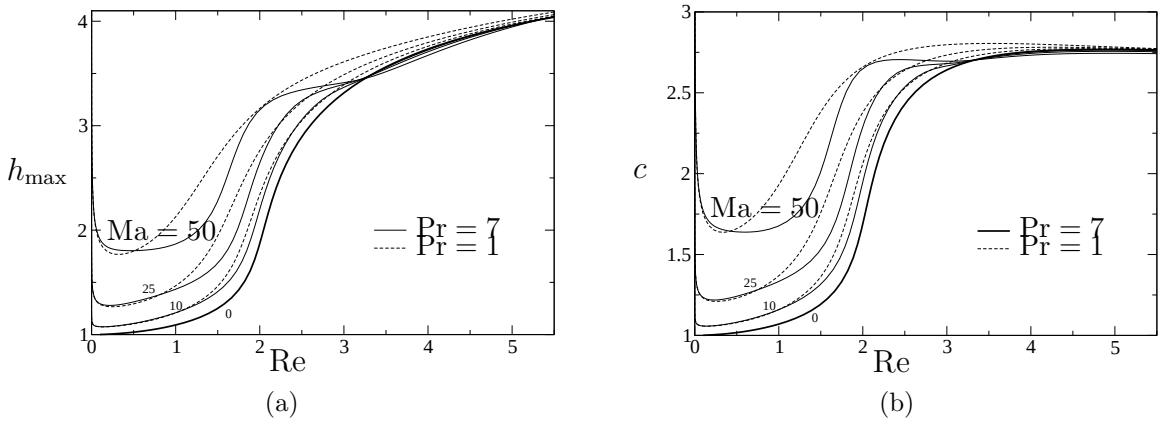

Figure 6.9: Speed and maximal height of solitary wave solutions computed with the selected second-order model (6.10) for different values of Pr and Ma. Other parameters are Ct = 0, Bi = 0.1 and Ka = 250.

small, $\partial_{yy}T \approx 0$ and the temperature field is nearly linear. $\theta \approx 1 - \mathrm{B}h$ such that $T \approx 1 - \mathrm{B}y$. Therefore, the isotherms are nearly aligned with the wall. Note also that the surface temperature θ also represented on figure 6.10 is nearly uniform.
The isotherms and streamlines computed for Re = 1 and Pr = 1 or 7 are reproduced on figure 6.11. The reduced parameters are now $\mathcal{R} = 0.61$, $\eta = 0.041$, $\mathcal{M} = 4.86$ and B = 0.14. Again, at Pr = 1, the isotherms are nearly aligned, B and Pr$\mathcal{R}$ being still relatively small. At Pr = 7, the isotherms are no more aligned with the wall and are more deflected upwards by the movement of the fluid in the crest. Therefore, the minimum of temperature achieved at the surface on the top of the wave is increased ($T_{\min} = 0.8$ compared to 0.765 for Pr = 1) and consequently the Marangoni effect reduced. The transport of heat by the motion of the fluid has a stabilizing effect in that case, *i.e.* in the *drag-gravity* regime. Nevertheless, at larger Reynolds numbers, *i.e.* in the *drag-inertia* regime, the wave amplitude and speed increase dramatically and a recirculation zone appears inside the solitary wave. Streamlines computed for Re = 2 and Re = 3 and represented on figures 6.12 and 6.13 do exhibit such recirculating zones, and two stagnation points at the surface on the back and the front of the solitary waves can be observed. Because the fluid in the moving hump circulates clockwise and is trapped, the waves can be said to transport mass. Comparisons to the streamlines computed if the thermocapillary effects is switched off (Ma = 0) at Re = 3 show that the Marangoni instability moves one of the stagnation point from the front of the wave to its crest (see figure 6.14). Because thermocapillary stresses push the fluid from the rear to the top of the crests, they reinforce the clockwise circulation in the crest. Meanwhile, the transport of heat by the downward fluid motion at the front of the recirculating zone cools the surface at its crest and the minimum of surface temperature matches closely with the stagnation point at the front. Therefore the two mechanisms reinforce each other promoting the speed and

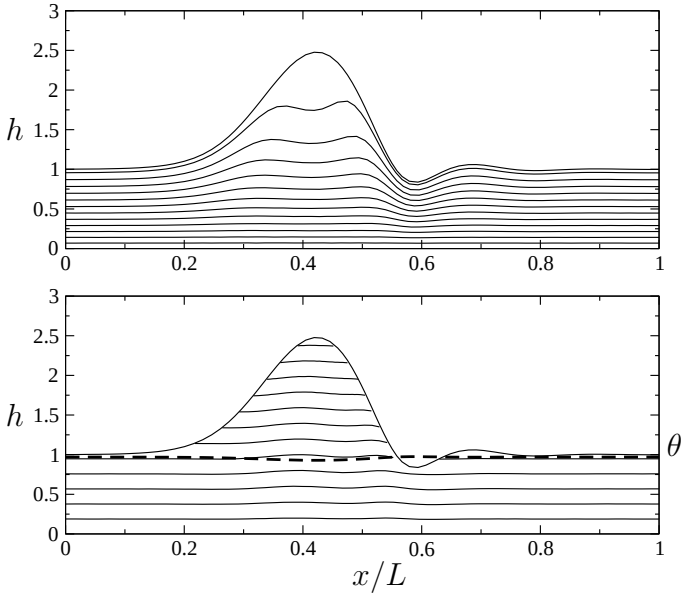

Figure 6.10: Streamlines in the moving frame (top) and isotherms (bottom) calculated for a right-moving solitary wave at Re = 0.01, Ka = 250, Pr = 7, Ma = 50 and Bi = 0.1. The temperature at the interface θ corresponds to the dashed line.

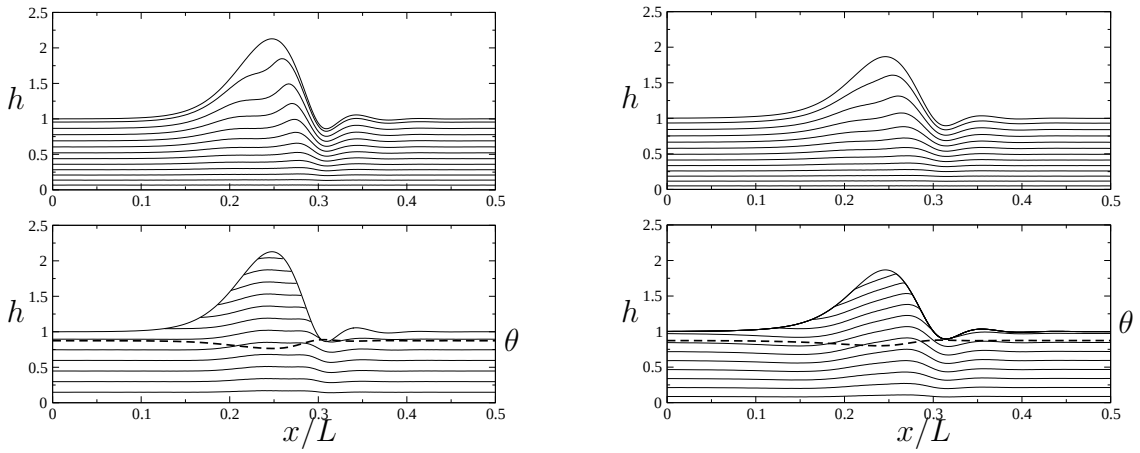

Figure 6.11: Streamlines (top) and isotherms (bottom). Same parameters as in figure 6.10 but Re = 1 and (a) Pr = 1, (b) Pr = 7.

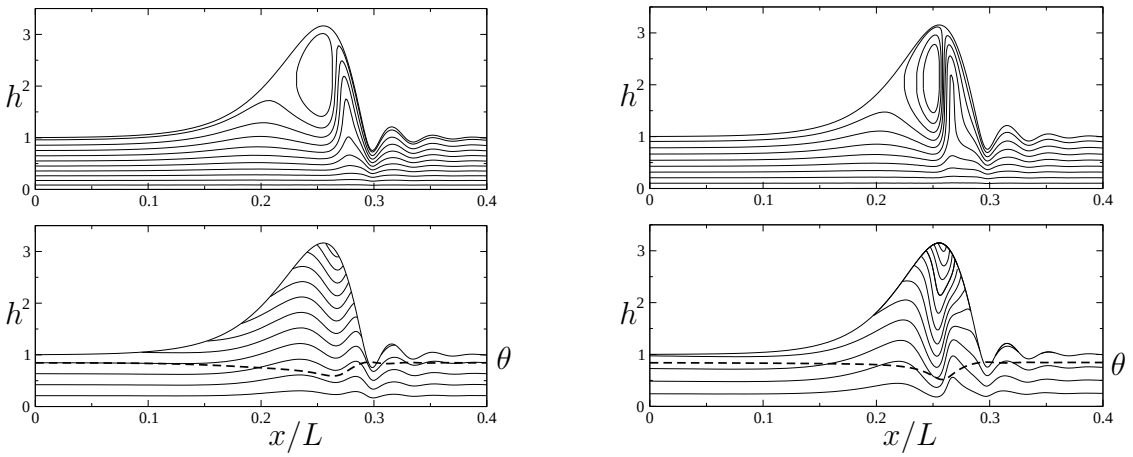

Figure 6.12: Streamlines (top) and isotherms (bottom). The Reynolds number is Re = 2 and (a) Pr = 1, (b) Pr = 7. Other parameters defined in the caption of figure 6.10.

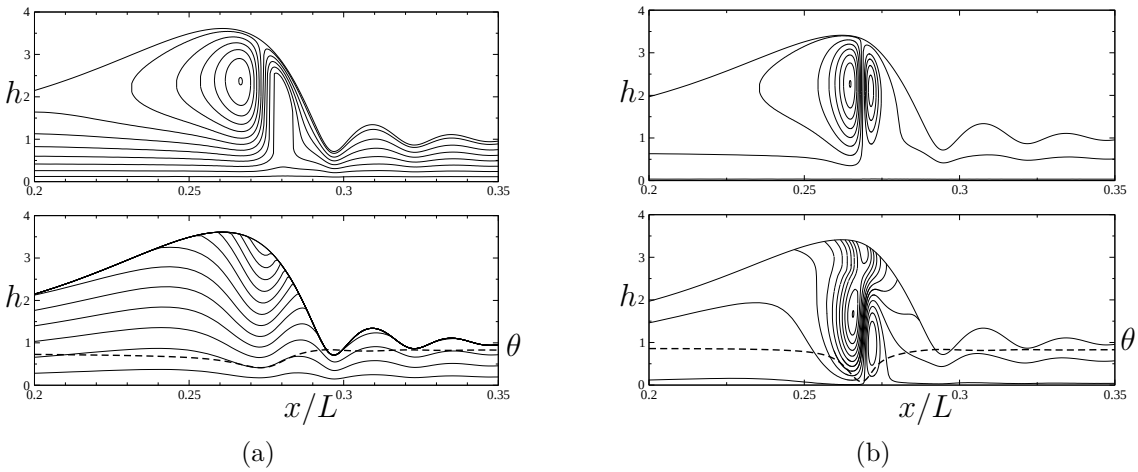

Figure 6.13: Streamlines (top) and isotherms (bottom). Re = 3 and (a) Pr = 1, (b) Pr = 7.

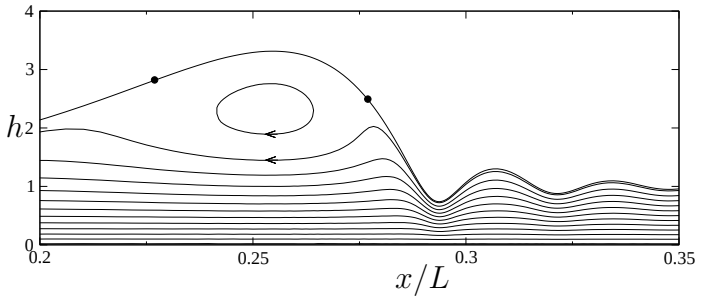

Figure 6.14: Streamlines in the moving frame of the wave. Parameters are Ma = 0, Re = 3, Ct = 0 and Ka = 250.

amplitude of the wave. This explains that a recirculating zone can be observed at Re = 2 and Ma = 50 whereas it is not present if Ma = 0. Indeed, the abrupt increase of amplitude and speed of the solitary waves corresponding to the transition from the drag-gravity to the drag-inertia regime occurs for smaller values of the Reynolds number if the Marangoni effect is present (see figure 6.9).

Comparison of figures 6.12(a) and 6.12(b) indicate also that increasing the Prandtl number from Pr = 1 to Pr = 7 enhances the cooling process of the crest and reduces the minimum of temperature from $T_{\min} = 0.591$ to 0.517 thus contributing to the Marangoni effect. At Re = 3, the effect is even stronger as can be seen from figure 6.13. However, if the H and S instability modes reinforce each other for Re = 2 or Re = 3, the speed and amplitudes of the solitary waves do decrease with the Prandtl number as indicated on figure 6.9. This paradox can be explained only by noting that pushing one of the stagnation point to the crest, thermocapillarity does tighten the streamlines and isotherms in the front of the recirculating zone. Moreover, the circulation in the hump is promoted by the Marangoni stresses at the surface. Therefore, large temperature and velocity gradients appear in that region. As a consequence, the dissipation of heat and momentum is increased, which contributes to stabilize the growth of the instability and to limit the speed and amplitude of the waves.

Notice that at Re = 3 the minimum of temperature drops from 0.414 when Pr = 1 to 0.051 when Pr = 7. This minimum is no more located at the surface but in the core of the recirculating zone. This result should be taken cautiously since for higher values of Re, unphysical negative values of the dimensionless temperature appear in the fluid as shown in figure 6.15. Turning back to dimensional quantities, this means that the temperature at the surface would be locally smaller than the temperature of the air. Such results obviously have no physical basis. To understand the appearance of this unphysical behaviour, let us consider the high Péclet number limit PrRe $\gg 1$. In such a case, the heat diffusion can be neglected and the temperature field is basically transported by the flow as a passive scalar. Therefore, considering stationary waves in their moving frame, the isotherms should coincide with the streamlines in the moving frame. Since large amplitude waves exhibit recirculation zones, some isotherms should

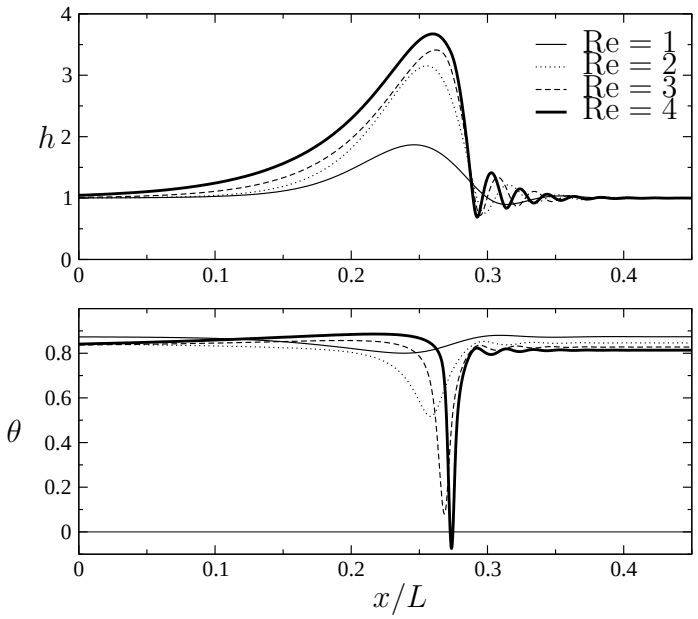

Figure 6.15: Film thickness and surface temperature of homoclinic solutions calculated for various Re and Ka = 252, Pr = 7, Ma = 50 and Bi = 0.1.

be closed. Consequently, the temperature gradient could be horizontal and thus the hypothesis $\partial_y T \gg \partial_x T$ necessary to the derivation of our models would be violated at least locally. Another potential reason for the appearance of negative temperature is also the neglect in the averaged heat balance (6.10c) of the transport of heat due to the Marangoni flow (Mar_θ). Though these terms are formally of second-order, they could be quite strong due to the enhancement of the Marangoni flow by the hydrodynamic mechanism. Different possibilities – not examined here – could be offered to cure this strong limitation in the applicability of the three-unknown model (6.10). One of them would be to consider more unknowns such as t_1 for the description of the heat transfer process in the flow, as already mentioned. The second one is to relax the assumption $\partial_y T \gg \partial_x T$ in the derivation process by considering all terms involving the temperature to be of the same order.

To check the arguments given as a possible explanation of the failure of our model to describe the solitary-wave regime at high Péclet number, we have computed the one-hump solitary-wave branch corresponding to the first-order model (equations (5.36) all second-order terms Dis_q, Dis_θ, Ine_q, $\mathrm{Ine}_{q\theta}$, Ine_θ, Mar_q, Mar_θ being set to zero). The speed of amplitudes of the solitary waves are displayed on figure 6.16 as function of the Reynolds number for Ka = 250, Ct = 0, Bi = 0.1 and two values of the Prandtl number (Pr = 1 or Pr = 7). In both cases, a limit point, for which the branch of solutions is lost, is encountered. This loss follows the formation of steep gradients of temperature in the bulk of the flow as is evident in view of the isotherms displayed on figure 6.17 at Re = 2.5 and Pr = 7. Notice that, quite surprisingly, the loss of solutions appear at values of Re smaller for Pr = 1 than for Pr = 7. This paradoxical result can be understood considering that the transition between the drag-gravity

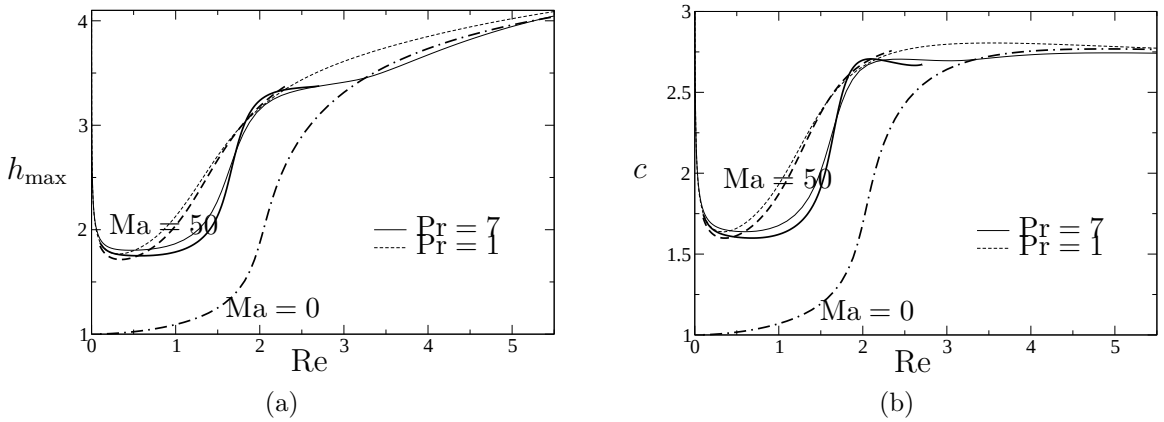

Figure 6.16: Speed and maximal height of solitary wave solutions computed with the first-order model (thick lines) and the selected second-order model (thin lines)

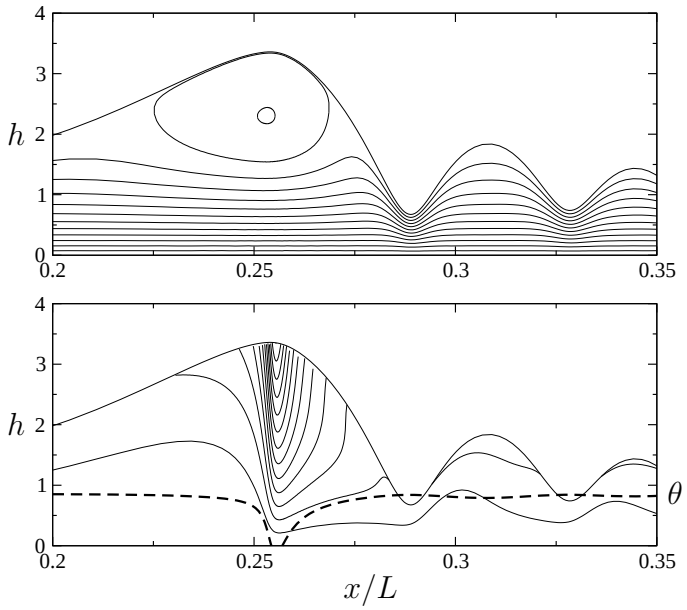

Figure 6.17: Streamlines (top) and isotherms (bottom). Re = 2.5 and Pr = 7. First-order model

and the drag-inertia regimes is delayed by the upward displacement of the isotherms by the flow as already observed on figure 6.11. Consequently, the second-order terms do contribute to delay the breakdown of our modelling. This effect is certainly due to the second-oder diffusion terms which reduce the range of unstable wavenumber and smooth the gradients (the reader is invited to compare the amplitude of the fore-running waves preceding the main hump in figures 6.13 and 6.17).

Chapter 7

Three-dimensional dynamics

This chapter is devoted to a numerical investigation of three-dimensional instabilities of film flows and comparisons with available experiments. We first present the phenomenology of the transition between two-dimensional (2D) and three-dimensional (3D) instability (§7.1). Turning to 3D flows, we will extend our models developed in chapters 5 and 6 to include the spanwise coordinate z (§7.2). Next, numerical simulations of the model will be compared to the 3D patterns observed in experiments of Liu *et al.* [84] and Alekseenko *et al.* [1] for isothermal conditions (§7.3). Finally, we investigate the effect of thermocapillarity on three-dimensional nonlinear dynamics (§7.3.3).

7.1 Transition from 2D to 3D waves

Many experimental studies have been devoted to the wavy regime of film flows since the first observations by Kapitza & Kapitza [69]. Most of them are described in the review by Alekseenko *et al.* [1]. Recent measurements can be found in [91, 143]. Gollub and coworkers reported an extensive study of the film dynamics in the case of weakly inclined planes and for a water-glycerin mixture [83, 81, 82, 84]. Controlling the entrance flow rate, they applied a periodic forcing at the inlet and observed the film response at a given frequency. Their experiments give the clearest picture of the wide phenomenology of the interacting waves on film flows and complete the description offered by Chang [15]. The different observations are summed up schematically on figure 7.1. The spatial evolution of the film can be split up into four phases corresponding to four different regions on the inclined plane. The first one is the inception region where the primary instability of the flat film to infinitesimal disturbances develops spatially and temporally. The observed primary waves are two-dimensional, which is consistent with the Squire's theorem (see §1.4.2), indeed shown to apply to free surface flows by Yih [146]. Next, the wave amplitude saturates and the shape of the waves remains quasi-stationary over a distance corresponding to a few wavelengths (II). These waves are quite slow and present large crests and deep thin troughs. They form the γ_1 wave family using the terminology defined by Chang *et al.* [19] (see §2.5.1). The saturated waves then undergo a secondary instability which, close to

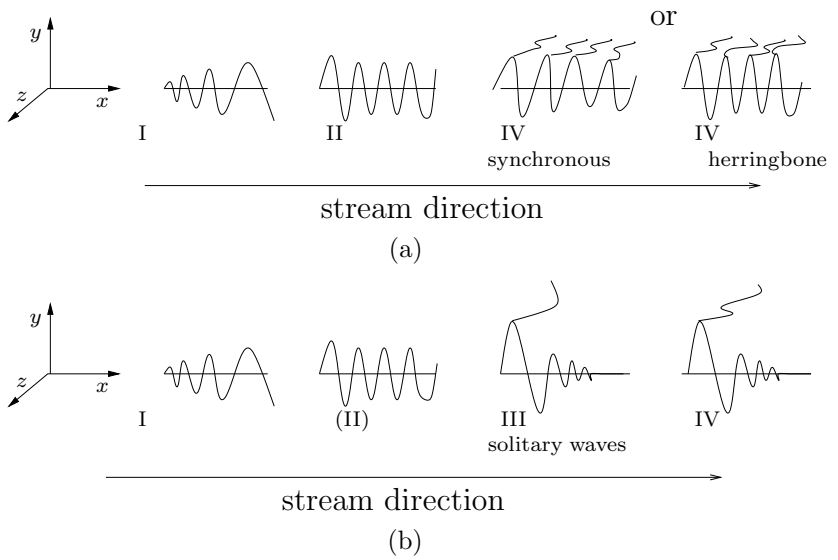

Figure 7.1: Phenomenological sketch of the spatial evolution of film flows [15, 84]: (a) at high forcing frequency ; (b) at low frequency. Courtesy of Ruyer-Quil [107].

the threshold and for low frequency, is two-dimensional and leads to large amplitude fast hump preceded by small capillary ripples, or solitary waves (III). This family of wave are the γ_2 waves in Chang's terminology. Two-dimensional waves are generally unstable to transverse perturbations which leads to the last stage of secondary three-dimensional instabilities (IV), generally accompanied by chaotic dynamics. As for boundary layers, Liu *et al.* reported two different scenarios. Concerning the first one, their investigations showed that the wave crests are usually deformed in phase, and will thus be referred to as a **synchronous instability**. In the second less commonly observed scenario, two successive crests are deformed with a π phase shift. This leads to checkerboard (or herringbone) patterns and is characteristic of a **subharmonic instability**. At high forcing frequency, the 3D instability mechanisms show up before the secondary 2D instabilities such that the flow becomes chaotic before the formation of the 2D solitary waves. Therefore, region III disappears at high frequency, whereas at low frequency, forcing can lead directly to the solitary wave formation and saturated γ_1 waves (region II) may not be observed.

To our knowledge, the transition of film flows towards 3D dynamics was first theoretically investigated by Trifonov [140]. Trifonov computed the branches of 2D solutions of the Kapitza-Shkadov model (IBL) that remain stationary in their frame of reference, and analyzed their stability versus transverse modulations. His study revealed that the subharmonic instability was always the most dangerous, in contrast with experimental results. Actually, Liu *et al.* 's experiments [84] show that in the case of the γ_1 family, the transverse modulations of the troughs grew faster than the modulations of the peaks and lead to a train of isolated depressions distributed synchronously. Chang *et al.* [14] completed the study of Trifonov using the boundary-layer equation (1.100). As for Trifonov's results, their computations showed a quite different sce-

nario from the experimental ones reported by Liu *et al.* , since their stability analysis of the γ_1 family predicted only the subharmonic instability. However, Trifonov and Chang *et al.* considered only a vertical wall and quite low Reynolds numbers whereas Liu *et al.* 's experiments [84] were performed for an inclined wall where the hydrostatic pressure plays a significant role. As a consequence their results still need to be theoretically explained.

7.2 Three-dimensional model

Let us turn to the three-dimensional formulations of the models, or more precisely to the two-dimensional (x and z) averaged equations that describe the three-dimensional film flow up to moderate Re. This means that we will again get rid of the $y-$coordinate of the 3D boundary layer system of equations presented in §1.5, by using the weighted residual technique developed in chapter 5 for the 2D version.
Considering the trivial Nusselt flat film solution (1.43), the gravity acceleration has no component in the spanwise direction and therefore the spanwise velocity w is trivially equal to zero. Therefore, w is necessarily triggered by the modulations of the free surface and formally appears (at least) at order ε. This property can be used to simplify the systems of equations which model the flow dynamics in three dimensions, as done by Ruyer-Quil & Manneville for isothermal conditions [109]. However, this assumption will not be used here and the systems of equations published in [109] will then be generalized hereafter. Two reasons motivate this choice. First, experimentally observed wave patterns have a significant curvature along the z-axis which is due to the lateral no-slip boundary conditions [82, 84]. In such a configuration, the local velocity field may not be oriented in the preferred streamwise direction and the previous argument may fail. Secondly, comparisons of the spanwise wavelength corresponding to the maximal growth-rate of the secondary 3D instabilities show a better agreement with the results obtained by Liu *et al.* if w is assumed to be of order unity rather than of order ε [112]. Therefore, and similarly to the projection for the streamwise velocity (5.25a), four additional fields are needed to represent the spanwise velocity, which reads as

$$w = \frac{3}{h}\left(p - r_1 - r_2 - r_3\right) F_0(\bar{y}) + 45\frac{r_1}{h}F_1(\bar{y}) + 210\frac{r_2}{h}F_2(\bar{y}) + 434\frac{r_3}{h}F_3(\bar{y}) \tag{7.1}$$

where the spanwise flow rate $p = \int_0^h w\,dy$ appears as well as three corrections r_1, r_2 and r_3 associated to the same polynomials F_1, F_2 and F_3 as the ones used for the streamwise velocity (5.23). Formally, the problem here consists in thirteen equations for the thirteen unknowns h, q, s_1, s_2, s_3, p, r_1, r_2, r_3, θ, b_1, b_2 and b_3. This system being complex, we will restrict ourselves to its isothermal version for which only seven unknowns are involved, namely h, q, s_1, s_2, p, r_1, r_2; the corresponding system is presented in appendix D.2 and is referred to as the **full model** in the following. In contrast, extending the reduced model (6.10) to 3D (non-isothermal) flow is quite simple. Indeed, the leading order transverse flow rate being zero, *i.e.* $p^{(0)} = 0$, the

corrections r_1, r_2 and r_3 for p will not contribute to the second-order inertial corrections if we adopt the same strategy as discussed in chapter 6. Therefore, the resulting averaged spanwise momentum equation – as for the heat equation – can then be straightforwardly derived from the spanwise boundary-layer equation (1.100b) applying the Galerkin method (*i.e.* assuming the velocity and the temperature profiles to be parabolic and linear, respectively, as for $F_0(\bar{y})$ and $G_0(\bar{y})$). The three-dimensional extension of our **reduced model** can then finally be written in the following form:

$$\partial_t h = -\partial_x q - \partial_z p\,, \tag{7.2a}$$

$$\begin{aligned}\mathcal{R}\,\partial_t q = {} & \mathcal{R}\left[\frac{9}{7}\frac{q^2}{h^2}\partial_x h - \frac{17}{7}\frac{q}{h}\partial_x q\right] + \left\{\mathcal{R}\left[-\frac{8}{7}\frac{q\partial_z p}{h} - \frac{9}{7}\frac{p\partial_z q}{h} + \frac{9}{7}\frac{qp\partial_z h}{h^2}\right] + \frac{5}{6}h - \frac{5}{2}\frac{q}{h^2}\right. \\ & +\eta\left[4\frac{q\,(\partial_x h)^2}{h^2} - \frac{9}{2}\frac{\partial_x q\partial_x h}{h} - \frac{13}{16}\frac{\partial_z p\partial_x h}{h} - \frac{43}{16}\frac{\partial_x p\partial_z h}{h} - \frac{73}{16}\frac{p\partial_{xz}h}{h} - 6\frac{q\partial_{xx}h}{h}\right. \\ & \left.\left.-\frac{\partial_z q\partial_z h}{h} + \frac{3}{4}\frac{q\,(\partial_z h)^2}{h^2} + \frac{13}{4}\frac{p\partial_x h\partial_z h}{h^2} - \frac{23}{16}\frac{q\partial_{zz}h}{h} + \frac{9}{2}\partial_{xx}q + \partial_{zz}q + \frac{7}{2}\partial_{xz}p\right]\right. \\ & \left.-\frac{5}{6}\zeta h\,\partial_x h - \mathcal{M}\left(\frac{5}{4}\partial_x\theta - \underline{\frac{\mathcal{R}}{224}hq\partial_{xx}\theta}\right) + \frac{5}{6}h\,(\partial_{xxx}h + \partial_{xzz}h)\right\} \\ & \times\left(1 - \underline{\frac{\mathcal{R}}{70}q\partial_x h} + \underline{\mathcal{M}\frac{5}{56}\frac{\partial_x\theta}{h}}\right)^{-1}\,,\end{aligned} \tag{7.2b}$$

$$\begin{aligned}\mathcal{R}\,\partial_t p = {} & \mathcal{R}\left[\frac{9}{7}\frac{p^2}{h^2}\partial_z h - \frac{17}{7}\frac{p}{h}\partial_z p - \frac{8}{7}\frac{p\partial_x q}{h} - \frac{9}{7}\frac{q\partial_x p}{h} + \frac{9}{7}\frac{qp\partial_x h}{h^2}\right] - \frac{5}{2}\frac{p}{h^2} \\ & +\eta\left[4\frac{p\,(\partial_z h)^2}{h^2} + \frac{13}{4}\frac{q\partial_x h\partial_z h}{h^2} - \frac{9}{2}\frac{\partial_z p\partial_z h}{h} - 6\frac{p\partial_{zz}h}{h} - \frac{\partial_x p\partial_x h}{h} - \frac{43}{16}\frac{\partial_z q\partial_x h}{h}\right. \\ & \left.-\frac{13}{16}\frac{\partial_x q\partial_z h}{h} + \frac{3}{4}\frac{p\,(\partial_x h)^2}{h^2} - \frac{23}{16}\frac{p\partial_{xx}h}{h} - \frac{73}{16}\frac{q\partial_{xz}h}{h} + \frac{9}{2}\partial_{zz}p + \partial_{x^2}p + \frac{7}{2}\partial_{xz}q\right] \\ & -\frac{5}{6}\zeta h\,\partial_z h - \frac{5}{4}\mathcal{M}\partial_z\theta + \frac{5}{6}h\,(\partial_{xxz}h + \partial_{zzz}h)\,.\end{aligned} \tag{7.2c}$$

$$\begin{aligned}\mathrm{Pr}\mathcal{R}\,\partial_t\theta = {} & 3\frac{(1-\theta-\mathrm{B}h\theta)}{h^2} + \mathrm{Pr}\mathcal{R}\left[\frac{7}{40}(1-\theta)\frac{(\partial_x q + \partial_z p)}{h} - \frac{27}{20}\frac{(q\partial_x\theta + p\partial_z\theta)}{h}\right] \\ & +\eta\left[\left(1-\theta-\frac{3}{2}\mathrm{B}h\theta\right)\left(\frac{(\partial_x h)^2}{h^2} + \frac{(\partial_z h)^2}{h^2}\right) + \frac{\partial_x h\partial_x\theta}{h} + \frac{\partial_z h\partial_z\theta}{h}\right. \\ & \left.+(1-\theta)\frac{(\partial_{xx}h + \partial_{zz}h)}{h} + \partial_{xx}\theta + \partial_{zz}\theta\right]\,,\end{aligned} \tag{7.2d}$$

where the *nonlinear set* of parameters has been used. Equation (7.2a) is the mass conservation equation, equations (7.2b,7.2c) express the averaged momentum balances in both directions x and z, and equation (7.2d) is the energy balance. The 3D **approximated model** is embedded into (7.2) and recovered by omitting the underlined terms corresponding to the second-order corrections of the streamwise parabolic profile due to inertia and Marangoni flow.

7.3 Three-dimensional simulations

In this section, we compare direct numerical simulations of (7.2) with experimental results available in the literature. In addition, we will compare in isothermal conditions ($\mathcal{M} = 0$) our reduced model (7.2a,b,c) with the embedded approximated model and the full model given in appendix D.2. Periodic boundary conditions in both x and $z-$directions are enforced. This allows to represent the solution in Fourier space and to use the good convergence properties of spectral methods, as was done in §4.5. The numerical scheme is again pseudo-spectral, products and non-linearities being evaluated in the real space and derivatives in Fourier space. The Fast Fourier Transform algorithm is therefore used extensively. The time stepping is chosen to be explicit in order to quickly adapt our scheme to the different models. In practice, a fifth-order Runge-Kutta scheme was used [102], which allows to estimate the error by difference with an embedded fourth-order Runge-Kutta scheme. The error on each variable is limited to 10^{-5}.
In order to measure the three-dimensionality of the flow, let us define, following Joo *et al.* [52], a streamwise E_x and a spanwise E_z energy of deformations

$$E_x(t) \equiv \frac{1}{N_x\, N_z} \sum_{j=0}^{N_z} \left(\sum_{p=1}^{N_x} a_p(z_j,t)^2 \right)^{1/2} \tag{7.3a}$$

$$E_z(t) \equiv \frac{1}{N_z\, N_x} \sum_{i=0}^{N_x} \left(\sum_{q=1}^{N_z} b_q(x_i,t)^2 \right)^{1/2} \tag{7.3b}$$

where the spatial Fourier coefficients $a_p(z,t)$ and $b_q(x,t)$ are defined as

$$a_p(z,t) = \sum_{i=0}^{N_x} h(x_i,z,t) \exp\left\{ \mathrm{i}pk_x x_i \right\} , \tag{7.4a}$$

$$b_q(x,t) = \sum_{j=0}^{N_z} h(x,z_j,t) \exp\left\{ \mathrm{i}qk_z z_j \right\} , \tag{7.4b}$$

where $k_x = 2\pi/L_x$ and $k_z = 2\pi/L_z$ are the streamwise and spanwise fundamental wavenumbers, L_x and L_z being the length and width of the computational domain; $x_i = i\, L_x/N_x$ and $z_j = j\, L_z/N_z$ are the coordinates of the regularly spaced grid points whose numbers are N_x and N_z in the corresponding direction.
Because of the spatial periodicity of the computational domain, the mass is conserved and the averaged film thickness $\langle h \rangle$ is fixed. This corresponds to the *closed flow* condition as defined in §2.4. As stated in that section, periodic stationary 2D waves which result from a periodic forcing at the inlet rather correspond to an *open flow* condition – *i.e.* a prescribed averaged flow rate –, the average $\langle h \rangle$ over one wavelength being sensitively different than the inlet Nusselt thickness h_{N} (see equation 2.33). Because the Reynolds number varies as the cube of the average film thickness, fixing $\langle h \rangle = h_{\mathrm{N}}$ at the initial stage of the simulation may introduce important discrepancies. Therefore, to enable an accurate comparison with the experimental data and wave

patterns reported in experiments we adjust the initial condition such that to match the averaged thickness $\langle h \rangle_0$ of the 2D stationary waves – computed using AUTO97 – when the condition $\langle q \rangle = \frac{1}{3}$ is enforced. *.
We then formally use as initial condition simple harmonic disturbances plus a white noise on the form

$$h(x, z, 0) = \langle h \rangle_0 + A \cos(a\, k_x\, x) + B \cos(b\, k_z\, z) + C\, \tilde{r}(x, z), \tag{7.5}$$

where $\tilde{r}(x, z)$ is a random function defined on the interval $[-1, 1]$, A, B, C are amplitudes and a, b represent the numbers of harmonic waves in each direction. In the following sections, three different cases will be considered, along which specific initial conditions:

§7.3.1 Isothermal simulations with periodic forcing: $A = 0.1$ unless specified otherwise, $B = 0$ and $C = 10^{-3}$. The computational domain is a square ($L_x = L_z$) whose size is arbitrarily taken to be five times the length of the corresponding 2D waves. The computation is started with $a = 5$. To save computational time, whenever possible the 2D stationary waves are computed first (*i.e.* $N_z = 1$ and $C = 0$) and then introduced in the 3D computational domain with the white noise.

§7.3.2 Isothermal simulations with white noise: $A = B = 0$, $C = 10^{-3}$ and $L_x = L_z$.

§7.3.3 Non-isothermal simulations with periodic forcing: $A = B = 0.1$, $C = 0$, $a = b = 1$ and $\langle h \rangle_0 = 1$

The parameters not given above are specified in the sections themselves.

7.3.1 Isothermal simulations with periodic forcing

Let us study the secondary 3D instability in isothermal conditions with a periodic forcing in order to compare with experimental results obtained by Liu *et al.* [84]. The reduced and approximated models in isothermal conditions are recovered by omitting the heat equation (7.2d) and setting $\mathcal{M} = 0$ in the momentum equations (7.2b,c).
On table 7.1 we have summarized the values of the parameters used in our numerical simulations. The numbers of grid points in x and $z-$directions are chosen large enough, $N_x \times N_z = 128 \times 64$ in the computations in order to limit the aliasing error. We first start by considering the flow conditions corresponding to the stability diagram reported by Liu *et al.* [84] for an inclination angle $\beta = 4°$ and Ka = 2340. For the first case in table 7.1, parameters are selected in the region of the frequency–Reynolds plane (f, Re) – see figure 6 in [84] – where herringbone patterns were

*The artefact used here to establish the correspondence between closed and open flow is rather artificial. However, due to the convective nature of the flow dynamics, the evolution in time and in space are closely related. Thereby, the time needed for a wave to develop in a periodic domain (closed flow) can be related (through the phase speed) to the distance needed for the same wave to develop in space (open flow). In the same manner, a periodic forcing (time modulations) imposed at the inlet of an open flow (say by mean of flow rate modulations) can be reproduced by space modulations in a periodic domain as initial conditions.

Case	Re	$\beta\,(^\circ)$	Ka	f(Hz)	k	c	Q	$\langle h\rangle_0$
1	40.0	4.0	2340	13	1.565	0.824	-0.480	0.987
2	60.0	4.0	2340	13	1.494	0.689	-0.335	0.970
3	42.7	4.0	2340	7	0.953	0.703	-0.353	0.975
4	48.0	6.4	2002	10	0.980	0.628	-0.274	0.965

Table 7.1: Wavenumber, speed, flow rate in the frame of reference and averaged thickness (k, c, Q and $\langle h\rangle_0$) corresponding to the stationary travelling wave generated by an inlet periodic forcing at frequency f. Cases 3 and 4 correspond respectively to the case of figure 7 and figure 11 by Liu *et al.* [84].

observed experimentally, namely subharmonic instability. All simulations of the full, reduced and approximated models do agree with the experimental data by showing the presence of staggered crests and troughs which are similar in shape to the snapshots displayed in [84]. On figure 7.2 the iso-thickness contours of the wave patterns are shown at different times. Note that at large times, the film evolves towards a staggered succession of quite smooth and large bumps, and thin and deep depressions.

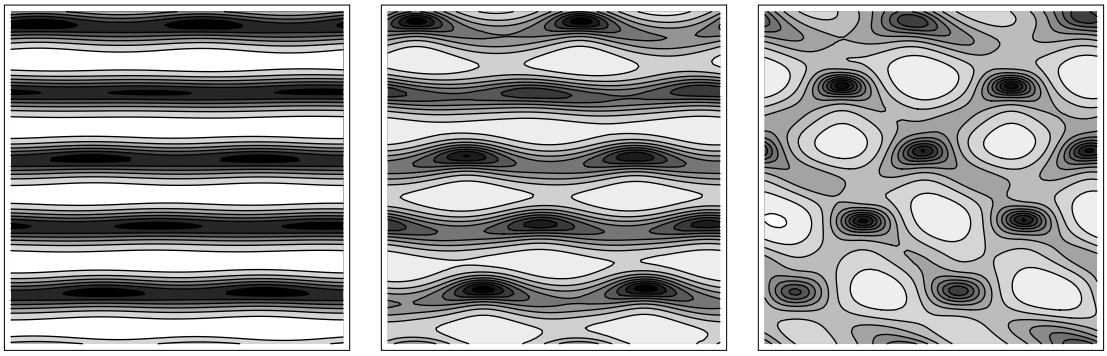

(a) (b) (c)

Figure 7.2: Free surface deformations giving rise to a herringbone pattern, computed for Case 1 with the reduced model in isothermal conditions at a) time=150, b) time=175, c) time=195. The dark (bright) zones stand for depressions (elevations). The iso-thickness contours are separated by 0.06. The domain is of size $k/5$ in both directions with a grid of 128×64.

Increasing the Reynolds number, we move next to a region of the plane (f, Re) where the synchronous secondary instability was reported by Liu *et al.* [84] (Case 2). The time integration of the models gives a rather more complex picture of the 3D flow. Indeed, the snapshots obtained using the full or the reduced models and shown in figure 7.4 indicate a state intermediate between a synchronous and a subharmonic scenario. However, it shares a lot of similarities with the experimental observations. Crests are hardly deformed whereas troughs tend to form deep isolated depressions. Contrary to the two other models, the simulation of the approximated model shows

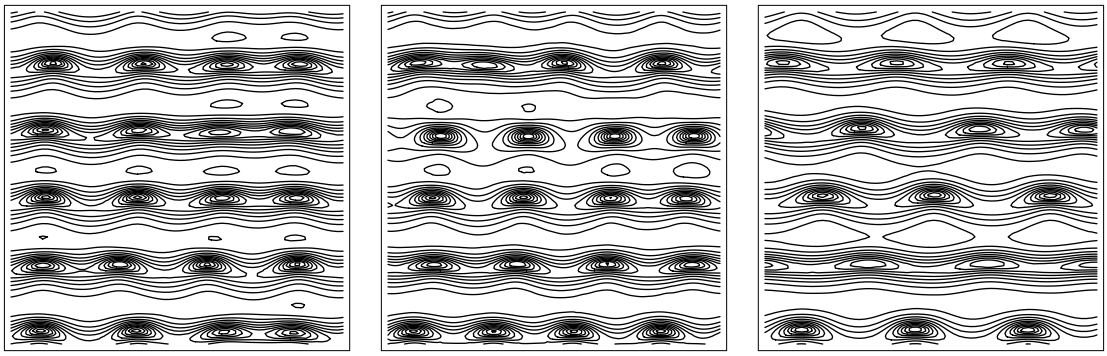

(a) (b) (c)

Figure 7.3: Free surface deformations computed for the Case 2 at $E_z \approx 0.05$ with a) the full model (time=t+125), b) the reduced model (time=t+125), c) the approximated model (time=t+155). The iso-thickness contours are separated by 0.08. The domain is of size $k/5$ in both directions with a grid of 128×64. Note that for a) and b), computations have also been performed with a grid of 128×128 and no significative change has been observed. The large white zones represent the crests of the waves.

clearly staggered troughs and more deformed crests indicating a subharmonic instability. Comparisons of the wavelength selected by the instability indicate also a good agreement between the full and the reduced models whereas the approximated model predicts longer spanwise modulations as can be observed on figure 7.3.

Recently, Ruyer-Quil *et al.* [112] focused on the three-dimensional stability analysis of the γ_1 stationary waves in their moving frame. They performed a classical Floquet analysis (as the one presented in §2.7) of the wave stability against both streamwise and spanwise modulations. They obtained a good prediction of the experimental spanwise wavenumber k_z for both the full and the reduced models. Furthermore, they found the corresponding growth rate to remain rather constant with the detuning parameter φ (or Floquet coefficient) for the full and the reduced models. This explains why the corresponding snapshots presented on figure 7.3a,b are intermediate between the herringbone ($\varphi = \frac{1}{2}$) and synchronous ($\varphi = 0$) patterns. Actually, the growth rates for $0 < \varphi < \frac{1}{2}$ being very close, the instability is not really selective and the form of the observed patterns are likely to be controlled by the nature of the noise. This feature can explain for a large part the inability of the Floquet analysis to predict the nature of the 3D patterns (herringbone or synchronous) accurately. Note however that Ruyer-Quil *et al.* reported that the growth rate of the most amplified spanwise perturbation predicted by the approximated model indicates a clear selection of the subharmonic instability which is in line with the snapshot of figure 7.3c.

As admitted by Liu *et al.* [84] the 3D instability is likely to be convective and thus dominated by the geometrical irregularities of the inlet distributor. These irregularities being time independent, they trigger in-phase modulations of the fronts evolving downstream. Therefore, such an experimental noise may trigger more easily a syn-

chronous instability than a subharmonic one. This statement is further backed up by the fact that Liu *et al.* were compelled to apply controlled perturbation to enhance the subharmonic instability.
Next, two sets of parameters corresponding explicitly to some experiments performed by Liu *et al.* have been selected for comparison with the snapshots given in figures 7 and 11 of reference [84]. The iso-thickness contours obtained by integration in time of our models are shown on figure 7.4 for the Case 3 in table 7.1. All of them show a complex wave pattern which is rather staggered. Again, the Floquet analysis performed by Ruyer-Quil *et al.* [112] shows that the instability is not very selective, *i.e.* the growth rate does not change with the detuning parameter. Note that the good agreement between the computations made with the three models strongly supports our hypothesis of a favoured occurrence of the synchronous instability due to specificities of the noise introduced in experiments.

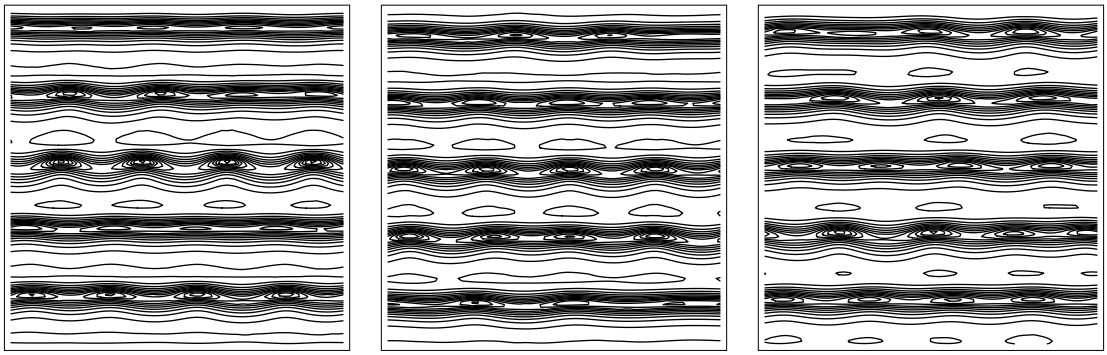

(a) (b) (c)

Figure 7.4: Free surface deformations computed for the Case 3 at $E_z \approx 0.022$ with a) the full model (time=585), b) the reduced model (time=575), c) the approximated model (time=615). Iso-contours and domain size are defined in the legend of figure 7.2. The large white zones represent the crests of the waves.

More intriguing is the fourth case corresponding to a more pronounced inclination angle (Case 4 in table 7.1 corresponding to $\beta = 6.4°$). Our integrations in time show that if the 3D initial noise is omitted, no stationary wave is selected, the system evolving towards a time periodic state, the waves undergo a periodic amplitude modulation. The fundamental mode and its harmonics exchange energy continuously. The energy of perturbation E_x oscillates also in time as shown on figure 7.5. This behaviour was equally observed by Ramaswamy *et al.* [104] who described this regime as quasi-periodic. These authors performed direct numerical simulations of the basic equations and found the quasi-periodic regime to be quite widespread in the case of a vertical plane if the Reynolds number becomes large. Using the vocabulary of dynamical system theory, instead of evolving towards a limit cycle (stationary wave) in the phase space, the flow tends to a torus (quasi-periodic regime).
For all computations done in Case 4, the 3D instability mechanism and the destabilization of the stationary travelling wave leading to a modulated 2D wave pattern

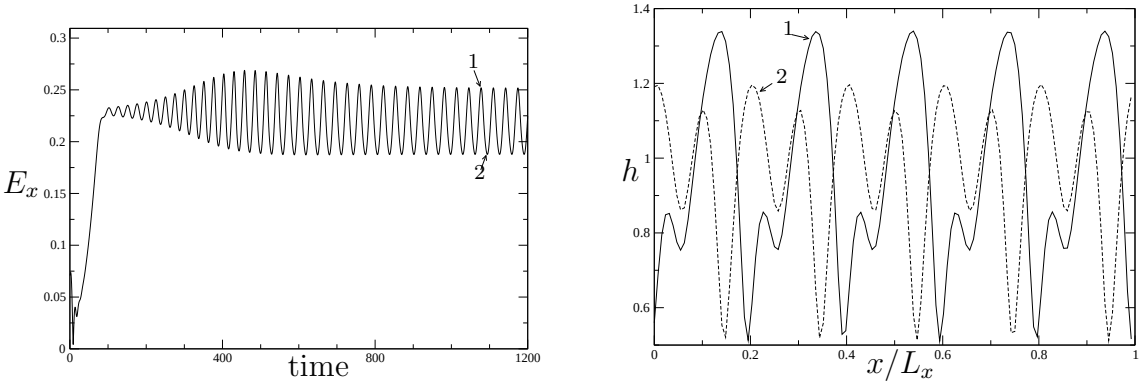

Figure 7.5: Energy E_x as function of time (a) and wave-profiles (b) of the 2D waves computed using the full model (D.2).

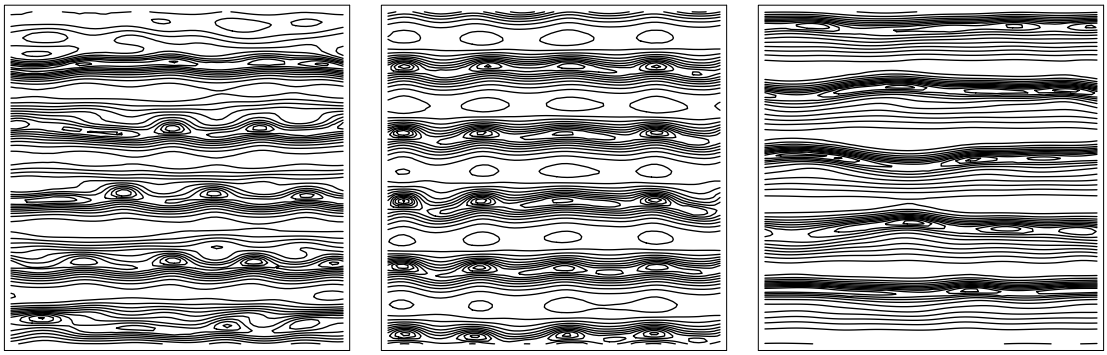

Figure 7.6: Free surface deformations computed for the Case 4 at $E_z \approx 0.05$ with a) the approximated model (time=295), b) the reduced model (time=305), c) the full model (time=345).

were found to coexist. The evolution of the film is therefore controlled by the initial condition of the computation and in particular the amplitude A of the initial sinusoidal wave.
On figure 7.6, are compared the wave patterns obtained using the full, reduced and approximated models for the same initial condition namely a sinusoidal wave of amplitude $A = 0.2$ and a white noise with $C = 10^{-3}$. Note that both the full and the approximated models predict a staggered pattern whereas the reduced model does predict a synchronous instability which corresponds to the experimental observations.

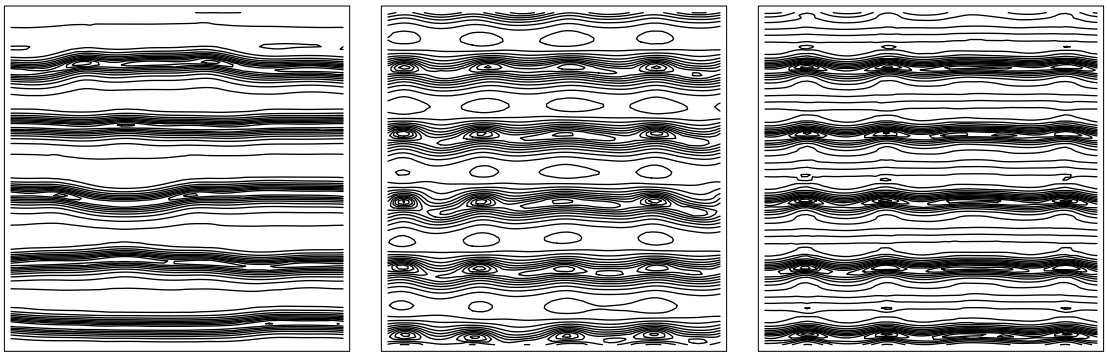

(a) (b) (c)

Figure 7.7: Free surface deformations computed for the Case 4 using the reduced model at $E_z \approx 0.4$: a) $A = 0.1$ (time=300), b) $A = 0.2$ (time=305) c) $A = 0.3$ (time=215).

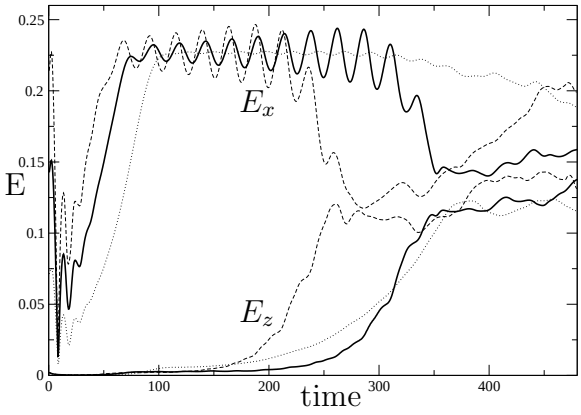

Figure 7.8: Energy of deformations for Case 4, in the streamwise (spanwise) direction E_x (E_z), computed with the reduced model. The dotted, solid and dashed line correspond, respectively, to $A = 0.1$, 0.2 and 0.3.

To test the influence of the initial amplitude A on the final evolution of the film, three computations were performed for $A = 0.1$, 0.2 and 0.3. The obtained wave patterns are shown on figure 7.7. Significant qualitative differences can be noted between them. At low initial amplitude A, the final transverse modulation seems to

have longer wavelengths than for larger values of A. Most significantly, it seems to be subharmonic whereas the 3D pattern is clearly synchronous if A is large enough. Such an observation can be understood by looking at the energy of the deformation as function of time as given on figure 7.8. When $A = 0.1$, the system clearly approaches the unstable stationary wave solution and remains close to it for a long time. Therefore, the Floquet analysis still applies and the obtained staggered pattern is in line with the predicted subharmonic instability. Such is not the case for larger value of A, the modulation of the 2D pattern occurring much before the 3D instability appears. The observed synchronous pattern is thus the complex result of two ingredients, the growing 2D modulation and the 3D instability.

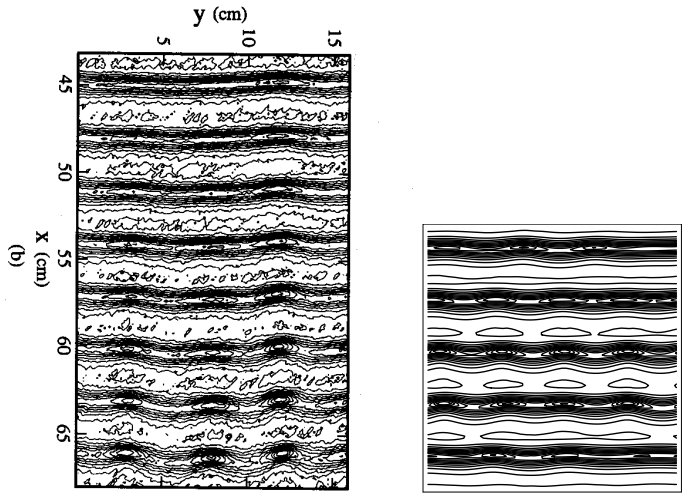

Figure 7.9: Comparison between an experimentally observed pattern [84] and the computations obtained using the reduced model corresponding to Case 3.

Now, let us make some qualitative comparisons of the experimental and numerical wave patterns for Case 3 and Case 4 as shown on figure 7.9 and 7.10. Due to the choice of periodic boundary conditions, our computations cannot fit well experimental results. In experiments the observed evolution of the film is convective and the waves grow in space (downstream) whereas numerical wave patterns rather grow in time. Nevertheless, our simulations share the same qualitative features as in experiments. In particular, we predict the strong modulation of the troughs, whereas crests remain nearly undeformed, leading to the formation of isolated depressions. The spanwise wavelengths are similar and the iso-thickness contours do compare quite satisfactorily.

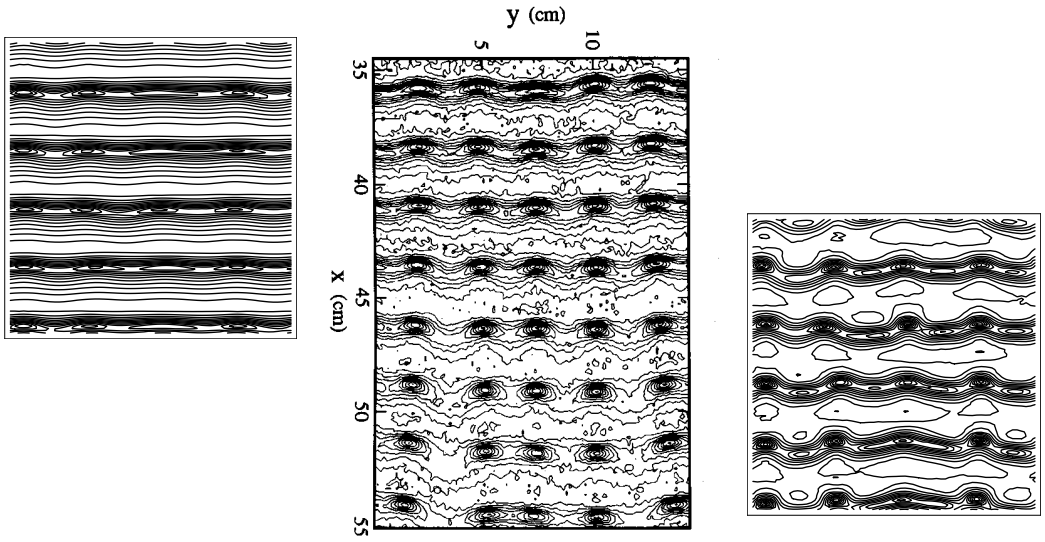

Figure 7.10: Comparison between an experimentally observed pattern [84] and the computations obtained using the reduced model corresponding to Case 4.

Model validation

Two statements straightforwardly follow from previous investigations:

(i) The approximated model is unable to reproduce the synchronous wave pattern while the addition of second-order inertial corrections, yielding the reduced model (see underlined terms in equation 7.2b), enables to reproduce the experimental observations both qualitatively and quantitatively.

(ii) The full second-order model seems unable to reproduce the synchronous instability in some cases;

Therefore, the reduced model (7.2), being accurate and simple, is a good candidate for a further study of the 3D wave patterns and in particular the horseshoe solitary waves which seem to dominate the flow dynamics at larger Reynolds number or further downstream the plate. This is the goal of the following section.

7.3.2 Isothermal simulations with natural noise

The three-dimensional character of perturbations is the peculiarity of any film flow at large distances from the inlet, even when no periodic forcing is applied. Figure 7.11 shows experimental pictures of non-stationary solitary waves separated by a smooth thin residual layer with approximately constant thickness h_{res}. The area of the film surface occupied by the residual layer decreases with an increase of the Reynolds number.

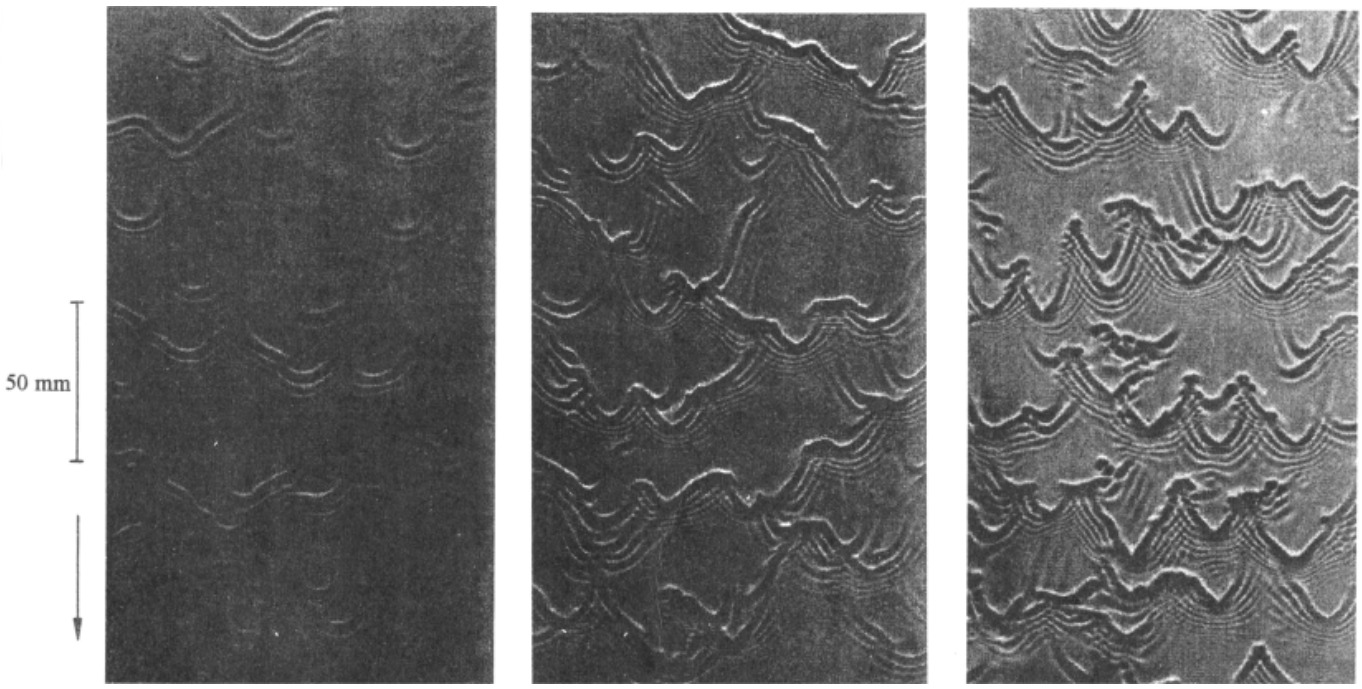

Figure 7.11: Wave patterns on a film falling down an inclined plane, $\beta = 75°$. They were obtained experimentally by Alekseenko *et al.* (figure 1.6. in [1]) for a 16% water ethanol solution at 25°C whose properties are $\rho = 972kg/m^3$, $\nu = 1.55 \times 10^{-6}m^2/s$ and $\sigma = 40.8 \times 10^{-3}N/m$. The dimensionless numbers are Ka = 1106, Ct = 0.268 and (a) Re = 8: $\mathcal{R} = 4.7$, $\mathcal{C} = 0.053$, $\eta = 0.038$; (b) Re = 16: $\mathcal{R} = 11.0$, $\mathcal{C} = 0.0612$, $\eta = 0.052$; (c) Re = 45: $\mathcal{R} = 38.8$, $\mathcal{C} = 0.077$, $\eta = 0.083$.

Results of time-dependent simulations corresponding to the experimental parameters of figure 7.11 are reported in figure 7.12. Here, since no periodic forcing is imposed, we evaluate $\langle h \rangle_0$ by calculating (using AUTO97) the corresponding 2D stationary solutions with the wavelength estimated from the experimental pictures 7.11; there we get very roughly for Re = 8, 16 and 45, the values of 40, 30 and 25 mm, respectively. The average thickness is then found to be $\langle h \rangle_0 \approx 0.9$ for the three cases. In the same manner, the phase speeds of the 2D stationary solutions (resp. 0.20, 0.32 and 0.65 m/s) allow us to estimate roughly the distance L covered by the wave from $t = 0$, yielding the time scales $\mathcal{L}l_\nu = 4.57$, 3.11 and 1.75 $\times 10^{-3} s$, respectively.
By comparing figures 7.11 and 7.12, remark that the grey level seems not to measure the same quantities in both set of pictures. For simulations, the grey level quantifies the film thickness (bright means thick and dark means thin) while for experiments, it is difficult to figure out precisely what is the coding. However, the presence of sharp bright zones suggests that the grey level quantifies the slopes of the free surface deformations (bright for positive slopes and dark for negative slopes).
In the first row of figure 7.12, the waves are predominantly two-dimensional. They are quasi-linear for Re = 8 – bright and dark zones occupy identical areas – and become more nonlinear, with larger amplitude, by increasing Re. For Re = 8 and 16, some waves have started to connect to each other while for Re = 45, they rather form isolated waves whose the center is above (upstream) the sides (see figure 7.12c). Indeed, those waves belong to the slow γ_1 family which represents waves with deep and sharp troughs.
The second row of figure 7.12 corresponds to the decay of the two-dimensional waves. The largest amplitude waves travel faster and tend to catch up the preceeding slower ones, leaving behind them an increasing flat zone. Interestingly, for Re = 45, the waves are still more isolated but with the center below (downstream) the sides (see figure 7.12f). This indicate that the waves have bifurcated from the γ_1 to the γ_2 family whose waves travel faster, with crests that have higher amplitudes than the troughs.
As time is running, the coalescence process yields solitary waves with preceding capillary ripples and large flat zones in between. Figure 7.12g,j and 7.12h,k share a lot of similarities with the experimental figures 7.11a and 7.11b, respectively. Alekseenko *et al.* [1] have indicated that their pictures represent non-stationary situations, and that the stabilized waves are defined by the wavelength of solitary waves, which takes values from 10 to 50 cm. However, for Re = 8, this wavelength has been found to be approximately constant up to $t = 1500$ in the simulations (not shown on the figure). On the contrary, for larger Re, the stabilization of wavy regime could not be reached. The simulations were stopped before due to prohibitive computing time and unfortunately, the straight V-shape waves observed in experiments for Re = 45 could not be recovered even though figure 7.12i announces their birth with the presence of the expected horseshoe-like waves directed downstream. It can be also observed on 7.12i, like on figure 7.11c, that the capillary ripples of two neighbouring waves cross each others nearly without interaction.
The caption of figure 7.11 provides the value of η that measures the viscous dissipation. The square root of this parameter represents the ratio between the film thickness and

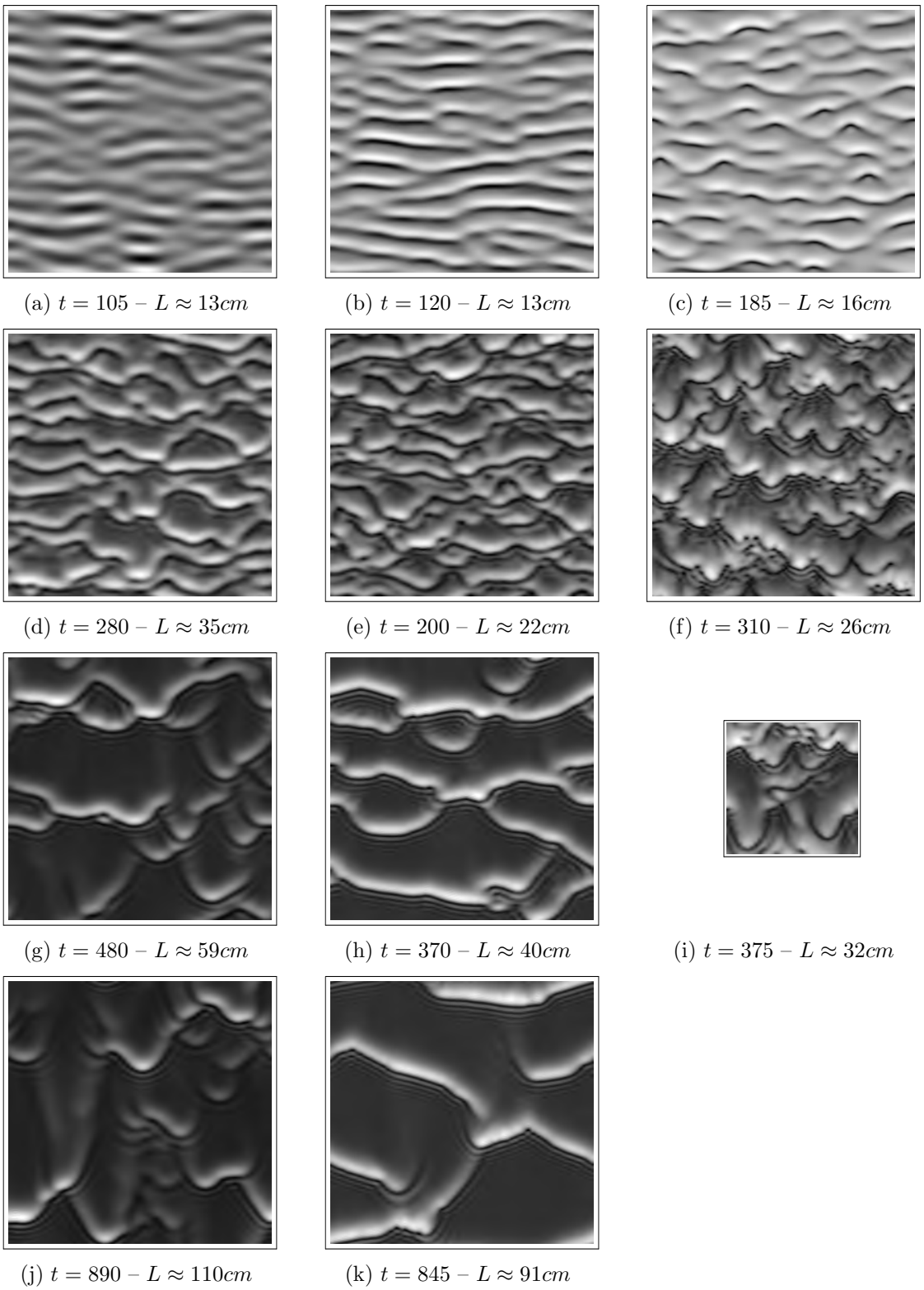

(a) $t = 105$ – $L \approx 13cm$ (b) $t = 120$ – $L \approx 13cm$ (c) $t = 185$ – $L \approx 16cm$

(d) $t = 280$ – $L \approx 35cm$ (e) $t = 200$ – $L \approx 22cm$ (f) $t = 310$ – $L \approx 26cm$

(g) $t = 480$ – $L \approx 59cm$ (h) $t = 370$ – $L \approx 40cm$ (i) $t = 375$ – $L \approx 32cm$

(j) $t = 890$ – $L \approx 110cm$ (k) $t = 845$ – $L \approx 91cm$

Figure 7.12: Numerical simulations computed with the 3D reduced model in isothermal conditions. The three columns correspond to the three experimental situations reported in figure 7.11. The scaling has been respected, i.e. the large boxes are $100\times$ 100mm^2 and the small one, $50\times$ 50mm^2. The dimensionless time is indicated together with the estimated distance L from the inlet. The mesh points are 256×256 except (c,f) that are 512×256.

the characteristic length of the capillary ripples preceding main solitary waves (see §1.6). For $\mathrm{Re} = 45$, $\sqrt{\eta} \approx 0.3$ indicates that even though separation of scale inherent to the boundary layer approximation is not fully verified here, a good qualitative agreement with experiments can still be observed with our reduced model quite far in the nonlinear regime.

7.3.3 Non-isothermal simulations with periodic forcing

In this section are performed simulations of a falling film with an uniform temperature at the wall yielding thermocapillary effects. Joo *et al.* [54] studied this problem for small Reynolds numbers, in a regime where the Benney equation is valid. They demonstrated a mechanism of rivulet formation based solely on instability phenomena. Ramaswamy *et al.* [105] confirmed the observations by Joo *et al.* obtained with the Benney equation (2.10), by performing full-scale simulations with the Navier-Stokes/Fourier equations. Similarly, we want to compare here the results obtained by Ramaswamy *et al.* with our 3D reduced model (7.2). Figure 7.13 shows results of simulations corresponding to the case of figure 9 in [105]. The simulation is started with a simple harmonic disturbance of the form

$$h(x, z, 0) = 1 + 0.1\cos(k_x\, x) + 0.1\cos(k_z\, z), \tag{7.6}$$

as shown in figure 7.13a. The wavenumbers have been chosen as $k_x = k_z = 0.335$ to be below those for the maximal linear growth rate in each direction, which are $k_{x\max} = 0.56$ and $k_{z\max} = 0.53$. Actually, these appropriate values allow for interesting secondary flow development. The perturbation (7.6) creates a trough in the centre of the domain. Then, thermocapillarity sets in, displacing the fluid from the hotter troughs towards the surrounding colder crests. However, the growth rate of the hydrodynamic mode is dominant at initial stage and surface waves develop (figure 7.13b). The local phase speed being proportional to the square of the local film thickness according to the leading-order evolution equation (2.6), the crests travel faster than the troughs (c). In the absence of the mean flow in the spanwise direction, the liquid is displaced laterally due to thermocapillarity. Therefore, as time progresses, the thinning of the liquid layer persists and forms a valley surrounded by rivulets aligned with the flow (d). As already mentioned in §4.5, this process is similar to the evolution of a heated thin film on a horizontal substrate [76, 95]. Likewise, it exhibits the formation of a secondary rivulet between the main one (e,f), the mechanism of which is explained in §4.5. As found by Boos & Thess [11] for horizontal layers, a true 'cascade of structures' takes place in thinner zones (g), precursor to the film rupture. Ramaswamy *et al.* [105] reported that the Benney equation compares well with their full-scale computations up to $t = 120^{\dagger}$ and then diverges up to $t = 146$ when blow-up occurs. Beyond this time, the Benney equation fails to follow the dynamics of the flow. The last stage before rupture obtained by Ramaswamy *et al.* with their full-scale computations is at $t = 153$, which is in excellent agreement with figure 7.13f.

[†]Due to a different scaling used by Ramaswamy *et al.* [105], the time differs in that reference by a factor $\mathcal{L}/h_{\mathrm{N}}^2 = 6.7$ according to §1.6 (with $h_{\mathrm{N}} = 1$).

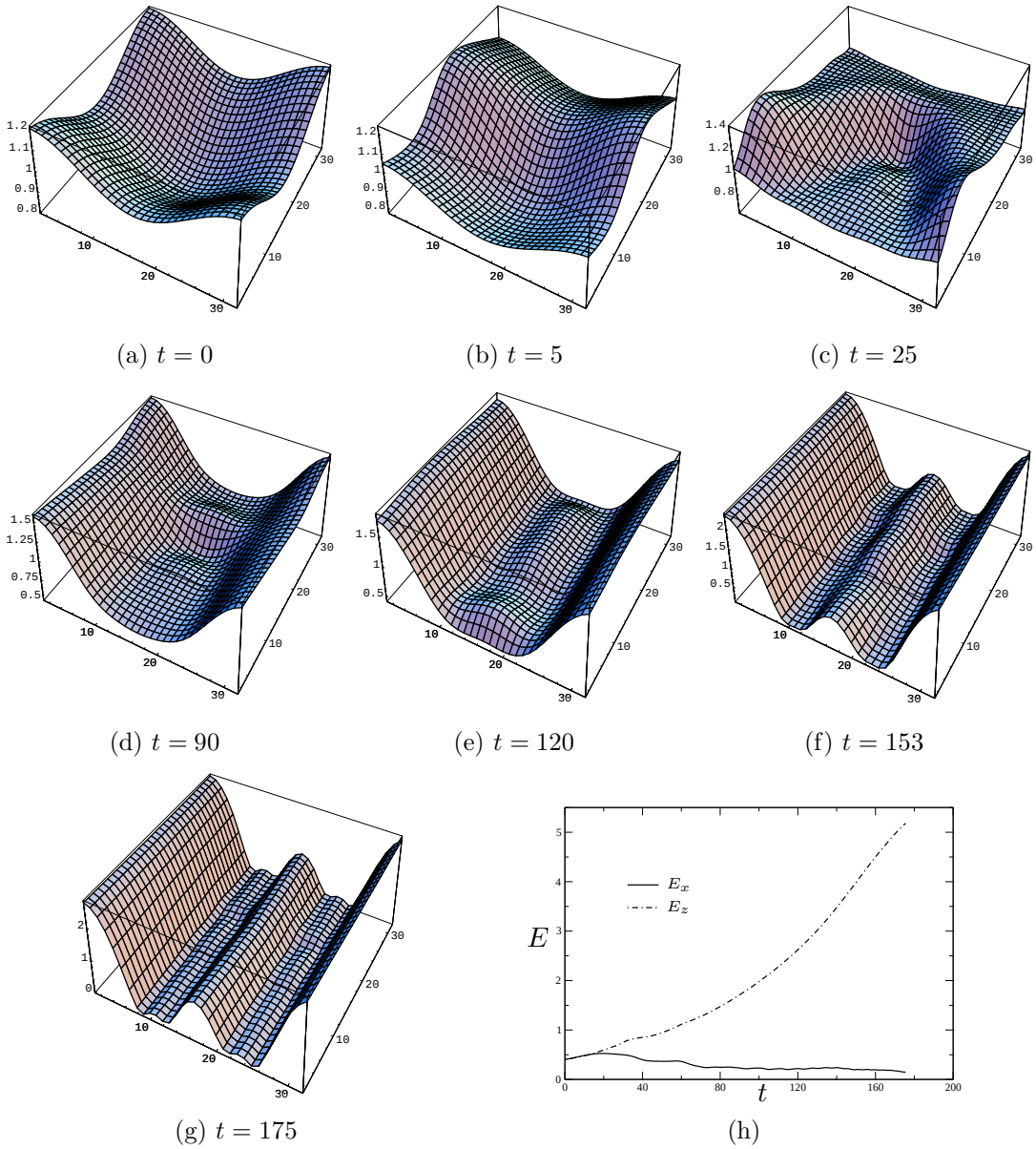

Figure 7.13: Inception and development of rivulet aligned with the flow computed with the reduced model (7.2) arising for Re = 1/3, Ka = 300, Ma = 10, Bi = 1, Pr = 7 and Ct = 0. The domain is square with size $2\pi/k_x$ where $k_x = k_z = 0.335$. The flow direction is from the right top towards the left bottom.

However, our simulation runs beyond this time and exhibits finer structures in the film before its rupture (see figure 7.13g). The reason why the full-scale computations with Navier-Stokes/Fourier equations did not provide such further evolution of the film is not obvious but is likely related to the choice of the number of mesh points used in [105]. The authors would have most probably been able to compute larger time with refined grid resolution. However, this would have been at the expense of computing time, which demonstrate the restriction of full-scale simulations. Thereby, we would like to emphasize here the great advantage of working with a model of reduced dimensionality. Actually, the mesh points are 32×32 and the time necessary for computing the case of figure 7.13, with an accuracy of 10^{-4}, is about one hour on a standard desktop computer.

Figure 7.13h shows the energy of deformations in both directions versus time. The energy along the streamwise direction N_x saturates which indicates the formation of longitudinal rivulets aligned with the mean flow.

Now, let increase the Reynolds number up to $\mathrm{Re} = 2$, out of the range of validity of the Benney equation – see figure 2.8 for $(\mathcal{R}, \mathcal{MB}) = (1.5, 1.33)$ – and keep the other parameters identical. Now, the wavenumbers for the maximal linear growth rate are $k_{x\max} \approx 0.62$ and $k_{z\max} \approx 0.34$ (approximated values calculated in the long-wave limit), which yields $k_x \sim k_{x\max}/2$ while $k_z \sim k_{z\max}$. Figure 7.14 shows that the hydrodynamic mode quickly generates high amplitude waves (a,b) that evolves to a solitary-like wave with preceding capillary ripples (c). However, the thermocapillary mode leads the film to rupture before the surface wave saturates as depicted by the evolution of E_x and E_z (d). An interesting interaction between the two modes can be pointed out here: as the thermocapillary flow feeds the core of the rivulet, the mean film thickness at the crest increases, and so the local flow rate. Hence, the wave solution does not saturate and rather follows the change of the 'local Reynolds number', by increasing its amplitude and its phase speed (look at the squeezing of the oscillations in time on figure 7.14e). This process vanishes at $t > 620$ when the film approaches the wall enough for the viscous stress to slow down the thermocapillary flow.

Figure 7.14 demonstrates that the hydrodynamic waves and the longitudinal rivulets can coexist and interact along a distance that is about 50 wavelengths here. Furthermore, this distance increases with the Reynolds number. It seems therefore possible with our model to recover experimental observations like the ones given on figure 7 of the Introduction. However, a quantitative comparison should be addressed in a future investigation.

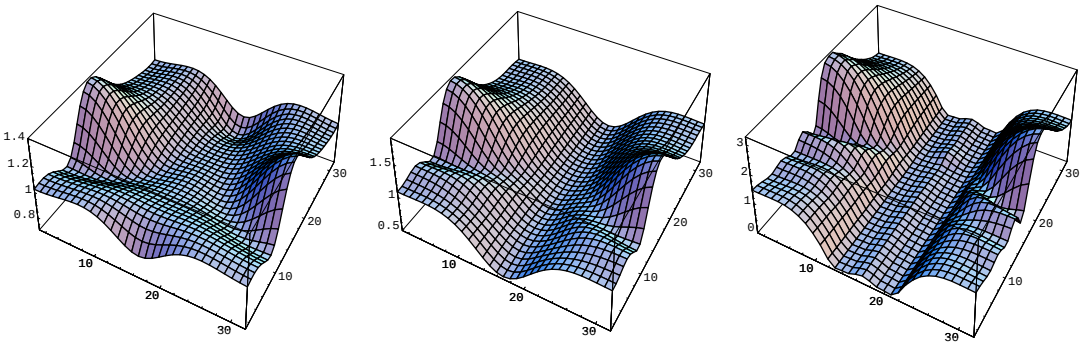

(a) $t = 40$ (b) $t = 400$ (c) $t = 690$

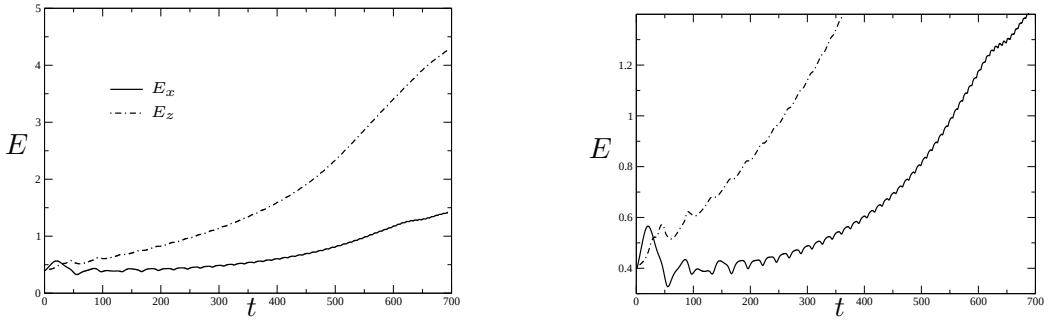

(d) (e) zoom of (d)

Figure 7.14: Same as for figure 7.13 with Re = 2.

Chapter 8

Further topics

In this chapter, we show how our reduced model can be obtained in the case of the heat flux condition using the weighted residual approach together with the Galerkin method (§8.1). We also consider the small Biot number limit and show how it modifies the reduced model (§8.2). This limit will be justified by using a simple argument corresponding to realistic situations in experiments.

8.1 Heat flux condition

Up to now, the weighted residual approach has been applied for the problem with a constant temperature imposed at the wall. Let us here generalized in the case when the wall is not a perfect conductor. In this case, a constant heat flux is rather imposed at the wall and an additional parameter appears, namely the Biot number Bi_w that measures the conducting property of the wall. If $\mathrm{Bi}_\mathrm{w} \gg 1$, the wall is a good conductor and if $\mathrm{Bi}_\mathrm{w} \ll 1$, the wall is a good insulator. This was discussed in details in §1.3.2 and the corresponding boundary condition is given by (1.23b). Here we will first keep constant the imposed heat flux such that $F_\mathrm{w}(x) = 0$ and the boundary condition at the wall reads explicitely

$$\partial_y T = -1 + \mathrm{Bi}_\mathrm{w} T. \tag{8.1}$$

The following procedure with the Galerkin method being similar to the one presented in §5.2, we present hereafter only the modifications concerning the heat flux condition. In the weighted residual approach, since we want the film surface temperature θ to be the relevant variable of our averaged model (see discussion based on equation 5.14), let us rewrite the linear zeroth-order temperature profile across the film (2.4f) (with $F_\mathrm{w} = 0$) as function of the surface temperature θ:

$$T^{(0)} = \theta + \mathbb{F}(h - y) \quad \text{where} \quad \mathbb{F} = \frac{1 - \mathrm{Bi}_\mathrm{w}\theta}{1 + \mathrm{Bi}_\mathrm{w} h}. \tag{8.2}$$

The effective heat flux $\mathbb{F}(x, t)$ at the wall logically decreases with the intensity Bi_w of the heat losses from the liquid to the wall and with the increase of the film surface

temperature θ. To satisfy the boundary condition (8.1), we write the temperature field as

$$T(x,y,t) = -\mathbb{F}(x,t)\ y + \sum_{i=0}^{i_{\max}} b_i(x,t) g_i\left(\frac{y}{h(x,t)}\right), \tag{8.3}$$

where $g_0 = 1$ corresponds to the base state and the set of test functions is completed with $g_i(\bar{y}) = \bar{y}^{i+1}$, $i \leq 1$ to obtain the polynomial basis for the projection.

8.1.1 Formulation at first-order

First, it is important to mention that the heat and mechanical equilibriums of the flat film (at zeroth-order) are two decoupled problems, the coupling appearing only at first-order through interfacial deformations. Moreover, playing judiciously with the zeroth-order solution of the surface temperature (2.5b)

$$\theta^{(0)} = \frac{1}{\mathrm{Bi} + \mathrm{Bi_w}(1 + \mathrm{Bi}h)} \tag{8.4}$$

yields the same formulation of the second-order terms Mar_q as obtained in (6.4) for the temperature condition*. Therefore, the momentum equation 6.10b of the reduced model will remain unchanged with the heat flux condition and we will have to focus only on the heat equation in what follows.
Turning to the weighted residuals for the heat equation (5.7b) and with the same arguments as in §5.2, the unknowns b_i, $i \geq 1$ may only play a role through the integral $\int_0^h w_j \partial_{yy} T$. Two integrations by parts give, making use of the boundary condition at the surface (5.6f) and the heat flux condition at the wall (8.1),

$$\begin{aligned}\int_0^h w_j \left(\frac{y}{h}\right) \partial_{yy} T\, dy &= -\mathrm{Bi} w_j(1) T\Big|_h + w_j(0)(1 - \mathrm{Bi_w} T\Big|_0) \\ &\quad + \frac{1}{h}\left[{w_j}'(0) T\Big|_0 - {w_j}'(1) T\Big|_h\right] + \frac{1}{h^2}\int_0^h {w_j}''\left(\frac{y}{h}\right) T\, dy\,. \end{aligned} \tag{8.5}$$

Here, to put the emphasis on $\theta \equiv T\Big|_h$, we choose for the first weight function ${w_{i_{\max}}}'(0) = 0$, ${w_{i_{\max}}}'' = 0$ so that $w_{i_{\max}} \propto 1 = g_0$. It is therefore appropriate to replace the physically meaningless unknown b_0 by θ through the substitution

$$b_0 = \mathbb{F}h + \theta - \sum_{i=1}^{i_{\max}} b_i\,. \tag{8.6}$$

Evaluating now the first residual (5.7b) corresponding to $w_{i_{\max}} = g_0 = 1$, we then get

$$\mathrm{Pr}\left[\mathbb{F}\partial_t h + \frac{1}{2} h \partial_t \mathbb{F} + \partial_t \theta + \frac{3}{8}\left(\frac{\mathbb{F} q \partial_x h}{h} + \mathbb{F}\partial_x q + q \partial_x \mathbb{F}\right) + \frac{q \partial_x \theta}{h}\right] - \frac{(\mathbb{F} - \mathrm{Bi}\theta)}{h} = 0. \tag{8.7}$$

*Remember that those terms are induced in the momentum equation by the Marangoni flow produced by the gradient of temperature at the film surface.

Now, substituting $\mathbb{F} = (1 - \mathrm{Bi_w}\theta)/(1 + \mathrm{Bi_w}h)$ and using the equivalence $\partial_t h = -\partial_x q$ lead to the dynamical equation for θ:

$$\begin{aligned}\mathrm{Pr}\partial_t\theta &= \left\{\frac{(1-\mathrm{Bi_w}\theta)}{h(1+\mathrm{Bi_w}h)} - \frac{\mathrm{Bi}\theta}{h} + \mathrm{Pr}\left[\frac{(5+\mathrm{Bi_w}h)(1-\mathrm{Bi_w}\theta)}{8(1+\mathrm{Bi_w}h)^2}\partial_x q - \frac{3}{8}\frac{(1-\mathrm{Bi_w}\theta)}{(1+\mathrm{Bi_w}h)^2}\frac{q}{h}\partial_x h\right.\right. \\ &\left.\left. - \left(1 - \frac{3}{8}\frac{\mathrm{Bi_w}h}{(1+\mathrm{Bi_w}h)}\right)\frac{q}{h}\partial_x\theta\right]\right\} \times \left(1 - \frac{\mathrm{Bi_w}h}{2+2\mathrm{Bi_w}h}\right)^{-1}. \qquad (8.8)\end{aligned}$$

Equation (8.8), where the unknowns b_i do not appear, is consistent at $\mathcal{O}(\varepsilon)$ and can be substituted to (5.17c) in the model (8.8) to get our model in terms of three coupled evolution equations for h, q and θ that accounts for the heat flux condition at the wall.

It is worth noting that (8.7) is formulated in such a way that it may be used in the case of a non-uniform heat flux distribution at the wall (this is by using (1.23b) instead of (8.1) as boundary condition). Indeed, the introduction of the non-uniform component of the heat flux distribution $F_\mathrm{w}(x)$ is made through $\mathbb{F}$ such that the corresponding dynamical equation is obtained by rather substituting $\mathbb{F} = (1+F_\mathrm{w})(1-\mathrm{Bi_w}\theta)/(1+\mathrm{Bi_w}h)$ in (8.7).

8.1.2 Formulation at second-order

As in §5.3, we want to extend here our formulation to take into account the second-order thermal diffusion terms. For this purpose, we need the explicit expressions for the amplitudes b_i of the projection at first-order. This is by cancelling the five coefficients of the fourth-order polynomial obtained by projecting the temperature field (8.3) and the velocity field (5.5a) into the energy equation (5.6c). Since the amplitudes a_i are known from (5.21a-5.21e) as well as b_0 from (8.6), and that the b_i's, $i \geq 1$ are at least of $\mathcal{O}(\varepsilon)$, the five coefficients of the polynomial provide the expression of the b_i's as function of h, θ, q and their derivatives:

$$b_1 = \frac{1}{2}\mathrm{Pr}h^2\left(h\partial_t\mathbb{F} + \partial_t\theta - \mathbb{F}\partial_x q\right) \qquad (8.9a)$$

$$b_2 = -\frac{1}{6}\mathrm{Pr}h\left(h^2\partial_t\mathbb{F} - 3q\left[\mathbb{F}\partial_x h + h\partial_x\mathbb{F} + \partial_x\theta\right]\right) \qquad (8.9b)$$

$$b_3 = -\frac{1}{8}\mathrm{Pr}h\left(-h\mathbb{F}\partial_x q + q\left[3\mathbb{F}\partial_x h + 3h\partial_x\mathbb{F} + \partial_x\theta\right]\right) \qquad (8.9c)$$

$$b_4 = \frac{1}{40}\mathrm{Pr}h\left(-h\mathbb{F}\partial_x q + 3q\left[\mathbb{F}\partial_x h + h\partial_x\mathbb{F}\right]\right) \qquad (8.9d)$$

$$b_5 = 0. \qquad (8.9e)$$

Contrarily to the case of a constant temperature at the wall, here the amplitude b_1 is non zero. The temperature T is therefore, at first-order, a combination of five independent fields, namely θ, b_1, b_2, b_3 and b_4. As a consequence, a consistent formulation of a model for the dynamics of the flow at second-order would require fourteen unknowns when considering the heat flux condition at the wall – instead of thirteen with the temperature condition –. However, rather than solving fourteen equations,

let us used the same approach as for the temperature condition, and construct a set of orthogonal test functions for the temperature field from linear combinations of g_0, g_1, g_2, g_3 and g_4 such that $G_0 \equiv g_0$:

$$\begin{aligned} G_0 &= 1\,, && (8.10a)\\ G_1 &= 1-3\bar{y}^2\,, && (8.10b)\\ G_2 &= 1-15\bar{y}^2+16\bar{y}^3\,, && (8.10c)\\ G_3 &= 1-45\bar{y}^2+112\bar{y}^3-70\bar{y}^4\,, && (8.10d)\\ G_4 &= 1-105\bar{y}^2+448\bar{y}^3-630\bar{y}^4+288\bar{y}^5\,. && (8.10e) \end{aligned}$$

Therefore, the temperature field can be accurately described at $\mathcal{O}(\varepsilon)$ from

$$T = -\mathbb{F}y + (\mathbb{F}h+\theta-t_1-t_2-t_3-t_4)\,G_0\Big(\frac{y}{h}\Big) + \frac{1}{2}\sum_{i=1}^{4}(-1)^i\,t_i\,G_i\Big(\frac{y}{h}\Big)\,. \qquad (8.11)$$

The set of test functions G_i must be completed at second order with ten polynomials of degree up to fourteen. Nevertheless, since G_i'', $0 \le i \le 3$ are not linear combinations of G_i, $0 \le i \le 3$, the five first residuals do not form a closed set of equations for θ, t_1, t_2, t_3 and t_4. Yet, a basis for the set of polynomials of degree up to five satisfying the heat flux condition at the wall can be obtained by introducing only one polynomial orthogonal to the first four G_i. This polynomial G_5 is given explicitly by

$$G_5(\bar{y}) = 1-\frac{70}{3}\bar{y}+140\bar{y}^2-336\bar{y}^3+350\bar{y}^4-132\bar{y}^5\,. \qquad (8.12)$$

The temperature field can now be written at second-order as

$$\begin{aligned} T &= -\mathbb{F}y + (\mathbb{F}h+\theta-t_1-t_2-t_3-t_4)\,G_0\Big(\frac{y}{h}\Big) - \frac{1}{2}t_1G_1\Big(\frac{y}{h}\Big) + \frac{1}{2}t_2G_2\Big(\frac{y}{h}\Big)\\ &\quad -\frac{1}{2}t_3G_3\Big(\frac{y}{h}\Big) + \frac{1}{2}\left(t_4-\sum_{i=6}^{8}t_i\right)G_4(\bar{y}) - 3t_5G_5\Big(\frac{y}{h}\Big) + \sum_{i=6}^{8}t_i\frac{G_i(y/h)}{G_i(1)}\,. \qquad (8.13) \end{aligned}$$

The choice of this formulation ensures that the evaluation of $\int_0^h G_j''(\bar{y})T\,dy$, $0 \le j \le 5$ does not require the definitions of G_i, $j \ge 6$. By applying next the Galerkin method to the heat equation, the six first residuals $\mathcal{R}_T(G_i)$, $0 \le i \le 5$ constitute a closed set. Since the amplitude t_5 is of $\mathcal{O}(\varepsilon^2)$, its space and time derivatives can be neglected at this order, so that an explicit formulation as function of h, θ, t_1, t_2, t_3 and t_4 can be obtained, thus expressing the slaving of the former to the latter. Cumbersome algebraic manipulation may allow us to get a set of five evolution equations for θ, t_1, t_2, t_3, t_4 that coupled with the five other evolution equations (5.4, 5.27) will provide our full second-order model, for ten unknowns, in the case of a heat flux condition at the wall. However, we will make a short-cut here based on considerations already developed in the case of the temperature condition (see chapter 6). Actually, our purpose is again to get a three-unknown 'reduced' model for h, q and θ which remains asymptotically correct up to $\mathcal{O}(\varepsilon^2)$ with the long-wave expansion. Yet, the temperature being coupled through its gradient in the momentum equation, the second-order

terms in the heat equation do not participate to the second-order gradient expansion. Furthermore, we already stated that it seems not possible to take into account the second-order corrections appearing in the averaged heat equation – which are induced by the deviations of the temperature and velocity profiles from the flat-film Nusselt solution – if the temperature field is assumed to be slaved to the free surface temperature θ only. Therefore, we will restrict ourself to the second-order averaged heat equation obtained from the first residual $\mathcal{R}_T(G_0)$ with $G_0 = 1$, as for the first-order. We get

$$\frac{\mathbb{F} - \mathrm{Bi}\theta}{h} - \mathrm{Pr}\left[\frac{1}{2}h\partial_t\mathbb{F} + \partial_t\theta + \frac{3}{8}q\left(\partial_x\mathbb{F} + \mathbb{F}\frac{\partial_x h}{h}\right) - \frac{5}{8}\mathbb{F}\partial_x q + \frac{q\partial_x\theta}{h}\right]$$
$$+\left[2\partial_x\mathbb{F}\partial_x h + \left(\mathbb{F} - \frac{1}{2}\mathrm{Bi}\theta\right)\frac{(\partial_x h)^2}{h} + \frac{\partial_x h\partial_x\theta}{h} + \frac{1}{2}h\partial_{xx}\mathbb{F} + \mathbb{F}\partial_{xx}h + \partial_{xx}\theta\right] = 0 \quad (8.14)$$

whose the second line are the second-order terms accounting for heat diffusion. Remember that 8.14 should be coupled with the continuity and the momentum equations (6.10a,6.10b) and that this system of three equations constitutes the reduced model – in the sense that it remains asymptotically correct – in the case of a heat flux condition. Furthermore, as for its first-order version (8.7), (8.14) is formulated to apply for a non-uniform heating whose the distribution F_{w} may be embedded into $\mathbb{F}$.

8.2 Small Biot number limit

8.2.1 Analogy with forced convection

Up to know, we used an arbitrary value for the Biot number based on the assumption that the heat transfer coefficient at the liquid-gas interface is small. Let us now justify this assumption by considering the classical problem of forced convection along a heated plate (see *e.g.* Holman [49]). The boundary layer theory yields an expression for the Nusselt number

$$\mathrm{Nu_L} = \frac{\alpha \mathrm{L}}{\mathrm{k}} = 0.664\mathrm{Re_L^{1/2}Pr^{1/3}}, \quad (8.15)$$

which quantifies the heat transfer from the plate to the fluid layer; L is the length of the heated plate and $\mathrm{Re_L} = U_\infty L/\nu$ where U_∞ is the relative velocity between the plate and the fluid. Considering the case of a local heating studied in chapter 4, we shall make the following analogy: let the air be the fluid and the liquid film (assumed to be flat for simplicity) be the 'plate' in our forced convection problem; this 'plate' moving at the film surface velocity. The characteristic temperature difference between the film surface and the air far from the interface is about $10K$. For $\mathrm{Re} = 1.5$, the film surface velocity is $U_\infty = 4\,cm/s$. Setting merely $L = 6.7\,mm$ as the length of the heater (even though the interface temperature remains constant along a much larger distance than L), we are able to estimate the heat transfer coefficient at the liquid-gas interface, provided that the ambient air is at $22°C$ and that the air properties are given at 'the average boundary layer temperature' (defined as the arithmetic

mean between the 'plate' and the ambient air). Therefore, $\nu_{\rm air} = 15.69 \times 10^{-6}\, m^2/s$, $k_{\rm air} = 0.02624\, W/mK$ and $\Pr = 0.708$ at the air temperature of $300K$. The heat transfer coefficient, using (8.15), reads therefore

$$\alpha = 3.92 \left(\frac{U_\infty}{L}\right)^{1/2} \approx 10\, W/m^2K, \tag{8.16}$$

If the Reynolds number is increased up to $\mathrm{Re} = 10$, $U_\infty = 14cm/c$ and $\alpha \approx 20\, W/m^2K$. As expected, the basic value of the heat transfer coefficient at the liquid-gas interface is very small. Nevertheless, our approximation underestimates the effective heat transfer at the liquid-gas interface that is generally improved by wave motion and residual evaporation. These effects may increase by one or several order of magnitude the heat transfer coefficient. For this reason, we chose arbitrarily $\alpha = 100W/m^2K$ in table C.1 and values of similar order of magnitude for α all along this work.

8.2.2 Temperature condition (TC)

We shall consider now the limit $\mathrm{Bi} \ll 1$ in the case of the temperature condition (1.23a). Then, the basic state temperature gradient can be assumed to be independent of the film thickness h, $b_{\rm s} \approx \mathrm{Bi}$, as discussed in §1.3.1. The basic state temperature gradient is then uniquely defined by the heat transfer α and the diffusivity κ and not by the flow rate. Many studies have been devoted to the Marangoni instability using explicitly the temperature gradient $b_{\rm s}$ to scale the temperature field [133, 25, 46]. Following this approach but avoiding the reference to the Nusselt film thickness, let us define a reference temperature $T_{{\rm s}_\nu}$ corresponding to the surface temperature of a flat film of thickness equal to the length-scale l_ν (*i.e.* $h_{\rm N} = 1$). A dimensionless temperature $T^\star$ is thus introduced using the difference $T_{\rm w} - T_{{\rm s}_\nu}$ such that $T^\star = 1$ at the wall and $T^\star = 0$ at the surface of the film of thickness l_ν. T and $T^\star$ are then related by

$$T = \frac{1 + \mathrm{Bi}\, T^\star}{1 + \mathrm{Bi}}\,, \tag{8.17}$$

so that the temperature gradient of the base state can be written

$$b_{\rm s}^\star \equiv \frac{\Theta^\star\big|_{y=0} - \Theta^\star\big|_{y=h_{\rm N}}}{h_{\rm N}} = \frac{1 + \mathrm{Bi}}{1 + \mathrm{Bi} h_{\rm N}}\,. \tag{8.18}$$

The heat transfer boundary condition (1.14), using (8.17), reads now in dimensionless form,

$$-\boldsymbol{\nabla} T^\star \cdot \mathbf{n} = \mathrm{Bi} T^\star + 1\,. \tag{8.19}$$

Takashima [133] considered the linear stability analysis of a thin film in the limit of a vanishing Biot number ($\mathrm{Bi} = 0$) and a constant Marangoni number $\mathrm{M}^\star$ (see (1.46)). Obviously, taking this limit is not consistent with the problem at hand since $\mathrm{M}^\star$, which depends on Bi, also vanishes. Nevertheless, Ma can be quite large (in the case of a large temperature difference between the wall and ambient) so that $\mathrm{M}^\star$ can be of

order one even if Bi is small (Bi $\ll 1$). Thus, Takashima's limit corresponds in fact to a constant temperature gradient $\alpha(T_{\rm w}-T_\infty)/\lambda$ or $b_{\rm s}^\star=1$ and can be taken simply by neglecting the term Bi$T^\star$ in (8.19) as

$$-\nabla T^\star\cdot\mathbf{n}=1\,. \tag{8.20}$$

The number of parameters is consequently reduced by one, the Marangoni and Biot numbers being combined to the product BiMa.
In this limit, the change of variables from the dimensionless temperature T to $T^\star$ given by (8.17) is translated to the corresponding definition of the temperature at the free surface $\theta=(1+{\rm Bi}\theta^\star)/(1+{\rm Bi})$. The approximation of the heat transfer at the surface leading from (8.19) to (8.20) can be applied in our modelling by expanding $\theta\approx 1+{\rm Bi}(\theta^\star-1)$. Then the modified system of equations is obtained simply by substituting $\theta^\star$ for θ in (6.10) and keeping the leading order terms in Bi to get

$$\partial_t h = -\partial_x q\,, \tag{8.21a}$$

$$\begin{aligned}\partial_t q = {}& \frac{9}{7}\frac{q^2}{h^2}\partial_x h-\frac{17}{7}\frac{q}{h}\partial_x q\\ &+\left\{\frac{5}{6}h-\frac{5}{2}\frac{q}{h^2}+4\frac{q}{h^2}(\partial_x h)^2-\frac{9}{2h}\partial_x q\partial_x h-6\frac{q}{h}\partial_{xx}h+\frac{9}{2}\partial_{xx}q\,.\right.\\ &\left.-\frac{5}{6}Bh\partial_x h+\frac{5}{6}{\rm Ka}h\partial_{xxx}h-{\rm MaBi}\left(\frac{5}{4}\partial_x\theta^\star-\frac{1}{224}hq\partial_{xx}\theta^\star\right)\right\}\\ &\times\left(1-\frac{1}{70}q\partial_x h+{\rm MaBi}\frac{5}{56h}\partial_x\theta^\star\right)^{-1},\end{aligned} \tag{8.21b}$$

$$\begin{aligned}{\rm Pr}\partial_t\theta^\star = {}& 3\frac{(1-\theta^\star-h)}{h^2}+{\rm Pr}\left[\frac{7}{40}\frac{(1-\theta^\star)}{h}\partial_x q-\frac{27}{20}\frac{q}{h}\partial_x\theta^\star\right]\\ &+(1-\theta^\star)\left(\frac{\partial_x h}{h}\right)^2+\frac{\partial_x h\partial_x\theta^\star}{h}+(1-\theta^\star)\frac{\partial_{x^2}h}{h}+\partial_{xx}\theta^\star\,.\end{aligned} \tag{8.21c}$$

The Marangoni and Biot numbers appearing through their product only, one parameter disappears and the parametric study of the waves is simplified.

8.2.3 Heat fluc condition (HFC)

Considering the small Biot number limit (Bi $\ll 1$) in the case of the heat flux condition 1.23b, the base state temperature gradient (see §1.3.2) can again be assumed to be independent of the film thickness, $b_{\rm s}\approx {\rm Bi}/{\rm Bi}_{\rm w}$. However, M* as given by (1.49) and $b_{\rm s}$ depend here on Bi$_{\rm w}$, the value of which we should try to estimate. Taking an ideal situation like the one sketched on figure 8.1, the heat loss at the wall reads

$$q_{\rm loss}=\frac{\lambda_{\rm w}}{h_{\rm w}}\Delta T_{\rm w}$$

where $h_{\rm w}$ is the thickness of the wall along which applies the temperature difference $\Delta T_{\rm w}=T_{\rm w}-T_\infty$ and $\lambda_{\rm w}$ is the heat conductivity of the wall. Identifying the heat

transfer coefficient at the wall as $\alpha_\mathrm{w} = \lambda_\mathrm{w}/h_\mathrm{w}$, the wall Biot number becomes

$$\mathrm{Bi}_\mathrm{w} = \frac{\lambda_\mathrm{w}}{\lambda}\frac{\bar{h}_\mathrm{N}}{h_\mathrm{w}}. \tag{8.22}$$

An experimental apparatus where the conductivity ratio $\lambda_\mathrm{w}/\lambda$ is of $\mathcal{O}(1)$ and the thickness ratio $\bar{h}_\mathrm{N}/h_\mathrm{w}$ is of $\mathcal{O}(10^{-2})$ is realistic such that $\mathrm{Bi}_\mathrm{w} = \mathcal{O}(10^{-2})$ could be of the same order of magnitude than Bi. For simplicity, let us therefore consider the approximation $\mathrm{Bi}_\mathrm{w} \approx \mathrm{Bi}$. Then, the temperature gradient across the layer reads $b_\mathrm{s} \simeq \frac{1}{2}$ such that the problem becomes independent of the Biot numbers, with $\mathrm{M}^\star = \mathrm{Ma}/2$.

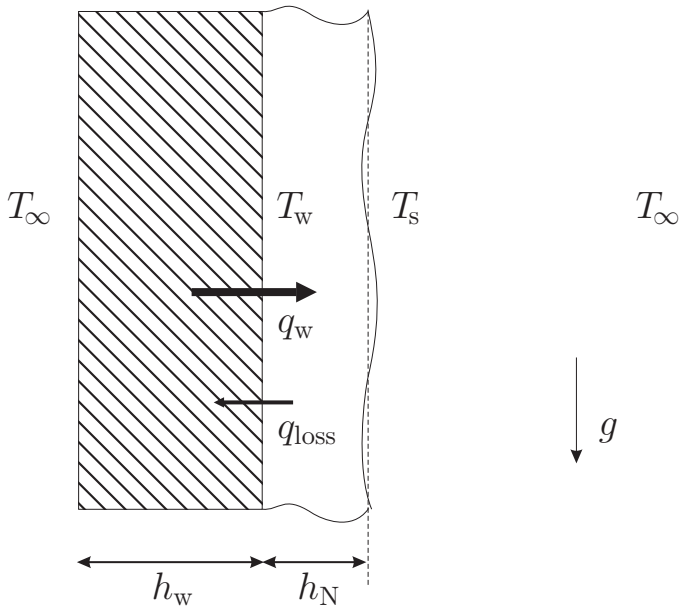

Figure 8.1: Sketch of the heat fluxes at the wall.

Now, we can follow the same approach as for the TC case, what consists in defining a reference temperature difference ΔT_s across a film of thickness l_ν (*i.e.* $h_\mathrm{N} = 1$), and introduce again a dimensionless temperature based on it such that $T^\star = 1$ at the wall and $T^\star = 0$ at the surface. T and $T^\star$ are here related by

$$T = \frac{1 + \mathrm{Bi}\, T^\star}{\mathrm{Bi} + \mathrm{Bi}_\mathrm{w}(1 + \mathrm{Bi})}, \tag{8.23}$$

so that the temperature gradient of the base state can be written

$$b_\mathrm{s}^\star = \frac{\mathrm{Bi} + \mathrm{Bi}_\mathrm{w}(1 + \mathrm{Bi})}{\mathrm{Bi} + \mathrm{Bi}_\mathrm{w}(1 + \mathrm{Bi}h_\mathrm{N})}\,. \tag{8.24}$$

Notice that while T tends to infinity when both Biot numbers tend to zero, $T^\star$ does not. It represents therefore an advantage for the numerical point of view.
The heat transfer boundary condition (1.14), using (8.23), is identical to (8.19) and the small Biot limit $\mathrm{Bi} \ll 1$ leads also to the same simplification as for the TC case, *i.e.* that if $\mathrm{M}^\star$ remains of $\mathcal{O}(1)$, the base state temperature gradient $b_\mathrm{s}^\star = 1$ will

remain independent on the film thickness perturbations. Then, the reduced model is modified by substituting $\theta^\star$ for θ in (8.14) and keeping the leading order terms in Bi to get

$$\frac{\mathbb{F}^\star - 1}{h} - \mathrm{Pr}\left[\frac{1}{2}h\partial_t\mathbb{F}^\star + \partial_t\theta^\star + \frac{3}{8}q\left(\partial_x\mathbb{F}^\star + \mathbb{F}^\star\frac{\partial_x h}{h}\right) - \frac{5}{8}\mathbb{F}^\star\partial_x q + \frac{q\partial_x\theta^\star}{h}\right]$$
$$+\left[2\partial_x\mathbb{F}^\star\partial_x h + \mathbb{F}^\star\frac{(\partial_x h)^2}{h} + \frac{\partial_x h\partial_x\theta^\star}{h} + \frac{1}{2}h\partial_{xx}\mathbb{F}^\star + \mathbb{F}^\star\partial_{xx}h + \partial_{xx}\theta^\star\right] = 0, \qquad (8.25)$$

with $\mathbb{F}^\star = (1 - \mathrm{Bi}_{\mathrm{w}}\theta^\star)/(1 + \mathrm{Bi}_{\mathrm{w}}h)$. The continuity and momentum equations (8.21a, 8.21b) remain unchanged.

In conclusion, we have shown in this chapter appropriate valuable modifications to our reduced model, necessary for more realistic comparisons with common experimental situations. We then believe that the resulting new systems will be of special interest for future investigations and comparisons with experimental studies.

Conclusions and perspectives

The main objective of this work was to obtain the most appropriate models to describe the stability and the dynamics of a thin film flowing along a heated inclined plate. We have considered two heat boundary conditions at the plate, namely a temperature and a heat flux condition referred to as TC and HFC, respectively. The former is a particular case of the latter for a perfectly conducting wall, *i.e.* $\mathrm{Bi}_\mathrm{w} \to \infty$.

In **chapter 1**, we formulated the basic equations and calculated the base state solution of the problem. For both TC and HFC with a perfectly conducting ($\mathrm{Bi} \to \infty$) or insulating ($\mathrm{Bi} \to 0$) interface, the film surface temperature remains homogeneous and no Marangoni effect takes place. The same situation occurs for the HFC with an insulating plate ($\mathrm{Bi}_\mathrm{w} = 0$). On the contrary, for a finite value of Bi (and Bi_w for HFC), the long-wave thermocapillary instability can take place at the free surface. Under these conditions, we performed a linear stability analysis of the basic equations and analysed separately purely transverse (spanwise) and longitudinal (streamwise) normal mode disturbances. For the former, analytical condition for the critical Marangoni number can be obtained while for the latter, similar condition was obtained through a long-wave approximation. While the thermocapillary S-mode is present in both directions, the hydrodynamic H-mode occurs only for longitudinal disturbances.
We also presented three sets of dimensionless parameters depending on the problem considered. They are the *natural set*, the *base state set* and the *nonlinear set* of parameters. The first one is the most appropriate for comparison with experiments since it depends only on fluid properties and on control parameters (temperature difference across the layer and flow rate), the second one compares forces that are relevant at the instability onset of the base state solution while the third one compares forces relevant in the case of nonlinear waves such as large amplitude solitary waves with fore-running capillary ripples. The nonlinear set of parameters is numerically optimal for time-dependent simulations since all terms of the evolution equations are of order unity, including the surface tension terms.
Finally, we presented a hierarchy of models. Generally, the dynamics of a wavy laminar flow is well described by the boundary layer equations which basically neglect the inertia terms in the cross-stream momentum equation. However, these equations, as for the Navier-Stokes/Fourier equations, are fully three-dimensional. Hopefully, the dimensionality of these equations can be reduced by taking into account the coherence of the flow ensured by viscosity. Then two class of models can be considered depending on the flow regime: the long-wave equation (or Benney equation) for low Reynolds numbers and the weighted integral boundary layer equations for moderate

Reynolds numbers. Interestingly, as identified by Ooshida [93] considering solitary-wave solutions, these two classes correspond to two different driving forces in the flow. First, we have the *drag-gravity* regime corresponding to the balance of the gravitational acceleration with the viscous drag, with inertia playing only a 'perturbative' role. This regime is observable for low amplitude waves. Secondly, we have the *drag-inertia* regime appearing at larger Reynolds numbers where inertia plays a dominant role. This regime is observable for large amplitude waves of high speed.

In the first part of this work, we restricted ourselves to the drag-gravity regime where a single evolution equation (namely the Benney equation) generally provides satisfactory results. However, we paid a special attention to the validity domain of the Benney equation (BE) since the latter is known to exhibit non-physical finite-time blow-up.

In **chapter 2**, we therefore focused on the validity of stationary travelling wave solutions of the BE in terms of accuracy and boundedness. The accuracy was checked by comparison with a reference model developed in chapter 5 and valid at larger Reynolds numbers (*i.e.* in some region of the drag-inertia regime). The solutions that tend to blow up first, *i.e.* at the smallest Reynolds number, were found to be the one-humped solitary waves. We provided quantitative criteria for the boundedness of such solutions.

We paid a particular attention to the condition imposed for the flow that can be closed or open. While the former is commonly used in the literature, only the latter coincides with realistic experimental conditions. For the open flow condition the validity domain of the Benney equation is larger than for the closed flow condition. Furthermore, in the isothermal case, for the open flow condition the Hopf bifurcation (yielding waves) is always supercritical in a very small region close to the neutral curve. This is not the case using the closed flow condition. There the Hopf bifurcation is always subcritical above the Reynolds number at which none of the linearly unstable modes is bounded. The subcritical bifurcation of the Benney equation has also been investigated in the region where the Benney equation can still yield bounded solutions. In the isothermal case, subcritical bifurcations appear only with the closed flow condition. We showed that they are physically meaningless. Including the Marangoni effect, the situation is more tricky because for horizontal layers the Marangoni instability is known to be subcritical indeed. Therefore, the subcritical behaviour obtained with the Benney equation for inclined layers might be physical. However, for vertically falling films such behaviour has never been observed with the reference model, whereas the Benney equation even gives a threshold $\mathcal{MB} \approx 1$ above which all the bounded solution branches emerge by subcritical bifurcation and are therefore non-physical.

Finally, the stability of stationary solutions has been addressed for solutions that are conditionally bounded depending on the wavenumber. They were all found to be unstable to disturbances of larger spatial period. This gives the possibility to the sub-harmonics to develop and in consequence, to yield finite-time blow-up. This was confirmed by numerical simulations that show blow-up promoted by wave coalescence.

In **chapter 3** we considered the case of a non-homogeneously heated plate in the case of a sinusoidal temperature distribution imposed at the wall (the latter being vertical). We still used the Benney equation, which in this case contains an additional thermocapillary term accounting for the imposed non-uniform heating and inducing steady-state deformations of the film surface. Thereby, in addition to the characteristic temperature difference across the layer, a second one along the wall had to be considered, which quantifies the amplitude of the imposed temperature non-uniformity. The most interesting picture occurs when both characteristic temperature differences are of the same order of magnitude.
Numerical solutions of the evolution equation showed that the travelling wave obtained with an averaged uniform heating is modulated by an envelope given by the steady-state deformation resulting from the non-uniform heating. At small Marangoni number, the solution is merely the superposition between the travelling wave calculated as a stationary solution in a moving reference frame for a uniform heating, and the steady-state deformation calculated as a stationary solution in a laboratory fixed reference frame in the case of a non-uniform heating. At larger Marangoni number, the presence of the non-uniform heating affects nonlinearly the travelling waves and at some threshold, it may even suppress the wavy motion at the interface.
We also assessed the enhancement of the heat transfer due to the coexistence of sustained deformations and travelling waves. The latter have no significant effect on the heat transfer coefficient, while the former can increase it sensitively. We did not investigate the stability of the stationary solutions with regards to streamwise subharmonic disturbances. Such analysis should be done in the future to check if our conclusions still apply in the realistic situation of an open flow. In the same vein, the stability of the steady-state deformations with respect to spanwise deformations may reveal novel instabilities as it was studied in chapter 4 for the specific case of a step-function temperature profile imposed at the wall in the streamwise direction.

The intent of **chapter 4** has been to develop an understanding of the mechanisms by which a falling film on a locally heated plate looses stability and yield steady-state rivulet structures. Experiments were performed at small Reynolds numbers such that the Benney equation could serve as a model and provide satisfactory comparisons. Its stationary solutions (base state) and their stability were calculated numerically for an array of heaters, the period of which is chosen large enough to recover the single heater case. The steady-state deformation in this case forms a horizontal bump that is unstable with respect to transverse (spanwise) perturbations at any Marangoni number, even though a threshold $\mathrm{Ma}_{\mathrm{th}}$ was found in our stability analysis, above which a drastic increase of the growth rate is observed. We found on the one hand that below this threshold, long-wave thermocapillary mode (resp. surface tension) is the main responsible in destabilizing (resp. stabilizing) the flow, as for homogeneous heating. On the other hand, above this threshold, both body force (gravity) and thermocapillarity play important roles in destabilizing the fluid bump whereas the presence of the temperature gradient along the streamwise direction due to non-uniform heating was found to be stabilizing (which could explain the wave suppression found in chapter 3). Moreover, by raising Ma, the wavelength first

decreases for $Ma < Ma_{th}$ and then increases for $Ma > Ma_{th}$. This behaviour was observed experimentally. However, the critical Marangoni number Ma_c for large-amplitude rivulets instability was found in experiments to be smaller by a factor three than the theoretical threshold Ma_{th}. We then identified two mechanisms that can trigger the rivulet instability for smaller Marangoni number. First, our linear stability revealed that the bump is unstable in the transverse direction (mainly due to thermocapillarity) at any Ma even though the growth rate is small for $Ma < Ma_{th}$. We conjectured (based on experimental observations) that it induces spanwise perturbations (regular structure) of small but finite amplitudes, which can in turn modify the threshold for inception of large amplitude rivulet structure (actually, the Marangoni number was always increased gradually in experiments). Secondly, the heater being of finite size in the transverse direction, the lateral temperature gradient at the edges can produce an 'imperfect' bifurcation from the 'perfect' laterally infinite case with the spanwise modes starting from the sides of the heater and then filling the domain in the transverse direction.

Because of the quantitative discrepancies between theory and experiment, we performed a qualitative survey of the nonlinear dynamics through 3D numerical simulations. Despite of many approximations used in our model (periodic boundary conditions, small Prandtl number limit, inaccurate value of the heat transfer coefficient, ...), we could recover the main characteristics of the rivulet pattern as observed in experiments such that the bump shape, the rivulet structure, the location for dry spot formation, the secondary structure and the reverse flow accompanied by a stagnation point. However, the rivulet structure was steady in experiments while they always lead to rupture in our simulations. We believe the principal reason of this discrepancy is in essence due to periodic boundary conditions used in simulations that correspond to a closed flow. We then believe that using a 3D numerical scheme allowing for an open flow could provide in the future satisfactory agreement still using a simple model as the Benney equation.

Nevertheless, two mechanisms that were not studied in this work may as well be of primary importance in stabilizing the rivulet structure. They are the intermolecular forces (Van der Waals) when the film thickness is about 0.1 μm and solutocapillary effect that is more intensive in thin film regions and opposes to the thermocapillary effect when the mixture is negative – that is when the more volatile fluid has the lowest surface tension –, as it was the case in experiments. With some classical hypotheses (see *e.g.* Burelbach, Bankoff & Davis [12]), those effects can be included in our model without much effort and are of crucial importance for the investigation of dry spot formation in liquid mixtures.

Finally, even though the Reynolds number was smaller than unity in experiments, ensuring the validity of the Benney equation, the Prandtl number is usually larger than unity for common liquids. Therefore, convection of heat that has been neglected in our model, should be considered more carefully. This has been done in the second part of this work, but only for the case of uniform heating. Future investigations for rivulet instability should consider for instance a two-equation model for the film thickness and the surface temperature (as proposed by Kalliadasis *et al.* [68]).

The methodology developed in **chapter 5** is a combination of the classical long-wave theory with polynomial expansions for the temperature and velocity fields followed by a weighted residual approach. It allowed us to formulate a number of models of reduced dimensionality (*i.e.* without dependence on the cross-stream coordinate), referred to as weighted integral boundary layer models, consistent at first or second order in the long-wave expansion parameter (or film parameter ε). These models are basically valid for much larger Reynolds number and Prandtl number than the single Benney equation. The full two-dimensional second-order model includes nine unknows defined at the free surface, namely the film thickness h, the flow rate q, the surface temperature θ and three corrections to each field q and θ accounting for the departure of velocity and temperature profiles across the film from their parabolic and linear shapes, respectively. Admittedly, our full second-order model is of little use because of its complexity. Using arguments from the linear stability of the film in the zero wavenumber limit, we showed that only h, q and θ play a significant role and the other fields are virtually slaved to their dynamics, at least for some range of Reynolds and Prandtl numbers. As a consequence, the 'appropriate' elimination of the corrective fields yields a whole family of models of reduced dimensionality in terms of the three variables h, q and θ. 'Appropriate' means here that the resulting *reduced second-order models* would lead to exact asymptotic results as described by the second-order long-wave expansion.

In **chapter 6** we developed a strategy to select the 'best candidate' among the whole family of reduced models. To this purpose, we compared their stability analyses to the Orr-Sommerfeld analysis of the linearized basic momentum and heat equations. The selected model does agree with the Orr-Sommerfeld analysis for small and moderate Reynolds and Marangoni numbers. Computation of its principal homoclinic orbits (the solitary waves) do not exhibit the non-physical turning points and therefore time-dependent integrations of the model do not lead to the non-physical finite time blow-up encountered with the Benney equation.
Once the reduced model selected, the two long-wave instability modes (S and H) of a liquid film flow down a heated plane at a constant temperature have been investigated. We have computed the shape, streamlines and isotherms of the one-hump solitary waves for different Reynolds and Prandtl numbers. In the drag-gravity regime, the transport of heat by the flow contributes to warm up the crest of the wave and the inertial terms in the averaged heat equation have a stabilizing effect. In the drag-inertia regime where the amplitudes and speeds of the waves become very large, recirculation zones can be observed and the effect of the transport of heat by the flow is reversed. One of the stagnation points is displaced from the front face to the crest of the wave. The Marangoni effect thus amplifies the recirculation flow in the crest and promotes a strong downward flow at the crest. As a consequence, the transport of heat by the flow contributes to cool the crest and to increase the Marangoni effect. Nevertheless, the strong circulation and the downward flow create a strong shear and therefore increase the effect of viscous dissipation, which reduces in turn the amplitude and speed of the waves if the Prandtl number is raised.
The interaction of the hydrodynamic H-mode and the Marangoni S-mode is not trivial

especially if one considers the dynamics of the large-amplitude solitary waves. The preliminary observations gathered in this study needs to be compared to experiments. Such comparisons would be facilitated by the fact that most fluids used in applications correspond to high Kapitza numbers.
Another open question is the study of large Péclet number flows. The formulation of reduced models was limited here to systems of equations in terms of three unknowns only. Our linear stability analysis and computations of solitary waves suggest that other fields than θ are needed to correctly represent the heat transport process. In particular, an important perspective is to overcome the spurious appearance of temperatures lower than the temperature of the air that we observed for large amplitude waves if the Reynolds and Prandtl numbers are not small. Therefore, our aim will be to obtain reliable models in term of h, q, θ and t_1 (first correction of the linear temperature profile across the layer), compatible with the long-wave expansion up to second order, and enabling to extend the present study to higher Reynolds and Prandtl numbers.

In **chapter 7**, we turned to larger Reynolds numbers, where secondary instabilities generate three-dimensional patterns, under periodic forcing. We essentially compared the full second-order model, the reduced model and an *approximated model* (which parabolic velocity and linear temperature profiles). As demonstrated by Ruyer-Quil *et al.* [112], our models predict the subharmonic scenario (herringbone pattern) to be the predominant one which contradicts experimental observations. This discrepancy was understood considering that the the secondary transition is not really selective, the maximal growth rate varying slowly with the detuning parameter φ. Integrations in time of the three-dimensional models using periodic boundary conditions show a good agreement with the experimental snapshots given by Liu *et al.* [84] for isothermal conditions. However, numerical simulations of the approximated model lead systematically to herringbone patterns whereas synchronous instabilities are observed using the full or the reduced models. Our simulations show also that the classical two-steps scenario of a secondary 3D instability of the primary 2D wave-train could be wrong in some cases where the 2D simulation do not evolve first to saturated periodic waves but to modulated ones as was observed previously in the direct numerical simulations of Ramaswamy *et al.* [104]. In such cases the 3D wave pattern is the result of the competition between the growing modulation and the secondary instability and should therefore be dependent on the compared levels of noise in the streamwise and spanwise directions. If our simulations of the reduced model are able to reproduce the experimentally observed synchronous wave pattern, such was not the case with the full-second order model.
We also tested our 3D model in isothermal conditions in the case of white noise in a large domain of size about 15 linear wave lengths in both directions (streamwise and spanwise). Our simulations share a lot of similarities with experimental pictures obtained by Alekseenko *et al.* [1], mainly the coalescence of two dimensional waves and the development of 3D large amplitude solitary waves with extended region of residual thin film in between. For the largest Reynolds number considered (Re = 45), we encountered numerical limits. For such regime, we suggest therefore to use an implicit

numerical scheme for better stability, which would furthermore allow to consider the more realistic open flow condition (*i.e.* non-periodic boundary conditions). This is performed using "soft" boundary conditions at the downstream boundary, ensuring no upstream reflections.
Finally, we have performed preliminary 3D simulations in the case of a uniformly heated plate with our reduced model. The presence of rivulets aligned with the flow as described by Joo *et al.* at small Reynolds number was recovered. At larger Reynolds number, the co-existence between longitudinal rivulets and solitary waves has been evidenced, as observed experimentally (see figure 7 of the Introduction). A more systematic survey will be needed in the future to explore the development of solitary waves in presence of a uniform heating.

In **chapter 8**, we applied our modelling strategy to the case of a heat flux condition on the one hand and show, on the other hand, how to modify our model in the case of the small Biot number limit. Indeed, those two cases are of particular interest in practical applications and may be useful in future studies.

To conclude, one of the advantages of the Benney equation is to describe with a single evolution equation the different physical effects in a falling film, namely in our case, viscosity, gravity, surface tension and thermocapillarity. We believe this ensures that the Benney equation will remain a competitive model to study thin film flows at low Reynolds numbers, especially to identify new phenomena. Actually, many other effects may be added to the Benney equation like evaporation [53], Van der Waals forces [134], chemical reaction [139], topological effects [66], non-uniform heating [87, 64, 120], etc. However, the validity of the Benney equation should in the future also be addressed including these additional effects.
The weighted integral boundary layer model (or reduced model) obtained in this work provides a larger validity range than the Benney equation and is recommended for flow regimes where the Benney equation is not valid anymore, *i.e.* at moderate Reynolds and Péclet number. The WIBL model has furthermore the great advantage to enable, *a posteriori*, reconstruction of the velocity and the temperature fields – with corrections to the parabolic and linear profiles, respectively – across the layer (which is not possible with the classical Shkadov's integral boundary layer model). The validation of our reduced model was threefold: good linear properties, boundedness of solitary-wave solutions and satisfactory comparisons with experiments. Of course the best validation would have been to compare the branch of solitary-wave solutions with the one computed directly from the full-scale boundary-layer equations. Such comparison is not yet available but will be decisive in our model validation.
The procedure developed in the second part of this work was made possible by the simple zeroth order solution, which corresponds to polynomial velocity and temperature profiles. We specifically showed that models based on the assumption of a 'perturbative' role of the inertial terms – valid for the drag-gravity regime at low or moderate Reynolds numbers – can be extended to larger Reynolds numbers where inertia is a dominant effect if special care is taken for the formulation of the inertial corrections. Our hope is that our strategy may be helpful in the modelling of other

situations of interest in practical applications, where physicists wish to extrapolate approximated equations obtained asymptotically and apply them to situations where the small parameter is no longer small. This might include thin films in the presence of active impurities (surfactants), evaporation or chemical reactions. It might also include other geometries that can be connected to the 'flat film case' with the help of appropriate expansions, as for instance the case of flow in Hele-Shaw cell made of thin gaps [113].

Appendix A

Falling film applications

Falling film evaporators in the food industry

Falling film evaporators, as the one sketched on figure A.1, are especially popular in the food industry where many substances are heat sensitive. A thin film of the product to be concentrated flows down inside of heat exchanging tubes. Steam condenses on the outside of the tubes supplying the required energy to the inside of the tubes.

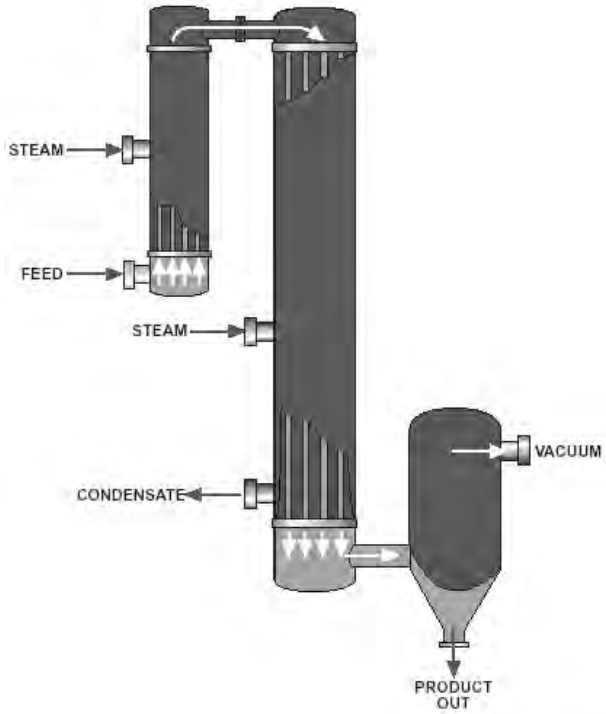

Figure A.1: Sketch of a tubular falling film evaporator [152].

The simple heat transfer balance for falling film evaporators is:

$$Q = U\,A\,(T_{\mathrm{c}} - T_{\mathrm{b}})\,,$$

where U is the overall heat transfer coefficient, A is the heat transfer area, T_c is the temperature of the condensing steam and T_b is the boiling point of the process liquid. The overall heat transfer coefficient consist of the steam side condensing coefficient (usually about $5700 W/m^2K$), a metal wall with small resistance (depending on steam pressure, wall thickness), and a liquid film coefficient on the process side [153].
Evaporating fruit and vegetable juices present a special challenge for chemical engineers. Juices are heat sensitive and their viscosities increase significantly as they are concentrated. Small solids in the juices tend to stick at the tube wall (heat transfer surface) thus causing spoilage and burning. Juice evaporations are usually performed in a vacuum (see figure A.1) to reduce boiling temperatures (due to heat sensitivity). High flow circulation rates help avoid build-ups on the tube walls.
For some juices (as orange), it is unavoidable that the flavor changes as concentration increases. Some of the volatile, flavor-containing components are lost during evaporation. In this case, some of the raw juice is mixed with the concentrate to replace the lost flavors.
It is worth saying that in European sugar industry, falling film evaporators represent the state of the art and this technique is already common world-wide [124]. Since the last decade, falling film evaporators are both, falling film tubes and falling film plates; the heating surface is smooth in both cases.

Crystallizer

The falling film crystallizer contains vertical tubes as shown on figure A.2. Crystal layers are grown from a falling film of melt on the inside of the cooled tubes. Impurities are rejected from the crystals and concentrated in the remaining melt. Falling film crystallization is generally used for relatively pure feeds and high capacities.

Evaporator and crystallizer applications

Here are listed products that are processed with falling film evaporators or crystallizers: Alcohols, Apple Juice, Boric Acid, Brewer's Malt, Calcium Salts, Caprolactam, Caustic Soda, Citrus Juice, Coffee Extract, Collagen, Copper Sulfate, Distiller Slop, Ethanol Stillage, Fruit Juices, Gelatin, Glucose, Glycerin, Grape Juice, Green Liquor, Kraft Liquor, Methanol Stillage, Milk, Phosphoric Acid, Potassium Salts, Red Liquor, Sodium slats, Solvents Separation, Steepwater, Stickwater, Stillage, Sugars, Sulfates, Sulfites, Sulfides, Syrups, Tomato Juice, Urea, Waste Lubrication Oil, Waste Water, Whey [154].

Absorption in a Falling Film

There are a number of different experimental methods for determining the absorption of gas in a liquid. The principle of these methods is however the same in most cases; to obtain a well-defined velocity profile in the liquid phase in order to obtain an analytical estimation of the diffusion boundary layer [9, 38, 101]. This well-defined velocity profile can be obtained by using for instance thin liquid falling films (see [77]).

Figure A.2: Falling film crystallization: the melt flows down on the inside surface of the tubes, whereas the medium used for cooling is distributed to wet the external surface of the tubes [151].

This is the principle of typical measuring equipments for gas absorption as sketched in figure A.3. A liquid film is formed by a guiding funnel that creates an annular flow with a free liquid surface facing the centre of a tube. The gas is introduced in the middle of the tube and is absorbed on the free surface of the liquid. The composition of the liquid and the gas is measured before and after entering the apparatus. The contact surface between the gas and the liquid is confined to the free surface inside of the tube. This implies that the contact area and the convection in this phase boundary are well-defined.
The mass transport properties in the gas phase are estimated from the relative velocity between the liquid flow and the gas flow. In most cases the magnitude of the forced convection in the gas is negligible and the transport properties can be obtained from the free convection that is induced in the gas phase by the flow of the liquid.

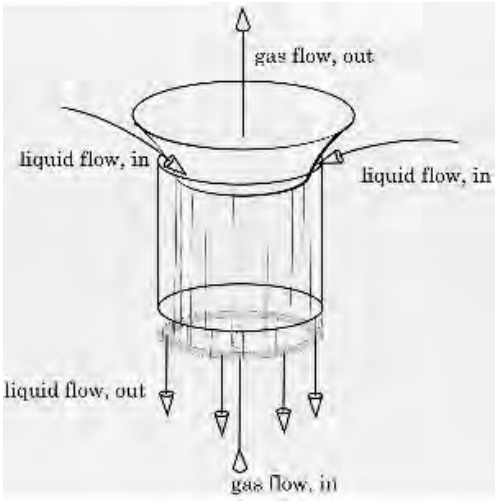

Figure A.3: Sketch of an absorption apparatus with a falling film [150].

Appendix B

Systems of 2D boundary layer equations

Natural set of parameters: $\{\mathrm{Re}, \mathrm{Ct}, \mathrm{Ka}, \mathrm{Ma}, \mathrm{Bi}, \mathrm{Pr}\}$

$$\partial_t u + u\partial_x u + v\partial_y u = 1 + \partial_{yy} u + 2\partial_{xx} u + \partial_x \left[\partial_x u\big|_h\right] - \mathrm{Ct}\partial_x h + \mathrm{Ka}\partial_{xxx} h \tag{B.1a}$$

$$\mathrm{Pr}\left(\partial_t T + u\partial_x T + v\partial_y T\right) = \partial_{yy} T + \partial_{xx} T \tag{B.1b}$$

$$\partial_y u\big|_h = -\mathrm{Ma}\partial_x \left[T\big|_h\right] + 4\partial_x h \partial_x u\big|_h - \partial_x v\big|_h \tag{B.1c}$$

$$\partial_y T\big|_h = -\mathrm{Bi}\left(1 + \frac{1}{2}(\partial_x)^2\right) T\big|_h + \partial_x h \partial_x T\big|_h \tag{B.1d}$$

Base state set of parameters $\{\mathrm{Re}, \mathrm{Ct}, \mathrm{We}, \mathrm{M}, \mathrm{B}, \mathrm{Pr}\}$

$$\mathrm{Re}\left(\partial_t u + u\partial_x u + v\partial_y u\right) = 1 + \partial_{yy} u + 2\partial_{xx} u + \partial_x \left[\partial_x u\big|_h\right] - \mathrm{Ct}\partial_x h + \mathrm{We}\partial_{xxx} h \tag{B.2a}$$

$$\mathrm{PrRe}\left(\partial_t T + u\partial_x T + v\partial_y T\right) = \partial_{yy} T + \partial_{xx} T \tag{B.2b}$$

$$\partial_y u\big|_h = -\mathrm{M}\partial_x \left[T\big|_h\right] + 4\partial_x h \partial_x u\big|_h - \partial_x v\big|_h \tag{B.2c}$$

$$\partial_y T\big|_h = -\mathrm{B}\left(1 + \frac{1}{2}(\partial_x)^2\right) T\big|_h + \partial_x h \partial_x T\big|_h \tag{B.2d}$$

Nonlinear set of parameters $\{\mathcal{R}, \mathcal{C}, \eta, \mathcal{M}, \mathrm{B}, \mathrm{Pr}\}$

$$\mathcal{R}\left(\partial_t u + u\partial_x u + v\partial_y u\right) = 1 + \partial_{yy} u + \eta\left(2\partial_{xx} u + \partial_x \left[\partial_x u\big|_h\right]\right) - \mathcal{C}\partial_x h + \partial_{xxx} h \tag{B.3a}$$

$$\mathrm{Pr}\mathcal{R}\left(\partial_t T + u\partial_x T + v\partial_y T\right) = \partial_{yy} T + \eta\partial_{xx} T \tag{B.3b}$$

$$\partial_y u\big|_h = -\mathcal{M}\partial_x \left[T\big|_h\right] + \eta\left(4\partial_x h \partial_x u\big|_h - \partial_x v\big|_h\right) \tag{B.3c}$$

$$\partial_y T\big|_h = -\mathrm{B}\left(1 + \frac{1}{2}\eta(\partial_x)^2\right) T\big|_h + \eta\partial_x h \partial_x T\big|_h \tag{B.3d}$$

The three above systems have to be completed by the following equations,

$$\partial_x u + \partial_y v = 0 \tag{B.4a}$$

$$\partial_t h + u\big|_h \partial_x h = v\big|_h \tag{B.4b}$$

$$u\big|_0 = v\big|_0 = 0 \tag{B.4c}$$

$$T\big|_0 = 1 + F_{\mathrm{w}}(x) \tag{B.4d}$$

The relations between all the parameters are

$$\begin{aligned}
\mathrm{Re} &= \frac{\mathcal{R}}{3\eta^{1/2}} \\
\mathrm{Ct} &= \frac{\mathcal{C}}{\eta^{1/2}} \\
\mathrm{Ka} &= \frac{\mathcal{R}^{2/3}}{\eta^{11/6}} = \mathrm{We}(3\mathrm{Re})^{2/3} \\
\mathrm{Ma} &= \frac{\mathcal{M}\mathcal{R}^{2/3}}{\eta^{5/6}} = \mathrm{M}(3\mathrm{Re})^{2/3} \\
\mathrm{Bi} &= \frac{\mathrm{B}}{(3\mathrm{Re})^{1/3}}
\end{aligned}$$

$$\begin{aligned}
\mathrm{We} &= \frac{1}{\eta^{3/2}} = \frac{\mathrm{Ka}}{(3\mathrm{Re})^{2/3}} \\
\mathrm{M} &= \frac{\mathcal{M}}{\eta^{1/2}} = \frac{\mathrm{Ma}}{(3\mathrm{Re})^{2/3}} \\
\mathrm{B} &= \mathrm{Bi}\,(3\mathrm{Re})^{1/3}
\end{aligned}$$

$$\begin{aligned}
\mathcal{R} &= \frac{3\mathrm{Re}}{\mathrm{We}^{1/3}} = \frac{(3\mathrm{Re})^{11/9}}{\mathrm{Ka}^{1/3}} \\
\mathcal{C} &= \frac{\mathrm{Ct}}{\mathrm{We}^{1/3}} = \frac{\mathrm{Ct}(3\mathrm{Re})^{2/9}}{\mathrm{Ka}^{1/3}} \\
\eta &= \frac{1}{\mathrm{We}^{2/3}} = \frac{(3\mathrm{Re})^{4/9}}{\mathrm{Ka}^{2/3}} \\
\mathcal{M} &= \frac{\mathrm{M}}{\mathrm{We}^{1/3}} = \frac{\mathrm{Ma}}{\mathrm{Ka}^{1/3}(3\mathrm{Re})^{4/9}}
\end{aligned}$$

Appendix C

Typical parameter values

Liquid	$l_{\nu_\perp}$ (μm)	$t_{\nu_\perp}$ (ms)	$\mathrm{Ka}_\perp$	$\mathrm{Ma}_\perp$ (ΔT=1K)	$\mathrm{Bi}_\perp$ (α=100W/m^2K)
Water at 20°C	47	2.2	3375	8.9	0.008
Water at 15°C	50	2.3	2950	7.7	0.009
FC-72 at 20°C	26	1.6	1100	9.7	0.045
MD-3F at 30°C	31	1.8	703	5.8	0.047
25%-Ethyl alcohol at 20°C	87	3.0	500	1.5	0.02

Table C.1: Rounded values of characteristic liquid parameters [144]. Those liquids are effectively used in experiments [56, 59, 116, 117, 119]. The value of the heat transfer coefficient α used to estimate the Biot number is justified in §8.2.

ρ	961.6	kg/m^3	density
ν	2.548×10^{-6}	m^2/s	kinematic viscosity
k	0.4786	W/mK	heat conductivity
σ_∞	35.53×10^{-3}	N/m	mean surface tension
γ	0.1103×10^{-3}	N/mK	surface tension variation with T
Pr	21.8	$--$	Prandtl number

Table C.2: Fluid properties for a 25 % ethyl-alcohol solution in water at 20°C.

Appendix D

Full second-order models

D.1 Two-dimensional with non-isothermal conditions

$$
\begin{aligned}
\partial_t q \;=\;& \frac{30}{31}h - \frac{90}{31}\frac{q}{h^2} - \frac{1050}{31}\frac{s_1}{h^2} - \frac{3690}{31}\frac{s_2}{h^2} - \frac{9066}{31}\frac{s_3}{h^2} - \frac{12}{5}\frac{q\partial_x q}{h} + \frac{6}{5}\frac{q^2\partial_x h}{h^2} \\
& - \frac{30}{31}\mathrm{Ct}h\partial_x h - \frac{213}{248}\mathrm{Ma}\partial_x\theta + \frac{1569}{248}\frac{q(\partial_x h)^2}{h^2} - \frac{12}{5}\frac{qs_1\partial_x h}{h^2} - \frac{4248}{2015}\frac{qs_2\partial_x h}{h^2} - \frac{5296}{3875}\frac{qs_3\partial_x h}{h^2} \\
& - \frac{1569}{248}\frac{\partial_x h\partial_x q}{h} + \frac{12}{5}\frac{s_1\partial_x q}{h} + \frac{1026}{403}\frac{s_2\partial_x q}{h} + \frac{11722}{3875}\frac{s_3\partial_x q}{h} + \frac{12}{5}\frac{q\partial_x s_1}{h} + \frac{4626}{2015}\frac{q\partial_x s_2}{h} \\
& + \frac{1538}{775}\frac{q\partial_x s_3}{h} + \frac{1069}{248}\partial_{xx}q - \frac{2847}{496}\frac{q\partial_{xx}h}{h} + \frac{30}{31}\mathrm{Ka}h\partial_{xxx}h\,, \qquad \text{(D.1a)}
\end{aligned}
$$

$$
\begin{aligned}
\partial_t s_1 \;=\;& \frac{1}{10}h - \frac{3}{10}\frac{q}{h^2} - \frac{126}{5}\frac{s_1}{h^2} - \frac{126}{5}\frac{s_2}{h^2} - \frac{126}{5}\frac{s_3}{h^2} + \frac{1}{35}\frac{q\partial_x q}{h} - \frac{3}{35}\frac{q^2\partial_x h}{h^2} \\
& - \frac{1}{10}\mathrm{Ct}h\partial_x h + \frac{3}{8}\mathrm{Ma}\partial_x\theta + \frac{93}{40}\frac{q(\partial_x h)^2}{h^2} + \frac{108}{55}\frac{qs_1\partial_x h}{h^2} - \frac{5022}{5005}\frac{qs_2\partial_x h}{h^2} + \frac{6}{35}\frac{qs_3\partial_x h}{h^2} \\
& - \frac{69}{40}\frac{\partial_x h\partial_x q}{h} - \frac{103}{55}\frac{s_1\partial_x q}{h} + \frac{9657}{5005}\frac{s_2\partial_x q}{h} - \frac{1}{35}\frac{s_3\partial_x q}{h} - \frac{39}{55}\frac{q\partial_x s_1}{h} + \frac{10557}{10010}\frac{q\partial_x s_2}{h} \\
& + \frac{19}{70}\frac{q\partial_x s_3}{h} - \frac{9}{40}\partial_{xx}q + \frac{21}{80}\frac{q\partial_{xx}h}{h} + \frac{1}{10}\mathrm{Ka}h\partial_{xxx}h\,, \qquad \text{(D.1b)}
\end{aligned}
$$

$$
\begin{aligned}
\partial_t s_2 \;=\;& \frac{13}{420}h - \frac{13}{140}\frac{q}{h^2} - \frac{39}{5}\frac{s_1}{h^2} - \frac{11817}{140}\frac{s_2}{h^2} - \frac{11817}{140}\frac{s_3}{h^2} - \frac{13}{420}\mathrm{Ct}h\partial_x h - \frac{13}{64}\mathrm{Ma}\partial_x\theta \\
& - \frac{3211}{4480}\frac{q(\partial_x h)^2}{h^2} - \frac{4}{11}\frac{qs_1\partial_x h}{h^2} + \frac{18}{11}\frac{qs_2\partial_x h}{h^2} - \frac{38}{25}\frac{qs_3\partial_x h}{h^2} + \frac{2613}{4480}\frac{\partial_x h\partial_x q}{h} - \frac{2}{33}\frac{s_1\partial_x q}{h} \\
& - \frac{19}{11}\frac{s_2\partial_x q}{h} + \frac{76}{25}\frac{s_3\partial_x q}{h} + \frac{6}{55}\frac{q\partial_x s_1}{h} - \frac{288}{385}\frac{q\partial_x s_2}{h} + \frac{73}{70}\frac{q\partial_x s_3}{h} + \frac{559}{2240}\partial_{xx}q \\
& - \frac{2847}{8960}\frac{q\partial_{xx}h}{h} + \frac{13}{420}\mathrm{Ka}h\partial_{xxx}h\,, \qquad \text{(D.1c)}
\end{aligned}
$$

$$\begin{aligned}\partial_t s_3 &= \frac{3}{868}h - \frac{9}{868}\frac{q}{h^2} - \frac{27}{31}\frac{s_1}{h^2} - \frac{8181}{868}\frac{s_2}{h^2} - \frac{158709}{868}\frac{s_3}{h^2} - \frac{3}{868}\mathrm{Ct}h\partial_x h + \frac{435}{1984}\mathrm{Ma}\partial_x\theta \\ &+\frac{3}{868}\mathrm{Ka}h\partial_{xxx}h + \frac{19953}{27776}\frac{q(\partial_x h)^2}{h^2} - \frac{342}{2015}\frac{qs_2\partial_x h}{h^2} + \frac{9894}{3875}\frac{qs_3\partial_x h}{h^2} - \frac{19023}{27776}\frac{\partial_x h\partial_x q}{h} \\ &-\frac{171}{2015}\frac{s_2\partial_x q}{h} - \frac{9358}{3875}\frac{s_3\partial_x q}{h} + \frac{171}{2821}\frac{q\partial_x s_2}{h} - \frac{13653}{10850}\frac{q\partial_x s_3}{h} - \frac{2973}{13888}\partial_{xx}q \\ &+\frac{17517}{55552}\frac{q\partial_{xx}h}{h}\,, \end{aligned} \tag{D.1d}$$

$$\begin{aligned}\mathrm{Pr}\partial_t\theta &= \frac{30009}{1273}\left(\frac{1-(1+\mathrm{Bi}h)\theta}{h^2}\right) - \frac{130950}{1273}\frac{t_1}{h^2} - \frac{1384362}{6365}\frac{t_2}{h^2} - \frac{1863792}{6365}\frac{t_3}{h^2} \\ &+\mathrm{Pr}\left[-\frac{3117}{203680}\frac{(1-\theta)\partial_x q}{h} - \frac{155877}{101840}\frac{q\partial_x\theta}{h} - \frac{3117}{81472}\frac{t_1\partial_x q}{h} + \frac{801101}{4480960}\frac{t_2\partial_x q}{h}\right. \\ &-\frac{1768473}{1323920}\frac{t_3\partial_x q}{h} + \frac{3117}{40736}\frac{q\partial_x t_1}{h} - \frac{364701}{2240480}\frac{q\partial_x t_2}{h} + \frac{7840671}{14563120}\frac{q\partial_x t_3}{h} \\ &-\frac{21819}{101840}\frac{(1-\theta)\partial_x s_1}{h} - \frac{10066647}{21182720}\frac{(1-\theta)\partial_x s_2}{h} - \frac{949089}{8147200}\frac{(1-\theta)\partial_x s_3}{h} \\ &\left.+\frac{245511}{50920}\frac{s_1\partial_x\theta}{h} - \frac{44102157}{10591360}\frac{s_2\partial_x\theta}{h} + \frac{295506139}{4073600}\frac{s_3\partial_x\theta}{h}\right] \\ &+\frac{27463}{1273}\frac{(1-\theta)(\partial_x h)^2}{h^2} - \frac{30009}{2546}\mathrm{Bi}\frac{\theta(\partial_x h)^2}{h} + \frac{27463}{1273}\frac{\partial_x h\partial_x\theta}{h} \\ &+\frac{(1-\theta)\partial_{xx}h}{h} + \partial_{xx}\theta\,, \end{aligned} \tag{D.1e}$$

$$\begin{aligned}\mathrm{Pr}\partial_t t_1 &= \frac{8176}{1273}\left(\frac{1-(1+\mathrm{Bi}h)\theta}{h^2}\right) - \frac{40880}{1273}\frac{t_1}{h^2} - \frac{34874}{1273}\frac{t_2}{h^2} - \frac{28784}{1273}\frac{t_3}{h^2} \\ &+\mathrm{Pr}\left[-\frac{97063}{407360}\frac{(1-\theta)\partial_x q}{h} - \frac{56327}{203680}\frac{q\partial_x\theta}{h} - \frac{166435}{488832}\frac{t_1\partial_x q}{h} - \frac{20340413}{26885760}\frac{t_2\partial_x q}{h}\right. \\ &-\frac{28729997}{174757440}\frac{t_3\partial_x q}{h} - \frac{225649}{244416}\frac{q\partial_x t_1}{h} + \frac{222059}{4480960}\frac{q\partial_x t_2}{h} + \frac{16530119}{43689360}\frac{q\partial_x t_3}{h} \\ &+\frac{1849169}{1222080}\frac{(1-\theta)\partial_x s_1}{h} + \frac{70164667}{42365440}\frac{(1-\theta)\partial_x s_2}{h} - \frac{11651371}{9776640}\frac{(1-\theta)\partial_x s_3}{h} \\ &\left.+\frac{294637}{76380}\frac{s_1\partial_x\theta}{h} - \frac{122474147}{21182720}\frac{s_2\partial_x\theta}{h} + \frac{88699283}{4888320}\frac{s_3\partial_x\theta}{h}\right] \\ &+\frac{8176}{1273}\frac{(1-\theta)(\partial_x h)^2}{h^2} - \frac{4088}{1273}\mathrm{Bi}\frac{\theta(\partial_x h)^2}{h} + \frac{8176}{1273}\frac{\partial_x h\partial_x\theta}{h}\,, \end{aligned} \tag{D.1f}$$

$$\mathrm{Pr}\partial_t t_2 = \frac{44838}{6365}\left(\frac{1-(1+\mathrm{Bi}h)\theta}{h^2}\right) - \frac{44838}{1273}\frac{t_1}{h^2} - \frac{3231144}{31825}\frac{t_2}{h^2} - \frac{2306304}{31825}\frac{t_3}{h^2}$$

$$
\begin{aligned}
&+\mathrm{Pr}\left[\frac{158337}{2036800}\frac{(1-\theta)\partial_x q}{h}+\frac{158337}{1018400}\frac{q\partial_x\theta}{h}+\frac{2674149}{5703040}\frac{t_1\partial_x q}{h}+\frac{13678523}{313667200}\frac{t_2\partial_x q}{h}\right.\\
&-\frac{446443197}{509709200}\frac{t_3\partial_x q}{h}-\frac{1222929}{2851520}\frac{q\partial_x t_1}{h}-\frac{204549663}{156833600}\frac{q\partial_x t_2}{h}-\frac{336704427}{1019418400}\frac{q\partial_x t_3}{h}\\
&+\frac{97173}{2036800}\frac{(1-\theta)\partial_x s_1}{h}-\frac{490225113}{211827200}\frac{(1-\theta)\partial_x s_2}{h}-\frac{64692369}{81472000}\frac{(1-\theta)\partial_x s_3}{h}\\
&\left.-\frac{352833}{254600}\frac{s_1\partial_x\theta}{h}-\frac{302607783}{105913600}\frac{s_2\partial_x\theta}{h}+\frac{1304283921}{40736000}\frac{s_3\partial_x\theta}{h}\right]\\
&+\frac{44838}{6365}\frac{(1-\theta)(\partial_x h)^2}{h^2}-\frac{22419}{6365}\mathrm{Bi}\frac{\theta(\partial_x h)^2}{h}+\frac{44838}{6365}\frac{\partial_x h\partial_x\theta}{h}\,, \qquad \text{(D.1g)}
\end{aligned}
$$

$$
\begin{aligned}
\mathrm{Pr}\partial_t t_3 \;=\;& \frac{45232}{6365}\left(\frac{1-(1+\mathrm{Bi}h)\theta}{h^2}\right)-\frac{45232}{1273}\frac{t_1}{h^2}-\frac{2818816}{31825}\frac{t_2}{h^2}-\frac{6293056}{31825}\frac{t_3}{h^2}\\
&+\mathrm{Pr}\left[-\frac{7579}{254600}\frac{(1-\theta)\partial_x q}{h}-\frac{7579}{127300}\frac{q\partial_x\theta}{h}-\frac{260999}{2138640}\frac{t_1\partial_x q}{h}+\frac{6804757}{10693200}\frac{t_2\partial_x q}{h}\right.\\
&-\frac{62613409}{139011600}\frac{t_3\partial_x q}{h}+\frac{210079}{1069320}\frac{q\partial_x t_1}{h}-\frac{555439}{1782200}\frac{q\partial_x t_2}{h}-\frac{58821361}{69505800}\frac{q\partial_x t_3}{h}\\
&-\frac{133699}{381900}\frac{(1-\theta)\partial_x s_1}{h}+\frac{8441321}{26478400}\frac{(1-\theta)\partial_x s_2}{h}+\frac{121848419}{30552000}\frac{(1-\theta)\partial_x s_3}{h}\\
&\left.-\frac{95509}{190950}\frac{s_1\partial_x\theta}{h}+\frac{55645211}{13239200}\frac{s_2\partial_x\theta}{h}+\frac{284237129}{15276000}\frac{s_3\partial_x\theta}{h}\right]\\
&+\frac{45232}{6365}\frac{(1-\theta)(\partial_x h)^2}{h^2}-\frac{22616}{6365}\mathrm{Bi}\frac{\theta(\partial_x h)^2}{h}+\frac{45232}{6365}\frac{\partial_x h\partial_x\theta}{h}\,, \qquad \text{(D.1h)}
\end{aligned}
$$

D.2 Three-dimensional with isothermal conditions

$$
\begin{aligned}
\mathcal{R}\,\partial_t q \;=\;& \frac{27}{28}h-\frac{81}{28}\frac{q}{h^2}-33\frac{s_1}{h^2}-\frac{3069}{28}\frac{s_2}{h^2}+\mathcal{R}\left[-\frac{12}{5}\frac{q s_1\partial_x h}{h^2}-\frac{126}{65}\frac{q s_2\partial_x h}{h^2}+\frac{12}{5}\frac{s_1\partial_x q}{h}\right.\\
&+\frac{171}{65}\frac{s_2\partial_x q}{h}+\frac{12}{5}\frac{q\partial_x s_1}{h}+\frac{1017}{455}\frac{q\partial_x s_2}{h}+\frac{6}{5}\frac{q^2\partial_x h}{h^2}-\frac{12}{5}\frac{q\partial_x q}{h}-\frac{6}{5}\frac{q\partial_z p}{h}-\frac{6}{5}\frac{p\partial_z q}{h}\\
&+\frac{6}{5}\frac{qp\partial_z h}{h^2}-\frac{6}{5}\frac{q r_1\partial_z h}{h^2}-\frac{63}{65}\frac{q r_2\partial_z h}{h^2}-\frac{6}{5}\frac{p s_1\partial_z h}{h^2}-\frac{63}{65}\frac{p s_2\partial_z h}{h^2}+\frac{6}{5}\frac{s_1\partial_z p}{h}+\frac{108}{65}\frac{s_2\partial_z p}{h}\\
&\left.+\frac{6}{5}\frac{r_1\partial_z q}{h}+\frac{63}{65}\frac{r_2\partial_z q}{h}+\frac{6}{5}\frac{q\partial_z r_1}{h}+\frac{576}{455}\frac{q\partial_z r_2}{h}+\frac{6}{5}\frac{p\partial_z s_1}{h}+\frac{63}{65}\frac{p\partial_z s_2}{h}\right]\\
&+\eta\left[\frac{5025}{896}\frac{q\left(\partial_x h\right)^2}{h^2}-\frac{5055}{896}\frac{\partial_x q\partial_x h}{h}-\frac{10851}{1792}\frac{q\partial_{x^2}h}{h}+\frac{2027}{448}\partial_{x^2}q+\partial_{z^2}q-\frac{2463}{1792}\frac{\partial_z q\partial_z h}{h}\right.\\
&+\frac{2433}{1792}\frac{q\left(\partial_z h\right)^2}{h^2}-\frac{5361}{3584}\frac{q\partial_{z^2}h}{h}+\frac{7617}{1792}\frac{p\partial_x h\partial_z h}{h^2}-\frac{4749}{3584}\frac{\partial_z p\partial_x h}{h}-\frac{10545}{3584}\frac{\partial_x p\partial_z h}{h}\\
&\left.-\frac{16341}{3584}\frac{p\partial_{xz}h}{h}+\frac{1579}{448}\partial_{xz}p\right]-\frac{27}{28}\zeta h\,\partial_x h+\frac{27}{28}h\left(\partial_{x^3}+\partial_{xz^2}\right)h\,, \qquad \text{(D.2a)}
\end{aligned}
$$

$$
\begin{aligned}
\mathcal{R}\,\partial_t s_1 \;=\;& \frac{1}{10}h-\frac{3}{10}\frac{q}{h^2}-\frac{126}{5}\frac{s_1}{h^2}-\frac{126}{5}\frac{s_2}{h^2}+\mathcal{R}\left[\frac{1}{35}\frac{q\partial_x q}{h}-\frac{3}{35}\frac{q^2\partial_x h}{h^2}+\frac{108}{55}\frac{qs_1\partial_x h}{h^2}\right.\\
&-\frac{5022}{5005}\frac{qs_2\partial_x h}{h^2}-\frac{103}{55}\frac{s_1\partial_x q}{h}+\frac{9657}{5005}\frac{s_2\partial_x q}{h}-\frac{39}{55}\frac{q\partial_x s_1}{h}+\frac{10557}{10010}\frac{q\partial_x s_2}{h}-\frac{2}{35}\frac{q\partial_z p}{h}\\
&+\frac{3}{35}\frac{p\partial_z q}{h}-\frac{3}{35}\frac{qp\partial_z h}{h^2}+\frac{54}{55}\frac{qr_1\partial_z h}{h^2}+\frac{54}{55}\frac{ps_1\partial_z h}{h^2}-\frac{54}{55}\frac{r_1\partial_z q}{h}-\frac{54}{55}\frac{p\partial_z s_1}{h}-\frac{2511}{5005}\frac{ps_2\partial_z h}{h^2}\\
&-\frac{2511}{5005}\frac{qr_2\partial_z h}{h^2}+\frac{2511}{5005}\frac{r_2\partial_z q}{h}+\frac{2511}{5005}\frac{p\partial_z s_2}{h}-\frac{49}{55}\frac{s_1\partial_z p}{h}+\frac{7146}{5005}\frac{s_2\partial_z p}{h}+\frac{3}{11}\frac{q\partial_z r_1}{h}\\
&\left.+\frac{1107}{2002}\frac{q\partial_z r_2}{h}\right]+\eta\left[\frac{93}{40}\frac{q\left(\partial_x h\right)^2}{h^2}-\frac{69}{40}\frac{\partial_x h\partial_x q}{h}+\frac{21}{80}\frac{q\partial_{x^2}h}{h}-\frac{9}{40}\partial_{x^2}q-\frac{57}{80}\frac{\partial_z q\partial_z h}{h}\right.\\
&\left.+\frac{81}{80}\frac{q\left(\partial_z h\right)^2}{h^2}-\frac{3}{40}\frac{q\partial_{z^2}h}{h}+\frac{27}{80}\frac{p\partial_{xz}h}{h}+\frac{21}{16}\frac{p\partial_x h\partial_z h}{h^2}-\frac{63}{80}\frac{\partial_z p\partial_x h}{h}-\frac{9}{40}\frac{\partial_z h\partial_x p}{h}-\frac{9}{40}\partial_{xz}p\right]\\
&-\frac{1}{10}\zeta h\partial_x h+\frac{1}{10}h\left(\partial_{x^3}+\partial_{xz^2}\right)h\,, \qquad \text{(D.2b)}
\end{aligned}
$$

$$
\begin{aligned}
\mathcal{R}\,\partial_t s_2 \;=\;& \frac{13}{420}h-\frac{13}{140}\frac{q}{h^2}-\frac{39}{5}\frac{s_1}{h^2}-\frac{11817}{140}\frac{s_2}{h^2}+\mathcal{R}\left[-\frac{4}{11}\frac{qs_1\partial_x h}{h^2}+\frac{18}{11}\frac{qs_2\partial_x h}{h^2}-\frac{2}{33}\frac{s_1\partial_x q}{h}\right.\\
&-\frac{19}{11}\frac{s_2\partial_x q}{h}+\frac{6}{55}\frac{q\partial_x s_1}{h}-\frac{288}{385}\frac{q\partial_x s_2}{h}-\frac{2}{11}\frac{qr_1\partial_z h}{h^2}-\frac{2}{11}\frac{ps_1\partial_z h}{h^2}+\frac{2}{11}\frac{r_1\partial_z q}{h}+\frac{2}{11}\frac{p\partial_z s_1}{h}\\
&+\frac{9}{11}\frac{qr_2\partial_z h}{h^2}+\frac{9}{11}\frac{ps_2\partial_z h}{h^2}-\frac{9}{11}\frac{r_2\partial_z q}{h}-\frac{9}{11}\frac{p\partial_z s_2}{h}-\frac{8}{33}\frac{s_1\partial_z p}{h}-\frac{10}{11}\frac{s_2\partial_z p}{h}-\frac{4}{55}\frac{q\partial_z r_1}{h}\\
&\left.+\frac{27}{385}\frac{q\partial_z r_2}{h}-\frac{3211}{4480}\frac{q\left(\partial_x h\right)^2}{h^2}\right]+\eta\left[\frac{2613}{4480}\frac{\partial_x h\partial_x q}{h}-\frac{2847}{8960}\frac{q\partial_{x^2}h}{h}+\frac{559}{2240}\partial_{x^2}q+\frac{3029}{8960}\frac{\partial_z q\partial_z h}{h}\right.\\
&-\frac{3627}{8960}\frac{q\left(\partial_z h\right)^2}{h^2}+\frac{299}{17920}\frac{q\partial_{z^2}h}{h}-\frac{559}{1792}\frac{p\partial_x h\partial_z h}{h^2}+\frac{4927}{17920}\frac{\partial_z p\partial_x h}{h}-\frac{533}{17920}\frac{\partial_x p\partial_z h}{h}\\
&\left.-\frac{5993}{17920}\frac{p\partial_{xz}h}{h}+\frac{559}{2240}\partial_{xz}p\right]-\frac{13}{420}\zeta h\partial_x h+\frac{13}{420}h\left(\partial_{x^3}+\partial_{xz^2}\right)h\,, \qquad \text{(D.2c)}
\end{aligned}
$$

$$
\begin{aligned}
\mathcal{R}\,\partial_t p \;=\;& -\frac{81}{28}\frac{p}{h^2}-33\frac{r_1}{h^2}-\frac{3069}{28}\frac{r_2}{h^2}+\mathcal{R}\left[\frac{6}{5}\frac{qp\partial_x h}{h^2}-\frac{6}{5}\frac{p\partial_x q}{h}-\frac{6}{5}\frac{q\partial_x p}{h}+\frac{6}{5}\frac{p^2\partial_z h}{h^2}\right.\\
&+\frac{6}{5}\frac{s_1\partial_x p}{h}+\frac{6}{5}\frac{r_1\partial_x q}{h}+\frac{6}{5}\frac{q\partial_x r_1}{h}+\frac{6}{5}\frac{p\partial_x s_1}{h}-\frac{6}{5}\frac{qr_1\partial_x h}{h^2}-\frac{6}{5}\frac{ps_1\partial_x h}{h^2}-\frac{63}{65}\frac{qr_2\partial_x h}{h^2}\\
&-\frac{63}{65}\frac{ps_2\partial_x h}{h^2}+\frac{63}{65}\frac{s_2\partial_x p}{h}+\frac{63}{65}\frac{q\partial_x r_2}{h}+\frac{108}{65}\frac{r_2\partial_x q}{h}-\frac{12}{5}\frac{pr_1\partial_z h}{h^2}-\frac{12}{5}\frac{p\partial_z p}{h}\\
&\left.+\frac{12}{5}\frac{r_1\partial_z p}{h}+\frac{12}{5}\frac{p\partial_z r_1}{h}+\frac{171}{65}\frac{r_2\partial_z p}{h}+\frac{576}{455}\frac{p\partial_x s_2}{h}-\frac{126}{65}\frac{pr_2\partial_z h}{h^2}+\frac{1017}{455}\frac{p\partial_z r_2}{h}\right]\\
&+\eta\left[\frac{5025}{896}\frac{p(\partial_z h)^2}{h^2}-\frac{5055}{896}\frac{\partial_z p\partial_z h}{h}-\frac{10851}{1792}\frac{p\partial_{z^2}h}{h}-\frac{2463}{1792}\frac{\partial_x p\partial_x h}{h}-\frac{5361}{3584}\frac{p\partial_{x^2}h}{h}+\partial_{x^2}p\right.\\
&+\frac{1579}{448}\partial_{xz}q+\frac{2027}{448}\partial_{z^2}p+\frac{2433}{1792}\frac{p(\partial_x h)^2}{h^2}+\frac{7617}{1792}\frac{q\partial_x h\partial_z h}{h^2}-\frac{10545}{3584}\frac{\partial_z q\partial_x h}{h}\\
&\left.-\frac{4749}{3584}\frac{\partial_x q\partial_z h}{h}-\frac{16341}{3584}\frac{q\partial_{xz}h}{h}\right]-\frac{27}{28}\zeta h\,\partial_z h+\frac{27}{28}h\left(\partial_{x^2z}+\partial_{z^3}\right)h\,, \qquad \text{(D.2d)}
\end{aligned}
$$

$$
\begin{aligned}
\mathcal{R}\,\partial_t r_1 \;=\;& -\frac{3}{10}\frac{p}{h^2} - \frac{126}{5}\frac{r_1}{h^2} - \frac{126}{5}\frac{r_2}{h^2} + \mathcal{R}\left[-\frac{3}{35}\frac{p^2\partial_z h}{h^2} - \frac{3}{35}\frac{qp\partial_x h}{h^2} + \frac{3}{35}\frac{q\partial_x p}{h} + \frac{1}{35}\frac{p\partial_z p}{h} \right. \\
& -\frac{2}{35}\frac{p\partial_x q}{h} + \frac{54}{55}\frac{qr_1\partial_x h}{h^2} + \frac{54}{55}\frac{ps_1\partial_x h}{h^2} - \frac{54}{55}\frac{s_1\partial_x p}{h} - \frac{54}{55}\frac{q\partial_x r_1}{h} + \frac{3}{11}\frac{p\partial_x s_1}{h} - \frac{49}{55}\frac{r_1\partial_x q}{h} \\
& +\frac{108}{55}\frac{pr_1\partial_z h}{h^2} - \frac{103}{55}\frac{r_1\partial_z p}{h} - \frac{39}{55}\frac{p\partial_z r_1}{h} + \frac{1107}{2002}\frac{p\partial_x s_2}{h} - \frac{5022}{5005}\frac{pr_2\partial_z h}{h^2} - \frac{2511}{5005}\frac{qr_2\partial_x h}{h^2} \\
& \left. -\frac{2511}{5005}\frac{ps_2\partial_x h}{h^2} + \frac{2511}{5005}\frac{s_2\partial_x p}{h} + \frac{2511}{5005}\frac{q\partial_x r_2}{h} + \frac{9657}{5005}\frac{r_2\partial_z p}{h} + \frac{7146}{5005}\frac{r_2\partial_x q}{h} + \frac{10557}{10010}\frac{p\partial_z r_2}{h} \right] \\
& +\eta\left[-\frac{69}{40}\frac{\partial_z p\partial_z h}{h} + \frac{93}{40}\frac{p(\partial_z h)^2}{h^2} + \frac{21}{16}\frac{q\partial_x h\partial_z h}{h^2} - \frac{3}{40}\frac{p\partial_{x^2} h}{h} + \frac{81}{80}\frac{p(\partial_x h)^2}{h^2} + \frac{27}{80}\frac{q\partial_{xz} h}{h} \right. \\
& \left. +\frac{21}{80}\frac{p\partial_{z^2} h}{h} - \frac{57}{80}\frac{\partial_x p\partial_x h}{h} - \frac{63}{80}\frac{\partial_x q\partial_z h}{h} - \frac{9}{40}\partial_z q\partial_x h - \frac{9}{40}\partial_{xz} q - \frac{9}{40}\partial_{z^2} p \right] - \frac{1}{10}\zeta h\partial_z h \\
& +\frac{1}{10}h(\partial_{x^2 z} h + \partial_{z^3} h)\,, \qquad \text{(D.2e)}
\end{aligned}
$$

$$
\begin{aligned}
\mathcal{R}\,\partial_t r_2 \;=\;& -\frac{13}{140}\frac{p}{h^2} - \frac{39}{5}\frac{r_1}{h^2} - \frac{11817}{140}\frac{r_2}{h^2} + \mathcal{R}\left[-\frac{2}{35}\frac{p\partial_x q}{h} - \frac{2}{11}\frac{qr_1\partial_x h}{h^2} - \frac{2}{11}\frac{ps_1\partial_x h}{h^2} + \frac{2}{11}\frac{s_1\partial_x p}{h} \right. \\
& +\frac{2}{11}\frac{q\partial_x r_1}{h} - \frac{4}{55}\frac{p\partial_x s_1}{h} - \frac{8}{33}\frac{r_1\partial_x q}{h} - \frac{4}{11}\frac{pr_1\partial_z h}{h^2} - \frac{2}{33}\frac{r_1\partial_z p}{h} + \frac{6}{55}\frac{p\partial_z r_1}{h} + \frac{27}{385}\frac{p\partial_x s_2}{h} \\
& +\frac{18}{11}\frac{pr_2\partial_z h}{h^2} + \frac{9}{11}\frac{qr_2\partial_x h}{h^2} + \frac{9}{11}\frac{ps_2\partial_x h}{h^2} - \frac{9}{11}\frac{s_2\partial_x p}{h} - \frac{9}{11}\frac{q\partial_x r_2}{h} - \frac{19}{11}\frac{r_2\partial_z p}{h} - \frac{10}{11}\frac{r_2\partial_x q}{h} \\
& \left. -\frac{288}{385}\frac{p\partial_z r_2}{h} \right] + \eta\left[+\frac{2613}{4480}\frac{\partial_z p\partial_z h}{h} - \frac{3211}{4480}\frac{p(\partial_z h)^2}{h^2} - \frac{559}{1792}\frac{q\partial_x h\partial_z h}{h^2} + \frac{299}{17920}\frac{p\partial_{x^2} h}{h} \right. \\
& -\frac{3627}{8960}\frac{p(\partial_x h)^2}{h^2} - \frac{5993}{17920}\frac{q\partial_{xz} h}{h} - \frac{2847}{8960}\frac{p\partial_{z^2} h}{h} + \frac{3029}{8960}\frac{\partial_x p\partial_x h}{h} + \frac{4927}{17920}\frac{\partial_x q\partial_z h}{h} \\
& \left. -\frac{533}{17920}\partial_z q\partial_x h + \frac{559}{2240}\partial_{xz} q + \frac{559}{2240}\partial_{z^2} p \right] - \frac{13}{420}\zeta h\partial_z h + \frac{13}{420}h(\partial_{x^2 z} h + \partial_{z^3} h)\,, \qquad \text{(D.2f)}
\end{aligned}
$$

Bibliography

[1] S.V. Alekseenko, V.E. Nakoryakov, and B.G. Pokusaev. *Wave flow in liquid films*. Begell House (New York), third edition, 1994.

[2] R. Aris. *Vectors, Tensors, and the Basic Equations of Fluid Mechanics*. Dover, New York, 1962.

[3] R.W. Atherton and G.M. Homsy. On the derivation of evolution equations for interfacial waves. *Chem. Eng. Comm.*, 2:57–77, 1976.

[4] N.J. Balmforth, G.R. Ierley, and E.A. Spiegel. Chaotic pulse trains. *SIAM J. Appl. Math.*, 54(5):1291–1334, 1994.

[5] A. Bejan. *Convection heat transfer*. Wiley-VCH (New York), 1995.

[6] T.B. Benjamin. Wave formation in laminar flow down an inclined plane. *J. Fluid Mech.*, 2:554–574, 1957. corrigendum, 3:657.

[7] D.J. Benney. Long waves on liquid films. *J. Math. Phys.*, 45:150–155, 1966.

[8] A.L. Bertozzi and M. Pugh. Long-wave instabilities and saturation in thin film equations. *Comm. Pure Appl. Math.*, 51:625–661, 1998.

[9] R.B. Bird, W.E. Stewart, and E.N. Lightfoot. *Transport Phenomena*. John Wiley & Sons, 1960.

[10] R.V. Birikh, V.A. Brisman, M.G. Velarde, and J.C. Legros. *Liquid interfacial systems - oscillations and instability*. Marcel Dekker, Inc., 2003.

[11] W. Boos and A. Thess. Cascade of structures in long-wavelength marangoni instability. *Phys. Fluids*, 11:1633, 1999.

[12] J.P. Burelbach, S.G. Bankoff, and S.H. Davis. Nonlinear stability of evaporating/condensing liquid films. *J. Fluid Mech.*, 195:463–494, 1988.

[13] P.M. Chaikin and T.C. Lubensky. *Principles of Condensed Matter Physics*. Cambridge University Press, 1995.

[14] H.-C. Chang. Wave evolution on a falling film. *Ann. Rev. Fluid Mech.*, 26:103–136, 1994.

[15] H.-C. Chang, M. Cheng, E.A. Demekhin, and D.I. Kopelevitch. Secondary and tertiary excitation of three-dimensional patterns on a falling films. *J. Fluid Mech.*, 270:251–275, 1994.

[16] H.-C. Chang and E.A. Demekhin. *Complex wave dynamics on thin films.* Elsevier, D. Möbius and R. Miller, 2002.

[17] H.-C. Chang, E.A. Demekhin, and E. Kalaidin. Interaction dynamics of solitary waves on a falling film. *J. Fluid Mech.*, 294:123–154, 1995.

[18] H.-C. Chang, E.A. Demekhin, and E. Kalaidin. Generation and suppression of radiation by solitary pulses. *SIAM J. Appl. Math.*, 58(4):1246–1277, 1998.

[19] H.-C. Chang, E.A. Demekhin, and D.I. Kopelevitch. Nonlinear evolution of waves on a vertically falling film. *J. Fluid Mech.*, 250:433–480, 1993.

[20] H.-C. Chang, E.A. Demekhin, and D.I. Kopelevitch. Local stability theory of solitary pulses in an active medium. *Physica D*, 97:353–375, 1996.

[21] K.P. Cheng, W. Saric, and H.A. Stone. On the deviatoric normal stress on a slip surface. *Phys. Fluids*, 12:3280–3281, 2000.

[22] C.I. Christov and M.G. Velarde. Dissipative solitons. *Physica D*, 86:323–347, 1995.

[23] P. Colinet, J.C. Legros, and M.G. Velarde. *Nonlinear Dynamics of Surface-Tension-Driven Instabilities.* Wiley-VCH (New York), 2001.

[24] M.C. Cross and P.C. Hohenberg. Pattern formation outside of equilibrium. *Rev. Mod. Phys.*, 65:851–1112, 1993.

[25] Stephen H. Davis. Thermocapillary instabilities. *Ann. Rev. Fluid Mech.*, 19:403–435, 1987.

[26] E.A. Demekhin, I.A. Demekhin, and V.Y. Shkadov. Solitons in viscous films down a vertical wall. *Izv. Ak. Nauk SSSR, Mekh. Zhi. Gaza*, 4:9–16, 1983.

[27] E.A. Demekhin and M.A. Kaplan. Construction of exact numerical solutions of the stationary traveling type for viscous thin films. *Izv. Ak. Nauk SSSR, Mekh. Zhi. Gaza*, 6:73–81, 1989.

[28] E.A. Demekhin, M.A. Kaplan, and V.Y. Shkadov. Mathematical models of the theory of viscous liquid films. *Izv. Ak. Nauk SSSR, Mekh. Zhi. Gaza*, 6:73–81, 1987.

[29] E.A. Demekhin and V.Y. Shkadov. Three-dimensional waves in a liquid flowing down a wall. *Izv. Ak. Nauk SSSR, Mekh. Zhi. Gaza*, 5:21–27, 1984.

[30] E. Doedel, A. Champneys, T. Fairfrieve, Y. Kuznetsov, B. Sandstede, and X. Wang. Auto 97 continuation and bifurcation software for ordinary differential equations. *Montreal Concordia University*, 1997. AUTO97 and its HOMCONT package are freely distributed and can be found on the web for example at the address: `ftp.concordia.ca/pub/doedel/auto`.

[31] P.G. Drazin. *Nonlinear systems*. Cambridge University Press, 1992.

[32] S. Fauve. *Pattern forming instabilities. Hydrodynamics and Nonlinear Instabilities*. editors C. Godrèche & P. Manneville Cambridge University Press, 1998.

[33] B.A. Finlayson. *The method of weighted residuals and variational principles, with application in fluid mechanics, heat and mass transfer*. Academic Press, 1972.

[34] C.A.J. Fletcher. *Computational Techniques for Fluid Dynamics, 1*. Springer-Verlag (New York), second edition, 1991.

[35] A.M. Frank. 3d numerical simulation of regular structure formation in a locally heated falling film. *Eur. J. Mech. B/Fluids*, 22:445–471, 2003.

[36] B. Friedman. *Principles and techniques of applied mathematics*. John Wiley & Sons, 1956.

[37] D.P. Frisk and E.J. Davis. The enhancement of heat transfer by waves in stratified gas-liquid flow. *Int. J. Heat Mass Transfer*, 15:1537, 1972.

[38] G. F. Froment and K. B. Bischoff. *Chemical Reactor Analysis and Design*. John Wiley & Sons, second edition, 1990.

[39] P.L. Garcia-Ybarra, J.L. Castillo, and M.G. Velarde. Bénard-Marangoni convection with a deformable interface and poorly conducting boundaries. *Phys. Fluids*, 30, 1987.

[40] I. Gimbutis. *Heat transfer to a falling fluid film*. Mosklas, Vilnius, 1988.

[41] B. Gjevik. Occurrence of finite-amplitude surface waves on falling liquid films. *Phys. Fluids*, 13:1918–1925, 1970.

[42] B. Gjevik. Spatially varying finite-amplitude wave trains on falling liquid films. *Acta Polytech. Scand. Me.*, 61:1–16, 1971.

[43] A.A. Golovin, A.A. Nepomnyashchy, and L.M. Pismen. Pattern formation in large-scale marangoni convection with deformable interface. *Physica D*, 81:117–147, 1995.

[44] S.L. Goren and P.V.S. Mani. Mass transfer through horizontal lquid films in wavy motion. *AIChE J.*, 14:57–61, 1968.

[45] D.A. Goussis and R.E. Kelly. On the thermocapillary instabilities in a liquid layer heated from below. *Int. J. Heat Mass Transfer*, 33:2237–2245, 1990.

[46] D.A. Goussis and R.E. Kelly. Surface wave and thermocapillary instabilities in a liquid film flow. *J. Fluid Mech.*, 223:25, 1991. corrigendum in J. Fluid Mech.226:663.

[47] C. Hirsh. *Numerical computation of internal and external flows*. John Wiley & Sons, 1994.

[48] T. Hocherman and P. Rosenau. On ks-type equations describing the evolution and rupture of a liquid interface. *Physica D*, 67:113, 1993.

[49] J.P. Holman. *Heat Transfer*. Mc Graw-Hill, 1989.

[50] P. Huerre and M. Rossi. *Hydrodynamic instabilities in open flows, in 'Hydrodynamics and nonlinear instabilities'*. by C. Godrèche and P. Manneville, Cambridge University Press, 1998.

[51] J.M. Hyman and B. Nicolaenko. *Directions in Partial Differential Equations: Coherence and chaos in Kuramoto-Velarde equation*. by M.G. Grandall, P.H. Rabinovitz and R.E.L. Turner, Academic Press(New York), 1987.

[52] S.W. Joo and S.H. Davis. Instabilities of three-dimensional theory viscous falling films. *J. Fluid Mech.*, 242:529, 1992.

[53] S.W. Joo, S.H. Davis, and S.G. Bankoff. Long-wave instabilities of heated falling films: two-dimensional theory of uniform layers. *J. Fluid Mech.*, 230:117–146, 1991.

[54] S.W. Joo, S.H. Davis, and S.G. Bankoff. A mechanism for rivulet formation in heated falling films. *J. Fluid Mech.*, 321:279–298, 1996.

[55] O.A. Kabov. Heat transfer from a heater with small linear dimension to free falling liquid film. *Proceedings First Russian National Conf. on Heat Transfer*, 6:90–95, 1994.

[56] O.A. Kabov. Heat transfer from a small heater to a falling liquid film. *Heat Transfer Res.*, 27:221, 1996.

[57] O.A. Kabov. Cooling of local heat source by subcooled liquid film. *Invited Lecture, NATO Advanced Study Institute on Energy Conservation Through Heat Transfer Enhancement of Heat Exchangers, May 25 – June 5, 1998, Golden Dolphin, Turkey*, 1998.

[58] O.A. Kabov. Formation of regular structures in a falling liquid film upon local heating. *Thermophys. Aeromech.*, 5:547–551, 1998.

[59] O.A. Kabov and E.A. Chinnov. Heat transfer from a local heat source to a subcooled falling liquid film evaporating in a vapor-gas medium. *Russ. J. Eng. Thermophys.*, 7:1, 1997.

[60] O.A. Kabov, E.A. Chinnov, and J.C. Legros. Three-dimensional deformations in non-uniformly heated falling liquid film at small and moderate reynolds numbers. *In Proceedings of the Conference on Transport Phenomena with Moving Boundaries,* $11^{th} - 12^{th}$ *October, Berlin, Germany*, 2003.

[61] O.A. Kabov, A. Diatlov, and I.V. Marchuk. Heat transfer from a vertical heat source to a falling liquid film. *Proceedings of the First International Symposium on Two-Phase Flow Modelling and Experimentation, Rome*, pages 203–210, 1995.

[62] O.A. Kabov, I.V. Marchuk, and V.M. Chupin. Thermal imaging study of the liquid film flowing on vertical surface with local heat source. *Russ. J. Eng. Thermophys.*, 6:104–138, 1996.

[63] O.A. Kabov, I.V. Marchuk, A.V. Muzykantov, J.C. Legros, E. Istasse, and J.-L. Dewandel. Regular structures in locally heated falling liquid films. 2^{nd} *Intern. Symp. on Two-Phase Flow Modelling and Experimentation, Eds. G.P. Celata, P. Di. Marco and R.K. Shah, May, Pisa (Italy)*, 2:1225–1233, 1999.

[64] O.A. Kabov, B. Scheid, I.V. Marchuk, and J.C. Legros. Free surface deformation by thermocapillary convection in a flowing locally heated thin liquid layer. *Mekh. Zhi. Gaza*, 3:200–208, 2001.

[65] O.A. Kabov, B. Scheid, I.A. Sharina, and J.C. Legros. Heat transfer and rivulet structures formation in a falling thin liquid film locally heated. *Int. J. Therm. Sci.*, 41:664, 2002.

[66] S. Kalliadasis, C. Bielarz, and G.M. Homsy. Steady free-surface thin film flows over topography. *Phys. Fluids*, 12:1889, 2000.

[67] S. Kalliadasis, E.A. Demekhin, C. Ruyer-Quil, and M.G. Velarde. Thermocapillary instability and wave formation on a film flowing down a uniformly heated plane. *J. Fluid Mech.*, 492:303–338, 2003.

[68] S. Kalliadasis, A. Kiyashko, and E.A. Demekhin. Marangoni instability of a thin liquid film heated from below by a local heat source. *J. Fluid Mech.*, 475:377–408, 2003.

[69] P.L. Kapitza and S.P. Kapitza. Wave flow of thin layers of a viscous fluid. In D. Ter Haar, editor, *Collected papers of P.L. Kapitza*, pages 690–709. Pergamon, 1965 (1949).

[70] D. Kataoka and S. Troian. A theoretical study of instabilities at the advancing front of thermally driven coating films. *J. Colloid Interface Sci.*, 192:350–362, 1997.

[71] D. Kataoka and S. Troian. Stabilizing the advancing front of thermally driven climbing films. *J. Colloid Interface Sci.*, 203:335–344, 1998.

[72] T. Kawahara. Formation of saturated solitons ina nonlinear dispersive system with instability and dissipation. *Phys. Rev. Lett.*, 51:381–383, 1983.

[73] T. Kawahara and S. Toh. Pulse interactions in an unstable dissipative-dispersive nonlinear system. *Phys. Fluids*, 31:3103–2111, 1988.

[74] H.B. Keller. *Numerical solution of bifurcation and nonlinear eigenvalue problems*. Applications of bifurcation theory, Rabinowitz P. H., Academic Press(New York), third edition, 1977.

[75] I.L. Kliakhandler, A.V. Porubov, and M.G. Velarde. Localized finite-amplitude disturbances and selection of solitary waves. *Phys. Rev. E*, 62(4):4959–4962, 2000.

[76] S. Krishnamoorthy and B. Ramaswamy. Spontaneous rupture of thin liquid films due to thermocapillarity: A full-scale direct numerical simulation. *Phys. Fluids*, 7:2291, 1995.

[77] O. Levenspiel. *Chemical Reaction Engineering*. John Wiley & Sons, third edition, 1990.

[78] V.G. Levich. *Physico-chemical hydrodynamics*. Fizmatgiz (Moscou), 1959.

[79] S.P. Lin. Finite amplitude side-band stability of a viscous fluid. *J. Fluid Mech.*, 63:417–429, 1974.

[80] S.P. Lin and W.Y. Jiang. The mechanism of suppression or enhancement of three-dimensional surface waves in film flow down a vertical plane. *Phys. Fluids*, 14(2):4088, 2002.

[81] J. Liu and J.P. Gollub. Onset of spatially chaotic waves on flowing films. *Phys. Rev. Lett.*, 70:2289–2292, 1993.

[82] J. Liu and J.P. Gollub. Solitary wave dynamics of film flows. *Phys. Fluids*, 6:1702–1712, 1994.

[83] J. Liu, J.D. Paul, and J.P. Gollub. Measurements of the primary instabilities of film flows. *J. Fluid Mech.*, 250:69–101, 1993.

[84] J. Liu, J.B. Schneider, and J.P. Gollub. Three-dimensional instabilities of film flows. *Phys. Fluids*, 7:55–67, 1995.

[85] I.V. Marchuk and O.A. Kabov. Numerical modeling of thermocapillary reverse flow in thin liquid films under local heating. *Russ. J. Eng. Thermophys.*, 8:17–46, 1998.

[86] I.V. Marchuk and O.A. Kabov. Numerical simulation of heat transfer in a falling liquid film with allowance for heat conduction in heaters. *Russ. J. Eng. Thermophys.*, 10:147–165, 2000.

[87] S. Miladinova, S. Slavtchev, G. Lebon, and J.C. Legros. Long-wave instabilities of non-uniformly heated falling films. *J. Fluid Mech.*, 453:153–175, 2002.

[88] S. Miladinova, D. Staykova, G. Lebon, and B. Scheid. Effect of non-uniform plate heating on the three-dimensional secondary instability of falling films. *Acta Mechanica*, 30:1–13, 2002.

[89] C. Nakaya. Waves on a viscous fluid down a vertical wall. *Phys. FluidsA*, 1:1143, 1989.

[90] A.A. Nepomnyashchy, M.G. Velarde, and P. Colinet. *Interfacial phenomena and convection*. Chapman & Hall/CRC, 2002.

[91] T. Nosoko, P.N. Yoshimura, T. Nagata, and K. Okawa. Characteristics of two-dimensional waves on a falling liquid film. *Chem. Eng. Sci.*, 51:725–732, 1996.

[92] W. Nusselt. Die oberflachenkondensation des wasserdampfes. *Z. VDI*, 50:541–546, 1916.

[93] T. Ooshida. Surface equation of falling film flows with moderate reynolds number and large but finite weber number. *Phys. Fluids*, 11:3247–3269, 1999.

[94] A.C. Or, R.E. Kelly, L. Cortelezzi, and J.L. Speyer. Control of long-wavelength marangoni-bénard convection. *J. Fluid Mech.*, 387:321–341, 1999.

[95] A. Oron. Nonlinear dynamics of three-dimensional long-wave marangoni instability in thin liquid films. *Phys. Fluids*, 12:1633, 2000.

[96] A. Oron. Dynamics of a condensing liquid film under disjoining/conjoining pressures. *Phys. Fluids*, 13:1107, 2001.

[97] A. Oron, S.H. Davis, and S.G. Bankoff. Long-scale evolution of thin liquid films. *Rev. Mod. Phys.*, 69:931–980, 1997.

[98] A. Oron and O. Gottlieb. Nonlinear dynamics of temporally excited falling liquid films. *Phys. Fluids*, 14:2622–2636, 2002.

[99] M.K.R. Panga and V. Balakotaiah. Low-dimensional models for vertically falling viscous films. *Phys. Rev. Lett.*, 90(15):1, 2003.

[100] J.R.A. Pearson. On convection cells induced by surface tension. *J. Fluid Mech.*, 4:489–500, 1958.

[101] R. Perry and D. Green. *Perrys Chemical Engineering Handbook*. Mc Graw-Hill, seventh edition, 1997.

[102] W.H. Press, S.A. Teukolsky, W.T. Vetterling, and B.P. Flannery. *Numerical recipes in C - The Art of Scientific Computing*. Cambridge University Press(New York), second edition, 1992.

[103] A. Pumir, P. Manneville, and Y. Pomeau. On solitary waves running down an inclined plane. *J. Fluid Mech.*, 135:27–50, 1983.

[104] B. Ramaswamy, S. Chippada, and S.W. Joo. A full-scale numerical study of interfacial instabilities in thin-film flows. *J. Fluid Mech.*, 325:163–194, 1996.

[105] B. Ramaswamy, S. Krishnamoorthy, and S.W. Joo. Three-dimensional simulation of instabilities and rivulet formation in heated falling films. *J. Comp. Phys.*, 131:70–88, 1997.

[106] P. Rosenau, A. Oron, and J.M. Hyman. Bounded and unbounded patterns of the benney equation. *Phys. FluidsA*, 4(6):1102, 1992.

[107] C. Ruyer-Quil. *Dynamique d'un film mince s'écoulant le long d'un plan incliné*. PhD thesis, École polytechnique, LadHyx, France, 1999.

[108] C. Ruyer-Quil and P. Manneville. Modeling film flows down inclined planes. *Eur. Phys. J.B*, 6:277–292, 1998.

[109] C. Ruyer-Quil and P. Manneville. Improved modeling of flows down inclined planes. *Eur. Phys. J.B*, 15:357–369, 2000.

[110] C. Ruyer-Quil and P. Manneville. Further accuracy and convergence results on the modeling of flows down inclined planes by weighted-residual approximations. *Phys. Fluids*, 14:170–183, 2002.

[111] C. Ruyer-Quil, B. Scheid, S. Kalliadasis, M.G. Velarde, and R.Kh. Zeytounian. Thermocapillary long waves in a liquid film flow. part 1. low dimensional formulation. *submitted to J. Fluid Mech.*, 2003.

[112] C. Ruyer-Quil, B. Scheid, and P. Manneville. Onset of three-dimensional instabilities of film flows. *in preparation*, 2004.

[113] Christian Ruyer-Quil. Inertial corrections to the Darcy law in a Hele-Shaw cell. *C. R. Acad. Sci. Série IIb*, 329:337–342, 2001.

[114] Christian Ruyer-Quil and Paul Manneville. Comment on "low-dimensional models for vertically falling viscous films". submitted to Phys. Rev. Lett., 2003.

[115] T.R. Salamon, R.C. Armstrong, and R.A. Brown. Traveling waves on vertical films: Numerical analysis using the finite element method. *Phys. Fluids*, 5:2202, 1994.

[116] B. Scheid. Study of thermocapillary effects on locally heated falling liquid films. *Student thesis, DEC2 in Applied Sciences*, ULB - Chimie-Physique E.P., 1999.

[117] B. Scheid. Study of the marangoni effect on the velocity and the temperature fields on falling liquid film locally heated. *Student thesis, DEA in Applied Sciences*, ULB - Chimie-Physique E.P., 2000.

[118] B. Scheid. Nonlinear evolution of non-uniformly heated falling liquid films. *Student thesis, Civil Engineer in electromechanics*, ULB - Chimie-Physique E.P., 2001.

[119] B. Scheid, O.A. Kabov, C. Minetti, P. Colinet, and J.C. Legros. Measurement of free surface deformation by reflectance-schlieren method. *Proc.* 3^{rd} *Eur. Thermal-Sci. Conf., Heidelberg*, 2:651–657, 2000.

[120] B. Scheid, A. Oron, P. Colinet, U. Thiele, and J.C. Legros. Nonlinear evolution of non-uniformly heated falling liquid films. *Phys. Fluids*, 14:4130, 2002.

[121] B. Scheid, C. Ruyer-Quil, S. Kalliadasis, M.G. Velarde, and R.Kh. Zeytounian. Thermocapillary long waves in a liquid film flow. part 2. linear stability and nonlinear waves. *submitted to J. Fluid Mech.*, 2003.

[122] B. Scheid, C. Ruyer-Quil, U. Thiele, O.A. Kabov, J.C. Legros, and P. Colinet. Validity domain of the benney equation including marangoni effect for closed and open flows. *submitted to J. Fluid Mech.*, 2004.

[123] H. Schlichting. *Boundary-Layer Theory.* Mc Graw-Hill, seventh edition, 1979.

[124] B.-C. Schulze. Economical aspects of heat transfer enhancement in falling film evaporators. *ASE (Advanced Services & Engineering)*, pages 1–17, 1999.

[125] L.E. Scriven and C.V. Sterling. On cellular convection driven surface tension gradients: effects of mean surface tension and surface viscosity. *J. Fluid Mech.*, 19:321–340, 1964.

[126] V.Y. Shkadov. Wave flow regimes of a thin layer of viscous fluid subject to gravity. *Izv. Ak. Nauk SSSR, Mekh. Zhi. Gaza*, 2:43–51, 1967. english translation in *Fluid Dynamics***2** (Faraday Press, N.Y., 1970), 29-34.

[127] V.Y. Shkadov. Solitary waves in a layer of viscous liquid. *Izv. Ak. Nauk SSSR, Mekh. Zhi. Gaza*, 1:63–66, 1977.

[128] J.M. Skotheim, U. Thiele, and B. Scheid. On the instability of a falling film due to localized heating. *J. Fluid Mech.*, 475:1, 2003.

[129] K.A. Smith. On convective instability induced by surface gradients. *J. Fluid Mech.*, 24:401–414, 1966.

[130] M.K. Smith. The mechanism for the long-wave instability in thin liquid films. *J. Fluid Mech.*, 217:469–485, 1990.

[131] M.A. Spaid and G.M. Homsy. Stability of newtonian and viscoelastic dynamic contact lines. *Phys. Fluids*, 8:460, 1995.

[132] S. Sreenivasan and S.P.Lin. Surface tension driven instability of a liquid film flow down a heated incline. *Int. J. Heat Mass Transfer*, 21:1517, 1978.

[133] M. Takashima. Surface driven instability in a horizontal liquid layer with a deformable free surface. *J. Phys. Soc. Japan*, 50:2745–2756, 1981.

[134] M.J. Tan, S.G. Bankoff, and S.H. Davis. Steady thermocapillary flows of thin liquid layers. *Phys. FluidsA*, 2:313–321, 1966.

[135] U. Thiele and E. Knobloch. Front and back instability of a liquid film on a slightly inclined plate. *Phys. Fluids*, 15:892–907, 2003.

[136] U. Thiele and E. Knobloch. Thin liquid films on a slightly inclined heated plate. *Physica D*, 190:213–248, 2004.

[137] U. Thiele, K. Neuffer, M. Bestehorn, Y. Pomeau, and M.G. Velarde. Sliding drops on an inclined plane. *Colloid Surf. A*, 206:87–104, 2002.

[138] U. Thiele, M.G. Velarde, and K. Neuffer. Dewetting: Film rupture by nucleation in the spinodal regime. *Phys. Rev. Lett.*, 87(2):1–4, 2001.

[139] P.M.J. Trevelyan, S. Kalliadasis, J.H. Merkin, and S.K. Scott. Dynamics of a vertically falling film in the presence of a first chemical reaction. *Phys. Fluids*, 14:2402, 2002.

[140] Yu. Ya. Trifonov. Bifurcations of two-dimensional into three-dimensional wave regimes for a vertically flowing liquid film. *Izv. Ak. Nauk SSSR, Mekh. Zhi. Gaza*, 5:109–114, 1989.

[141] S.J. VanHook, M.F. Schatz, J.B. Swift, W.D. McCormick, and H.L. Swinney. Long wavelength surface-tension-driven benard convection: Experiment and theory. *J. Fluid Mech.*, 345:45–78, 1997.

[142] M.G. Velarde and R.K. Zeytounian. *Interfacial phenomena and the marangoni effect*. CISM courses and lectures n° 428, Springer Wien New York, 2002.

[143] M. Vlachogiannis and V. Bontozoglou. Observations of solitary wave dynamics of film flows. *J. Fluid Mech.*, 435:191, 2001.

[144] R.W. Weast and S.M. Selby. *Handbook of Chemistry and Physics*. The Chemical Rubber CO. (Ohio), 63^{th} edition, 1966.

[145] G.B. Whitham. *Linear and nonlinear waves*. John Wiley & Sons, 1974.

[146] C.-S. Yih. Stability of two-dimensional parallel flows for three dimensional disturbances. *Quart. Appl. Math.*, 12:434, 1955.

[147] C.-S. Yih. Stability of liquid flow down an inclined plane. *Phys. Fluids*, 6:321–334, 1963.

[148] L.-Q. Yu, F.K. Wasden, A.E. Dukler, and V. Balakotaiah. Nonlinear evolution of waves on falling films at high reynolds numbers. *Phys. Fluids*, 7:1886–902, 1995.

[149] R.Kh. Zeytounian. The Bénard–Marangoni thermocapillary-instability problem. *Phys.–Uspekhi*, 41:241–267, 1998.

[150] `http://polysep.ucla.edu/c210/Femlab/porous%20catalyst%20pellet_files/chemmod4.htm`.

[151] `http://www.sulzer.com/com/NewsAndMedia/TechnicalReview/Archive/2003_2_Stepanski_e.pdf`.

[152] `http://www.apv.com/Technologies/Downloads/Evaporator_HB.pdf`.

[153] `http://www.cheresources.com/evapzz.shtml`.

[154] `http://www.alaquainc.com/ÂlaquaInc/products/evaporator.asp`.

Summary

This thesis analyses the dynamics of a thin liquid film falling down a heated plate. The heating yields surface tension gradients that induce thermocapillary stresses on the free surface, thus affecting the stability and the evolution of the film. Accounting for the coherence of the flow due to viscosity, two main approaches that reduce the dimensionality of the original problem are usually considered depending on the flow rate (as measured by the Reynolds number): the 'long wave' asymptotic expansion for small Reynolds numbers and the 'integral boundary layer' approximation for moderate Reynolds numbers. The former suffers from singularities and the latter from incorrectness of the instability threshold for the occurrence of hydrodynamic waves. Thus, the aim of this thesis is twofold: in a first part, we define quantitatively the validity of the 'long wave' evolution equation (Benney equation) for the film thickness h including the thermocapillary effect; and in a second part, we improve the 'integral boundary layer' approach by combining a gradient expansion to a weighted residual method. In the **first part**, we further investigate the Benney equation in its validity domain in the case of periodically inhomogeneous heating in the streamwise direction. It induces steady-state deformations of the free surface with increased transfer rate in regions where the film is thinner, and also in average. The inhomogeneities of the heating also modify the nature of travelling wave solutions at moderate temperature gradients and allows for suppressing wave motion at larger ones. Moreover, large temperature gradients (for instance positive ones) in the streamwise direction produce large local film thickening that may in turn become unstable with respect to transverse disturbances such that the flow may organize in rivulet-like structures. The mechanism of such instability is elucidated via an energy analysis. The main features of the rivulet pattern are described experimentally and recovered by direct numerical simulations. In the **second part**, various models are obtained, which are valid for larger Reynolds numbers than the Benney equation and account for second-order viscous and inertial effects. We then elaborate a strategy to select the optimal model in terms of linear stability properties and existence of nonlinear solutions (solitary waves), for the widest possible range of parameters. This model – called *reduced model* – is a system of three coupled evolution equations for the local film thickness h, the local flow rate q and the surface temperature θ. Solutions of this model indicate that the interaction of the hydrodynamic and thermocapillary modes is non-trivial, especially in the region of large-amplitude solitary waves. Finally, the three-dimensional evolution of the solutions of the *reduced model* in the presence of periodic forcing and noise compares favourably with available experimental data in isothermal conditions and with direct numerical simulations in non-isothermal conditions.

Key words: thin films, long-wave expansion, interfacial instabilities, thermocapillarity, solitary waves, rivulet-like patterns, weighted residuals

Résumé

Cette thèse analyse la dynamique d'un film mince s'écoulant le long d'une paroi chauffée. Le chauffage crée des gradients de tension superficielle qui induisent des tensions thermocapillaires à la surface libre, altérant ainsi la stabilité et l'évolution du film. Grâce à la cohérence de l'écoulement assurée par la viscosité, deux approches permettant de réduire la dimensionnalité du problème original sont habituellement considérées suivant le débit (mesuré par le nombre de Reynolds): l'approximation asymptotique dite 'longues ondes' pour les faibles nombres de Reynolds et l'approximation 'intégrale couche limite' pour les nombres de Reynolds modérés. Cependant, la première approximation souffre de singularités et la dernière de prédictions imprécises du seuil de stabilité des ondes hydrodynamiques à la surface du film. Le but de cette thèse est donc double: dans une première partie, il s'agit de déterminer, de manière quantitative, la validité de l'équation d'évolution 'longues ondes' (ou équation de Benney) pour l'épaisseur du film h, en y incluant l'effet thermocapillaire; et dans une seconde partie, il s'agit d'améliorer l'approche 'intégrale couche limite' en combinant un développement en gradients avec une méthode aux résidus pondérés. Dans la **première partie**, nous étudions l'équation de Benney, dans son domaine de validité, dans le cas d'un chauffage inhomogène et périodique dans la direction de l'écoulement. Cela induit des déformations permanentes de la surface libre avec un accroissement du transfert de chaleur dans les régions où le film est plus mince, mais aussi en moyenne. Un chauffage inhomogène modifie également la nature des solutions d'ondes progressives pour des gradients de températures modérés et conduit même à leur suppression pour des gradients de températures plus importants. De plus, ceux-ci, lorsqu'ils sont par exemple positifs le long de l'écoulement, produisent des épaississements localisés du film qui peuvent à leur tour devenir instables par rapport à des perturbations suivant la direction transverse à l'écoulement. Ce dernier s'organise alors sous forme d'une structure en rivulets. Le mécanisme de cette instabilité est élucidé via une analyse énergétique des perturbations. Les principales caractéristiques des structures en rivulets sont décrites expérimentalement et retrouvées par l'intermédiaire de simulations numériques. Dans la **seconde partie**, nous dérivons une famille de modèles valables pour des nombres de Reynolds plus grands que l'équation de Benney, qui prennent en compte les effets visqueux et inertiels du second ordre. Nous élaborons ensuite une stratégie pour sélectionner le modèle optimal en fonction de ses propriétés de stabilité linéaire et de l'existence de solutions non-linéaires (ondes solitaires), et ce pour la gamme de paramètres la plus large possible. Ce modèle – appelé *modèle réduit* – est un système de trois équations d'évolution couplées pour l'épaisseur locale de film h, le débit local q et la température de surface θ. Les solutions de ce modèle indiquent que l'interaction des modes hydrodynamiques et thermocapillaires n'est pas triviale, spécialement dans le domaine des ondes solitaires de grande amplitude. Finalement, l'évolution tri-dimensionnelle des solutions du *modèle réduit* en présence d'un forçage périodique ou d'un bruit se compare favorablement aux données expérimentales disponibles en conditions isothermes, ainsi qu'aux simulations numériques directes en conditions non-isothermes.

Mots-clés: films minces, développement longues ondes, instabilités interfaciales, thermocapillarité, ondes solitaires, structure en rivulets, résidus pondérés